This is to certify that the

dissertation entitled

Microwave Processing of Ceramics and Ceramic Composites Using a Single-Mode Microwave Cavity

presented by

Ki-Yong Lee

has been accepted towards fulfillment
of the requirements for

Ph.D. degree in Materials Science

Elden D. Case
Major professor

Date May 13, 1998

MICROWAVE PROCESSING OF CERAMICS AND CERAMIC COMPOSITES USING A SINGLE-MODE MICROWAVE CAVITY

By

Ki-Yong Lee

A DISSERTATION

Submitted to
Michigan State University
in partial fulfillment of the requirements
for the degree of

DOCTOR OF PHILOSOPHY

Department of Materials Science and Mechanics

1998

ABSTRACT

MICROWAVE PROCESSING OF CERAMICS AND CERAMIC COMPOSITES USING A SINGLE-MODE MICROWAVE CAVITY

By

KI-YONG LEE

This research seeks i) to use a single-mode microwave cavity to process ceramics and ceramic based composites, ii) to study the conditions or parameters needed to successfully apply the microwaves to processing of materials, and iii) to study the interactions between materials and microwaves.

In sintering studies, alumina ceramics and alumina matrix 10wt% zirconia composites were microwave-heated between 1500°C and 1600°C giving a density of about 96% up to nearly 100% of theoretical without 'thermal runaway' or cracking. The density, hardness, and toughness for individually- and batch-processed specimens were relatively uniform with respect to the cavity mode and specimens' location inside the insulation called 'casket' during microwave heating. For example, the mean and standard deviation of the hardness was 16.19 GPa ± 0.58 GPa for a total of 24 alumina specimens microwave-heated in batches of 6 specimens each. This corresponds to a coefficient of variation of only 0.036.

Microwave power was successfully utilized to burn out organic binder from ceramic powder compacts without cracking the specimens and without using any insulation

material to enclose the specimens. The extent of binder burn-out significantly depended on material composition due to the dielectric properties of each material. For example, Al_2O_3/10wt% SiC burned out the binder more successfully than either monolithic alumina or alumina containing 10wt% zirconia.

In a joining study, ceramic materials and glass ceramics were successfully joined using a spin-on material interlayer under ambient or low externally applied pressures. Notches of submillimeter dimension were made in the specimens prior to joining. During the joining process the notch dimensions changed by no more than a few percent.

In addition, this study revealed that compared to conventional heating, microwave heating has remarkable effects in crack healing. For alumina specimens with initial Vickers cracks about 350μm long, the cracks were nearly completely healed by microwave heating at 1742K, while conventional heating healed the identical cracks by only about 40% to 50% of the initial crack length.

In microwave hybrid heating utilizing a casket, the casket plays an important role. The measured steady-state inner wall casket temperature, T_i, varied from about 1100°C to 1500°C depending on the casket geometry at 600 Watts input power. In addition, for a microwave input power of 200 Watts to 700 Watts, T_i ranged from 740°C to 1574°C depending on a combination of casket geometry and microwave power. Based on the experimental data, a simple model equation was developed to describe T_i in terms of the casket geometry and the microwave power level. A least-squares fitting indicated that the model equation well described the experimental data obtained in this study. The R^2, coefficient of determination value was 0.954 for all 144 data used for fitting without grouping the data.

To

the memory of my deceased father, Duk-Ho Lee.

ACKNOWLEDGMENTS

I would like to thank my adviser, Professor Eldon D. Case for providing me the opportunity to perform this research and to continue my graduate studies under his direction. His continuous encouragement, guidance, advice, and support were invaluable to the completion of this work. It was a joy to work together with Dr. Case. Every moment we spent on working together will be remembered in my heart forever.

My thanks are extended to Dr. Asmussen, Dr. Bieler, and Dr. Eick for being my committee members. In particular, Professor Asumssen's academic counsel and financial support throughout this work are greatly appreciated.

Special thanks should go to Brett Wilson for the help with lab apparatuses and for the instruction with lab skills. I would like to appreciate the help of Jong-Gi Lee, Benjamin Tyszka, Martin Traub, Kiersten Seiber, Luke Cropsey, and Paul Dearhouse on some of work included in this thesis. I also thank Ung-Sik Kim, Bo-Keun Kim, and Mark Perin for the helpful discussion.

I gratefully thank my mother, Jung-Sook Kang and my deceased father, Duk-Ho Lee who gave me their endless love, care and support. Finally, I wish to thank my wife, Sun-Hee Lee, my daughter, Mee-Sul, and my son, Dong-Hoon for their love and understanding. Especially, without my wife's patience and encouragement, I could not have completed this work.

TABLE OF CONTENTS

APPEN

APPEN

APPEN

APPE

APPE

APPE

APPE

APPE

LIST OF TABLES

LIST OF FIGURES

INTRODUCTION

For the last decade, microwave processing of materials (including inorganic and organic materials) has been intensively developed and established since microwave processing as a relatively new technology is known to provide many potential advantages; energy savings, reduced processing time, and uniform and enhanced physical properties of processed materials due to inherent heating characteristics of microwave heating such as rapid, internal and volumetric heating characteristics. However, unlike food processing by well-developed user-friendly microwave ovens, microwave processing of materials encounters problems such as inability to heat low dielectric-loss ceramics, thermal runaway, cracking, non-uniform heating, etc. Also, compared to conventional heating, microwave heating can be relatively complex in that it requires not only fundamentals of material processing but also various disciplines such as electromagnetics, material science, physics, thermodynamics, etc. to better understand the interactions between microwave energy and materials, and in turn to optimize a specific material process. Thus without a high degree of technical knowledge and economic consideration, one may not succeed in using microwave energy as versatile tools to effectively process various types of materials.

The subtopics of the research included in this study are i) literature review and theoretical background for microwave processing (Introduction), ii) sintering (Chapter 1),

iii) binder burn-out (Chapter 2), iv) joining (Chapter 3), v) crack healing (Chapter 4), vi) effects of casket geometry and microwave power on microwave heating (Chapter 5), and vii) thermal etching (Chapter 6). The experimental procedures, results and discussion will be addressed under each subtopic.

Additional experimental data and results obtained in this study are included in APPENDICES. In particular, Appendices A and B include photos of microwave processing apparatus and material properties for microwave susceptor materials ("caskets") generally used for microwave heating in this study. Appendices I, II, III, IV, V, and VI include additional data for Chapters 1, 2, 3, 4, 5 and 6, respectively.

1. GOALS OF THIS STUDY

This study explores various aspects of microwave processing of ceramics (sintering, binder burn-out, and joining). In addition, the relationship between casket geometry and steady-state temperature of the microwave-heated casket is studied in order to provide a means of designing the microwave caskets required for sintering and joining. Also, thermal etching is studied in order to obtain information on mass diffusion during microwave heating, since diffusion is important in all high temperature processing of ceramics.

1.1. For Sintering

The goal is to use a single-mode microwave cavity to sinter low dielectric-loss ceramic materials such as aluminas and alumina matrix composites without problems such as thermal runaway and cracking (Chapter 1) [1-3]. In addition, the

alumina/zirconia particulate composites sintered in both the microwave cavity and the conventional furnace are to be compared in terms of microstructures and densities as a function of maximum hold temperatures for final densification.

1.2. For Binder Burn-out

Organic binders were burnt out from ceramic powder compacts without placing the specimens in a refractory casket. The smoke and volatiles produced during burn-out were removed more efficiently than would be the case if the specimens were enclosed in a refractory casket (Chapter 2) [4-6]. Also, the binder burn-out research seeks to maximize the binder burn-out rate without inducing cracking in the ceramic powder compacts.

1.3. For Joining

Joining of monolithic and composite ceramic materials used a spin-on interlayer (Chapter 3) [7,8]. Materials joined included alumina, alumina composites, and MaCor™, a commercial glass ceramic. The joints should be mechanically strong, such that the bond strength is an appreciable fraction (say, at least 50%) of the strength of the bulk material, where the bond strength will in part be assessed by an indentation crack deflection at the interface. The work joined densified ceramic components, machining holes and/or channels of submillimeter dimension in individual components, and then joining the components while not modifying the dimensions of the channels or holes by more than a few percent.

1.4. For Crack Healing

Distributed damage due to microcracks can affect a variety of material properties such as elastic modulus, strength, and toughness. Reducing the size and/or the number density of microcracks can enhance material properties. Also the gap between the components to be joined can be considered as a crack. To better understand the mechanism for joining ceramics using microwaves as well as to study crack healing itself, a study was performed on crack healing of Vickers-indented polycrystalline alumina via both microwave heating and conventional heating (Chapter 4) [9]. The crack healing rates for both the heating methods were analyzed and compared utilizing a model equation reported in the literature.

1.5. For Thermal Etching

Microwave sintering and joining (which are included in this study) are performed at high temperatures, at which diffusion plays an important role. However, it is still unknown what diffusion mechanism dominates during microwave heating. This study includes AFM measurements of grooving width, depth and angles for both conventionally- and microwave-etched polycrystalline alumina specimens (Chapter 6) [10,11]. From the AFM data we should be able to calculate activation energies for diffusion during microwave heating.

The thermal etching studies will be done in tandem with crack healing studies (Crack healing in ceramics is an important potential processing step that might be employed after components have been densified and has been ground to a final shape). Crack healing itself is likely to be closely related to the joining process.

1.6. For Effect of Casket Geometry on Microwave Heating

In microwave hybrid heating which utilizes a casket composed of a microwave susceptor material, the casket plays an important role by providing thermal insulation and preheating a low dielectric-loss material to be microwave-processed. The effect of casket geometry was investigated for caskets composed of hollow, partially stabilized zirconia cylinder with aluminosilicate end plates (Chapter 5) [12,13]. The length of the casket used in this study ranged from 4 cm to 7 cm. The inner radius, a, of the casket ranged from 2.54cm to 3.81cm, while the outer radius, b, ranged from 3.81cm to 5.08cm, yielding the radius ratio, b/a of 1.27 to 2.00. Future study may include zirconia cylinders having inner radii of 1.27cm and/or 5.08cm.

The partially stabilized zirconia cylinders were selected for the casket geometry/microwave heating study since sintering and joining work included in this study used these materials. In addition, other researchers have used zirconia and/or aluminosilicate specimen enclosures (caskets) [14-19].

2. GENERAL LITERATURE REVIEW

During the last decade, interest has grown in microwave processing of materials. Many attractive advantages of the new and exciting technology of processing materials utilizing microwaves have been well documented in the literature including MRS Symposium Proceedings volumes 124 [20], 189 [21], 269 [22], 347 [23], and 430 [24], and Ceramic Transactions, volumes 21 [25], 36 [26], and 59 [27].

2.1. DIFFERENCES BETWEEN MICROWAVE AND CONVENTIONAL HEATING

Microwave heating is fundamentally different from conventional heating (Figure 1) [28]. Electrical furnaces used for conventional heating of materials are composed of heating elements and insulation (Figure 1a). For microwave heating, the cavity used to heat the material is composed of a metal shell and microwave port through which electromagnetic waves are guided into the cavity from the microwave power supply (Figure 1b). In conventional processing heat is generated by an external heating source which deposits thermal energy on the surface of the material. Subsequently this thermal energy is transferred to the center of the material by thermal diffusion. In microwave processing, heat is created within the material through the interactions between electromagnetic fields and the molecular and electronic structure of the material.

As a result of the inherent difference between microwave and conventional heating, the thermal gradients and the heat flow in microwave processed materials are opposite to those in conventionally heated materials (Figure 2) [29]. As a consequence, one can heat

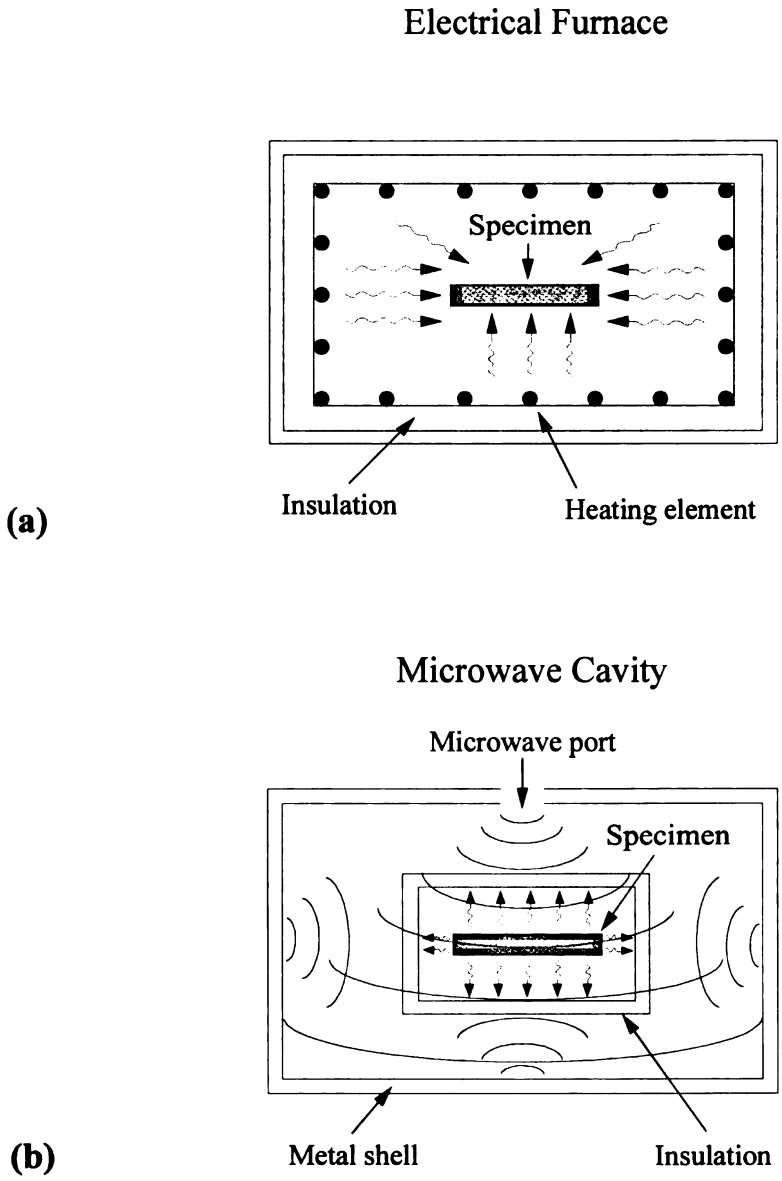

Figure 1. Heating patterns in conventional (a) and microwave furnaces (b) [28].

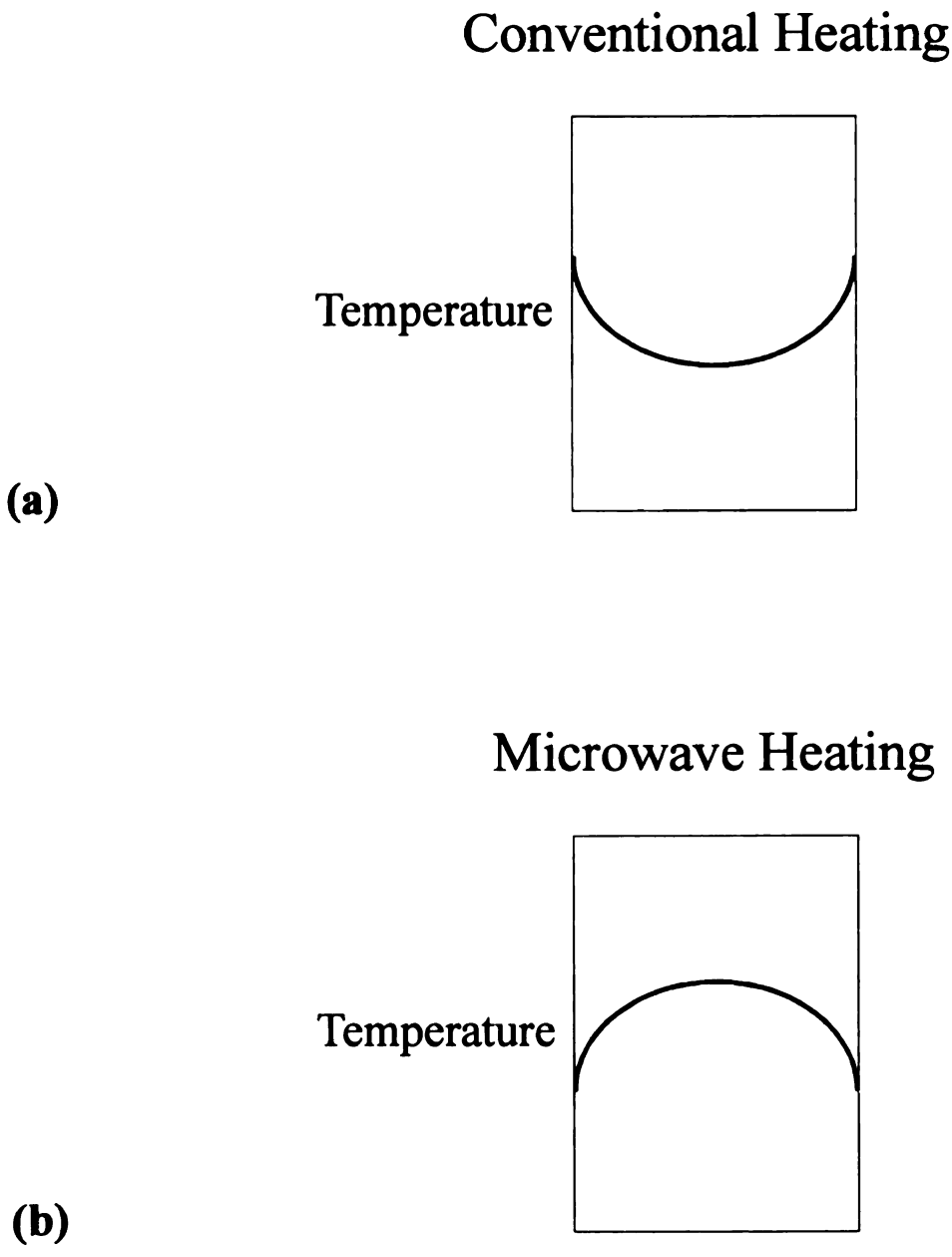

Figure 2. Temperature gradients generated during conventional (a) and microwave (b) heating of materials [29].

materials very rapidly and uniformly by microwave processing. Due to these inherent heating characteristics of microwave heating, many attractive advantages have been proposed and proved in literature. For example, an Ontario Ministry of Energy study [30] showed microwave drying and sintering uses less energy than conventional drying and sintering by a factor of about two and ten, respectively. In addition to the energy savings, the nature of microwave heating (i.e. internal and volumetric heating) results in a set of "microwave effects," including lower sintering temperatures and a considerable decrease in processing time [31,32], smaller grain sizes [33], and lower diffusional activation energies [32] compared to conventional processing. Also, several researchers [34-36] report microwave processing improves microstructure and mechanical properties.

Janney and Kimrey [31] reported that Al_2O_3, doped with 0.1 wt% MgO and sintered under vacuum by 28 GHz microwave energy was densified much faster than by conventional sintering (Figure 3). The apparent activation energy calculated for microwave sintering was 160 kJ/mol, which was much lower than 575 kJ/mol for conventional sintering (Figure 4a) [31]. Janney and Kimrey [37] also compared grain growth in microwave annealed alumina with conventional annealing results (Figure 4b). The apparent activation energy for microwave grain growth using the Arrhenius rate equation was 480 kJ/mol, which was about 20% lower than 590 kJ/mol for conventional grain growth (Figure 4b) [37]. The activation energies for conventional annealing and sintering agree well with each other, while the activation energy for microwave sintering does not agree with the activation energy for microwave annealing. The difference in activation energies may be due to different sintering mechanisms dominating the microwave processes compared to conventional processes [37].

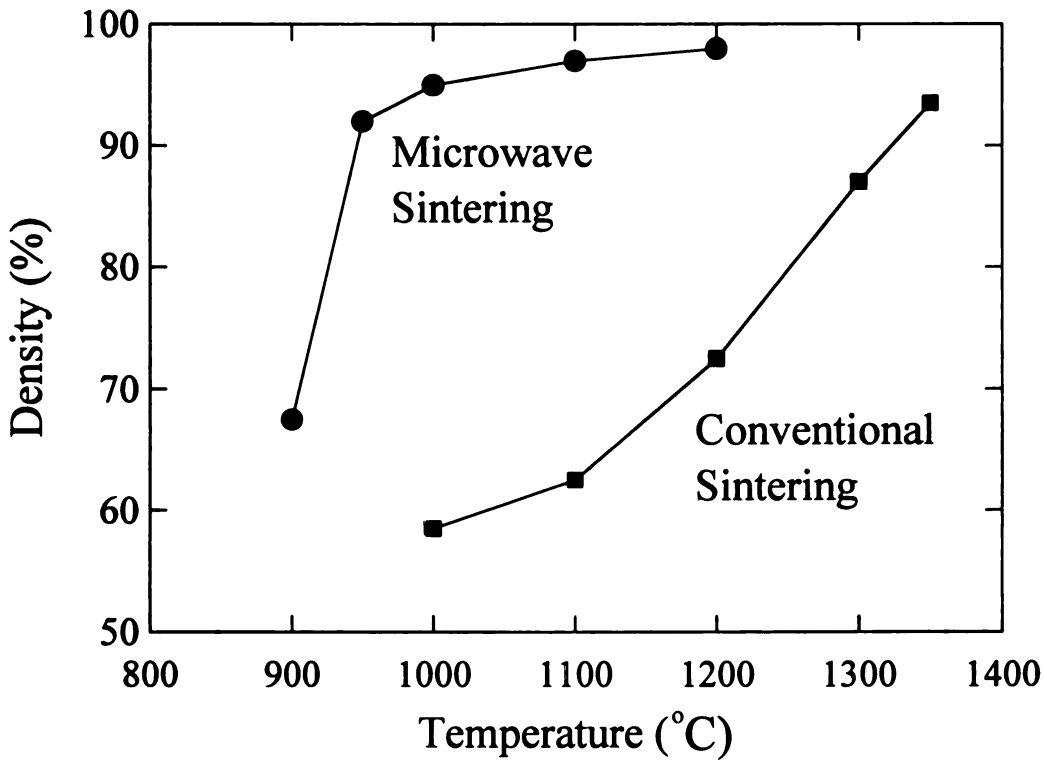

Figure 3. Density versus temperature of microwave (28 GHz) and conventionally sintered MgO doped alumina [31].

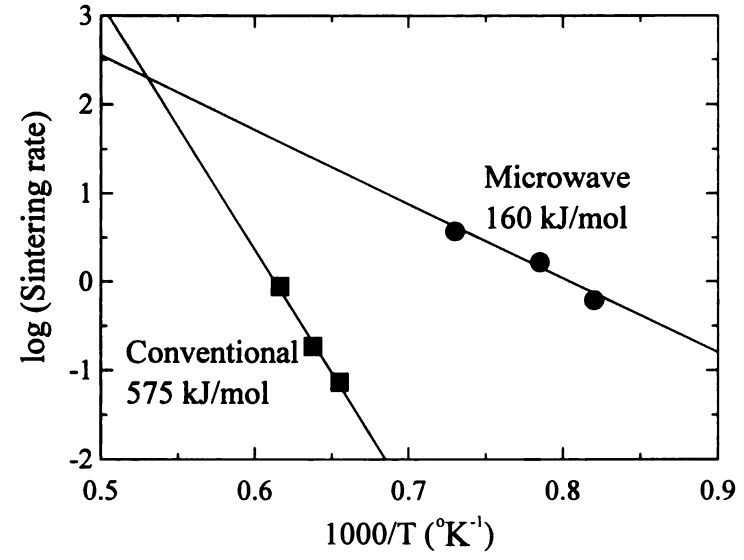

(a)

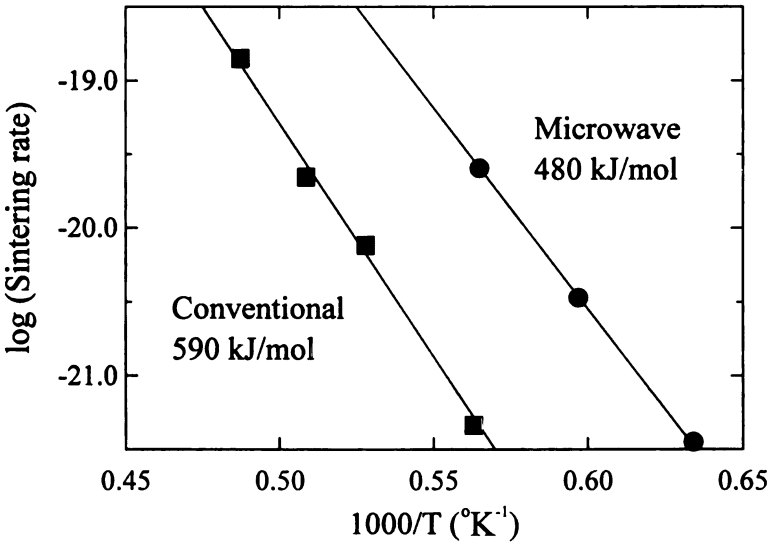

(b)

Figure 4. (a) The apparent activation energies for microwave (28 GHz) and conventionally sintered MgO doped alumina [31] and (b) the apparent activation energies for microwave (28 GHz) and conventional grain growth of MgO doped alumina [37].

2.2. FUNDAMENTALS OF MICROWAVE HEATING

2.2.1. Interactions between Microwaves and Materials

The term '*microwave*' refers to alternating current signals with frequencies between 300 MHz (3×10^8 Hz) and 300 GHz (3×10^{11} Hz) [38]. For a microwave signal, the period, $T = 1/f$, ranges from 3 ns (3×10^{-9} sec) to 3 ps (3×10^{-12} sec), respectively. The corresponding wavelengths range from $\lambda = c/f = 1$ meter to $\lambda = 1$ millimeter, respectively, where $c = 3 \times 10^8$ meter/sec, the speed of light in vacuum.

The frequency range used for microwave heating lies between 400 MHz and 40 GHz [39]. However, the allowed frequencies are restricted to discrete bands (Table 1) [39]. Most microwave frequency bands are used for communications and radar, which is regulated by the Federal Communications Commission (Internet address, http://www.fcc.gov). The FCC allocated 915 MHz, and 2.45, 5.85, and 20.2-21.2 GHz for industrial, scientific, and medical (ISM) use [40]. Only 915 MHz and 2.45 GHz are significantly applied for industrial and medical use because of the suitability of these frequencies for such purposes. Other frequencies available on a limited basis as power sources are 28, 60, 140 GHz, and 500 MHz.

In using microwaves in various applications including processing of materials, one must consider health effects of microwave radiation. Guidelines for human exposure to radiofrequency electromagnetic fields are established by FCC (Internet address, http://www.fcc.gov/oet/info/documents/bulletins/#65). The first exposure standard for microwave radiation, based on the amount of radiation necessary to heat human tissue one degree Celsius, was 10 mW/cm^2 which was a tenth of the energy level required to provide one degree heating [40]. The current revised standard, based on an exposure

Table 1. Frequency allocation for industrial, scientific, and medical applications and areas permitted [39].

Frequency (MHz)	Frequency tolerance	Area permitted
433.92	± 0.2%	Austria, Netherlands, Portugal, Switzerland, West Germany, Yugoslavia
896	± 10 MHz	Great Britain
915	± 13 MHz	North and South America
2375	± 50 MHz	Albania, Bulgaria, Czechoslovakia, Hungary, Rumania, USSR
2450	± 50 MHz	Worldwide except where 2375 MHz is used
3390	± 0.6%	Netherlands
5800	± 75 MHz	Worldwide
6780	± 0.6%	Netherlands
24150	± 125 MHz	Worldwide
40680		Great Britain

level of 0.4 W/kg, is 0.5 mW/cm^2 at 2.45 GHz, above which potentially hazardous damage may occur.

Depending on the material, incident microwave energy can be transmitted, absorbed, or reflected. During microwave processing, a waveguide transmits microwaves from a microwave generator to a microwave cavity in which material is heated. Thermal energy for heating materials can be directly produced inside materials either by electrical current induction at high frequency for conducting materials or by dielectric or magnetic energy absorption for non-conducting materials [41].

Sutton [28] schematically showed the interactions of microwaves with different types of materials (Figure 5). As shown in Figure 6, metals are opaque to microwaves (i.e. good reflectors) and thus metals are very difficult to heat by microwave power [28]. Low-loss ceramic materials such as Al_2O_3, MgO, SiO_2, and most glasses are transparent to microwaves at ambient temperature [28]. For these low-loss materials, there is a critical temperature, T_{cr}, above which the materials begin to absorb and couple more efficiently with microwave power. On the other hand, dielectrically lossy ceramic materials such as Co_2O_3, MnO_2, NiO, and CuO absorb microwaves at room temperature [28]. For microwave-transparent ceramics, absorption of microwave energy can be enhanced by adding conductive or magnetic phases in the form of fibers, particles, or other additives [28,42]. The conductive or magnetic phases absorb microwave energy more rapidly than the matrix and thus can be heated selectively and rapidly [28].

The interaction (or absorption) of microwaves by a dielectric material is related to the material's complex permittivity, ε^* (Farad/meter), composed of real part, ε', and imaginary part, ε'', by [28,43,44]

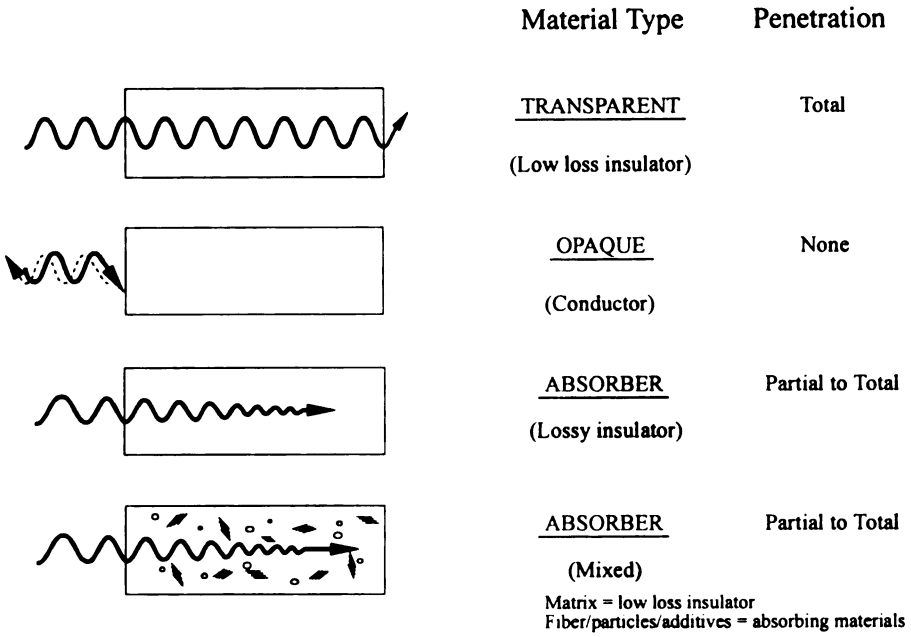

Figure 5. Interaction of microwaves with materials at ambient temperature [28].

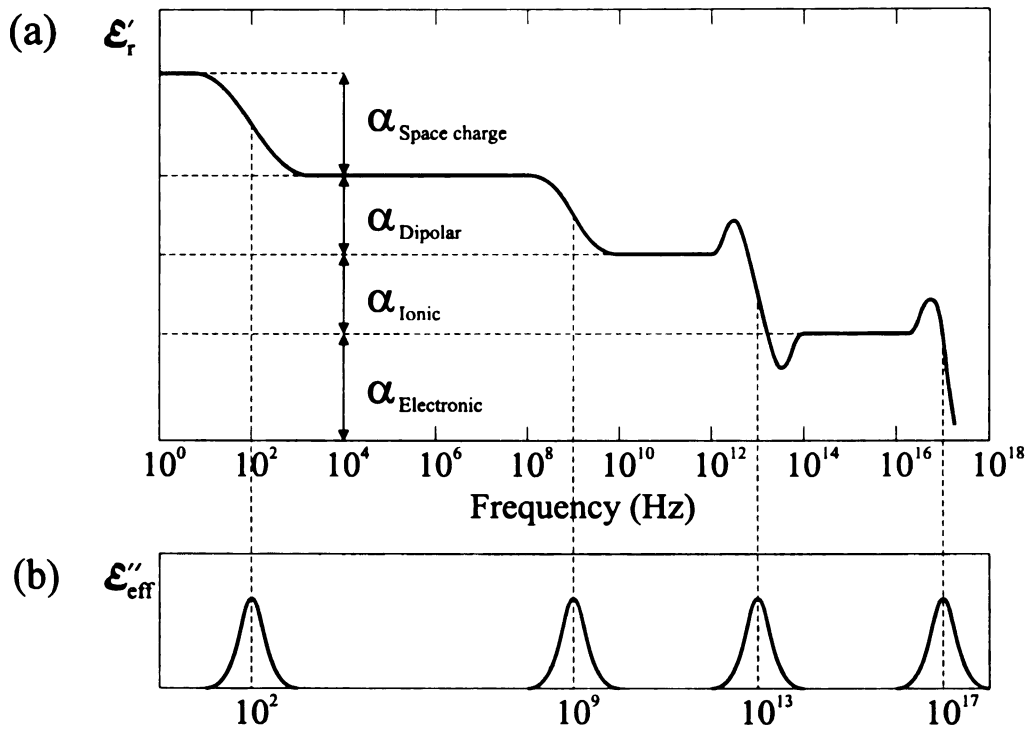

Figure 6. Variation of (a) relative dielectric constant and (b) relative effective dielectric loss factor with frequency [46-48]. Loss peaks shown at frequencies of 10^2, 10^9, 10^{13}, and 10^{17} Hz correspond to mechanisms, respectively.

$$\varepsilon^* = \varepsilon' - j\varepsilon'' = \varepsilon_o(\varepsilon'_r - j\varepsilon''_{eff}) \quad (1)$$

where $j = \sqrt{-1}$

ε_o = permittivity of free space ($\varepsilon_o = 8.86 \times 10^{-12}$ Farad/meter)

ε'_r = relative dielectric constant

ε''_{eff} = effective relative dielectric loss factor.

When microwaves penetrate and propagate through a dielectric material, internal electric fields are generated. These internal electric fields induce translational motions of free or bound charges (e.g., electrons or ions) and rotational motions of charge complexes such as dipoles [28]. The extent to which the charges and dipoles respond to the electric fields is represented by ε'_r, which is in turn a measure of polarizability of a material in the electric fields [28, 52]. The resistance of the induced motions due to inertial, elastic, and frictional forces (which are frequency dependent) causes losses, attenuates the electric fields, and results in volumetric and internal heating. All the loss mechanisms are combined in one loss parameter, ε''_{eff}, by (Figure 6) [43,45-48]

$$\varepsilon''_{eff} = \varepsilon''_s + \varepsilon''_d + \varepsilon''_i + \varepsilon''_e + \frac{\sigma_{IX}}{2\pi f \varepsilon_o} \quad (2)$$

where ε''_s = Space charge polarization loss
(normally noted in heterogeneous materials)

ε''_d = Dipolar losses which are usually encountered in the microwave region of the frequency band

ε''_i = Ionic losses which are usually encountered in infrared portion of the frequency band

ε''_e = Electronic polarization losses which are encountered in the

optical region of the frequency band

σ_{DC} = DC electrical conductivity of the material which is temperature and material dependent (Siemens/meter)

f = frequency of the incident microwave energy (Hz).

Thus the effective dielectric loss factor, ε''_{eff}, measures the loss due to a summed effect of the loss mechanisms in the frequency band and the loss due to DC conductivity. Equation 2 thus can be rewritten as [43,45]

$$\begin{aligned} \varepsilon''_{eff} &= \varepsilon''_c + \frac{\sigma_{DC}}{2\pi f \varepsilon_o} \\ &= \frac{\sigma_{AC}}{2\pi f \varepsilon_o} \end{aligned} \tag{3}$$

where $\varepsilon''_c = \varepsilon''_s + \varepsilon''_d + \varepsilon''_i + \varepsilon''_e$ is a combined loss factor due to space charge polarization loss, dipolar loss, ionic loss, and electronic loss for a given frequency band. Therefore, we can express the AC (alternating current) conductivity, σ_{AC}, as [28,45]

$$\sigma_{AC} = \sigma_{DC} + 2\pi f \varepsilon_o \varepsilon''_c = 2\pi f \varepsilon_o \varepsilon''_{eff} \tag{4}$$

where σ_{AC} is the total effective conductivity (Siemens/meter) caused by conduction and displacement currents. Of all the loss mechanisms, dipolar losses (ε''_d) and conductive losses (due to σ_{DC}) are two main physical loss mechanisms by which microwaves interact with ceramics, resulting in internal heating [49]. At radio frequencies (1-100 MHz) the dominant mechanism is due to conductive currents flowing within the materials, which in turn is due to the movement of ionic constituents [39]. The σ_{DC} losses can be enhanced by the presence of impurity constituents such as salts. For the frequencies ranging from 1 to 10 GHz the losses are due to the existence of permanent dipole molecules which tend to re-orientate under the influence of an external electric field, E (Figure 7) [39]. Inertial,

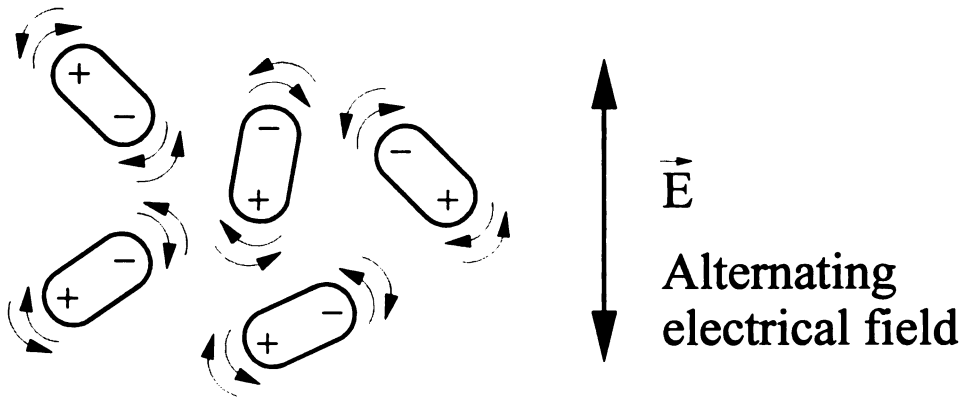

Figure 7. Dipolar reorientation in an applied electric field can result in heating [39].

elastic, and frictional motions between adjacent dipoles can lag the polarization in the extremely rapidly alternating electric field. Therefore, power can be dissipated in the dielectric material by such motions as depicted in Figure 7.

Walkiewicz, Kazonich and McGill studied conduction losses in microwave heating [50]. Walkiewicz et al. heated various metal powders, inorganic chemicals, and minerals in a microwave oven at power levels near 1 kW and recorded the temperatures after a few minutes of heating (Table 2 shows the results [50]). Conduction plays an important role in microwave heating (Table 2). In general, as the resistivity decreases (that is, the conductivity increases), materials absorb microwaves more easily and thus heating becomes easier. It is not easy to heat insulators like alumina and silica, while transition metal oxides and sulfides such as magnetite and pyrite are easy to heat to higher temperature [50]. However, in spite of their high electrical conductivity, metals are not heated as well as semimetals and narrow-band semiconductors because electric fields cannot penetrate much below the surface of metals [50].

When a material exhibits dielectric losses in the microwave frequency range, we can

expect very efficient energy conversion (90% in the conversion process of microwaves to thermal energy). If a suitable microwave applicator is used, refractory materials can be heated to high temperature [41]. An alternative expression frequently used to describe dielectric losses, is the loss tangent, tanδ, defined as the ratio of the effective relative loss factor to the relative dielectric constant [28,49]

$$\tan\delta = \frac{\varepsilon''_{eff}}{\varepsilon'_r} = \frac{\sigma_{AC}}{2\pi f \varepsilon_o \varepsilon'_r}. \tag{5}$$

Table 2. Heating characteristics and resistivities for minerals, chemicals, and metal powders heated by microwave power of 2.45 GHz [50,51]. The materials were heated for 7 minutes or less at microwave input power levels ranging from 500 Watts to 2000 Watts in a rectangular aluminum waveguide [51].

Material Type	Materials	Resistivity Range	Heating Characteristic
Oxide minerals	SiO_2, Al_2O_3, $KAlSi_3O_8$, $CaCO_3$	10^4 - 10^{14} (Ω-m)	Very little heating only about 80°C
Alkali halides	KCl, KBr, NaCl, NaBr, LiCl	10^4 - 10^5 (Ω-m)	Very little heating only about 50°C
Carbon and graphite	C	~10 (Ω-m)	Easily heated to 1000°C
Mixed valent oxides	Fe_3O_4, CuO, Co_2O_3, NiO	10^{-2} - 10^{-4} (Ω-m)	Easily heated to about 1000°C
Sulfide semiconductors	FeS_2, PbS, $CuFeS_2$	10^{-3} - 10^{-5} (Ω-m)	Easily heated to about 1000°C
Metal powders	Al, Co, Cu, Fe, Mg, Mo	10^{-6} - 10^{-8} (Ω-m)	Moderate heating to about 400°C

2.2.2. Variation of Dielectric Properties with Temperature and the Relation Between that Variation and Thermal Runaway

The dielectric constant, ε'_r, and loss tangent, $\tan\delta$, are not temperature independent (Figure 8). Since the value of ε'_r is a measure of polarizability of a material in an electric field, ε_r' increases with temperature due to an increase in polarizability caused by volumetric expansion [28]. On the other hand, the loss factor, ε''_{eff}, measures the extent to which electric charges and dipoles dissipate the energy stored in the electromagnetic field as heat in the material [52]. Thus the value of $\tan\delta$ which is defined in equation 5 is a measure of dielectric loss (or absorption) of microwave energy within the material [52]. Von Hippel [53] and Westphal, et al. [48,54] determined room-temperature dielectric properties of various materials including organics and inorganics (Tables 3 and 4). At room temperature $\tan\delta$ for the low-loss ceramics such as alumina is very low and the ceramics are essentially transparent to microwave radiation (Figure 8) [49,54]. However, as temperature increases, the total electromagnetic loss for a ceramic increases. While each loss mechanism contributes separately to the overall increase, conduction losses typically predominate at high temperatures [55]. Although conduction losses of dielectric materials are normally small near room temperature due to low conductivity, the exponential increase in conductivity (in particular due to ionic conductivity) with temperature results in a corresponding increase in the loss tangent [41,49,55]. Therefore the loss tangent initially rises slowly with increasing temperature, until some critical temperature, T_{crit}, is reached, beyond which $\tan\delta$ rises rapidly, resulting in more effective heating [28,49]. For alumina, T_{crit} is roughly 1000°C. Heating of low dielectric-loss ceramics from low temperatures to the point where it becomes more lossy often requires

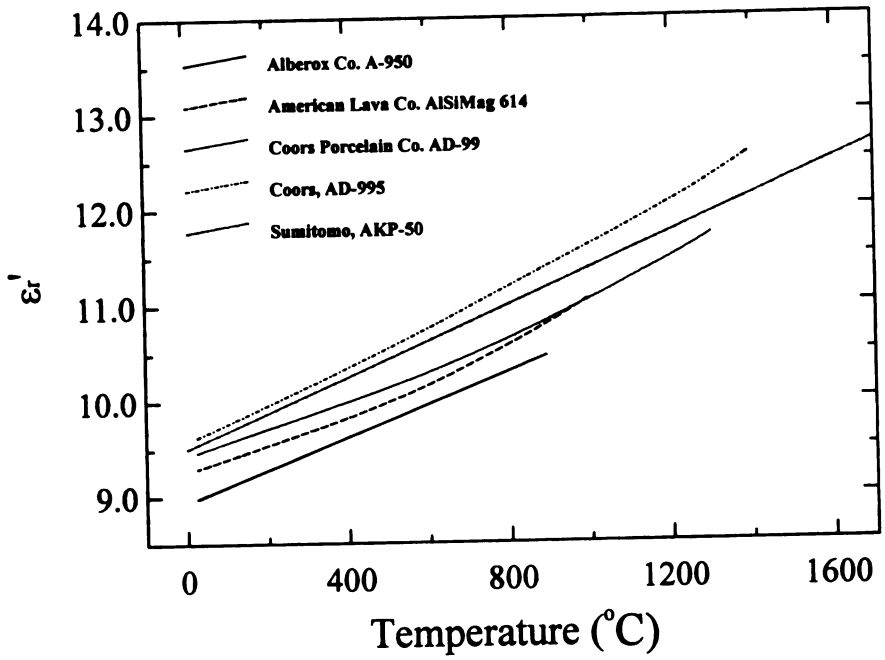

(a)

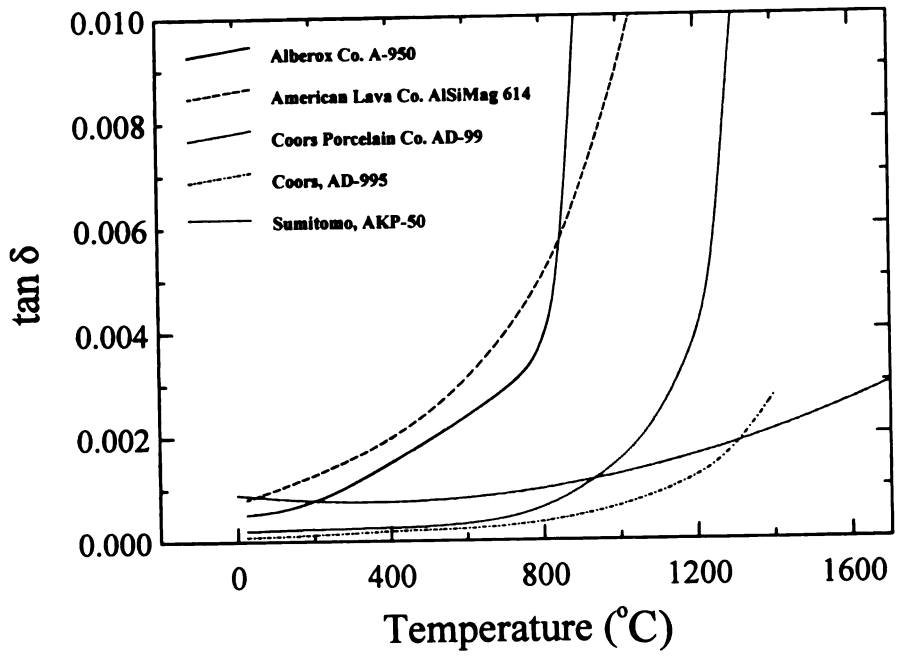

(b)

Figure 8. Typical variations of ε_r' (a) and tanδ (b) for aluminas as a function of temperature [40,54].

Table 3. Dielectric properties of various ceramics at room temperature (25°C) [54].

Material	Density (g/cm^3)	Freq. (GHz)	ε'_r	$\tan\delta$
AlN (Carborundum)		8.5	~8	~0.003
Al_2O_3 (Coors Co. AD-995)	3.840	3.33-3.80	9.63	0.00008
BeO (99.5%) (Amer. Lava Co. AlSiMag 754)	2.851	8.52	6.86	0.00031
BN (Carborundum Co.)	2.065	4.99-5.08	4.777	0.00033
CeF_4 (MIT, Lab. for Ins. Res.)		0.06	15.8	0.253
CoO (MIT, Lab. for Ins. Res.)		0.001	12.9	0.0005
$PbBr_2$ (MIT, Lab. for Ins. Res.)		0.001	52.7	0.0052
$MgOAl_2O_3$ (Union carbide)	3.574	4.07-4.23	8.28	0.0001
MgO (Kodak)		8.5	9.72	0.00045
MnF_2 (Columbia Univ.)		0.01	6.7	0.004
HgI_2	5.49	8.5	13.9	0.003
NiO		0.001	11.9	0.0154
Si crystal (MIT, Lab. for Ins. Res.)		14	12	0.0090
SiC (Carborundum)		3	60	0.58
SiO_2 (fused silica) (Amer. Opt. Co.)	2.196	5.37-5.50	3.818	0.00015
Si_3N_4 (Admiralty Materials Laboratory)	2.449	8.52	5.54	0.0036

Table 4. Dielectric properties of ceramics (at 1 MHz, room temperature) [48].

Material	$\tan\delta$	ε_r'	ε_{eff}''
Alumina (Al_2O_3)	0.0003 - 0.002	8.2 - 10.2	0.002 - 0.03
Spinel ($MgO{\cdot}Al_2O_3$)	0.0004	7.5	0.0003
Mullite ($3Al_2O_3{\cdot}2SiO_2$)	0.004 - 0.005	6.2 - 6.8	0.025 - 0.034
Magnesia (MgO)	0.001	8.2	0.002 - 0.01
Beryllia (BeO)	0.001	5.8	0.006
Zirconia (ZrO_2)	0.01	12.0	0.12
Thoria (ThO_2)	0.0003	13.5	0.004
Hafnia (HfO_2)	0.01	12	0.12
Ceria (CeO_2)	0.0007	15	0.011
Boron nitride (BN)	0.001	4.2	0.004
Silicon nitride (Si_3N_4)	0.0001	6.1	0.0006
Pyroceram	0.0017-0.013	5.5-6.3	0.01-0.07
Glass-bonded mica	0.0015-0.003	6.4-9.2	0.011-0.023
Mica	0.0002	5.4-8.7	0.001-0.002
Glass ($Na_2O{\cdot}CaO{\cdot}SiO_2$)	0.0005-0.01	4.0-8.0	0.002-0.08
Quartz (SiO_2)	0.0003	3.8-5.4	0.0015
Pb-Al silicate	0.001	8.2-15	0.008-0.015
Aluminum nitride (AlN)	0.0001	8.8-8.9	0.001
Silicon (Si)		11.9	

either external preheating by using a microwave susceptor material as insulation or adding a material with high loss at room temperature to the green body.

A material absorbs microwave energy more efficiently as the temperature increases above the critical temperature, T_{crit}, and the absorption of energy accelerates the increase in tanδ. Consequently, the net result is an exponential increase in temperature, which is called 'thermal runaway' or 'thermal breakdown' [48].

Thermal runaway depends on (1) the dielectric constants, (2) the porosity, (3) the shapes and the sizes of ceramic particles, and (4) the shapes and the sizes of the pores [56]. Thermal runaway is generally attributed to local heating or conduction losses, which generate heat faster than it can be removed. Thermal runaway can cause undesirable hot spots within a material, raising the local temperature to the point of melting or evaporation [48]. Also, around the local hot spot, cracks may develop depending on the material and the thermal gradients present.

If the cracking that may accompany thermal runaway is avoided, we may use the thermal runaway phenomenon to heat materials very rapidly. Thermal runaway (and cracking) can be controlled or prevented by two approaches [57]. Firstly, thermal runaway can be avoided by increasing the materials' thermal conductivity [57]. Thermal runaway does not occur in ceramics having high thermal conductivity such as SiC and ZrO_2. Adding thermally conductive fiber or powder to a low thermal conductive matrix not only improves the microwave absorption of the material, but also eliminates the thermal runaway (e.g. addition of 20 wt% TiC into Al_2O_3 [58]) [57]. Secondly, when changes in the power cause an instantaneous response in a given material, thermal runaway can be prevented by varying or pulsing the microwave input power [57]. As an

example, α-Al_2O_3 was sintered without thermal runaway by controlling the input power [33,57].

2.2.3. Heating Behaviors of Dielectric Materials

The heating rate and the triggering temperature (T_{crit}) for the efficient absorption of microwave power vary widely from material to material. McGill et al. [51] investigated the effects of microwave input power on the heating rates of selected chemicals and minerals, using input power levels ranging from 500 W to 2000 W (Figure 9). In general, as the input power increased, the heating rates increased. However, McGill et al. [51] observed that very low-loss materials such as SiO_2, $CaCO_3$, and $CaCl_2$ did not heat well at any of the power levels tested. Very high-loss materials such as Fe_3O_4 and CuO heated rapidly at all power levels tested. For some oxides such as Al_2O_3, Fe_2O_3, TiO_2, and ZnO, the temperature increased steadily as the input power increased [51]. On the other hand, Cr_2O_3, $FeCr_2O_4$ and some chlorides such as CuCl and $ZnCl_2$ showed very rapid and uncontrolled increase in temperature which is known as the 'thermal runaway' [51].

Sutton schematically showed the response of two different materials to microwave heating (Figure 10) [28]. Material A absorbs the microwave energy efficiently at room temperature and thus thermal runaway occurs as soon as the material is exposed to microwaves at a given power level. On the other hand, material B is less absorptive (i.e. low tan δ), so that the thermal runaway does not occur at the same power level used for material A. However, if we increase the power sufficiently, the initial rate of heating can be increased to the point where thermal runaway can be triggered [28]. Microwave heating of Fe_3O_4 at 2.45 GHz shows type A heating behavior [51], while Al_2O_3 shows

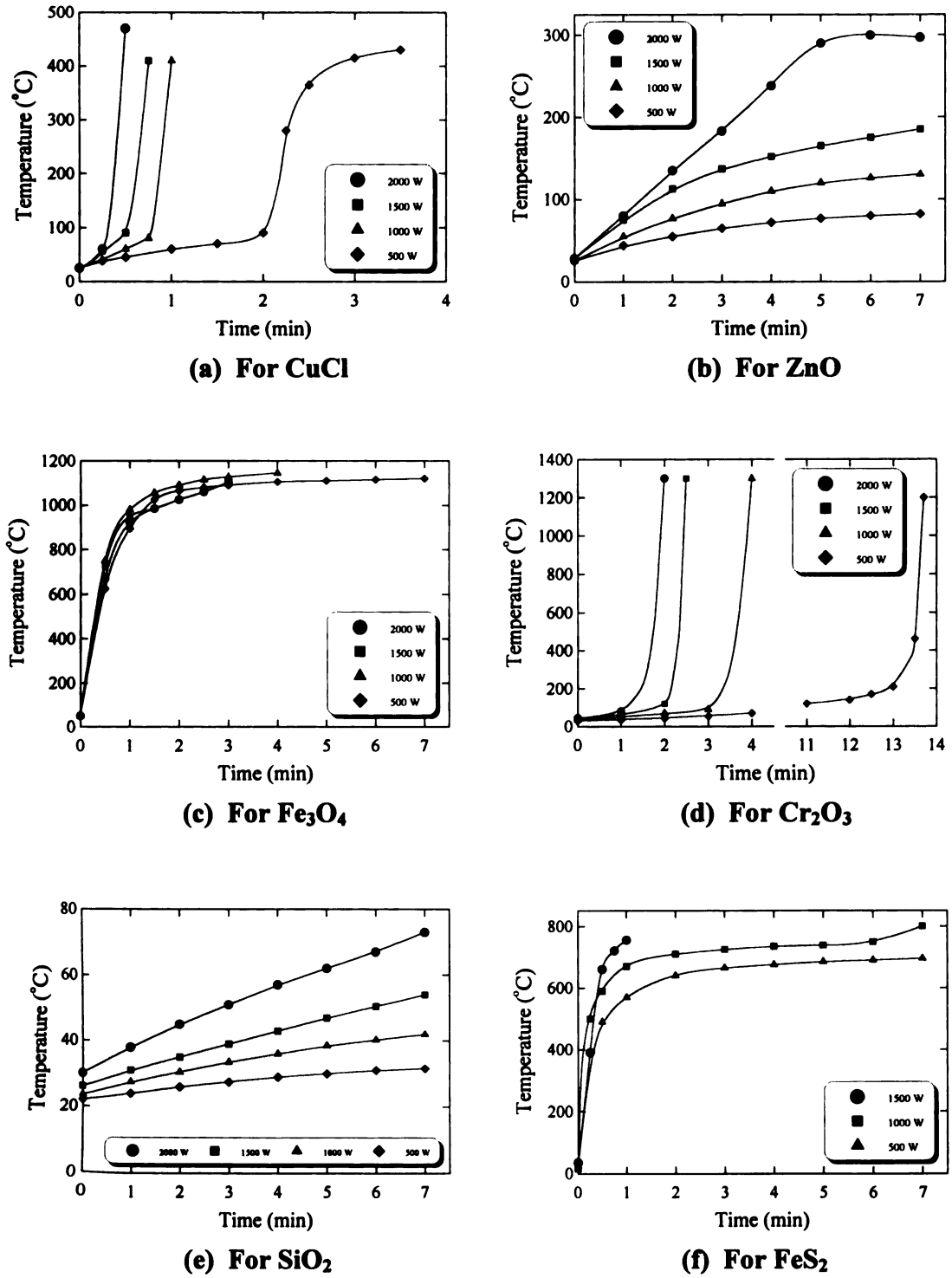

Figure 9. Effect of microwave input power on heating rate of various chemicals and minerals [51].

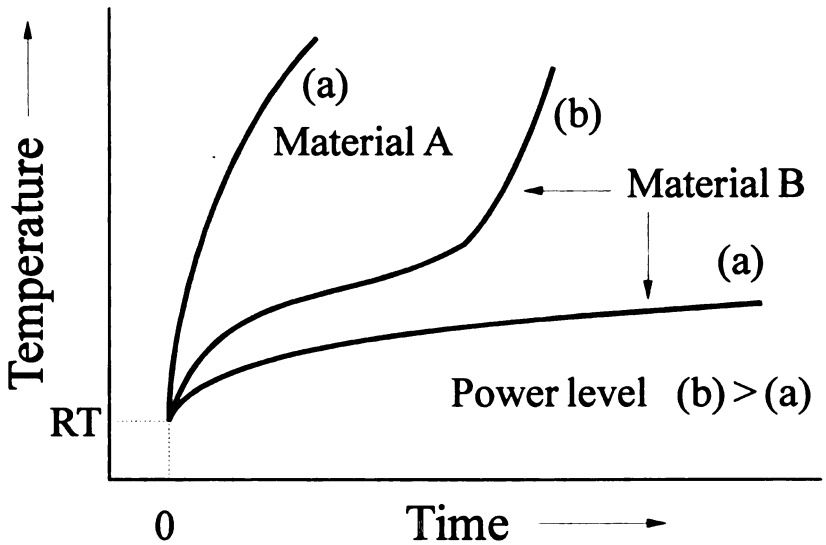

Figure 10. Schematic of the types of Response of materials to microwave heating [28].

type B heating behavior [59].

3. THEORETICAL BACKGROUND FOR MICROWAVE HEATING

3.1. FLOW OF ELECTROMAGNETIC POWER AND POWER DISSIPATION WITHIN A DIELECTRIC MATERIAL

Electromagnetic waves (including microwaves) carry electromagnetic power. The power dissipated in a ceramic material heated by microwaves can be estimated from a relation between energy transfer rate and the electric and magnetic field intensities. The derivation begins by considering Maxwell's equations [38,60-63]

$$\vec{\nabla} \times \vec{E} = -\frac{\partial \vec{B}}{\partial t} \qquad \text{Faraday's law} \qquad (6)$$

$$\vec{\nabla} \times \vec{H} = \vec{J} + \frac{\partial \vec{D}}{\partial t} \qquad \text{Ampere's circuital law} \qquad (7)$$

where $\vec{E}$ = electric field intensity (Volt/meter)

$\vec{H}$ = magnetic field intensity (Ampere/meter)

$\vec{B}$ = magnetic flux density (Tesla = Volt·sec/meter^2)

$\vec{J}$ = electric current density (Ampere/meter^2)

$\vec{D}$ = electric flux density (or electric displacement)

(Coulomb/meter^2)

t = time (sec).

In general, a source of electromagnetic energy sets up fields which store electric and magnetic energy and carry power which may be transmitted or dissipated as heat loss. We can now consider a free space or any medium of volume V enclosed by a closed surface S containing fields $\vec{E}$, $\vec{H}$ and current sources $\vec{J}_s$, $\vec{M}_s$ (Figure 11) [38]. To allow the power loss, the electric permittivity, ε, and the magnetic permeability, μ, are

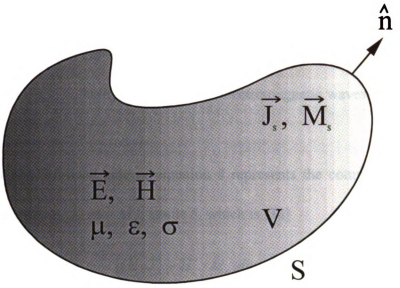

Figure 11. A volume V, enclosed by the closed surface S, containing fields $\vec{E}$, $\vec{H}$, and current sources $\vec{J}_s$, $\vec{M}_s$ [38].

often considered to be complex, such that $\varepsilon = \varepsilon' - j\varepsilon''$ and $\mu = \mu' - j\mu''$. Then the power balance equation known as Poynting's theorem (after the physicist J.H. Poynting, 1852-1914) is expressed as [38]

$$
\begin{aligned}
&-\frac{1}{2}\int_v (\vec{E}\cdot\vec{J}_s^{\,*} + \vec{H}^{*}\cdot\vec{M}_s)dv \\
&= \frac{1}{2}\oint_s (\vec{E}\times\vec{H}^{*})\cdot d\vec{s} + \frac{\sigma_{DC}}{2}\int_v \vec{E}\cdot\vec{E}^{*}dv + \frac{\omega}{2}\int_v (\varepsilon''\vec{E}\cdot\vec{E}^{*} + \mu''\vec{H}\cdot\vec{H}^{*})dv + j\frac{\omega}{2}\int_v (\mu'\vec{H}\cdot\vec{H}^{*} - \varepsilon'\vec{E}\cdot\vec{E}^{*})dv \\
&= \frac{1}{2}\oint_s (\vec{E}\times\vec{H}^{*})\cdot d\vec{s} + \frac{\sigma_{DC}}{2}\int_v |\vec{E}|^2 dv + \frac{\omega}{2}\int_v (\varepsilon''|\vec{E}|^2 + \mu''|\vec{H}|^2)dv + j\frac{\omega}{2}\int_v (\mu'|\vec{H}|^2 - \varepsilon'|\vec{E}|^2)dv
\end{aligned}
\tag{8}
$$

where

$\vec{J}_s$ = electric source current (Ampere/meter^2)

$\vec{J}_s^{\,*}$ = conjugate complex of $\vec{J}_s$

$\vec{M}_s$ = magnetization of source (Ampere/meter)

$\vec{E}^*$ = conjugate complex of $\vec{E}$

$\vec{H}^*$ = conjugate complex of $\vec{H}$

$\omega = 2\pi f$ = angular frequency,

here f = frequency of electromagnetic waves (Hz)

$j = \sqrt{-1}$.

The integral on the left-hand side of equation 8 represents the complex power, P_{source}, delivered by the sources $\vec{J}_s$ and $\vec{M}_s$, inside S, which is [38]

$$P_{source} = -\frac{1}{2}\int_v (\vec{E}\cdot\vec{J}_s^* + \vec{H}^*\cdot\vec{M}_s)dv\,. \tag{9}$$

The first term on the right-hand side of equation 8 represents complex power flow out of the closed surface S. The vector $\vec{E}\times\vec{H}^*$ represents the power flow per unit area. The quantity is defined as [38,60-63]

$$\vec{P} = \vec{E}\times\vec{H}^* \qquad (\mathrm{W/m^2}). \tag{10}$$

$\vec{P}$ is the Poynting vector, which is a power density vector associated with an electromagnetic field. Then the first integral on the right-hand side of equation 8 can be expressed as

$$P_{out} = \frac{1}{2}\oint_s (\vec{E}\times\vec{H}^*)\cdot d\vec{s} = \frac{1}{2}\oint_s \vec{P}\cdot d\vec{s}\,. \tag{11}$$

The real parts of P_{source} and P_{out} in equations 9 and 11 represent time-averaged total complex power supplied by a source within a region and the time-averaged complex power transmitted from the region, respectively.

The second and third integrals in equation 8 are real quantities representing the time-average power dissipated in the volume V due to conductivity, dielectric, and

magnetic losses. Defining this power as P_{loss}, then

$$P_{loss} = \frac{\sigma}{2}\int_V |\vec{E}|^2 dv + \frac{\omega}{2}\int_V (\varepsilon''|\vec{E}|^2 + \mu''|\vec{H}|^2) dv \tag{12}$$

which is sometimes referred to as Joule's law.

The last term in equation 8 includes the time-averaged stored magnetic energy, W_m, and the time-averaged stored electric energy, W_e, which are defined as

$$W_m = \frac{\mu}{4}\int_V \vec{H}\cdot\vec{H}^* dv \tag{13}$$

and

$$W_e = \frac{\varepsilon}{4}\int_V \vec{E}\cdot\vec{E}^* dv \tag{14}$$

where μ and ε are real scalar constants. Therefore, Poynting's theorem can be rewritten as [38,60,61]

$$P_{source} = P_{out} + P_{loss} + 2j\omega(W_m - W_e). \tag{15}$$

Thus this complex power balance equation can be interpreted as that the power delivered by the sources (P_{source}) is equal to the sum of the power transmitted through the surface S (P_{out}), the ohmic power dissipated as heat in the volume V (P_{loss}), and 2ω times the net reactive energy stored in the volume V [38].

For a source free region in which $\vec{J}_s = 0$ and $\vec{M}_s = 0$ (that is, in which power is supplied from a remote space by electromagnetic waves), $P_{source} = 0$, and the power transmitted into the volume, $P_{in} = -P_{out}$, so that equation 15 becomes [60-63]

$$P_{in} = -P_{out} = P_{loss} + 2j\omega(W_m - W_e). \tag{16}$$

Assuming low or no magnetic loss for a dielectric material (i.e. $\mu'' \approx 0$), the time-average power dissipated as heat in the volume V, P_{loss} can be written as

$$P_{loss} = \frac{\sigma_{DC}}{2}\int_v \left|\vec{E}\right|^2 dv + \frac{\omega}{2}\int_v \varepsilon''\left|\vec{E}\right|^2 dv$$
$$= \frac{1}{2}\int_v (\sigma_{DC} + \omega\varepsilon'')\left|\vec{E}\right|^2 dv \qquad (17)$$

From equation 4,

$$\sigma_{AC} = \sigma_{DC} + 2\pi f\varepsilon_o\varepsilon''. \qquad (18)$$

Thus equation 17 becomes

$$P_{loss} = \frac{1}{2}\int_v \sigma_{AC}\left|\vec{E}\right|^2 dv. \qquad (19)$$

Since P_{loss} is the time-average power dissipated in the volume V, the power absorbed and dissipated as heat per unit volume of ceramic materials, P_{abs} (W/m^3), which provides the basis for microwave heating, is related to the dielectric properties of the material from equations 4, 5, and 19 by [28,43,45,49]

$$P_{abs} = \sigma_{AC}\left|\vec{E}\right|^2$$
$$= 2\pi f\varepsilon_o\varepsilon''_{eff}\left|\vec{E}\right|^2 \qquad (20)$$
$$= 2\pi f\varepsilon_o\varepsilon'_r \tan\delta\left|\vec{E}\right|^2$$

where f = frequency of the incident microwave energy in Hz

ε_0 = 8.854 x 10^{-12} Farad/meter

= permittivity of free space

ε'_r = relative dielectric constant

tan δ = loss tangent

$\left|\vec{E}\right|$ = magnitude of internal electric field strength in Volt/meter.

3.2. SKIN DEPTH AND POWER PENETRATION DEPTH

As expected from equation 20, the microwave energy dissipated in a ceramic dielectric and the conduction losses increase by amplifying the electric field of the microwaves within the material [55]. However, depending on the material (Section 2.2.1), the internal electric field is not the same as the electric field at the surface of the material, since it is attenuated as the microwaves penetrate the material, reducing the electromagnetic power (Figure 5).

Therefore, to better understand the interactions between dielectric materials and microwaves that result in internal heating within the material, one can consider penetration depth of the electromagnetic power into the material (as measured by the skin depth).

As electromagnetic energy penetrates the material, its attenuation depends on the materials' dielectric properties. To obtain the expressions for the skin depth and the penetration depth, we begin with considering time-harmonic electromagnetics (i.e. sinusoidal variations of electromagnetic waves with time).

For spatially varying electric and magnetic fields that are sinusoidal functions of time (i.e. time-harmonic fields), the field vectors are typically represented by vector phasors that depend on space coordinates but not on time. The time-harmonic E field and H field can be written as [62]

$$\vec{E}(x,y,z,t) = \mathcal{R}e\,[\vec{E}(x,y,z)e^{j\omega t}] \tag{21}$$

$$\vec{H}(x,y,z,t) = \mathcal{R}e\,[\vec{H}(x,y,z,)e^{j\omega t}] \tag{22}$$

where $\vec{E}(x,y,z)$ and $\vec{H}(x,y,z)$ are vector phasors that contain information on direction, magnitude, and phase. Phasors are, in general, complex quantities [62]. For simplicity,

consider a uniform plane wave propagating in +z direction which is characterized by phasor electric field $\vec{E} = \hat{a}_x E_x$ and associated phasor magnetic field $\vec{H} = \hat{a}_x H_x$. Thus $\vec{E}$ and $\vec{H}$ are perpendicular to each other and both are transverse to the direction of propagation (Figure 12). This wave propagation pattern is a particular case of a transverse electromagnetic (TEM) wave. The phasor field quantities are functions of only the distance z along a single coordinate axis expressed as [62]

$$\vec{E} = \hat{a}_x E_x = \hat{a}_x E_o e^{-\gamma z} \tag{23}$$

where E_o = peak magnitude of the electric field wave. A propagation constant, γ, is defined as

$$\gamma = jk^* = j\omega\sqrt{\mu\varepsilon^*} \qquad (\text{meter}^{-1}) \tag{24}$$

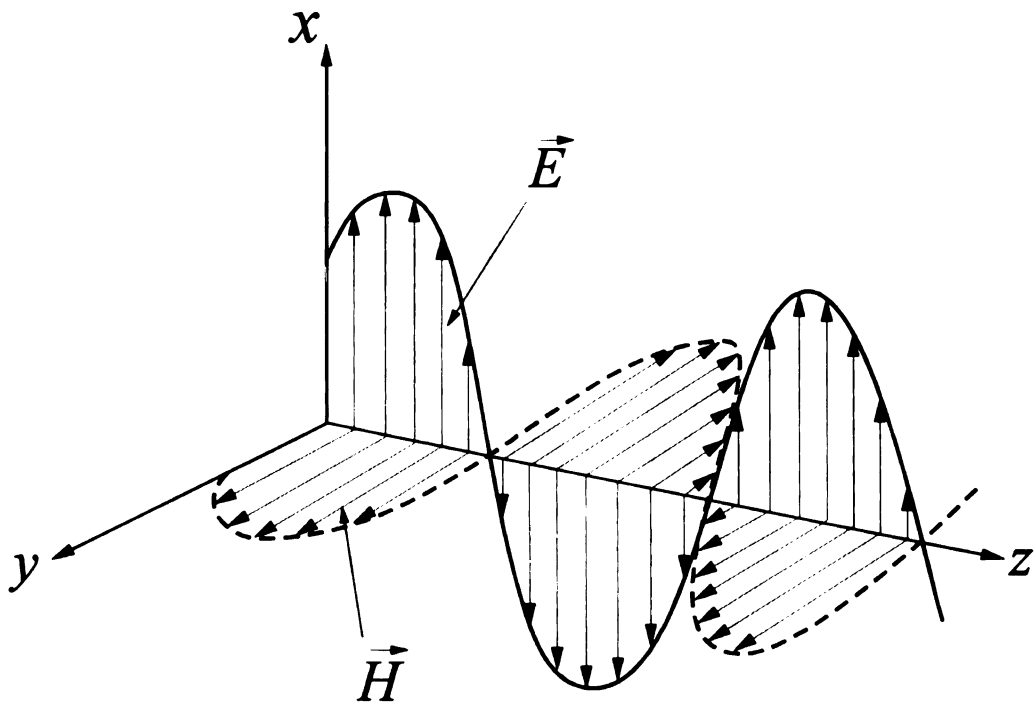

Figure 12. $\vec{E}$ and $\vec{H}$ fields of a uniform transverse electromagnetic plane wave [62].

where $k^* = \omega\sqrt{\mu\varepsilon^*}$ = complex wavenumber.

Since γ is complex, we can write [62]

$$\gamma = \alpha + j\beta \tag{25}$$

where α and β are the real and imaginary parts of γ, respectively. Thus the propagation factor $e^{-\gamma z}$ can be written as a product of two factors, such that

$$E_x = E_o e^{-\gamma z} = E_o e^{-\alpha z} e^{-j\beta z} \tag{26}$$

where both α and β are positive quantities. The first factor, $e^{-\alpha z}$, decreases as z increases and thus is an attenuation factor. α is called an 'attenuation constant' with units of neper per meter (Np/m). The second factor, $e^{-j\beta z}$, is a phase factor, and β is called a 'phase constant' and is expressed in radians per meter (rad/m).

On the other hand, from equations 1 and 3, it can be shown that

$$\begin{aligned} \varepsilon^* = \varepsilon' - j\varepsilon'' &= \varepsilon'\left(1 - j\frac{\varepsilon''}{\varepsilon'}\right) \\ &= \varepsilon'\left(1 + \frac{\sigma_{AC}}{j\omega\varepsilon'}\right) \end{aligned} \tag{27}$$

Therefore, from equation 24, the propagation constant, γ, is expressed in terms of dielectric properties such that

$$\gamma = \alpha + j\beta = j\omega\sqrt{\mu\varepsilon'}\left(1 - j\frac{\varepsilon''}{\varepsilon'}\right)^{1/2} \tag{28}$$

or

$$\gamma = \alpha + j\beta = j\omega\sqrt{\mu\varepsilon'}\left(1 + \frac{\sigma_{AC}}{j\omega\varepsilon'}\right)^{1/2}. \tag{29}$$

Now we define the skin depth, δ_s, as the distance through which the amplitude of a traveling plane wave decreases by a factor of e^{-1} or 0.368, such that from equation 26

[39,62] at δ_s,

$$E_o e^{-\alpha\delta_s} = e^{-1} E_o . \tag{30}$$

Thus

$$\alpha\delta_s = 1 . \tag{31}$$

Therefore,

$$\delta_s = \frac{1}{\alpha} \qquad \text{(meter)}. \tag{32}$$

For a low-loss dielectric material, $\varepsilon'' << \varepsilon'$ or $\sigma_{AC} / \omega\varepsilon' << 1$ [62], thus the propagation constant, γ, can be approximated by using the binomial expansion on equation 29 such that

$$\gamma = \alpha + j\beta \cong j\omega\sqrt{\mu\varepsilon'}\left[1 - j\frac{\varepsilon''}{2\varepsilon'} + \frac{1}{8}\left(\frac{\varepsilon''}{\varepsilon'}\right)^2\right]. \tag{33}$$

Thus the attenuation constant is [62]

$$\alpha \cong \frac{\omega\varepsilon''}{2}\sqrt{\frac{\mu}{\varepsilon'}} \qquad \text{(Neper/meter)}. \tag{34}$$

The skip depth for the low-loss ceramic is [62]

$$\delta_s \cong \frac{2}{\omega\varepsilon''}\sqrt{\frac{\varepsilon'}{\mu}} = \frac{2}{\sigma_{AC}}\sqrt{\frac{\varepsilon_o \varepsilon_r'}{\mu}} \qquad \text{(meter)}. \tag{35}$$

From equation 35, the skin depth for low-loss ceramics increases as the AC conductivity, σ_{AC}, decreases or the dielectric constant, ε'_r, increases.

In a ceramic for which dielectric conductivity dominates the losses, as in very wet ceramics (or good conductors such as metals) [39,62], then $\sigma_{AC} / \omega\varepsilon' >> 1$. Under this condition, in equation 29, $\sigma_{AC} / j\omega\varepsilon' << 1$, then [62]

$$\gamma = \alpha + j\beta \cong j\omega\sqrt{\mu\varepsilon'}\sqrt{\frac{\sigma_{AC}}{j\omega\varepsilon'}} = \sqrt{j}\sqrt{\omega\mu\sigma_{AC}}\ . \tag{36}$$

Also $\sqrt{j} = (e^{j\pi/2})^{1/2} = e^{j\pi/4} = (1+j)/\sqrt{2}$ and $\omega = 2\pi f$.

Thus

$$\alpha = \beta = \sqrt{\pi f\mu\sigma_{AC}}\ . \tag{37}$$

Therefore, the skin depth is [39,62]

$$\delta_s = \frac{1}{\sqrt{\pi f\mu\sigma_{AC}}}. \tag{38}$$

The skin depth increases as $\sqrt{f}$ and $\sqrt{\sigma_{AC}}$ decrease for a ceramic with dielectric losses dominated by conductivity. However, for a lossy ceramic material in which both dipolar and conductivity losses are present, approximations given by equations 33-37 are no longer valid [39].

In Section 3.1, equation 20 shows that the power density, P_{abs} (W/m^3), is proportional to the square of the internal electric field strength. Thus for a material in which electromagnetic waves propagate in + z direction, the power attenuation can be expressed in terms of the distance from the surface of the material as (Figure 13) [39]

$$P_{abs} = P_o e^{-2\alpha z} = P_o e^{-2z/\delta_s} \tag{39}$$

where P_o is the power at the surface and $\alpha = 1/\delta_s$ from equation 32.

Analogous to the definition of the skin depth, δ_s, the penetration depth, D_p, is defined as a depth at which the power at the surface is reduced by 1/e, such that at $z = D_p$ [39]

$$P_o e^{-2\alpha D_p} = P_o e^{-1}\ . \tag{40}$$

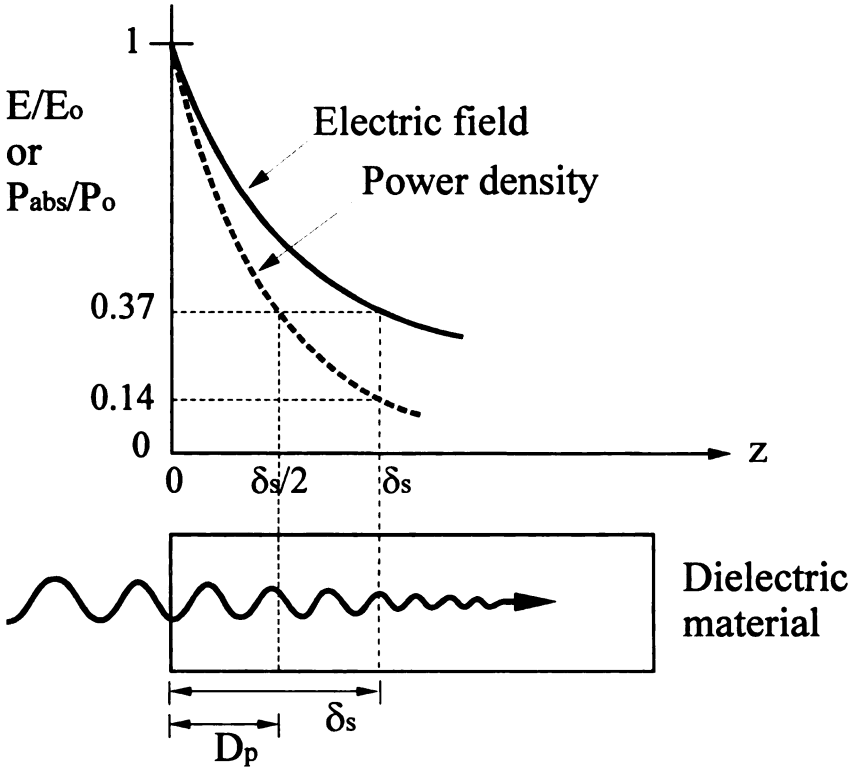

Figure 13. Skin depth of electric field intensity and power penetration depth [28,39].

Thus

$$2\alpha D_p = 1 . \tag{41}$$

Therefore, the power penetration depth is

$$D_p = \frac{1}{2\alpha} = \frac{\delta_s}{2} . \tag{42}$$

Therefore, from equations 26 and 39, at z = δ_s, the magnitude of the internal electric field and power density within the material are

$$E_z = E_o e^{-1} = 0.37 E_o \tag{43}$$

giving 63% attenuation of the electric field and

$$P_{abs} = P_o e^{-2} = 0.14 P_o \tag{44}$$

giving 86% dissipation of power (Figure 13) [39].

Metaxas and Binner [39] found the power penetration depth, D_p depended on dielectric properties for various ceramics (Table 5a). At the microwave band frequencies allocated for industrial uses, the power penetration depth could be very small. The size of the ceramic to be heated, in particular when the ceramic is very lossy, could be many times larger than D_p, resulting in unacceptable temperature non-uniformities [39].

The dielectric properties vary with temperature. Therefore the power penetration depth also changes as a function of temperature. For example, for hot pressed boron nitride with critical temperature, $T_c \approx 700^{\circ}C$, as temperature increases from 600°C to 950°C, D_p decreases from 7.62 m to 0.45 m (Table 5b) [399]. In particular, D_p rapidly decreased as the temperature increased above the critical temperature.

Table 5a. Power penetration depth, D_p, for various ceramic materials [39].

Material	Temperature (°C)	Frequency (MHz)	ε'_r	ε''_{eff}	tan δ	D_p (m)
Pyrolytic boron nitride	800	2450	3	2×10^{-4}		169
Calcium titanate	25	2450	180	2×10^{-3}		131
Steatite	25	2450	6	2×10^{-3}		23.9
Lime alumina silicate	25	2450	7	6×10^{-3}		8.6
Porcelain	25	2450	5	1.5×10^{-2}		2.9
Barium/strontium titanate	25	2450	2000	0.5		1.74
Barium titanate	25	2450	700	0.3		1.72
Hot pressed aluminum nitride	500	8500	9		4×10^{-3}	0.47
	700	8500	9		1.5×10^{-2}	0.12

Table 5b. Effect of temperature on power penetration depth, D_p, in hot pressed boron nitride with the critical temperature, $T_c \approx 700°C$ [39].

Temperature (°C)	ε'_r	tan δ	D_p (m)
600	4.22	6×10^{-4}	7.62
700	4.25	8×10^{-4}	5.70
800	4.28	20×10^{-4}	2.27
900	4.35	70×10^{-4}	0.64
950	4.4	100×10^{-4}	0.45

3.3. MICROWAVE APPLICATORS

The term 'microwave applicator' or 'microwave cavity' indicates a device that applies the microwave energy from the generator (such as magnetron or klystron microwave sources) to the workpiece (material to be heated). Industrial microwave applicators for materials processing (including ceramics), fall into three categories; traveling wave, single and multimode applicators [39]. This section gives brief descriptions for the single and multimode applicators.

Microwave cavities are simply metallic enclosures which confine the electromagnetic waves and cause multiple reflections of the waves from the cavity walls, establishing a standing wave pattern. Depending on the dimensions of the cavity and/or the operating microwave frequency, a fundamental standing wave pattern can be set up within the cavity [40]. Such a cavity is called a 'single-mode' cavity. The term 'mode' indicates a specific electromagnetic field standing wave pattern. Compared to the single-mode cavity, in a 'multimode' cavity, several fundamental standing waves or modes are superimposed to produce a standing wave pattern that consists of several modes [40].

The multimode applicators are most common type of applicators. For example, home microwave ovens are multimode applicators designed for in particular, food processing. In addition to domestic use, the multimode cavities are widely used in industry since the applicators are relatively inexpensive, simple to construct, easy to adapt to a wide range of material loads of different effective loss factors and sizes [28,39,64]. When microwaves are introduced into a multimode cavity, the microwaves reflect from the cavity wall to form a complex pattern of multiple standing wave patterns (i.e. modes), such that the electric field distribution in the multimode cavity is given by

the sum of all the modes excited at a particular frequency. Due to non-uniform field distributions formed in the multimode cavity, heating efficiency and uniformity vary depending on (1) the location of material within the cavity and (2) the size of the material to be processed. The lack of homogeniety in the electromagnetic field can lead to inhomogeneous heating and hot spots [28]. To improve the uniformity of heating, a turntable which rotates at a constant speed can move the load through the nodes and antinodes [39]. Another way to improve the heating uniformity is to use a mode stirrer which is a structure such as a metallic multiblade fan [39]. The mode stirrer rotates continuously and the resulting reflections of the field continuously perturbs the spatial distribution of the electromagnetic fields which yields a better uniformity inside the multimode applicator.

Compared to multimode cavities, the unloaded single-mode cavity is characterized by a standing wave pattern or mode that is well defined in space. Knowing how the electromagnetic field is distributed within the resonant cavity enables the material to be placed in the position of maximum electric field for optimum electromagnetic energy transfer, yielding high heating efficiency [28,39,52,65]. Therefore, maximizing the electric field strength at the processed specimen location yields rapid and uniform heating.

In exciting a specific mode in a single-mode microwave resonator cavity, two basic methods are used (Figure 14). In general, either a loop wire (or antenna, Figure 14a) or a straight wire (or antenna, Figure 14b) coupling probe placed at the position of maximum magnetic field or electric field intensity, respectively, can be used to excite a specific standing wave pattern (i.e. cavity mode) [38,60]. The maximum standing wave

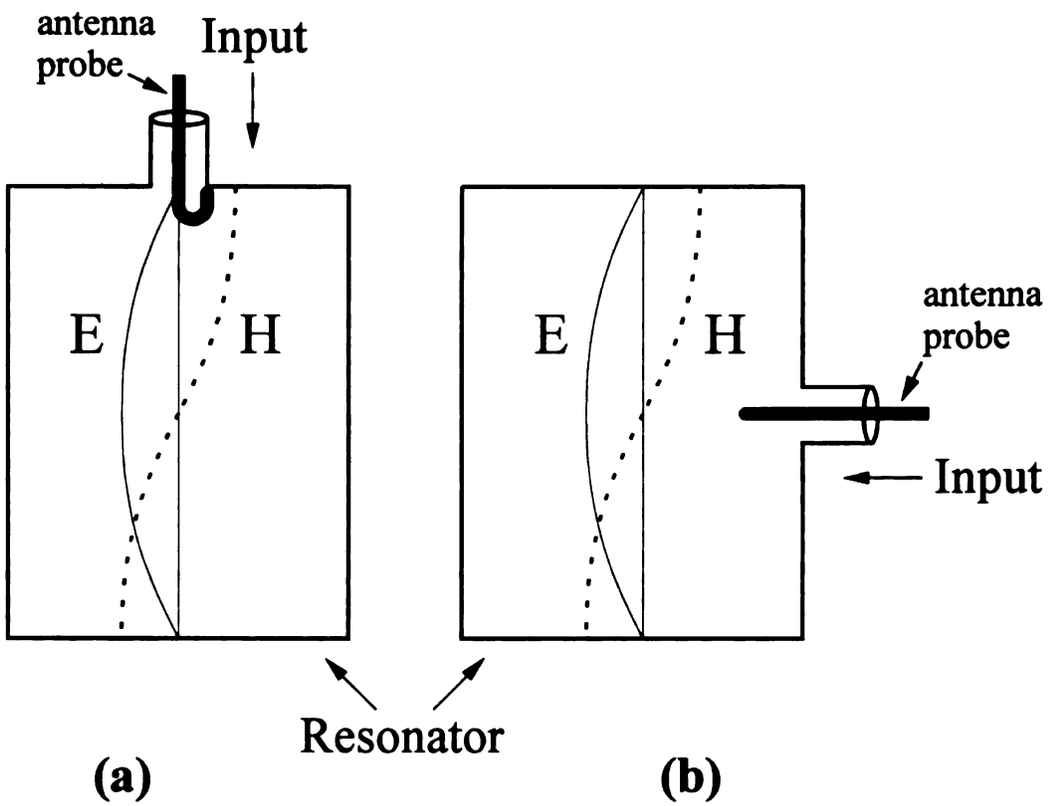

Figure 14. Methods of exciting wave modes in a resonator [60].

amplitude occurs when the frequency of the input electromagnetic waves is equal to the resonant frequency [60].

3.4. MICROWAVE CAVITY EQUIVALENT CIRCUITS AND QUALITY FACTOR

A series or parallel RLC lumped-element circuit often can be used to better understand and model the resonance and quality factor in a microwave resonator cavity [38,60]. In this section, as an example, a series RLC equivalent circuit will describe the resonance and quality factor (Figure 15).

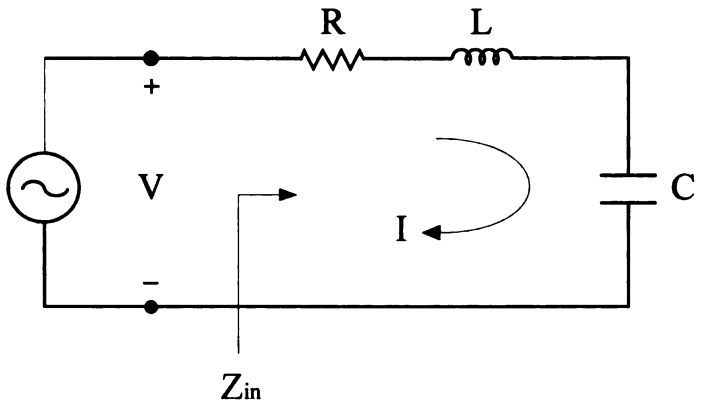

(a)

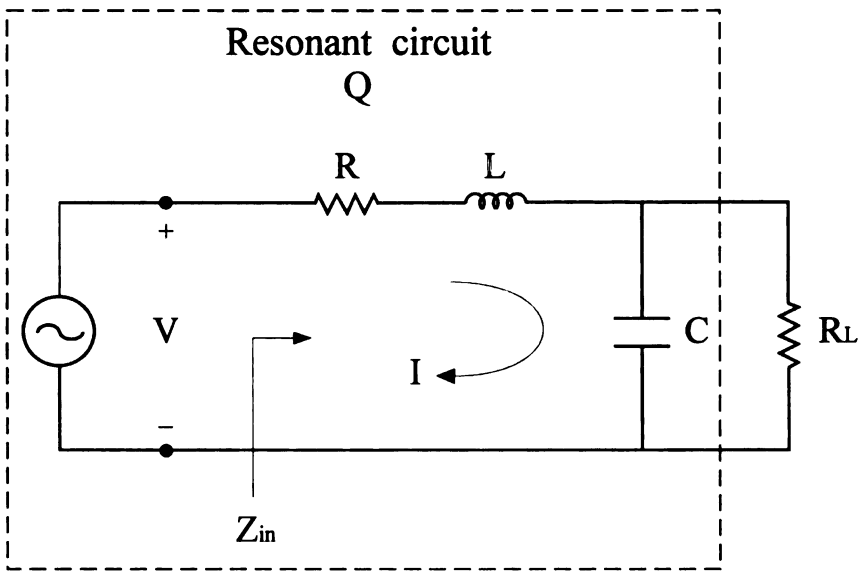

(b)

Figure 15. (a) A series RLC circuit equivalent to a microwave resonator and (b) a resonant circuit connected to an external load, R_L [38].

As discussed in Section 3.1, a cavity resonator stores energy in the electric and the magnetic fields for any particular mode pattern. In any practical cavity the cavity walls have a finite conductivity, resulting in nonzero surface resistance, which in turn causes power loss by resistance heating [62]. The stored electric and magnetic energies inside the cavity determine its equivalent inductance and capacitance. Also the energy dissipated by the finite conductivity of the cavity walls determines its equivalent resistance. For a series RLC lumped-element resonant circuit (Figure 15a), the input impedance is expressed as [38]

$$Z_{in} = R + j\omega L - j\frac{1}{\omega C} \tag{45}$$

where Z_{in} = input impedance (Ω)

R = resistance (Ω)

L = inductance (Henry = Weber/Ampere = Volt·sec/Ampere)

C = capacitance (Farad = Coulomb/Volt).

Then the power delivered to the resonant circuit, P_{in}, is [38]

$$\begin{aligned} P_{in} &= \frac{1}{2}VI^{*} = \frac{1}{2}Z_{in}|I|^{2} = \frac{1}{2}Z_{in}\left|\frac{V}{Z_{in}}\right|^{2} \\ &= \frac{1}{2}|I|^{2}\left(R + j\omega L - j\frac{1}{\omega C}\right) \end{aligned} \tag{46}$$

where V = source voltage (Volt)

I = current (Ampere)

I^{*} = conjugate complex of I (Ampere).

The power dissipated by the resistor, R, is given by

$$P_{loss} = \frac{1}{2}|I|^{2}R. \tag{47}$$

The average magnetic energy stored in inductor, L, is

$$W_m = \frac{1}{4}|I|^2 L \tag{48}$$

and the average electric energy stored in capacitor, C, is

$$W_e = \frac{1}{4}|V_c|^2 C = \frac{1}{4}|I|^2 \frac{1}{\omega^2 C} \tag{49}$$

where V_c is voltage across the capacitor. Equivalently, for electromagnetic waves [60]

$$W_m = \int_V \frac{1}{2}\mu|H|^2 dv \tag{50}$$

$$W_e = \int_V \frac{1}{2}\varepsilon|E|^2 dv\,. \tag{51}$$

Then substituting equations 47-51 into the complex power relation (equation 46) gives [38,60]

$$P_{in} = P_{loss} + 2j\omega(W_m - W_e)\,. \tag{52}$$

Also, equation 45 can be rewritten as

$$Z_{in} = \frac{2P_{in}}{|I|^2} = \frac{P_{loss} + 2j\omega(W_m - W_e)}{|I|^2/2}\,. \tag{53}$$

For the given RLC circuit (or microwave resonator) (Figure 15a), resonance occurs when the average stored magnetic and electric energies are equal, or

$$W_m = W_e\,. \tag{54}$$

Then at resonance

$$Z_{in} = \frac{P_{loss}}{|I|^2/2} = R\,. \tag{55}$$

That is, the input impedance at resonance is purely real impedance. Since at resonance $W_m = W_e$, thus from equations 48 and 49 the resonant frequency must be given by

[38,60,61]

$$\omega_o = 2\pi f_o = \frac{1}{\sqrt{LC}} \tag{56}$$

or

$$f_o = \frac{1}{2\pi\sqrt{LC}}. \tag{57}$$

Equivalently, for electromagnetic waves,

$$f_o = \frac{1}{2\pi\sqrt{\mu\varepsilon}} \cdot G = \frac{v}{2\pi} \cdot G \tag{58}$$

where v is wave propagation velocity in a medium with μ and ε. Geometric factor, G, depends on the geometry and dimensions of the cavity and/or cavity mode type (Transverse Electric, TE, or Transverse Magnetic, TM, modes). When the frequency of an impressed signal equals a resonant frequency, a maximum-amplitude standing wave occurs [60]. Theoretically, a given resonator has an infinite number of resonant modes where each mode corresponds to a definite resonant frequency. The mode having the lowest resonant frequency is known as the dominant mode.

Quality factor, Q, of a resonant circuit or microwave resonator is defined as [38,43, 52,60-62,66]

$$\begin{aligned} Q &= 2\pi \frac{(\text{time-averaged energy stored at a resonant frequency})}{(\text{energy dissipated in one period of this frequecy})} \\ &= \omega_o \frac{W_m + W_e}{P_{loss}} \end{aligned} \tag{59}$$

Thus Q (dimensionless) is a measure of the electromagnetic energy loss per cycle for a cavity resonator. A lower loss implies a higher Q. In the absence of any loading effects caused by external circuitry, the unloaded Q, Q_{unload} is a characteristic of the resonant

circuit (or cavity resonator) itself. At resonance $W_m = W_e$, such that from equations 48, 49, and 55

$$Q_{unload} = \omega_o \frac{2W_m}{P_{loss}} = \omega_o \frac{2W_e}{P_{loss}} = \frac{\omega_o L}{R} = \frac{1}{\omega_o RC}. \tag{60}$$

If a resonant circuit is coupled to an external load resistor, R_L, in series, the effective resistance in equation 45 is $R+R_L$, shown in Figure 15b. Then loaded Q, Q_{load} can be expressed as

$$Q_{load} = \frac{\omega_o L}{R + R_L} = \frac{1}{\frac{R + R_L}{\omega_o L}} = \frac{1}{\frac{R}{\omega_o L} + \frac{R_L}{\omega_o L}}. \tag{61}$$

From equation 60, $Q_{unload} = \frac{\omega_o L}{R}$ and if we define an external Q, Q_{ext}, as

$$Q_{ext} = \frac{\omega_o L}{R_L} \qquad \text{for series circuit.} \tag{62}$$

Then the loaded Q can be expressed as

$$\frac{1}{Q_{load}} = \frac{1}{Q_{ext}} + \frac{1}{Q_{unload}}. \tag{63}$$

Equivalently, for a resonant microwave cavity made of a conductive wall in the presence of a dielectric material, $Q_{unload} = Q_{cav}$, and $Q_{ext} = Q_{diel}$, so that [38]

$$\frac{1}{Q_{load}} = \frac{1}{Q_{diel}} + \frac{1}{Q_{cav}} \tag{64}$$

where $$Q_{cav} = \frac{2\omega_o W_m}{P_{loss}} = \frac{\omega_o L}{R} = \frac{1}{\omega_o RC}$$

= quality factor for a resonant cavity without a load

P_{loss} = power dissipated by the conducting cavity wall

$$Q_{diel} = \frac{2\omega_o W_e}{P_d} = \frac{\varepsilon'}{\varepsilon''} = \frac{1}{\tan\delta}$$

= quality factor of the cavity with a dielectric material, but with perfectly conducting walls

P_{diel} = power dissipated in the dielectric material.

When both wall losses and dielectric losses are present, the total power loss is $P_{loss} + P_{diel}$, so equation 64 gives the total Q for the resonant cavity loaded with dielectric material as

$$Q_{load} = \left(\frac{1}{Q_{diel}} + \frac{1}{Q_{cav}}\right)^{-1}. \tag{65}$$

Then the power dissipated inside the dielectric, P_{diel}, is given by [41,42]

$$P_{diel} \propto f\varepsilon''_{eff} Q_{load} |E|^2 \tag{66}$$

where quality factor Q_{load}, electric field E and dielectric losses $\varepsilon''_{\text{eff}}$ are not independent parameters.

As microwave energy is absorbed in a dielectric material, the material's temperature increases at a rate depending upon a number of distinct parameters. The heating rate is determined by competition between the loss due to the motion of charges and dipoles and conductive and radiative heat loss from the material [52]. For a single mode resonant cavity, Palaith and Silberglitt [52] gave a simplified equation for the heating rate in terms of incident power, and temperature of the material such that

$$\frac{dT}{dt} = 4Q_{load} \frac{1}{\rho C_p} \frac{\varepsilon''_{eff}}{\sqrt{\varepsilon'_r}} \frac{1}{V_c} P_o - \frac{\in \sigma}{\rho C_p} \left(\frac{area}{volume}\right)_{material} T^4 \tag{67}$$

where ρ is the mass density of the material, C_p is the specific heat capacity, V_c is the cavity volume, P_o is the microwave power incident on the cavity and T is the specimen

surface temperature expressed in Kelvins. ϵ is the surface emissivity of the material and σ is the Stefan-Boltzmann (or radiation) constant which has the value 5.67×10^{-12} joule $cm^{-2} K^{-4}$.

Therefore, high Q factors coupled with high electrical field strengths can cause very high heating rates [42]. Single-mode, resonant cavities with high Q values of several thousands are common and have been used by several investigators to heat ceramic materials [42,52]. Since most ceramics of interest are not strong absorbers until a temperature over 1000°C is reached, based on equation 66 this three-order-of magnitude enhancement of the power in the cavity is crucial in microwave heating of ceramics [52, 28].

3.5. NOTATION FOR MICROWAVE MODES IN A CYLINDRICAL MICROWAVE CAVITY

In this study a cylindrical resonant microwave cavity [64,65] has been used for various researches. The cavity can be internally tuned to various electromagnetic modes by adjusting the cavity height and position of the power launch probe. Thus this section and Section 3.6 will discuss fundamentals about a cylindrical microwave cavity such as notation for the electromagnetic resonance modes and a 'mode diagram' which shows resonance frequencies of each mode theoretically expected for given cavity dimensions.

For microwave cavities with either rectangular or circular cross sections, two sets of electromagnetic modes are admissible: transverse magnetic (TM) modes and transverse electric (TE) modes [38,60-63]. Since a microwave cavity is a hollow metallic enclosure which confines the electromagnetic fields, the electromagnetic waves are reflected from

wall to wall. This process results in a component of either electric or magnetic field being parallel to the axial direction of the cavity. Therefore transverse electromagnetic (TEM) modes (i.e. $E_z = H_z = 0$) are not admissible for hollow metallic microwave cavities. The system in which TEM modes can exist should involve two conductors, for example, coaxial lines and two-open-wire transmission line systems [38,60-63]. Customarily, for notation of cavity mode in a cylindrical cavity, a cylindrical coordinate system is used as shown in Figure 16. In Figure 16, a is a radius of the cavity and d is a cavity height.

For the TM modes, there are no axial magnetic fields (i.e. $H_z = 0$) but axial electric fields $E_z \neq 0$, such that [60]

$$E_z = E_{oz} J_n\left(\frac{P_{nm}}{a} r\right)\cos(n\phi)\cos\left(\frac{l\pi}{d} z\right) \qquad (\mathrm{TM_{nml}\ modes}) \qquad (68)$$

where E_{oz} = amplitude of the electric field

J_n = Bessel function of the first kind

P_{nm} = m_{th} x value at which $J_n(x) = 0$

n = number of periodicity in ϕ direction (n = 0,1,2,3...)

m = number of zero fields in radial direction (m =1,2,3...)

l = number of half-waves in axial direction (l = 0,1,2,3...).

TE modes have no axial electric fields (i.e. $E_z = 0$) but axial magnetic fields ($H_z \neq 0$), such that

$$H_z = H_{oz} J_n\left(\frac{Q_{nm}}{a} r\right)\cos(n\phi)\sin\left(\frac{l\pi}{d} z\right) \qquad (\mathrm{TE_{nml}\ modes}) \qquad (69)$$

where H_{oz} = amplitude of the magnetic field

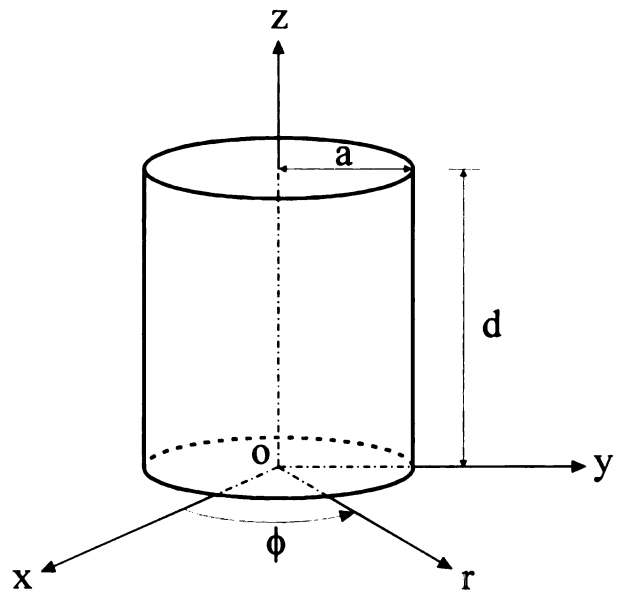

Figure 16. Cylindrical coordinate system used for notation of microwave cavity modes.

J_n = Bessel function of the first kind

Q_{nm} = m_{th} x value at which $J_n'(x) = 0$

n = number of periodicity in ϕ direction (n = 0,1,2,3...)

m = number of zero fields in radial direction (m = 1,2,3...)

l = number of half-waves in axial direction (l = 1,2,3,4...).

Using equations 68 and 69, relative distributions of electric field, E_z, and magnetic field, H_z, can be depicted for a given TM_{nml} mode (Figure 17) and TE_{nml} mode (Figure 18), respectively, as a function of angular position, ϕ, radial position, r, and axial position, z.

In considering the distributions of electromagnetic fields within the cavity which consists of good-conductive walls, there are fundamental boundary conditions to be

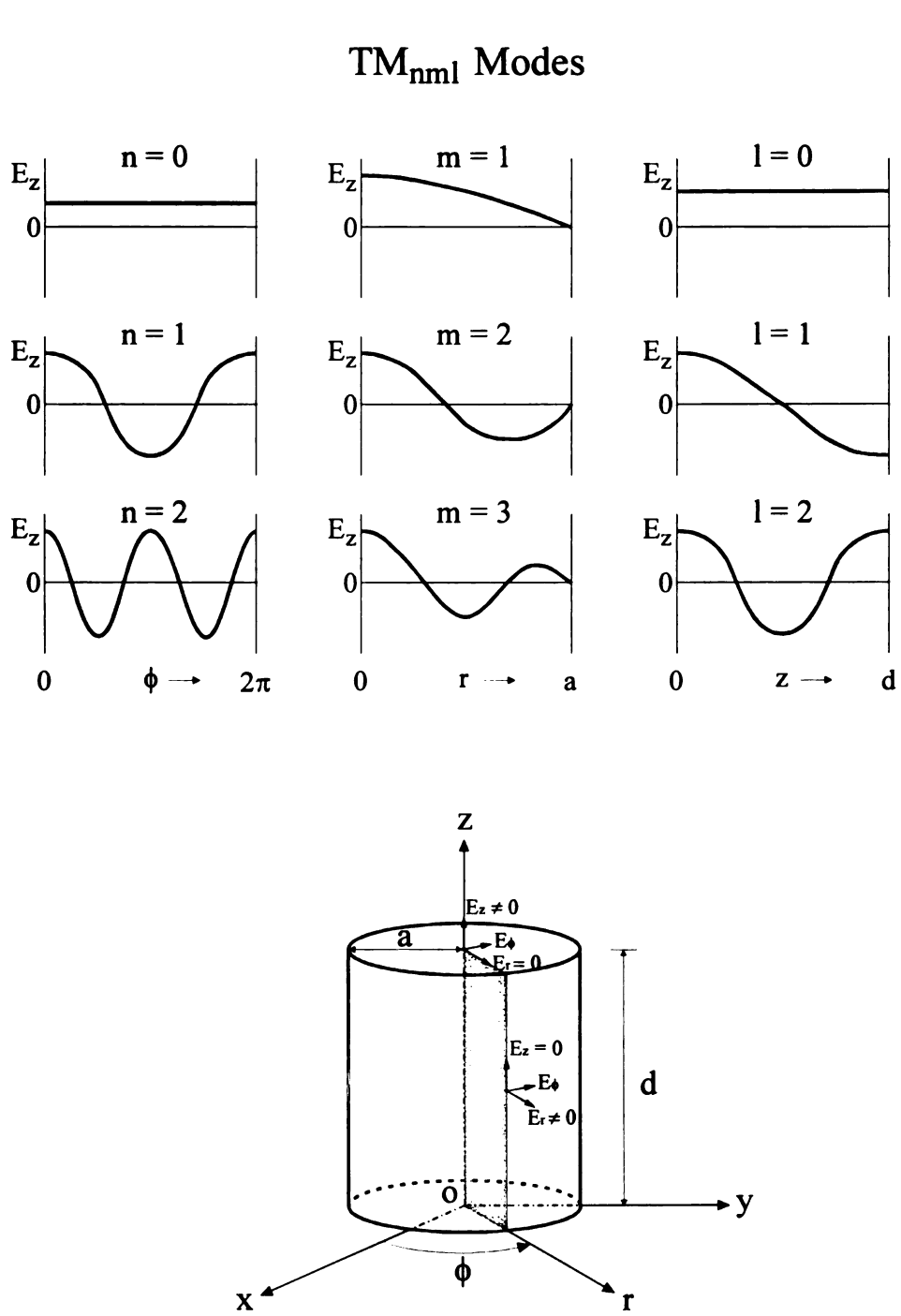

Figure 17. Notation for TM_{nml} modes for a cylindrical microwave cavity.

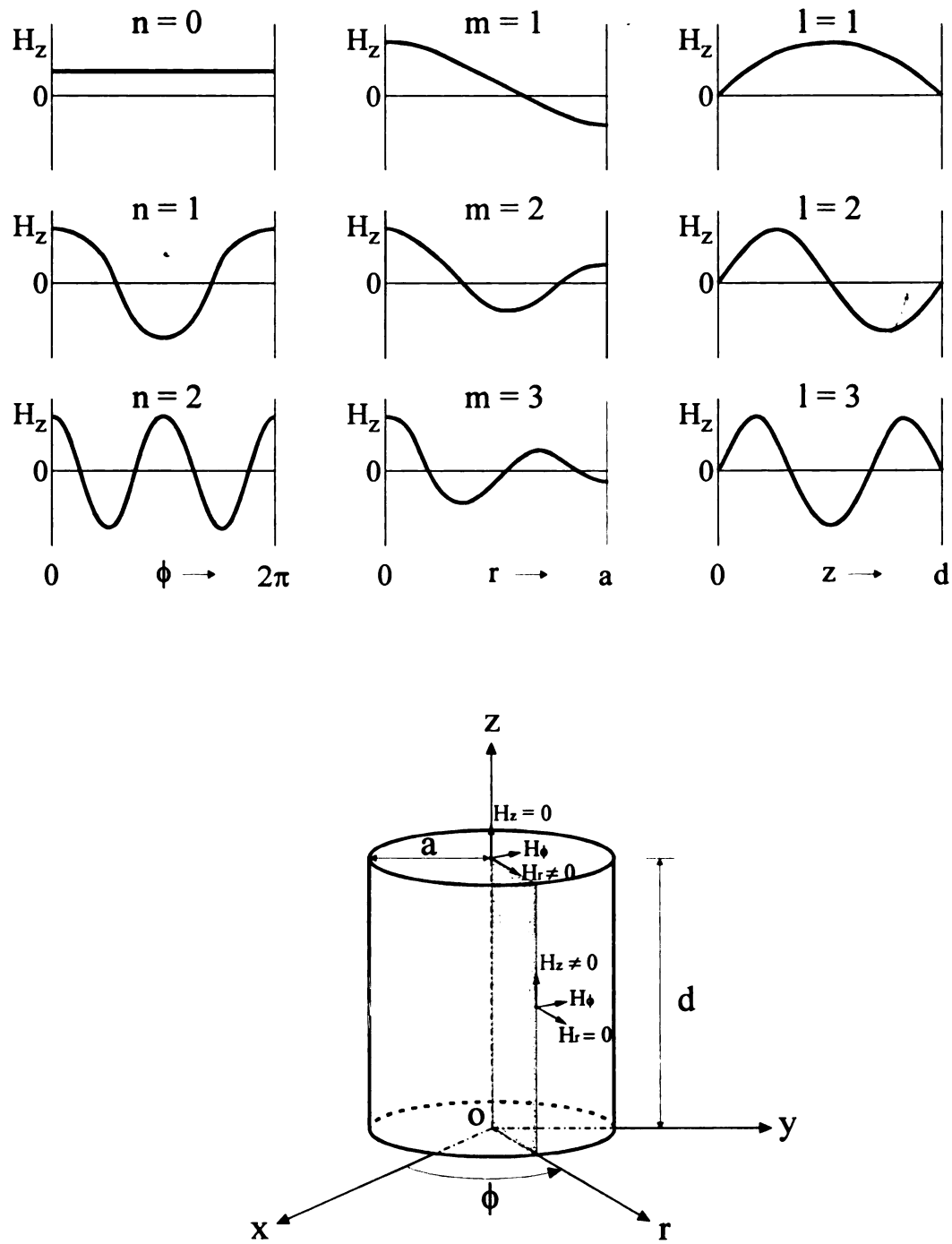

Figure 18. Notation for TE_{nml} modes for a cylindrical microwave cavity.

satisfied. For time-varying electromagnetic waves, following boundary conditions between two mediums should be satisfied [61,62]; i) the tangential component of an $\vec{E}$ field is continuous across an interface, ii) the tangential component of an $\vec{H}$ field ($\vec{H} = \vec{H}/\mu$) and thus the tangential component of the $\vec{B}$ field are discontinuous across an interface where a surface current exists, iii) the normal component of a $\vec{D}$ field ($\vec{D} = \varepsilon\vec{E}$) and thus the normal component of $\vec{E}$ field are discontinuous across an interface where a surface charge exists, and iv) the normal component of a $\vec{B}$ field ($\vec{B} = \mu\vec{H}$) and thus the normal component of $\vec{H}$ field are continuous across an interface. In order to simplify the analytical solution of field problems, good conductors are often considered perfect conductors in regard to boundary conditions. In the interior of a perfect conductor the electric field is zero and any charges the conductor will have will reside on the surface only. Subsequently, from Maxwell's equations (equations 6 and 7), $\vec{B}$ and $\vec{H}$ are zero in the interior of a conductor in a time-varying situation. Therefore, at the surface of the cavity walls, the tangential component of an $\vec{E}$ field should be zero. For example, $E_z = 0$ and $E_r \neq 0$ at the side wall of the cavity for a given TM_{nml} mode (Figure 17). Also, at the top and bottom plates of the cavity, $E_z \neq 0$ and $E_r = 0$ for a given TM_{nml} mode. Likewise, for a given TE_{nml} mode, $H_z \neq 0$, $H_r = 0$ at the side wall and $H_z = 0$, $H_r \neq 0$ at the top and bottom plates of the cavity (Figure 18).

Figures 19, 20 and Figures 21, 22 show three-dimensional views of field distributions for various TE and TM modes established within a cylindrical circular microwave cavity [61,62,64,67].

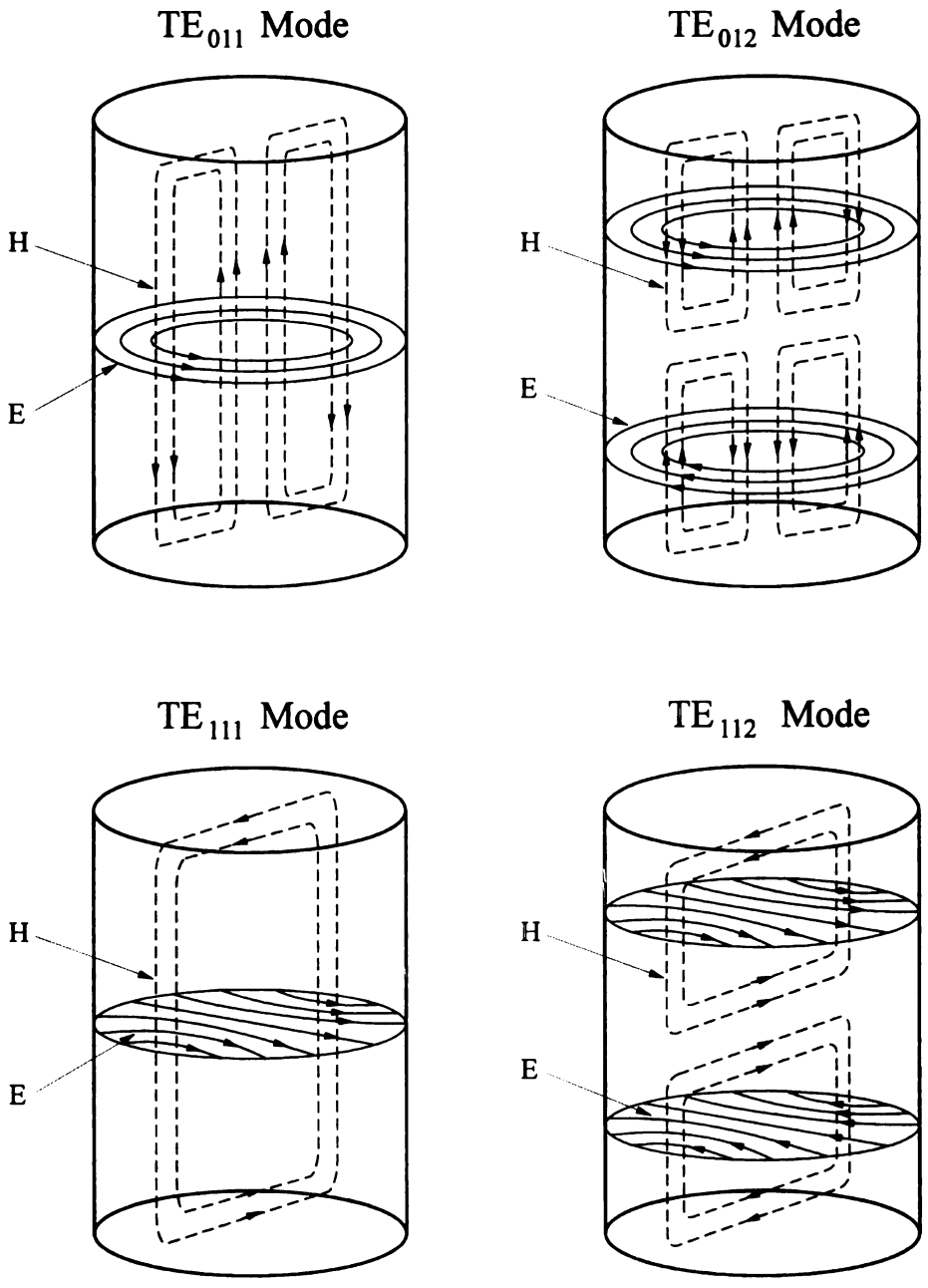

Figure 19. Field distributions of TE_{011}, TE_{012}, TE_{111}, and TE_{112} modes.

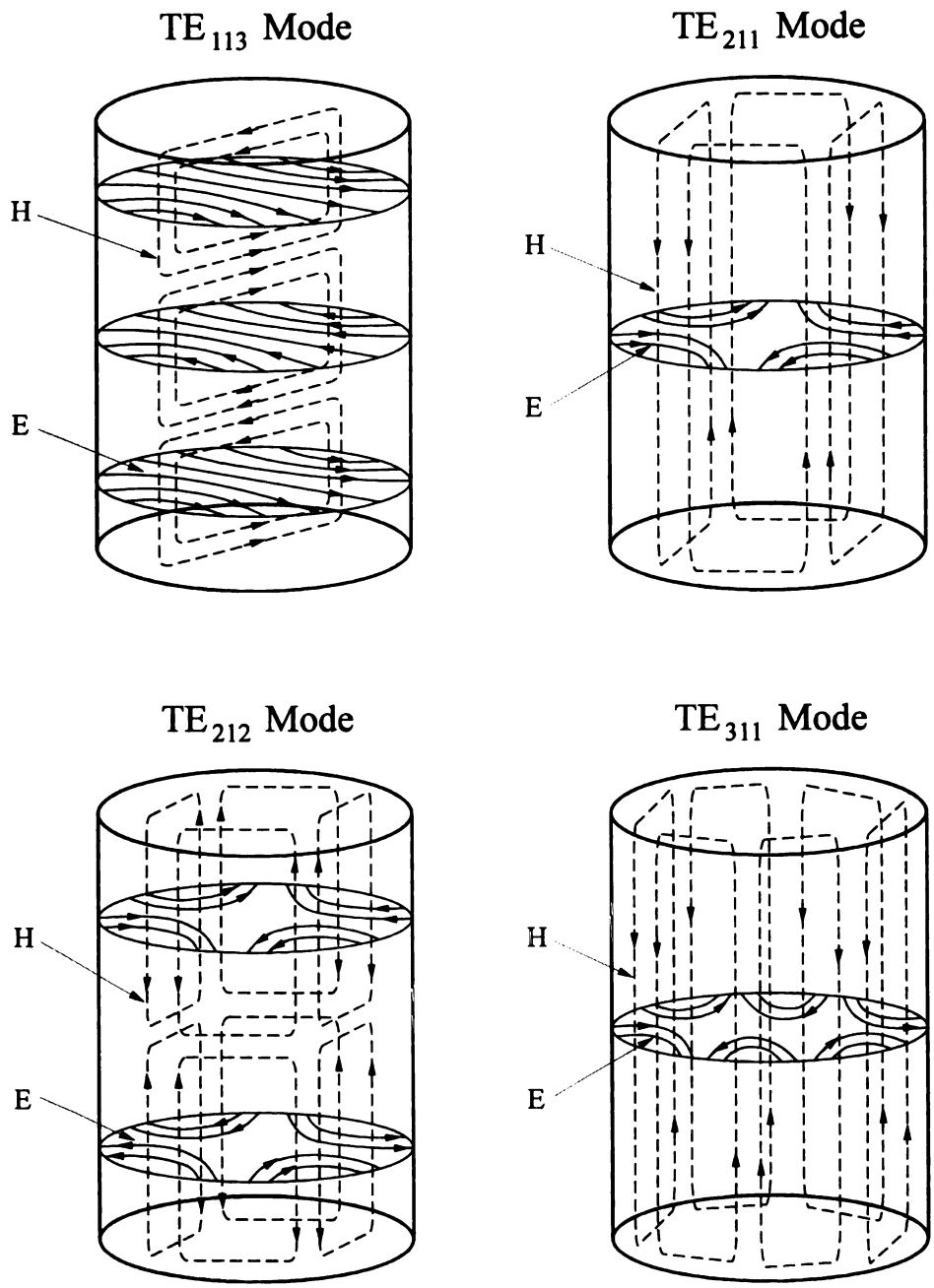

Figure 20. Field distributions of TE_{113}, TE_{211}, TE_{212}, and TE_{311} modes.

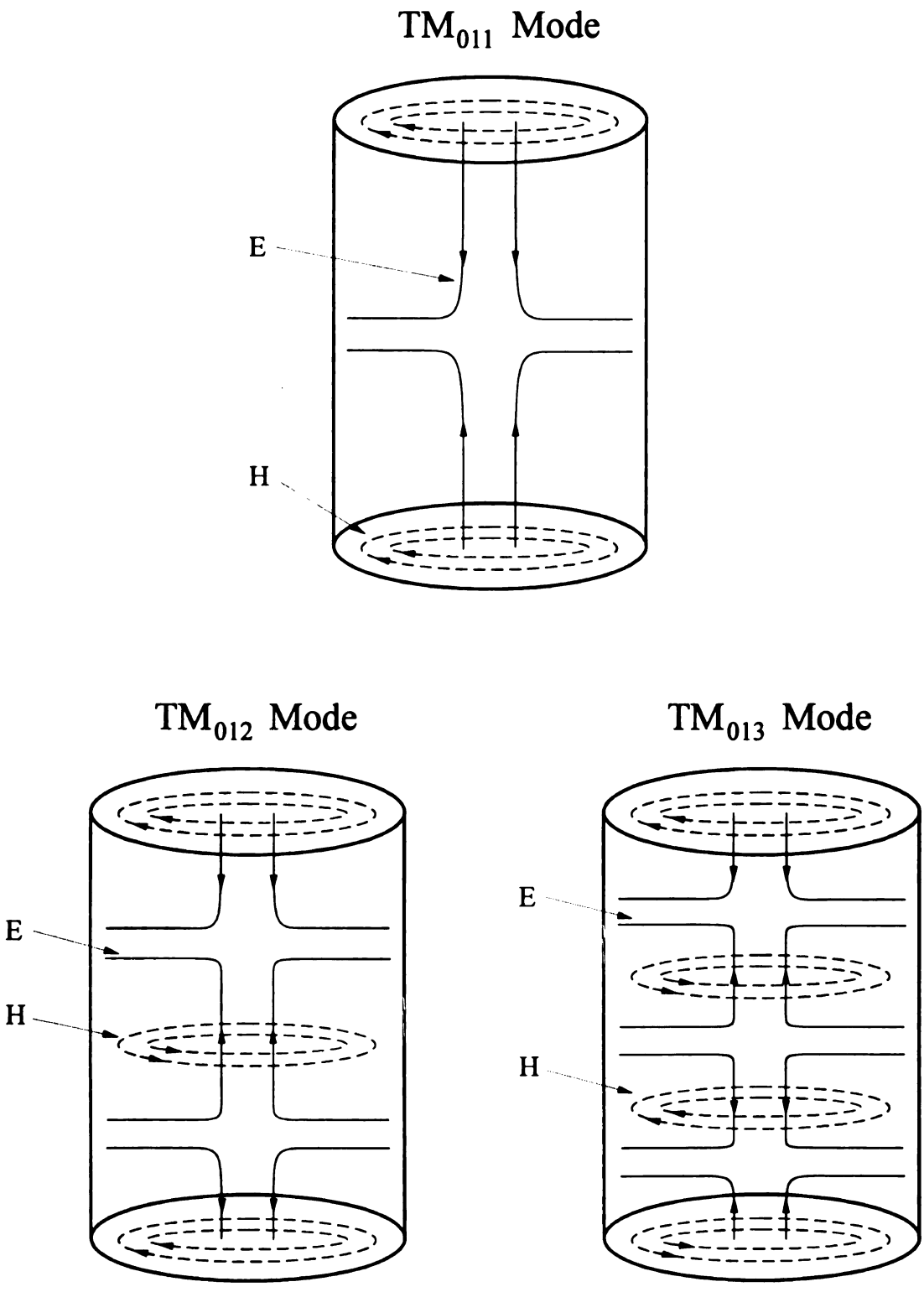

Figure 21. Field distributions of TM_{011}, TM_{012}, and TM_{013} modes.

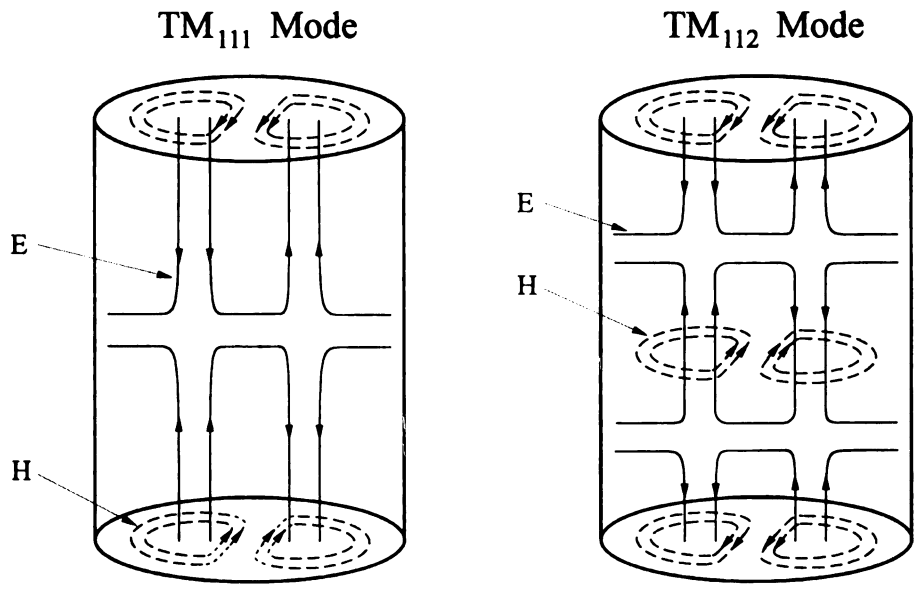

Figure 22. Field distributions of TM_{111} and TM_{112} modes.

3.6. MODE DIAGRAM FOR 7" IDEAL CYLINDRICAL SINGLE-MODE MICROWAVE CAVITY

A mode diagram is a diagram which allows one to expect which mode is admissible for a given geometry and dimension of a resonant cavity. Equation 58 states that the resonance frequency for an electromagnetic mode depends on the geometry and dimensions of a microwave cavity. The microwave used in this study is a cylindrical circular resonant cavity of 17.78 cm (7 inches) in diameter. The cavity has a movable top plate which determines the actual cavity height. The actual cavity height can be adjusted in the range of 7.3 cm to 21.95 cm. Thus various cavity modes can be established for a given cavity height of the cylindrical cavity.

The exact equation for a resonance frequency of a cylindrical circular single-mode resonant microwave cavity is [60]

$$(f_o)_{nml} = \frac{v}{2\pi}\sqrt{\left(\frac{P_{nm}}{a}\right)^2 + \left(\frac{l\pi}{d}\right)^2} \qquad \text{for } TM_{nml} \text{ modes} \qquad (70)$$

and

$$(f_o)_{nml} = \frac{v}{2\pi}\sqrt{\left(\frac{Q_{nm}}{a}\right)^2 + \left(\frac{l\pi}{d}\right)^2} \qquad \text{for } TE_{nml} \text{ modes} \qquad (71)$$

where v = velocity of EM waves in a medium = $1/\sqrt{\mu\varepsilon}$

= c, speed of light in a vacuum = $1/\sqrt{\mu_o\varepsilon_o}$

= 3×10^8 m/sec

a = radius of a cylindrical cavity

d = cavity height

P_{nm} = m_{th} x value at which $J_n(x) = 0$

$$Q_{nm} = m_{th}\ x \text{ value at which } J_n'(x) = 0$$

Thus for the cavity used in this study the value of a is fixed to 8.89 cm, while the cavity height, d, varies from 7.3 cm to 21.95 cm. P_{nm} and Q_{nm} can be determined from the Bessel Function of the first kind as shown in Figure 23 (Table 6).

Based on equations 70 and 71, resonant frequencies for various modes were calculated for the cavity heights ranging from 4 cm to 24 cm which include the allowed cavity heights for the cylindrical cavity used in this study (Figure 24, Table 7). Since the frequency of the microwave power source is 2.45 GHz, at which the present cavity is designed to operate, the frequency range is confined to 2 GHz to 3 GHz for plotting a mode diagram.

From the mode diagram, it can be assumed that TM_{011}, TE_{211}, TE_{011} (TM_{111}), TE_{112}, TM_{012}, TE_{311}, TE_{212}, TE_{113}, and TM_{013} modes are theoretically admissible for the present 7″ empty cylindrical resonant cavity operated at 2.45 GHz (Figure 24, Table 7). Thus the cavity without a material load can be tuned to one of those resonant modes by adjusting the cavity height by changing the position of the movable top plate of the cavity. However, it has been reported that once the cavity is loaded with a material to be heated, the empty cavity modes are modified and may become hybrid modes or even new modes may be introduced depending on the dielectric properties and location of the material [65]. In spite of this discrepancy between the theoretically expected modes and the practically operating modes, the mode diagram will be useful to predict, understand and analyze the interactions between the material and microwaves during microwave heating in a single-mode microwave cavity.

Table 6. Values of (a) P_{nm} and (b) Q_{nm} which are used to calculate resonance frequencies for TM_{nm} and TE_{nm} modes, respectively.

(a)

P_{nm}		m		
		1	2	3
n	0	2.405	5.520	8.654
	1	3.832	7.016	10.174
	2	5.135	8.417	11.620
	3	6.380	9.761	13.015

(b)

Q_{nm}		m		
		1	2	3
n	0	3.832	7.016	10.174
	1	1.841	5.331	8.536
	2	3.054	6.706	9.970
	3	4.201	8.015	11.346

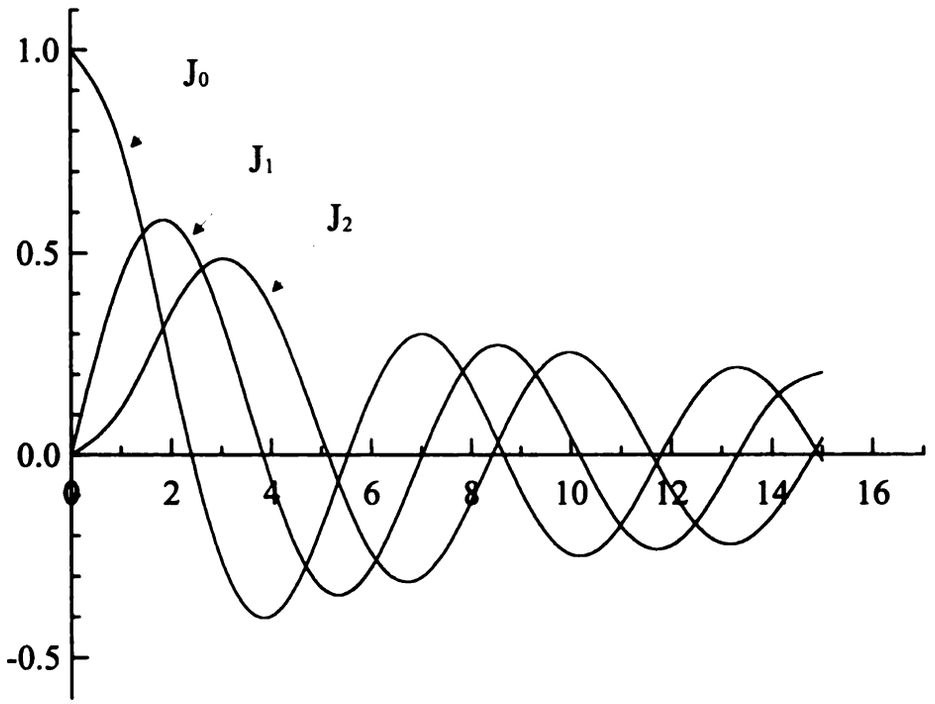

Figure 23. Bessel function of the first kind, for order n, where n = 1, 2, 3.

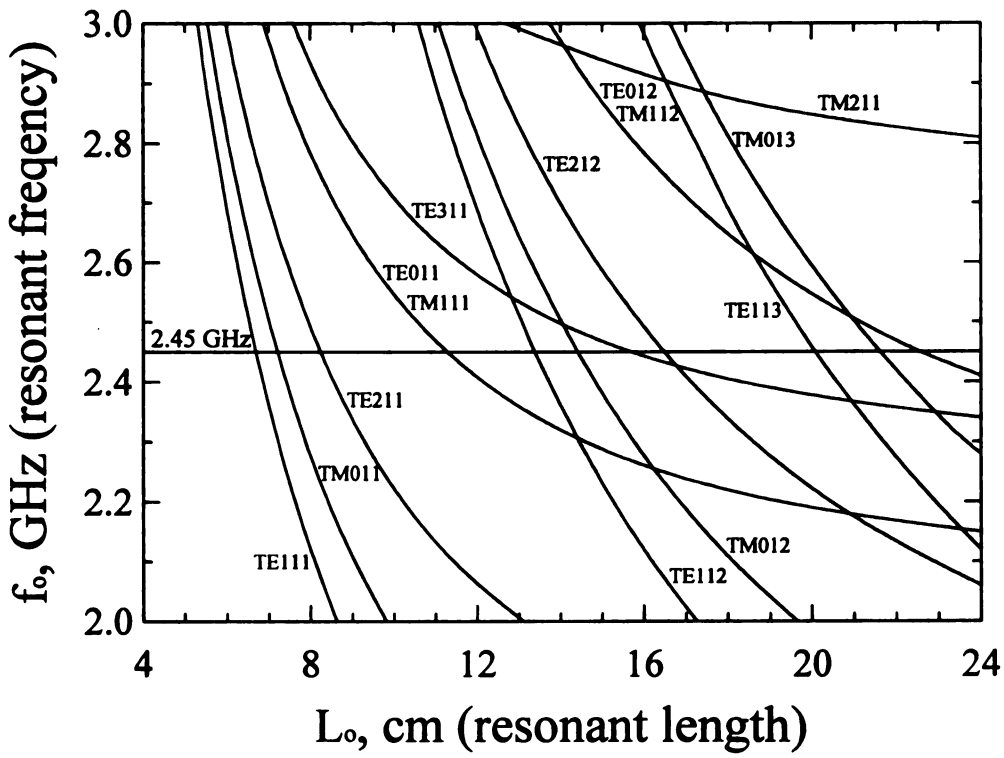

Figure 24. Mode diagram for 7″ ideal cylindrical single-mode microwave cavity.

Table 7. Data for resonant frequency versus resonant length of ideal 7″ empty cylindrical cavity.

f_o GHz	TE_{111}	TM_{011}	TE_{211}	TE_{011}	TM_{111}	TE_{112}	TM_{012}	TE_{311}	TE_{212}	TE_{113}	TM_{013}	TE_{012}	TM_{112}	TM_{211}
2.0	8.63	9.82	13.11			17.26	19.65		26.22	25.88	29.47			
2.1	8.10	9.06	11.44	35.93	35.93	16.19	18.12		22.88	24.29	27.18	71.87	71.87	
2.2	7.63	8.42	10.23	19.30	19.30	15.26	16.85		20.46	22.90	25.27	38.59	38.59	
2.3	7.22	7.88	9.30	14.61	14.61	14.45	15.76	33.61	18.61	21.67	23.65	29.22	29.22	
2.4	6.86	7.42	8.56	12.15	12.15	13.72	14.83	18.34	17.12	20.58	22.25	24.30	24.30	
2.45	6.69	7.21	8.24	11.29	11.29	13.38	14.41	15.71	16.48	20.07	21.62	22.57	22.57	
2.5	6.53	7.01	7.95	10.57	10.57	13.07	14.02	13.93	15.90	19.60	21.02	21.14	21.14	
2.6	6.24	6.65	7.44	9.44	9.44	12.48	13.30	11.61	14.87	18.71	19.94	18.88	18.88	
2.7	5.97	6.33	6.99	8.58	8.58	11.94	12.65	10.11	13.99	17.91	19.88	17.17	17.17	
2.8	5.73	6.04	6.61	7.90	7.90	11.45	12.08	9.05	13.22	17.28	18.17	15.80	15.80	31.01
2.9	5.50	5.78	6.27	7.34	7.34	11.00	11.55	8.23	12.54	16.51	17.33	14.68	14.68	16.73
3.0	5.30	5.54	5.97	6.87	6.87	10.59	11.08	7.59	11.94	15.89	16.62	13.74	13.74	12.70

REFERENCES

1. K.Y. Lee, E.D. Case, J. Asmussen, Jr., and M. Siegel, "Sintering of Alumina Ceramics in a Single Mode Cavity under Automated Control," Microwaves: Theory and Application in Materials Processing III, Cer. Trans., vol. 59, The American Ceramic Society Inc., Westerville, Ohio, pp. 473-480 (1995).

2. K.Y. Lee, L.C.G. Cropsey, B.R. Tyszka, and E.D. Case, "Grain Size, Density and Mechanical Properties of Alumina Batch-Processed in a Single-Mode Microwave Cavity," Mat. Res. Bull., vol. 32, no. 3, pp. 287-295 (1997).

3. Additional research report for sintering by K.Y. Lee, P.H. Dearhouse, E.D. Case, "Microwave Sintering of Aluminas and Alumina Matrix Zirconia Composites Using a Single-Mode Microwave Cavity."

4. K.Y. Lee, E.D. Case, J. Asmussen, Jr., and M. Siegel, "Microwave Sintering of Ceramic Matrix Composites and the Effect of Organic Binders on the Sinterability," Proceedings of the 11th Annual ESD Advanced Composites Conference, ESD, The Engineering Society, Ann Arbor, MI, pp. 491-503 (1995).

5. K.Y. Lee, E.D. Case, J. Asmussen, Jr., and M. Siegel, "Binder Burn-out in a Controlled Single-Mode Microwave Cavity," Scripta Materialia, vol. 35, no. 1, pp. 107-111 (1996).

6. K.Y. Lee, E.D. Case, and J. Asmussen, Jr., "Microwave Binder Burn-out for Batch Processing of Al_2O_3, Al_2O_3/SiC Platelet, and Al_2O_3/ZrO_2 Particle Powder Compacts," Microwaves: Theory and Application in Materials Processing V, Ceramic Transactions Vol. 80, pp. 539-546, Edited by D.E. Clark, W.H. Sutton, and D.A. Lewis, The American Ceramic Society, Westerville, Ohio (1997).

7. K.Y. Lee, E.D. Case, and D. Reinhard, "Microwave Joining and Repair of Ceramics and Ceramic Composites," Ceramic Engineering and Science Proceedings, vol. 18, pp. 543-550 (1997).

8. K.N. Seiber, K.Y. Lee, and E.D. Case, "Microwave and Conventional Joining of Ceramic Composites Using Spin-On Materials," Proceedings of the 12th Annual ASC Technical Conference on Composite Materials, Dearborn, MI, pp. 941-949 (1997).

9. B.A. Wilson, K.Y. Lee and E.D. Case, "Diffusive Crack Healing Behavior in Polycrystalline Alumina: A Comparison Between Microwave Annealing and Conventional Annealing," Materials Research Bulletin, vol. 32, no. 12, pp. 1607-1616 (1997).

10. K.Y. Lee, J.G. Lee, and E.D. Case "An AFM Study of Thermally-Induced Grain-Boundary Grooving in Polycrystalline Alumina: Part I, Groove Profile, Width, and Depth," to be submitted for publication in Journal De Physique III (1998).

11. K.Y. Lee, J.G. Lee, and E.D. Case, "An AFM Study of Thermally-Induced Grain-Boundary Grooving in Polycrystalline Alumina: Part II, Groove Angle, Surface Energy, Surface Diffusivity," to be submitted for publication in Journal De Physique III (1998).

12. K.Y. Lee, E.D. Case, and J. Asmussen, Jr., "The Steady-State Temperature as a Function of Casket Geometry for Microwave-Heated Refractory Caskets," Mat. Res. Innovat. 1(2): 101-116 (1997).

13. K.Y. Lee, E.D. Case, "Steady-State Temperature of Microwave-Heated Refractories as a Function of Microwave Power and Refractory Geometry," submitted for publication in Materials Science & Engineering A (1998).

14. M.C.L. Patterson, P.S. Apte, R.M. Kimber, and R. Roy, "Batch Process for Microwave Sintering of Si_3N_4," Mat. Res. Soc. Symp. Proc. vol 269, pp. 291-300 (1992).

15. J.D. Katz, and R.D. Blake, "Microwave Sintering of Multiple Alumina and Composite Components," Am. Cer. Soc. Bull. 70[8], 1304-1308 (1991).

16. D.K. Agrawal, Y. Fang, D.M. Roy, and R. Roy, "Fabrication of Hydroxyapatite Ceramics by Microwave Processing," Mat. Res. Soc. Symp. Proc. vol. 269, 231-236 (1992).

17. Y. Fang, D.K. Agrawal, D.M. Roy and R. Roy, "Rapid Sintering of Hydroxyapatite Ceramics by Microwave Processing," Cer. Trans. 21, Amer. Cer. Soc., 349-356 (1991).

18. T.T. Meek, R.D. Blake, and J.J. Petrovic, "Microwave Sintering of Al_2O_3 and Al_2O_3 - SiC Whisker Composites," Cer. Eng. Sci. Proc., vol. 8 (7-8), 861-71 (1987).

19. J. Cheng, J. Qiu, J. Zhou, and N Ye, "Densification Kinetics of Alumina During Microwave Sintering," Mat. Res. Soc. Symp. Proc. vol. 269, 323-328 (1992).

20. Materials Research Society Symposium Proceedings Volume 124, Microwave Processing of Materials, Editors: W.H. Sutton, M.H. Brooks and I.J. Chabinsky, Materials Research Society, Pittsburgh, Pennsylvania, 1988.

21. Materials Research Society Symposium Proceedings Volume 189, Microwave Processing of Materials II, Editors: W.B. Snyder, Jr., W.H. Sutton, M.F. Iskander and D.L. Johnson, Materials Research Society, Pittsburgh, Pennsylvania, 1990.

22. Materials Research Society Symposium Proceedings Volume 269, Microwave Processing of Materials III, Editors: R.L. Beatty, W.H. Sutton and M.F. Iskander, Materials Research Society, Pittsburgh, Pennsylvania, 1992.

23. Materials Research Society Symposium Proceedings Volume 347, Microwave Processing of Materials IV, Editors: M.F. Iskander, R.J. Lauf and W.H. Sutton, Materials Research Society, Pittsburgh, Pennsylvania, 1994.

24. Materials Research Society Symposium Proceedings Volume 430, Microwave Processing of Materials V, Editors: M.F. Iskander, J.O. Kiggans, Jr., J.C. Bolomey, Materials Research Society, Pittsburgh, Pennsylvania, 1996.

25. Microwaves: Theory and Application in Materials Processing, Ceramic Transactions vol. 21, Edited by D.E. Clark, F.D. Gac, and W.H. Sutton, The American Ceramic Society Inc., Westerville, Ohio, 1991.

26. Microwaves: Theory and Application in Materials Processing II, Ceramic Transactions vol. 36, Edited by D.E. Clark, W.R. Tinga, and J.R. Laia, Jr., The American Ceramic Society Inc., Westerville, Ohio, 1993.

27. Microwaves: Theory and Application in Materials Processing III, Ceramic Transactions vol. 59, Edited by ???, The American Ceramic Society Inc., Westerville, Ohio, 1995.

28. W.H. Sutton, "Microwave Processing of Ceramic Materials," Am. Ceram. Soc. Bull. 68[2], pp. 376-386 (1989).

29. M.A. Janney, H.D. Kimrey, and J.O. Kiggans, "Microwave Processing of Ceramics: Guidelines Used at the Oak Ridge National Laboratory," in Microwave Processing of Materials, III, R.L. Beatty, W.H. Sutton, and M.F. Iskander, eds., MRS Symp. Proc., vol. 269, pp. 173-85 (1992).

30. L.M. Sheppard, "Manufacturing Ceramics with Microwaves: The Potential for Economical Production," Am. Cer. Soc. Bull., 67[10], 1656-1661, 1988.

31. M.A. Janney, H.D. Kimrey, "Microwave Sintering of Alumina at 28 GHz," Ceramic Powder Science, II, B, Ceramic Transactions, vol. 1, pp. 919-24 (1988).

32. M.A. Janney and H.D. Kimrey, "Diffusion-Controlled Processes in Microwave-Fired Oxide Ceramics," Mater. Res. Soc. Symp. Proc., vol. 189, 215-227, 1991.

33. Y.L. Tian, D.L. Johnson and M.E. Brodwin, "Ultrafine Microstructure of Al_2O_3 Produced by Microwave Sintering," Ceramic Powder Science II, B, Ceramic Transactions, vol. 1, pp. 925-932 (1988).

34. A. De, I. Ahmad, E.D. Whitney, and D.E. Clark, "Microwave (Hybrid) Heating of Alumina at 2.45 GHz: I. Microstructural Uniformity and Homogeneity," Microwaves: Theory and Application in Materials Processing, Ceramic Transactions, vol. 21, pp. 319-28 (1991).

35. C.E. Holcombe, T.T. Meek, and N.L. Dykes, "Enhanced Thermal Shock Properties of Y_2O_3-2 wt.% ZrO_2 Heated Using 2.45 GHz Radiation," Mat. Res. Soc. Symp. Proc. vol. 124, 227-234, 1988.

36. M.C.L. Patterson, P.S. Apte, R.M. Kimber, and R. Roy, "Mechanical and Physical Properties of Microwave Sintered Si_3N_4," Mat. Res. Soc. Symp. Proc. vol 269, 301-310, 1992.

37. M.A. Janney, H.D. Kimrey, M.A. Schmidt, and J.O. Kiggans, "Grain Growth in Microwave-Annealed Alumina," J. Am. Ceram. Soc., 74 [7] 1675-81 (1991).

38 D.M. Pozar, Microwave Engineering, p. 34-38, p. 330-354, Addison-Wesley Publishing Company, Inc., Reading, Massachusetts (1990).

39. A.C. Metaxas and J.G.P. Binner, "Microwave Processing of Ceramics," in Advanced Ceramic Processing and Technology, vol. 1, chap. 8, pp. 285-367, edited by J.G.P. Binner, Noyes Publications, Park Ridge, New Jersey, U.S.A. (1990).

40. J.D. Katz, "Microwave Sintering of Ceramics," Annu. Rev. Mater. Sci., 22:153-70, 1992.

41. A.J. Berteau and J.C. Badot, "High Temperature Microwave Heating in Refractory Materials," J. Microwave Power, 11[4] pp. 315-320 (1976).

42. W.R. Tinga, "Fundamentals of Microwave Material Interactions and Sintering," Mat. Res. Soc. Symp. Proc., vol. 124, pp. 33-43 (1988).

43. A.C. Metaxas and R.J. Meredith, Industrial Microwave Heating, Peter Peregrinus, Ltd., London, UK (1983).

44. A.R. von Hippel, ed., Dielectric Materials and Applications, pp. 3-46, MIT Press, Cambridge, MA (1954).

45. Ralph W. Bruce, "Activation Energies for the Dielectric Loss Factor/AC Conductivity of Some Polycrystalline Ceramics," Microwaves: Theory and Application in Materials Processing, Cer. Trans. 21, Amer. Cer. Soc., 107-116 (1991).

46. Barsoum, Fundamentals of Ceramics, p. 543, The McGraw-Hill Companies, Inc., New York (1997).

47. W.D. Kingery, H.K. Bowen, and D.R. Uhlmann, Introduction to Ceramics, 2nd edition, p. 923, Wiley-Interscience Publication, New York (1976).

48. R.C. Buchanan, Ceramic Materials for Electronics, p. 33, 47, Marcel Dekker Inc., New York, N.Y. (1986).

49. J. Samuels and J.R. Brandon, "Effect of Composition on the Enhanced Microwave Sintering of Alumina-Based Ceramic Composites," J. Matls. Sci., 27, 3259-65 (1992).

50. R.E. Newnham, S.J. Jang, Ming Xu, and Frederick Jones, "Fundamental Interaction Mechanisms Between Microwaves and Matter," Microwaves: Theory and Application in Materials Processing, Cer. Trans. 21, Amer. Cer. Soc., 51-67 (1991).

51. S.L. McGill, J.W. Walkiewicz, and G.A. Smyres, "The Effect of Power Level on the Microwave Heating of Selected Chemical Minerals," Microwave Processing of Materials, Matls, Res. Soc. Proc., vol. 124, pp. 247-252 (1988).

52. D. Palaith, R. Silberglitt, "Microwave Joining of Ceramics," Am. Cer. Soc. Bull., vol. 68, no. 9, 1601-1606 (1989).

53. A.R. von Hippel, ed., Dielectric Materials and Applications, pp. 3-46, M.I.T. Press, Cambridge, MA (1954).

54. W. B. Westphal and A. Sils, "Dielectric Constant and Loss Data," Technical Report AFML-TR-72-39, Massachusetts Institute of Technology, Cambridge, MA (1972).

55. T.T. Meek, R.D. Blake, and J.J. Petrovic, "Microwave Sintering of Al_2O_3 and Al_2O_3 - SiC Whisker Composites," Cer. Eng. Sci. Proc., vol. 8 (7-8), 861-71 (1987).

56. V.K. Varadan, Y. Ma, A. Lakhtakia and V.V. Varadan, "Microwave Sintering of Ceramics," Mat. Res. Soc. Symp. Proc. Vol. 124, pp. 45-55 (1988).

57. Y-L. Tian, "Practices of Ultra-Rapid Sintering of Ceramics Using Single Mode Applicators," Microwaves: Theory and Application in Materials Processing, Cer. Trans. vol. 21, Amer. Cer. Soc., 283-300 (1991).

58. M.A. Janney, H.D. Kimrey, "Microwave Sintering of Alumina at 28 GHz," Ceramic Powder Science, II, B, Ceramic Transactions, vol. 1, pp. 919-24 (1988).

59. W.H. Sutton, "Microwave Firing of High Alumina Castables," Mat. Res. Soc. Proc. vol. 124, pp. 287-295 (1988).

60. S.Y. Liao, Microwave Devices and Circuits, 3rd ed., p. 16-21, p. 133-141, Prentice Hall, Englewood Cliffs, New Jersey (1990).

61. S. Ramo, J.R. Whinnery, and T. Van Duzer, Fields and Waves in Communication Electronics, 2nd ed., p. 146-147, p. 279-283, p. 411-444, p. 486-512, John Wiley & Sons, New York (1984).

62. D.K. Cheng, "Field and Wave Electromagnetics," 2nd edition, p. 307-387, p. 582-592, Addison-Wesley Publishing Company, Inc., Reading, Massachusetts (1989).

63. N.J. Cronin, Microwave and Optical Waveguides, p. 79-90, Institute of Physics Publishing, Bristol and Philadelphia (1995).

64. J. Asmussen and R. Garard, "Precision Microwave Applicators and Systems for Plasma and Materials Processing," Mat. Res. Soc. Symp. Proc. 124, 347-352 (1988).

65. J. Asmussen, H.H. Lin, B. Manring, and R. Fritz, "Single-mode or controlled multimode microwave cavity applicators for precision materials processing," Rev. Sci. Instrum., 58 [8] 1477-1486 (1987).

66. J.D. Jackson, Classical Electrodynamics, pp. 255-259, Wiley, New York, 1962.

67. Helszajn, Microwave Engineering: Passive, Active, and Non-Reciprocal Circuits, p. 140-141, McGraw-Hill, New York (1992).

CHAPTER 1

SINTERING

Part I. SINTERING OF ALUMINA CERAMICS IN A SINGLE MODE CAVITY UNDER AUTOMATED CONTROL[1]

ABSTRACT

An automated processing system featuring a single-mode microwave cavity operated at 2.45 GHz has been used to sinter a series of alumina powder compacts. The automated control allows repeatable heating schedules for the processing. The resulting sintered alumina specimens were crack-free and had small, uniform grain sizes.

1. INTRODUCTION

Microwave sintering can be an attractive processing technique since materials can be heated directly and/or indirectly via the interaction with electromagnetic fields. Typically microwave processing yields ceramic specimens having high densities and fine grain sizes. Also, microwave processing allows high heating rates (short processing times), compared to conventional heating.

---

[1] Ki-Yong Lee, Eldon D. Case, Jes Asmussen, Jr. and Marvin Siegel, Microwaves: Theory and Application in Materials Processing III, Cer. Trans., vol. 59, Am. Cer. Soc. Inc., Westerville, Ohio, pp. 473-480 (1995).

Multimode microwave cavities [1-6] require very high power due to the relatively low coupling efficiency of microwave energy with materials. Also, a multimode cavity's nonuniform electromagnetic field distribution can result in inhomogeneous heating and hot spots depending on the volume of the processed material and the location of the material within the microwave cavity [7]. Nevertheless multimode cavities are frequently used due to their low cost, ease of construction and adaptability [8].

To improve process control and heating uniformity, several investigators have designed and used single-mode microwave cavities [8-13]. Single mode cavities can maximize the electrical field strength at the location of processed material, potentially yielding higher heating rates and more uniform heating than is the case for conventional multimode cavities [7-9, 14]. Using an internally-tuned single-mode circular cylindrical cavity, Asmussen et al. [8, 14] demonstrated that microwave energy can be coupled efficiently into either low loss or lossy materials.

Most single mode cavities used for microwave processing ceramics are tuned by manually adjusting the positions of the electrical short and the probe to maximize the energy absorbed by the process material. Since the dielectric properties of material are functions of both porosity and temperature, the dielectric properties of the ceramic change during processing. This change in dielectric properties requires that the cavity be tuned continuously to maintain efficient microwave coupling and an optimum heating rate. Manual cavity tuning, however, is too slow and cumbersome to allow one to precisely tune the cavity as the material's dielectric properties can change rapidly during processing.

Recently Asmussen and Siegel [15] developed a single-mode cylindrical cavity that is tuned by computer-automated adjustments of the sliding electrical short and probe

positions. Two computer-driven controllers (Microstep Drive Sx Series, Compumotor, Fauver, MI) allow a rapid fine-tuning of the short and the probe positions to with an accuracy of ±0.1 mm. In this study Asmussen and Siegel's computer-controlled microwave processing system was used to obtain very similar heating schedules during processing of a series of alumina powder compacts. Such repeatability would be difficult using manual tuning techniques.

2. EXPERIMENTAL PROCEDURE

2.1. Experimental Apparatus

Figure 1 is a schematic of the microwave sintering apparatus. The microwave power supply (Sairem, Model MWPS 2000, Wavemat Inc., Plymouth, MI,) used in this study can supply from zero to 2000 Watts of continuous wave microwave power at 2.45 GHz. Microwave power is generated by a magnetron. Waveguides then feed the microwave power into the cavity through an adjustable tuning probe. Analog power meters connected to the waveguide through attenuators indicate the forward and reflected power levels.

The single mode microwave cavity (Model CMPR-250, Wavemat Inc., Plymouth, MI.) used in the study can be internally tuned to resonate in many different microwave cavity resonant modes by adjusting the short and the power launch probe (Figure 1). Cavity tuning was performed by continuous adjustments of the probe positions in order to minimize the reflected power after every change of forward power.

An optical pyrometer (Accufiber Optical Fiber Thermometer, Model 10, Luxtron Co., Beaverton, Oregon) was used to measure temperatures ranging from 500°C to 1900°C

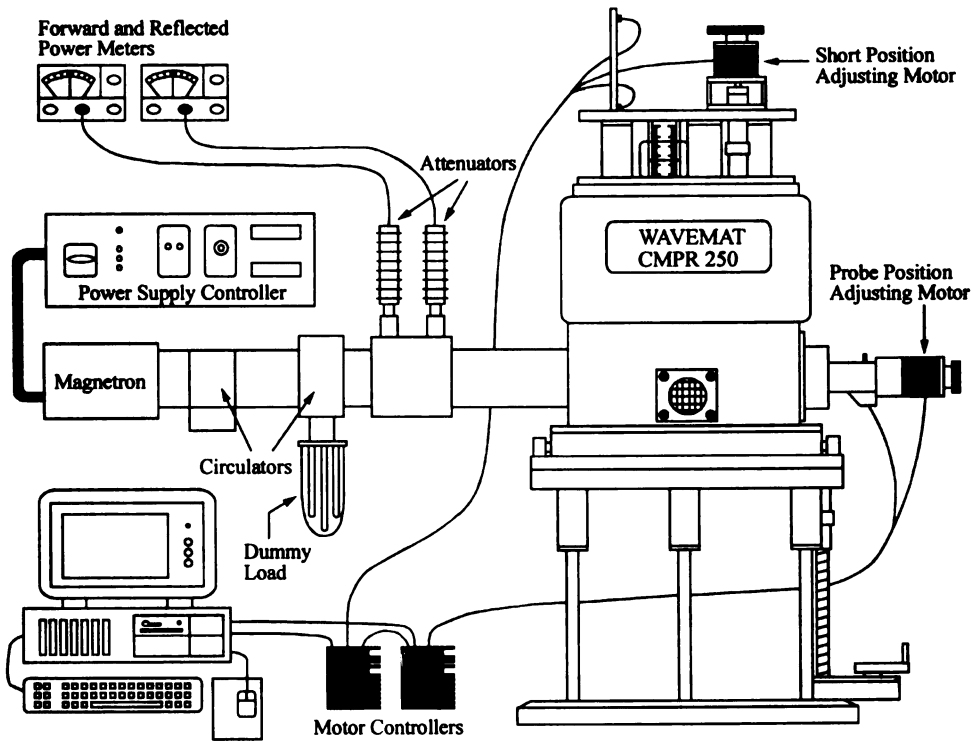

Figure 1. Schematic of microwave sintering apparatus.

with an accuracy of $\pm 1^{\circ}C$. A 5 mm diameter hole through the wall of the insulation casket allowed the pyrometer to be sited on the specimen during the experimentation.

2.2. Materials

Using the computer controlled single mode cavity, powder compacts of three different commercial alumina powders (Alcoa A-16 SG, Sumitomo AKP-30, and Sumitomo AKP-50) were processed. The average particle size for each of the powders is listed in Table 1. Each powder compact was cold pressed at about 20 MPa into a disk about 22 mm in diameter and 1.7 mm thick. The initial green densities of the compacts were approximately 50 percent with respect to the theoretical density of 3.987 g/cm^3 for alumina [16].

2.3. Microwave Sintering

Each of the alumina powder compacts was heated to $1575^{\circ}C$ using the TM_{012} microwave cavity resonant mode and then held at $1575^{\circ}C$ for 30 minutes. Alumina, which is a low loss material, has a loss tangent ranging from 0.0003 to 0.002 [17]. The low loss tangent of alumina at or near room temperature limits direct microwave coupling to the alumina. However, the alumina specimens were placed in a casket composed of a zirconia cylinder (Type ZYC, Zircar Products Inc.) 10 cm diameter and 7 cm height. Top and bottom discs for the casket were made from alumina insulating board (SALI, Zircar Products Inc.). The typical loss tangent value of zirconia is about 0.01 at room temperature [17]. Thus the zirconia casket helped to heat the alumina by radiant heating as well as providing thermal insulation.

3. RESULTS AND DISCUSSION

Under computer-automated control, the heating schedule from about 800 degrees to the maximum temperature of 1575 C was very similar for specimens of each of the alumina powder types (Figures 2 and 3). Over this temperature range, the heating schedule for the alumina also was very similar to the "empty casket" (no alumina specimen present) runs. However, the power level at which significant coupling first occurred (as evidenced by an initial, rapid temperature rise) did vary in the following way. For the AKP-30 and AKP-50 coupling became significant at about 600 Watts of input power, while the A16-SG and the empty casket first coupled at a input power of about 300 Watts and 275 Watts, respectively (Figure 3).

The rapid temperature rise subsequent to the initial coupling with the microwave power may be due to hot spots in the zirconia casket cylinder, which were observed as bright spots with the unaided eye. The differences in the initial heating of the AKP grade powders and the A16 powders may be due to differences in the dielectric properties of the powders.

The sintered alumina specimens had densities ranging from 97.1 to 99.6 percent of theoretical (Table 1), as measured by Archimedes method. Average grain sizes (Table 1) were determined by the linear intercept method using SEM micrographs of fracture surfaces.

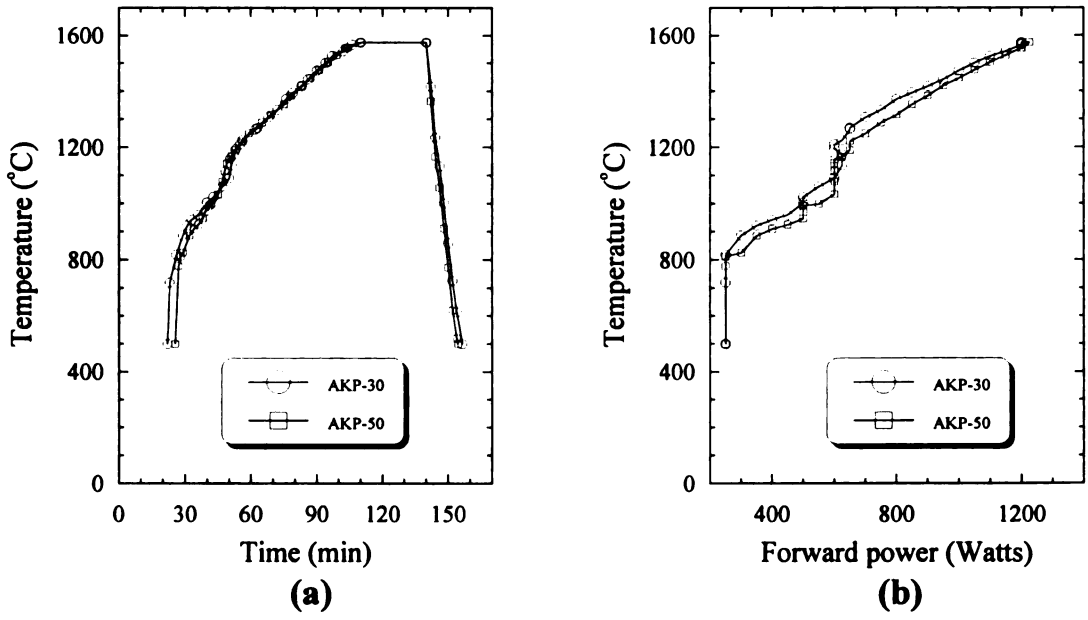

Figure 2. Heating schedule (a) and a plot of temperature vs. forward power (b) for AKP-30 and AKP-50.

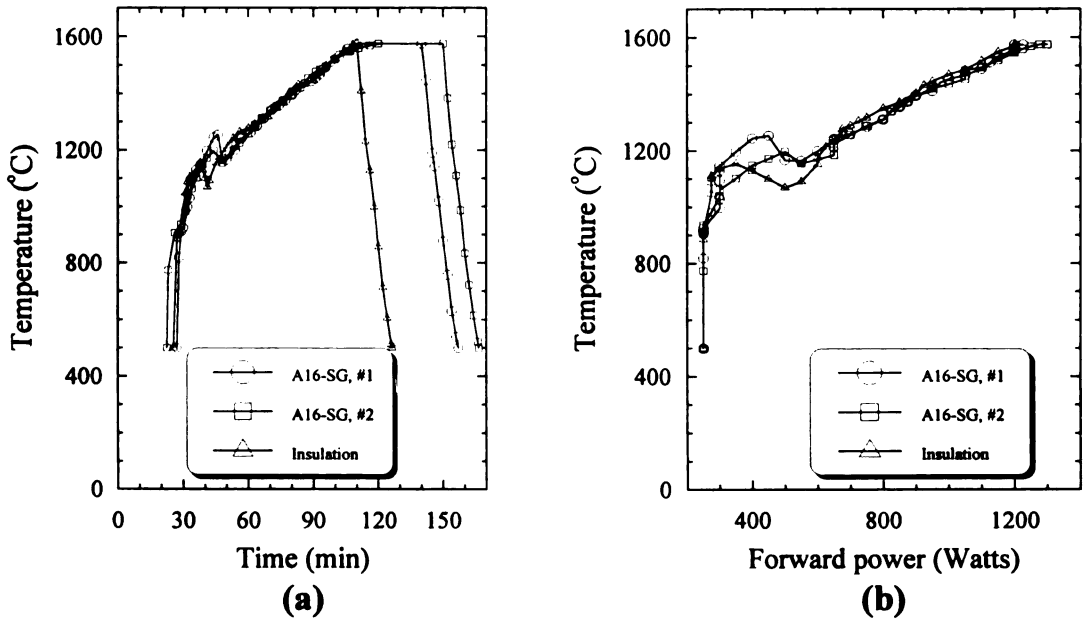

Figure 3. Heating schedule (a) and a plot of temperature vs. forward power (b) for Alcoa A16-SG.

Table 1. Results on microwave sintered alumina.

Material	Average particle size (μm)	Average grain size (μm)	% Densification
A16-SG	0.52	1.94 *	99.6
AKP-30	0.41	4.85 *	98.4
AKP-50	0.23	3.68 *	97.1

* Average intercept length was multiplied by a stereographic correction factor 1.5 to obtain the average grain size [18].

4. CONCLUSIONS

This study has demonstrated that an automated processing system featuring a single-mode microwave cavity can be controlled to provide repeatable heating schedules for a series of alumina powder compacts. The resulting alumina specimens were near theoretical density with a uniform, small-grain sized microstructure. Future studies will employ the automated processing system to sinter other ceramics and ceramic composites.

REFERENCES

1. A. De, I. Ahmad, E.D. Whitney, and D.E. Clark, Cer. Trans., vol. 21, pp. 319-28 (1991).

2. Y. Fang, D.K. Agrawal, D.M. Roy and R. Roy, Cer. Trans., vol. 21, pp. 349-356 (1991).

3. M.A. Janney, C.L. Calhoun, and H.D. Kimrey, Cer. Trans., vol. 21, pp. 311-318 (1991).

4. H.D. Kimrey, J.O. Kiggans, M.A. Janney, and R.L. Beatty, Mat. Res. Soc. Symp. Proc. vol. 189, pp. 243-256 (1991).

5. M.C.L. Patterson, P.S. Apte, R.M. Kimber, and R. Roy, Mat. Res. Soc. Symp. Proc. vol 269, pp. 291-300 (1992).

6. R.L. Smith, M.F. Iskander, O. Andrade, and H. Kimrey, Mat. Res. Soc. Symp. Proc. vol 269, pp. 47-52 (1992).

7. W.H. Sutton, Am. Ceram. Soc. Bull. 68[2] pp. 376-386 (1989).

8. J. Asmussen and R. Garard, Mat. Res. Soc. Proc. vol. 124, pp. 347-352 (1988).

9. Y-L. Tian, Cer. Trans. vol. 21, Amer. Cer. Soc., pp. 283-300 (1991).

10. B.Q. Tian and W.R. Tinga, Cer. Trans. vol. 21, Amer. Cer. Soc., pp. 647-654 (1991).

11. J.F. Gerling and G. Fournier, Cer. Trans. vol. 21, Amer. Cer. Soc., pp. 667-674 (1991).

12. H.S. Sa'adaldin, W.M. Black, I. Ahmad and R. Silberglitt, Mat. Res. Soc. Symp. Proc., vol. 269, pp. 91-96 (1992).

13. D.S. Patil, B.C. Mutsuddy, J. Gavulic, and M. Dahimene, Cer. Trans. vol. 21, Amer. Cer. Soc., pp. 301-309 (1991).

14. J. Asmussen, H.H. Lin, B. Manring, and R. Fritz, Rev. Sci. Instrum., 58 [8] 1477-1486 (1987).

15. J. Asmussen, Jr. and M. Siegel, to be published.

16. National Bureau of Standards (U.S.), Circ. 539, vol. 9, page 3 (1959).

17. R.C. Buchanan, ed., Ceramic Materials for Electronics, Marcel Dekker, Inc., N.Y., N.Y., page 4 (1986).

18. E. E. Underwood, A. R. Colcord, and R. C. Waugh, pages 25-52 in R. M. Fulrath and J. A. Pask, eds., Ceramic Microstructures, John Wiley and Sons, New York (1968).

Part II. GRAIN SIZE, DENSITY, AND MECHANICAL PROPERTIES OF ALUMINA BATCH-PROCESSED IN A SINGLE-MODE MICROWAVE CAVITY[2]

ABSTRACT

Four different microwave cavity modes, namely, TM_{111}, TE_{112}, TE_{113}, TM_{013}, were used to sinter alumina powder compacts in a batch process using a cylindrical single-mode microwave cavity. The grain size, mass density, hardness, and fracture toughness of the final densified products were examined in terms of (i) the position of the specimen within the microwave casket and (ii) the cavity mode.

1. INTRODUCTION

Although microwave processing of ceramics typically involves specimens processed one at a time, Katz et al. (1) and Patterson et al. (2) are among the researchers that have batch-processed ceramics using microwaves. Katz et al. (1) used a resonant microwave cavity to sinter 12.5 gram cylindrical powder compacts of alumina or alumina-5 vol% SiC in batches of 20 specimens each. A maximum microwave input power of about 4 kWatts yielded a sintering temperature of 1600°C. Using a multimode cavity at 2.45 GHz Patterson et al. (2) sintered 12, 24, and 90 specimen batches of Si_3N_4-5% Al_2O_3 and Si_3N_4-5% Y_2O_3 powder compacts. Specimens were placed in a powder bed of 40wt% SiC, 30wt% BN, and 30wt% Si_3N_4 held with an alumina crucible. The results of this

[2] Ki-Yong Lee, Luke C.G. Cropsey, Benjamin R. Tyszka, and Eldon D. Case, Materials Research Bulletin, vol. 32, No. 3, pp. 287-295 (1997).

study and the work of Katz et al. (1) and Patterson et al. (2) will be compared in the Summary and Conclusions section of this paper.

In this study, we used a circular, cylindrical single-mode microwave cavity for batch-processing alumina powder compacts. First, at low temperatures and low microwave input power, the heat distribution for various microwave cavity modes was directly determined using thermally-sensitive paper within a casket (zirconia/alumina enclosure). Next, alumina powder compacts were sintered and the grain size, mass density, hardness, and fracture toughness were determined as a function of (i) the specimen position within a casket and (ii) the cavity mode.

2. EXPERIMENTAL PROCEDURES

Disc-shaped compacts about 2.2 cm in diameter, 2 mm thick, and with a mean mass of 1.993 ± 0.003 grams were pressed from Sumitomo AKP30 alumina powder. Details of ball-milling and pressing the powders are given elsewhere (3,4). A cylindrical single-mode microwave cavity (CMPR-250, Wavemat Inc., MI) was used with a microwave power supply (Sairem, MWPS 2000, Wavemat Inc., MI) which generates microwaves of 2.45 GHz and maximum power of 2000 Watts (3-5).

The microwave modes identified for the cavity loaded with the casket were TE_{211}, TM_{111}, TE_{112}, TM_{012}, TE_{311}, TE_{212}, TE_{113}, and TM_{013} modes. These modes are standing-wave electromagnetic field patterns that are a function of cavity geometry and microwave frequency (6). The microwave cavity used for this study had a movable top plate, enabling one to change the cavity height and thus tune the cavity to either TM (transverse magnetic) or TE (transverse electric) modes (3-5). Two TM modes and two TE modes,

namely; TM_{111}, TE_{112}, TE_{113}, TM_{013}, were selected for microwave heating in this study, since TM_{111} and TE_{112} modes were separated from TE_{113} and TM_{013} modes by at least 6 cm in cavity height (Figure 1).

For low temperatures, the heat distribution inside the empty casket (without the alumina specimens) was investigated using a thermally-sensitive paper (Graphic Controls Corp., Buffalo, NY). Using a conventional electrical resistance furnace, it was determined that at about 120°C the color of the paper changed from white to light blue and that the paper turned to dark blue after an increase in time-temperature. The casket containing a circular piece of the thermal paper about 7 cm in diameter was centered along the axis of the microwave cavity. The microwave cavity was tuned to each of the four cavity modes (3-5).

A different mode was used to sinter each of four batches of alumina powder compacts, with six specimens per batch. The casket containing six specimens (Figure 2) was centered along the cavity axis. Temperature measurement techniques in the microwave cavity (via an optical pyrometer) are described elsewhere (4). For specimen temperatures above 500°C, the microwave input power was increased by 50 Watts every 3 minutes and the cavity was re-tuned until the temperature reached 1500°C. The initial input power for microwave coupling (4), the maximum input power, average heating rate from 500°C to 1500°C, and the sintering time and temperature are summarized in Table 1 for each of the four modes.

After sintering, the mass density of the 24 individual specimens was determined by Archimedes method. Fracture surfaces of each specimen were examined by SEM (JEOL, JSM 6400V) to determine the grain size using a line intercept method on the

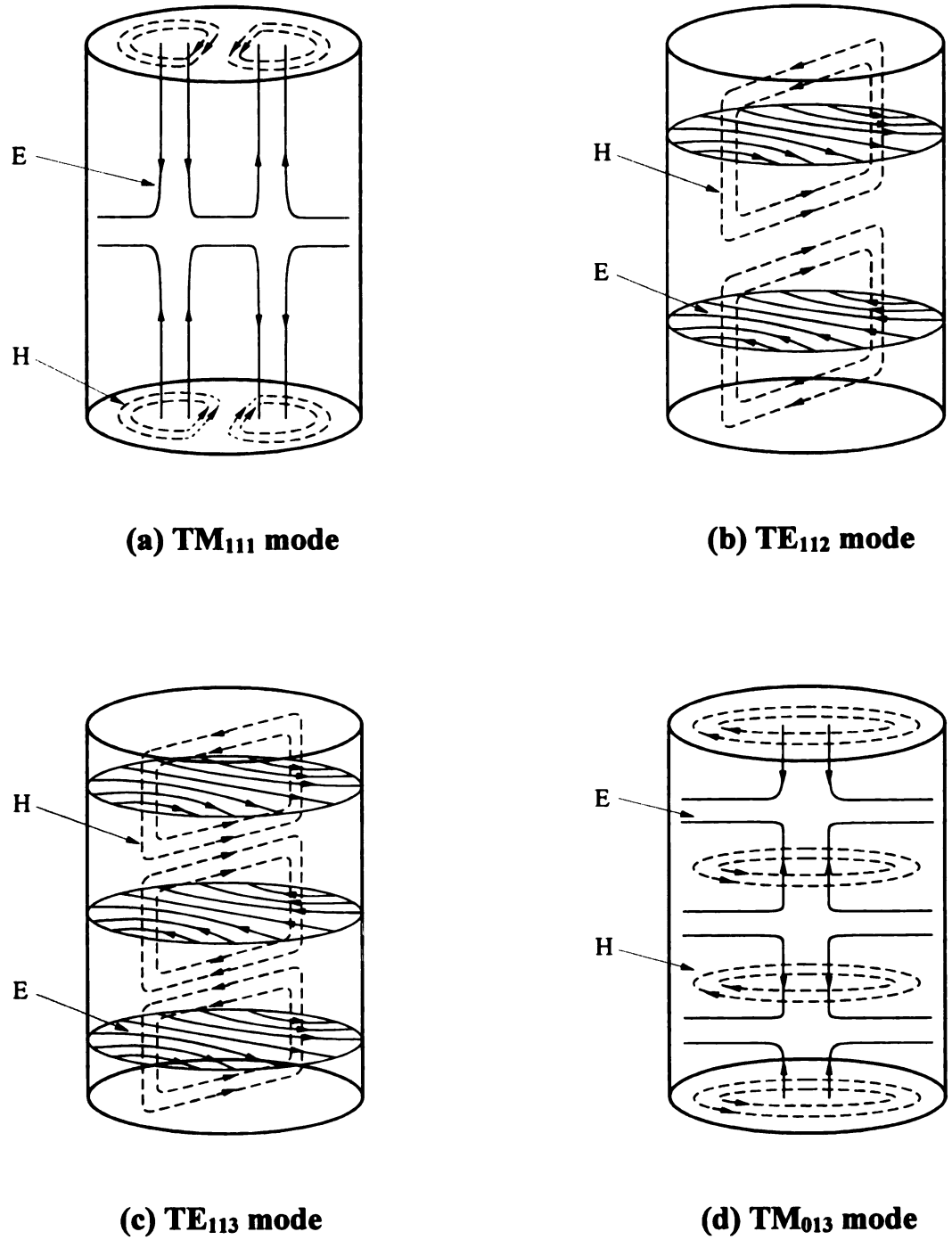

Figure 1. Schematics for electromagnetic field patterns of the indicated microwave cavity modes. Solid lines represent electric fields (E) and dotted lines represent magnetic fields (H).

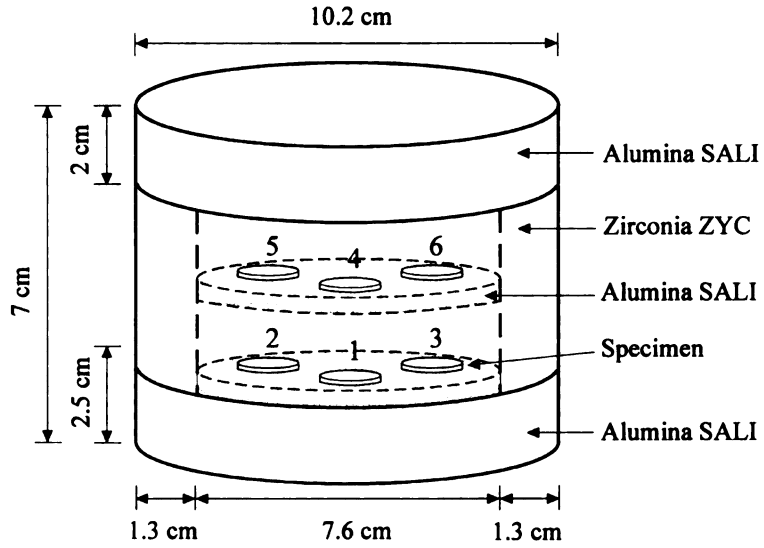

Figure 2. Schematic for casket used for microwave heating showing the positions of the six disc-shaped powder compact specimens included in each processing batch.

Table 1. Summary for microwave processing during batch processes.

Microwave cavity mode	Initial input power for coupling	Maximum input power	Average heating rate from 500°C	Sintering temperature and time
TM_{111}	130 Watts	1060 Watts	16.0 °C/min.	1500°C for 30 min.
TE_{112}	90 Watts	1250 Watts	14.0 °C/min.	1500°C for 30 min.
TE_{113}	100 Watts	1220 Watts	14.0 °C/min.	1500°C for 30 min.
TM_{013}	190 Watts	1130 Watts	17.3 °C/min.	1500°C for 30 min.

micrographs.

The sintered specimens were polished with consecutive grits of 17, 15, 10, 6, and 1 μm diamond paste compounds (Warren Diamond Powder Company) using a Leco VP-50 polishing machine. Ten Vicker's indentations were made on each specimen, with an indentation load, load time, and loading rate of 98 Newtons, 5 seconds, and 60 μm/second, respectively, to determine the hardness and fracture toughness of the specimens.

3. RESULTS AND DISCUSSION

At low input power, the nonuniform heat distribution observed for each cavity mode (Figure 3) likely resulted from spatial variation of the microwave power densities absorbed by the casket. The central portion of the SALI setter within the casket apparently did not couple well with the microwave field (Figure 3). The microwave-lossy zirconia cylinder did couple well and the interaction between the microwave field and the zirconia cylinder likely modifies the local electric field pattern (Figure 3).

Although at low microwave input power and low temperature the heat distribution within the empty casket was nonuniform, the specimens sintered at higher input power all had mass densities greater than 98.3% (Table 2). The mean grain size of batch-processed specimens was similar from mode to mode ranging from 6.00 μm for TE_{112} mode to 8.00 μm for TM_{111} mode, although the grain size was a weak function of the position of individual specimens within the casket (Table 2).

The hardness, H, of the sintered alumina was determined by (8,9) $H = \alpha P/a^2$, where 2a is the diagonal length of the indent, P is load and α is 0.4636, based on the area of the

Vicker's indenter contact (8,9). The fracture toughness, K_{IC}, was calculated by (8,10) $K_{IC} = \beta P(E/H)^{1/2}c^{-3/2}$, where 2c is the total radial crack length, β is a dimensionless constant equal to 0.016 ± 0.004, E is the elastic modulus (assumed to be 365.4 GPa, which corresponds to sintered alumina at 95% of theoretical density (11)), and H is the hardness determined at the load P.

For the 24 alumina specimens sintered in this study, the mean and standard deviation of the hardness was 16.19 GPa ± 0.58 GPa which corresponds to a coefficient of variation of only 0.036 (Figure 4a). The hardness values obtained in this study thus are reasonably consistent with the literature values for hardness of polycrystalline alumina of 13 GPa to 23 GPa (9,12-14). The fracture toughness ranged from 2.34 $MPa{\cdot}m^{1/2}$ to 3.03 $MPa{\cdot}m^{1/2}$ with the average value of 2.70 $MPa{\cdot}m^{1/2}$. The standard deviation was ±0.18 $MPa{\cdot}m^{1/2}$ which was 6.7% of the average toughness value. The toughness values determined in this study were somewhat lower than the literature values of about 3 to 5 $MPa{\cdot}m^{1/2}$ (9,12-14).

The variations in the hardness and fracture toughness were examined in terms of (i) the specimen position (Figure 2) and (ii) the operating microwave cavity mode (Figure 1). The average hardness and fracture toughness values for the specimens heated at the same position but in different batches (Figures 4a and 4b) differed by no more than 2.6% and 5.3%, respectively, from position to position. The hardness for the specimens heated at positions 1 and 4 (Figure 2) were somewhat higher than for the specimens heated at positions 2, 3, 5 and 6 (Figure 4a). The hardness of specimens heated at positions 3 and 6 were slightly lower than average (Figure 4a).

Unlike homogeneity in the hardness and toughness data as a function of specimen

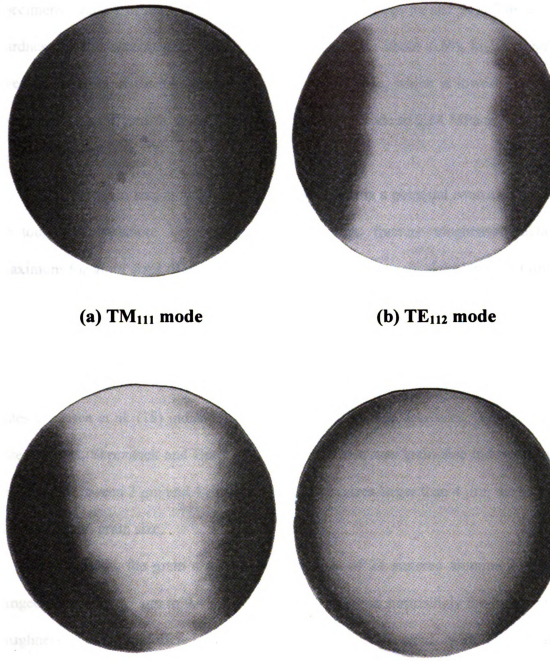

Figure 3. Heat distribution inside empty casket (Figure 2) as determined by thermally sensitive paper. The casket was heated in each cavity mode (a) for 5 minutes at 130 Watts, (b) for 1.5 minutes at 90 Watts, (c) for 2 minutes at 90 Watts, and (d) 4 minutes at 170 Watts. The dark areas in (a)-(d) indicate regions of microwave heating.

position, there are small apparent differences in hardness and toughness between specimens sintered in the four different cavity modes (Figures 5a and 5b). The average hardness of the specimens sintered in TE_{112} mode was about 6.6% higher than the average hardness of the specimens sintered in TE_{113} mode, which is lowest. Also, the toughness data differed from 2.45 $MPa \cdot m^{1/2}$ for TM_{111} mode to 2.84 $MPa \cdot m^{1/2}$ for TE_{112} mode by 15.9%.

Differing grain size among the sintered specimens is a potential source of hardness or toughness variation. For large-grained alumina, fracture toughness reaches a maximum for grain sizes of about 100 μm (15,16), but for grain sizes below 10 μm the trend is less clear. Fracture toughness may increase or decrease with the grain size depending on the test method or the specimen type (17). Rice et al. (15,16) show a relatively constant K_{IC} for alumina with grains smaller than 10 μm, while for similar grain sizes Claussen et al. (18) indicate K_{IC} increases as grain size decreases. For fine-grain-size alumina, Skrovanek and Bradt (19) found hardness was grain-size independent for grain sizes between 2 μm and 4 μm, but for the grain sizes larger than 4 μm, the hardness decreased with grain size.

In this study, the grain sizes for the entire set of 24 sintered alumina specimens ranged from only 5.7 μm to 9.4 μm (Table 2) and thus not surprisingly the hardness and toughness data are scattered within a relatively narrow band, with no definitive relationships between grain size and hardness or toughness. However, some possible trends in grain size do appear. For example, specimens sintered in TE_{112} mode with smallest average grain size, (Table 2) yielded relatively higher hardness and fracture toughness values (Figures 5a and 5b). Specimens sintered in TM_{111} mode with largest

Table 2. Density and grain size in terms of cavity modes and specimen location.

Cavity mode	TM_{111}		TE_{112}		TE_{113}		TM_{013}	
Position of specimen	Density (%)	Grain size (μm)	Density (%)	Grain size (μm)	Density (%)	Grain size (μm)	Density (%)	Grain size (μm)
1	99.9	6.96	98.6	6.40	99.8	7.90	99.6	8.52
2	100.0	8.10	100.0	5.89	99.9	8.22	99.0	7.58
3	99.7	8.40	99.5	6.18	99.1	7.09	99.8	8.48
4	99.8	7.80	99.3	5.80	98.3	7.36	99.5	6.70
5	100.0	7.34	99.9	5.65	99.8	7.97	99.9	6.74
6	99.8	9.42	99.4	6.10	99.9	7.65	99.3	7.39
Mean density or grain size	99.9 ±0.1	8.00 ±0.87	99.5 ±0.5	6.00 ±0.27	99.5 ±0.6	7.70 ±0.42	99.5 ±0.3	7.57 ±0.80

* Density (%) is relative with respect to the theoretical value of alumina (3.987 g/cm^3) (7).

** Grain sizes were determined by multiplying the average intercept length from the SEM micrographs of fracture surfaces by the stereographic correction factor 1.5.

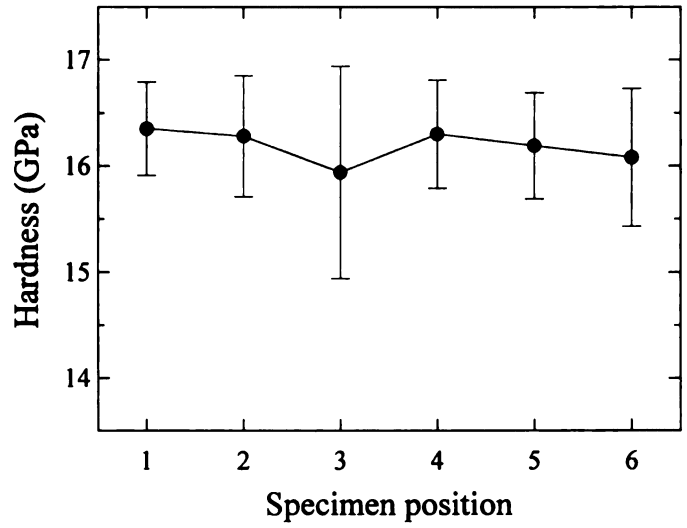

(a)

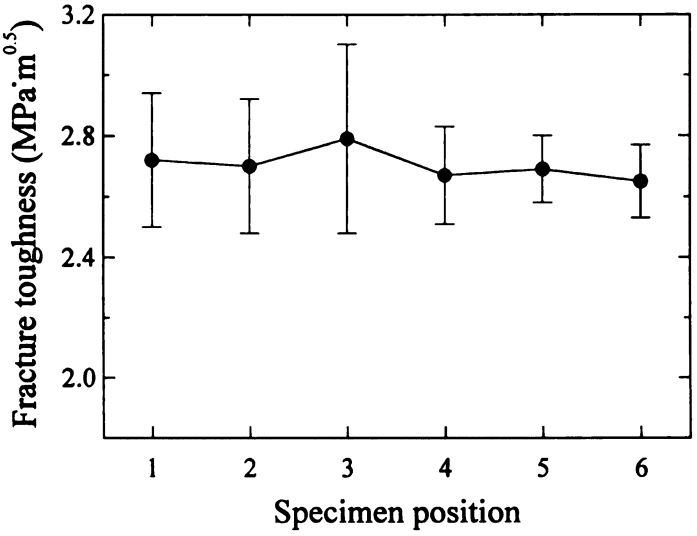

(b)

Figure 4. Hardness (a) and fracture toughness (b) for batch-processed alumina specimens in terms of specimen position. Error bars represent the standard deviation.

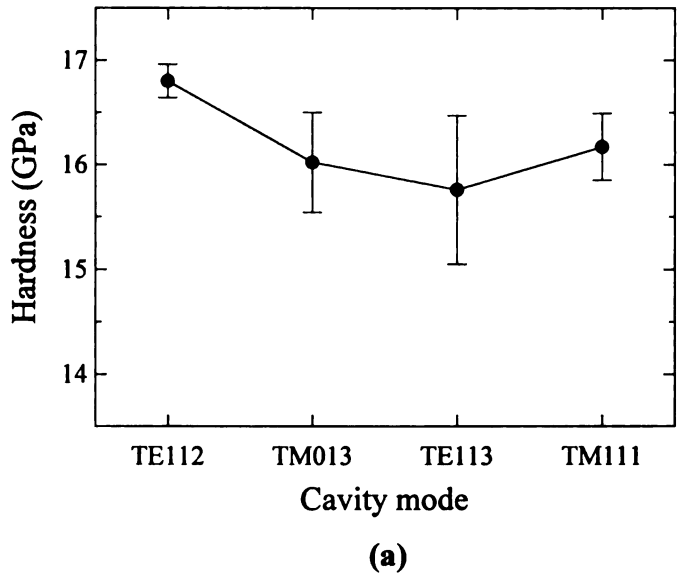

(a)

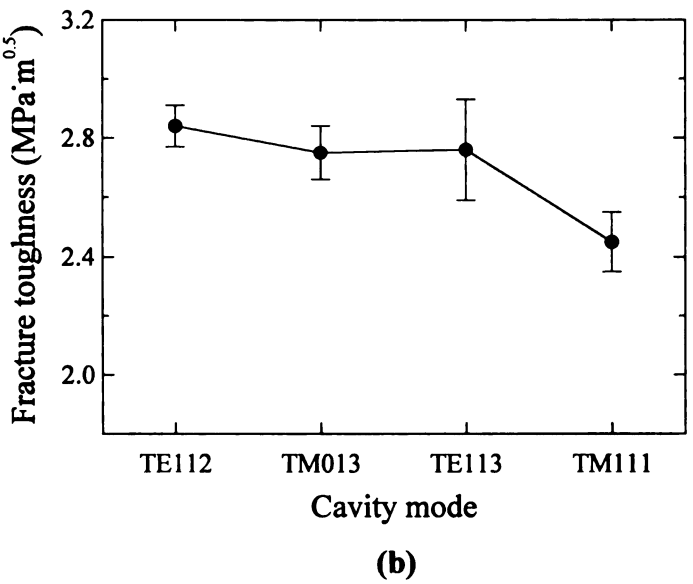

(b)

Figure 5. Hardness (a) and fracture toughness (b) for batch-processed alumina specimens in terms of cavity mode. Error bars represent the standard deviation.

average grain size have lower average fracture toughness than the specimens sintered in the other three cavity modes (Figure 5b).

4. SUMMARY AND CONCLUSIONS

In this study and the studies by Katz (2) and by Patterson (3), relatively uniform grain sizes and densities were achieved for batch-processed specimens under differing microwave processing conditions. Each of the three studies involved microwave power at a fixed frequency of 2.45 GHz, although Katz (2) and Patterson (3) each used about 4 kW of microwave power to achieve a sintering temperature of 1600°C, while this study used considerably lower input power (from 1.0 to 1.25 kW) to achieve a sintering temperature of 1500°C (Table 2). Two studies (this study and Katz (2)) used single-mode microwave cavities while Patterson (3) used a multimode cavity.

Each of the three studies employed a casket (specimen enclosure) during sintering. Patterson (3) used an alumina crucible, with a powder bed enclosing the specimens, while Katz used a casket composed of cylindrical aluminosilicate surrounded by zirconia board. At low temperatures, the temperature distribution in Patterson's (3) powder bed was nonuniform, while at higher (sintering) temperatures hot-spots within the powder bed were dissipated by thermal conduction, yielding isothermal conditions. Patterson's results parallel this study's results; at low temperature the thermally-sensitive paper indicated a nonuniform heat distribution within the empty zirconia casket, but the uniform final grain size and density of the sintered specimens (Table 1) indicate a relatively uniform temperature field within the casket at the sintering temperature.

Unlike the studies by Katz (2) and Patterson (3), this study determined hardness

and fracture toughness for each of the batch-processed specimens. Also, this study differed from those of Katz and Patterson in that four different microwave modes (Figure 1) were employed to heat the specimens. Despite the spatial variations in the electromagnetic fields within the cavity for a given mode, and despite the differences among electromagnetic field patterns from mode to mode (Figure 1), this study revealed only relatively small differences in hardness and fracture toughness as a function of (i) specimen position within the zirconia casket and (ii) the electromagnetic mode used to sinter the specimens. Thus, the microwave casket (specimen enclosure) in this study and in the studies by Katz (2) and Patterson (3) apparently can act to homogenize the temperature field for batch-processed ceramics, such that the grain size, density (2, 3, and this study), hardness, and fracture toughness (this study) can be relatively uniform.

ACKNOWLEDGEMENTS

The authors acknowledge the financial support of Research Excellence funds provided by the State of Michigan.

REFERENCES

1. J.D. Katz, and R.D. Blake, *Am. Cer. Soc. Bull.* **70**[8], 1304 (1991).

2. M.C.L. Patterson, P.S. Apte, R.M. Kimber, and R. Roy, in *MRS Symp. Proc.*, ed. R.L. Beatty et al., Vol. 269, p. 291, Materials Research Society, Pittsburgh, PA (1992).

3. K.Y. Lee, E.D. Case, J. Asmussen, Jr., and M. Siegel, in *Cer. Trans.*, Vol. 59, p. 473, The American Ceramic Society Inc., Westerville, Ohio (1995).

4. K.Y. Lee, E.D. Case, J. Asmussen, Jr., and M. Siegel, in *Proceedings of the 11th Annual ESD Advanced Composites Conference*, p. 491, Ann Arbor, Michigan (1995).

5. K.Y. Lee, E.D. Case, J. Asmussen, Jr., and M. Siegel, *Scripta Mat.*, **35**[1], 107 (1996).

6. K.Y. Lee, E.D. Case and J. Asmussen, Jr., submitted.

7. National Bureau of Standards (U.S.), Circ. 539, Vol. 9, p. 3 (1959).

8. J.B. Wachtman, in *Mechanical Properties of Ceramics*, p. 83, John Wiley & Sons, Inc., New York (1996).

9. I.J. McColm, in *Ceramic Hardness*, p. 10, Plenum Press, New York (1990).

10. G.R. Anstis, P. Chantikul, B.R. Lawn, and D.B. Marshall, *J. Amer. Cer. Soc.* **64**[9], 533 (1981).

11. W.D. Kingery, H.K. Bowen, and D.R. Uhlmann, in *Introduction to Ceramics*, 2nd ed., p. 777, John Willey & Sons, New York (1976).

12. R.F. Cook and G.M. Pharr, *J. Amer. Cer. Soc.* **73**[4], 787 (1990).

13. D.W. Richerson, in *Modern Ceramic Engineering*, 2nd edition, p. 179, 360, Marcel Dekker, Inc., New York (1992).

14. P.S. Apte, R.M. Kimber and M.C.L. Patterson, in *Structural Ceramics Processing, Microstructure and Properties Proc. of the Riso Int. Symp. on Metallurgy and Materials Science*, p. 167, Riso National Lab., Riso Library, Roskilde, Den. (1990).

15. R.W. Rice, S.W. Freiman, and P.F. Becher, *J. Amer. Cer. Soc.* **64**[6], 345 (1981).

16. R.W. Rice and S.W. Freiman, *J. Amer. Cer. Soc.* **64**[6], 350 (1981).

17. E. Dörre and H. Hübner, in *Alumina*, ed., B. Ilschner and N.J. Grant, p. 85, Springer-Verlag, New York (1984).

18. N. Claussen, B. Mussler, and M.V. Swain, *J. Amer. Cer. Soc.* **65**, c14 (1982).

19. S.D. Skrovanek and R.C. Bradt, *J. Amer. Cer. Soc.* **62**, 215 (1979).

Part III. MICROWAVE SINTERING OF ALUMINA AND ALUMINA MATRIX ZIRCONIA COMPOSITES USING A SINGLE-MODE MICROWAVE CAVITY[3]

ABSTRACT

In this study, alumina and alumina-based zirconia particulate composites have been successfully densified using 2.45 GHz microwaves in a cylindrical single-mode microwave cavity. The 'microwave effect,' that has been demonstrated by many researchers on a wide range of ceramics, was verified by comparing the densities and the microstructure of alumina/zirconia composites densified by microwave heating and conventional heating.

1. INTRODUCTION

Recently, researchers have successfully processed a variety of ceramics using microwave energy [1-7]. Microwave processing of ceramics can have a number of benefits, for example, an Ontario Ministry of Energy study [8] showed microwave drying and sintering uses less energy than conventional drying and sintering by a factor of about two and ten, respectively. In addition to the energy savings, the nature of microwave heating (i.e. internal and volumetric heating) results in a set of "microwave effects," including lower sintering temperatures [1], smaller grain sizes [9], and lower diffusional activation energies [10] compared to conventional processing. Also, several researchers

[3] Additional report for sintering by Ki-Yong Lee, Paul H. Dearhouse, Eldon D. Case, and Jes Asmussen Jr.

[11-13] report microwave processing can improve microstructure and mechanical properties.

A number of researchers have encountered problems with microwave sintering, including thermal runaway [14-16], inability to heat low dielectric loss materials without a microwave susceptor [17], and cracking of the processed materials [18,19]. The microwave sintering techniques used in this study employed a microwave susceptor (casket) to sinter 5.1 centimeter diameter alumina and alumina/zirconia specimens without thermal runaway and without cracking the specimens. However, the sintering procedure was developed such that it accommodated two types of casket-microwave interactions: (1) development of local hot spots in the cylindrical casket wall at temperatures between about 800°C and 1100°C and (2) local melting of the casket end plates at temperatures above 1550°C.

Recently Lee et al. [20] successfully densified alumina discs about 2 cm diameter using a cylindrical single-mode cavity equipped with a computer-controlled tuning system developed by Asmussen et al. [20]. In this study, the same single-mode microwave cavity [20,21] is used to densify 5.1 cm diameter disc-shaped ceramic powder compact specimens in TM_{111}, TE_{112}, TE_{113}, and TM_{013} microwave cavity modes. The ceramic materials used in this study included (i) three grades of alumina and (ii) alumina-matrix/zirconia particulate composites. In particular, we verified the advantages of microwave heating by comparing the microstructure and densities of Al_2O_3/ZrO_2 densified by the microwave heating and the conventional means. X-ray diffraction (XRD) of the sintered Al_2O_3/ZrO_2 composites showed the presence of both tetragonal and monoclinic zirconia phases dispersed within the composite specimens. The mass density

and grain size of sintered specimens were found to be relatively uniform with respect to both (i) the radial position within a given specimen and (ii) the cavity mode used to sinter the specimen.

2. EXPERIMENTAL PROCEDURES

2.1. Materials and Specimen Preparation

For the alumina powder compacts referred to here as Group A (Table I), one compact of each of three different grades of alumina powders (Sumitomo AKP30, AKP50, and Alcoa A16SG) was prepared to determine the microwave sintering behavior of each of the powder types. In addition, four Group B powder compacts (Table II) were fabricated to examine the grain size and density uniformity across the disc-shaped specimen after microwave sintering in various microwave cavity modes. Also, nine alumina/zirconia ceramic composites were made using AKP50 alumina powder and a 0.4 micron [21] zirconia powder (Fisher Scientific Company).

A hardened tool steel die was employed to form the disc-shaped powder compacts 51 millimeters in diameter. All alumina and alumina/zirconia powder compacts were pressed uniaxially at about 4.4 MPa using a Carver hydraulic press.

For the AKP50/10wt% ZrO_2 powder compacts, a mixture of alumina and zirconia powders were ball-milled in a plastic mill for 24 hours using alumina grinding media. Group B AKP30 alumina powders were ball-milled for 48 hours. The mass of the three Group A alumina specimens and the nine alumina/zirconia composite specimens was 10.031 $\pm$ 0.064 grams. The Group A alumina powder compacts were about 2.8 millimeter thick, while the alumina/zirconia powder compacts were about 2.7 millimeter

Table I. Summary of microwave sintering of aluminas.

Material	Average particle size (μm)	Sintering temperature (°C)	Heating rate (°C/min.)	Average grain size (μm)*	Relative density (%)
AKP50	0.23	1600	12.5	9.50	96.6
AKP30	0.41	1600 - 1535	12.6	12.50	96.6
A16SG	0.52	1595 - 1580	12.1	6.74	96.1

* Average intercept length was multiplied by a stereographic correction factor 1.5 to obtain the average grain size [124].

Table II. Summary for microwave processing of four AKP30 alumina specimens each in different cavity mode.

Microwave cavity mode	Initial input power for coupling	Maximum input power	Average heating rate from 500°C	Sintering temperature and time
TM_{111}	150 Watts	1275 Watts	14.3 °C/min.	1500°C for 30 min.
TE_{112}	130 Watts	1180 Watts	15.2 °C/min.	1500°C for 30 min.
TE_{113}	100 Watts	1450 Watts	14.5 °C/min.	1500°C for 30 min.
TM_{013}	200 Watts	1350 Watts	14.2 °C/min.	1500°C for 30 min.

thick. The four Group B AKP30 alumina specimens were 3.2 mm thick after uniaxial pressing, with average mass of 11.928 grams and a standard deviation of 0.0006 grams. The green (unfired) densities of all the powder compacts included in this study corresponded to about 45 percent of theoretical.

2.2. Microwave Sintering

All specimens were sintered in air using a 2.45 GHz microwave system that included a 2000 Watt microwave power supply (Sairem, MWPS 2000, Wavemat Inc., MI) and a cylindrical single-mode microwave cavity 17.78 centimeters in diameter (CMPR-250, Wavemat Inc., MI) (Figure 1). The microwave cavity was equipped with a computer-controlled tuning system for precise and fast tuning [20].

The single-mode cavity used in this study allows the microwave sintering to be done using a standing wave electromagnetic field pattern. Instead of single-mode cavities, most microwave applicators used to process materials are multimode cavities similar to domestic microwave ovens. Multimode cavities are relatively inexpensive and easy to construct, but the electromagnetic field distribution within the cavity is not well defined and the power efficiency is relatively low [22]. Also, the non-uniform field distribution within the multimode cavity promotes thermal instability in the processed material, which can lead to local melting or cracking in the specimen. Single-mode microwave cavities provide well defined electric field and enhanced power dissipation by the processed material [22]. Precise tuning of a single-mode cavity to a characteristic mode can optimize power dissipation in the processed material.

Each specimen was sintered using a microwave casket [20,21] composed of a

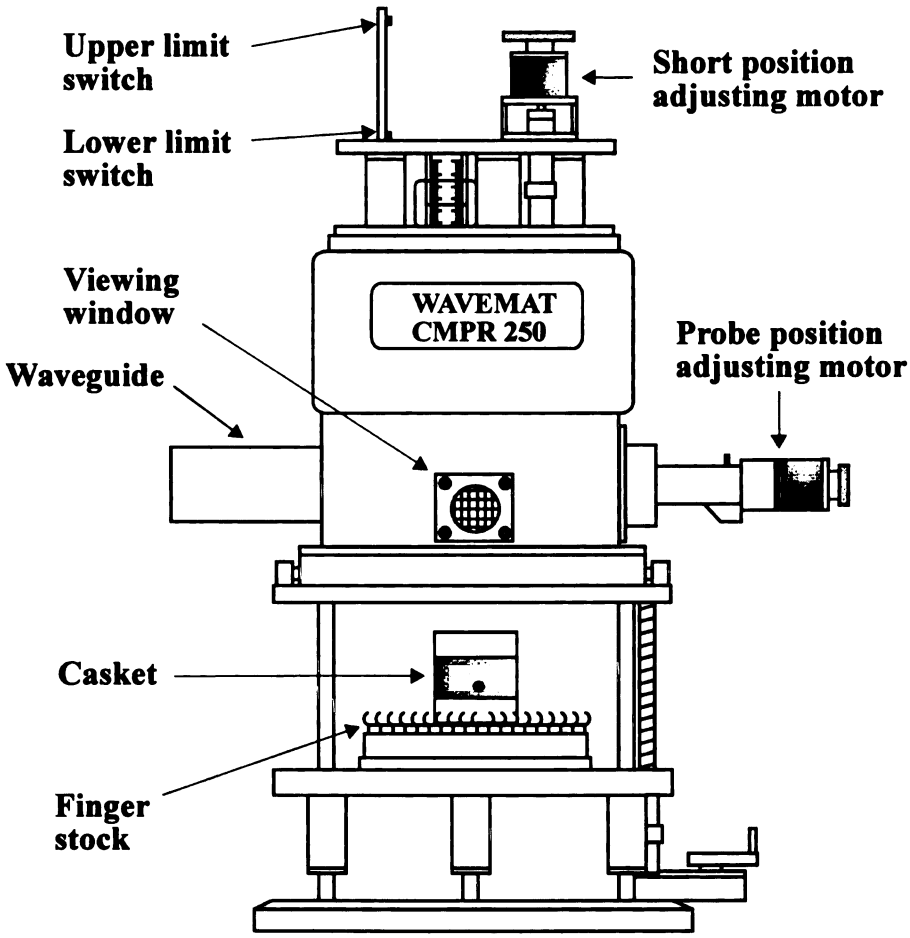

Figure 1. Schematic of microwave processing apparatus.

cylindrical zirconia microwave susceptor (Type ZYC, Zircar Products Inc.) having a 10.2 centimeter outside diameter and a 7.6 centimeter inside diameter (Figure 2). The top and the bottom plates of the casket (Figure 2), which were each about 2 cm thick, were cut from aluminosilicate refractory board (SALI, Zircar Products Inc.). In addition, aluminosilicate fiber (SAFFIL, K-Industrial Corp.) was used as a setter material for specimen inside the casket. The SAFFIL, which was shaped into a disc of about 7.5 centimeter in diameter and 0.5 centimeter thick, was placed directly on the SALI casket end plate, and the specimens were placed on the SAFFIL disk (Figure 2).

For the three Group A Al_2O_3 specimens and five AKP50/ZrO_2 specimens (Tables I and III), the microwave input power initially was set at 50 Watts with the cavity tuned to TM_{111} mode. Then the microwave input power was increased by 50 Watts every 3 minutes up to 150 Watts. The casket-specimen system was held for about 15 to 25

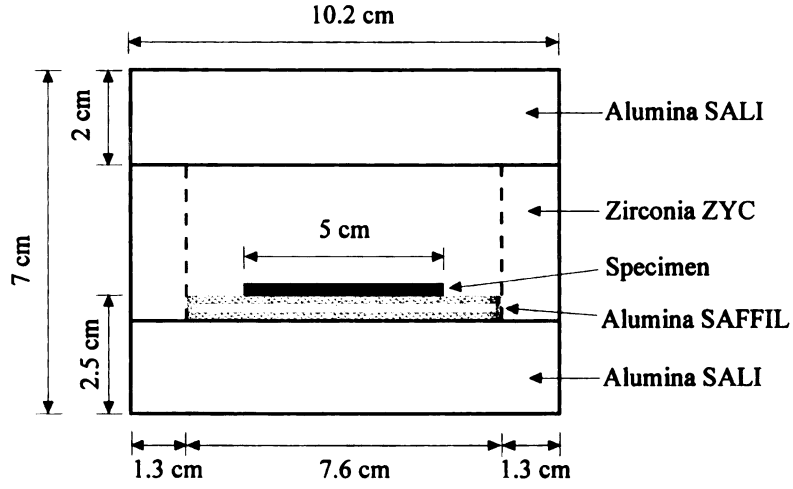

Figure 2. Schematic of a casket and the disc-shape powder compact specimen about 5 cm in diameter.

minutes at 150 Watts. Within about 5 to 10 minutes after the power was increased to 150 Watts, the casket began to heat significantly (corresponding to a specimen temperature of about 500°C). For further heating the microwave input power was increased, followed by tuning the cavity after every change of the power.

During microwave heating of the three Group A alumina compact specimens (Table I) the microwave input power was adjusted to maintain a heating rate of 10°C/min. for the temperature range of about 700°C to 1600°C (Figure 3a). As a result, an average heating rate of about 12.5°C/minute was obtained for the entire interval from room temperature (25°C) to the sintering temperature (Figure 3a, Table I).

Four Al_2O_3/10wt% ZrO_2 powder compact specimens were microwave processed; one specimen at each of the following four temperatures: 1150°C, 1250°C, 1350°C, and 1450°C. Four additional Al_2O_3/10wt% ZrO_2 powder compacts were processed at an identical set of temperatures using a conventional high temperature horizontal tube furnace (Thermtec Furnace, MRL Industries, California) at a fixed heating rate of 10°C/minute. A ninth composite specimen was microwave-sintered at 1550°C using a 10°C/minute rate, the same heating rate as that of the conventional furnace. No conventional sintering was performed at 1550°C since the maximum use temperature of the conventional furnace was 1500°C. The Group A alumina specimens and the nine AKP50/ZrO_2 composite specimens were each held at the maximum temperature for 20 minutes.

Unlike the three Group A alumina specimens and nine AKP50/ZrO_2 specimens

Table III. Summary of sintering of zirconia using microwave and conventional means.

Processing	Specimen	Sintering temp. (°C)	Sintering time (min.)	Average heating rate (°C/min.)	Average grain size (μm)*	Relative density (%)
Microwave	Al/Zr-1	1550	20	10	4.55	96
	Al/Zr-2	1450	20	22	2.42	95
	Al/Zr-3	1350	20	20	**	94.2
	Al/Zr-4	1250	20	19	**	72.4
	Al/Zr-5	1150	20	15	**	52.3
Conventional	CAl/Zr-1	1450	20	10	0.77	87.4
	CAl/Zr-2	1350	20	10	**	69.8
	CAl/Zr-3	1250	20	10	**	60.7
	CAl/Zr-4	1150	20	10	**	52.3

* Average intercept length was multiplied by a stereographic correction factor 1.5 to obtain the average grain size [24].

** Average grain size was not determined.

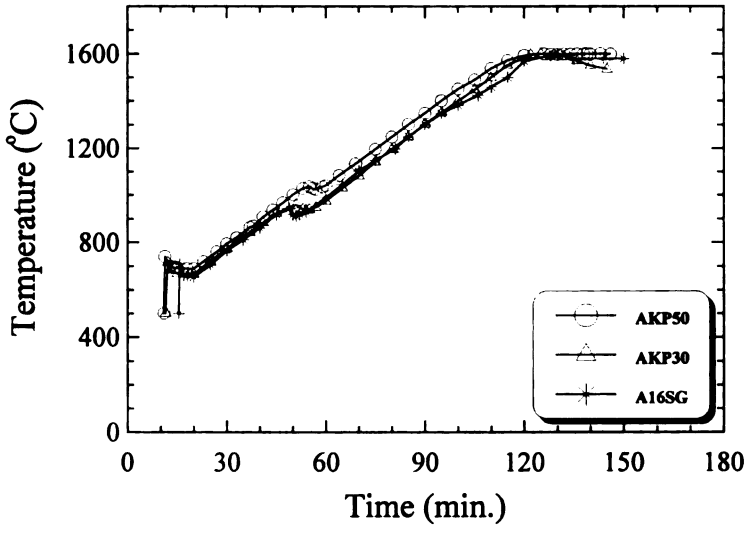

(a)

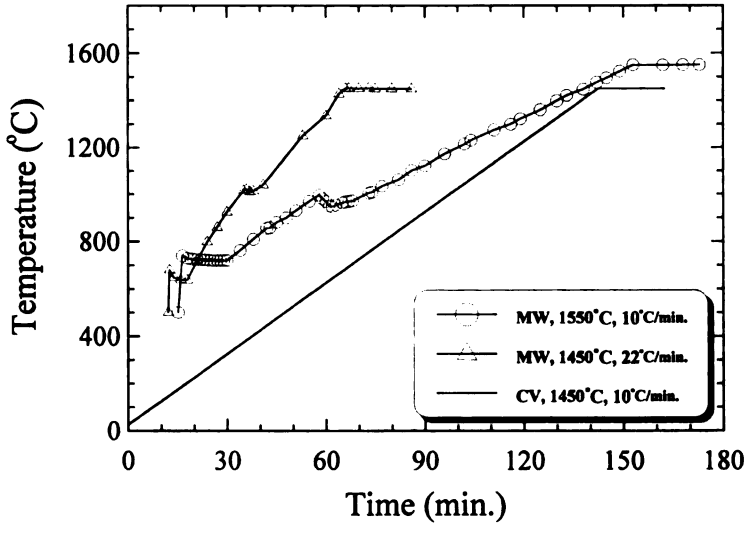

(b)

Figure 3. Heating schedules for (a) microwave heating of aluminas, and (b) microwave heating and conventional heating of AKP50/10wt% zirconia composite specimens.

sintered in TM_{111} mode, the four Group B AKP30 alumina specimens were heated one at a time in four different cavity modes, namely, the TM_{111}, TE_{112}, TE_{113}, and TM_{013} modes. A fixed microwave input power was used to initially couple the zirconia casket with the microwave field, where the magnitude of input power required for the initial coupling depended on the cavity mode (Table II) [23]. Immediately after the casket began to heat, the input power was increased by 50 Watts every 3 minutes until the temperature reached 1500°C. The Group B specimens were held at the 1500°C for 30 minutes for final densification (Table II).

To determine which zirconia phases were present in the final microwave-sintered alumina-matrix/zirconia specimens, the x-ray diffraction (XRD) pattern was examined for specimen Al/Zr-1 using Cu-Ka x-ray (λ = 1.5406 Å) (Scintag XDS 2000, Scintag Inc., U.S.A.). The specimen was scanned for the diffraction angle, 2θ, ranging from 20° to 70° at step size of 0.03°, with an accelerating voltage of 35 kV and current of 25 mA. The XRD patterns of AKP50 alumina powder and the pure zirconia powder also were examined to allow direct comparison with the alumina and zirconia phases in the Al/Zr-1 pattern.

Using a diamond saw, a bar-shaped specimen about 4 cm long was cut from each of the four sintered Group B alumina specimens (Figure 4). Each bar was fractured into three sections A, B, and C (Figure 4) to determine the mass density and grain size depending as a function of radial position within the specimen. Grain sizes of specimens were determined using a line intercept method on SEM (JSM-6400V, JEOL) micrographs obtained from fracture surfaces [24].

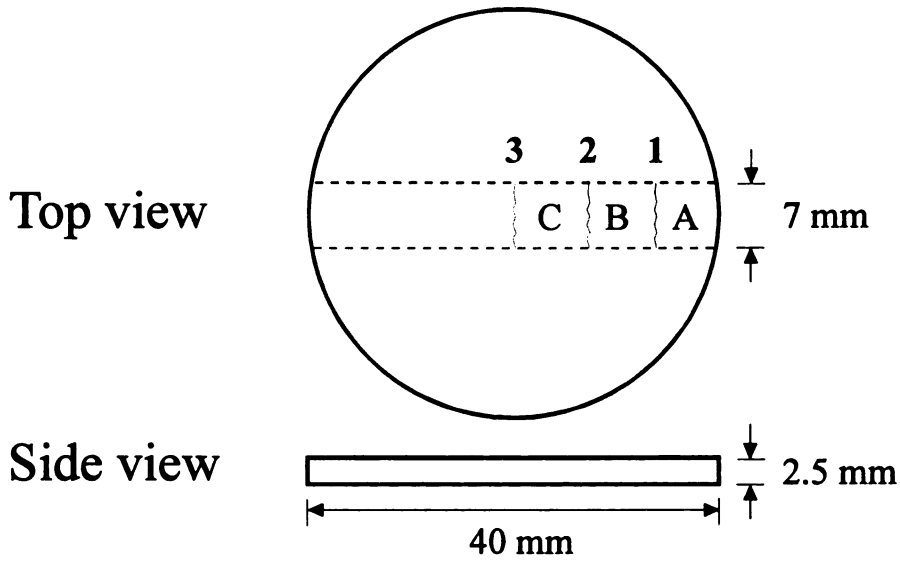

Figure 4. Schematic for microwave sintered AKP30 alumina specimen used to examine the uniformity in grain size and density along the diameter, showing the locations of sections A, B, and C.

3. RESULTS AND DISCUSSION

3.1. Microwave Sintering of Alumina

Using 3.987 g/cm^3 for the theoretical density of alumina [25] (Table I), relative densities of up to 96.6% of theoretical were calculated for the three different grades of pure alumina. Figures 5a, 5b, and 5c show the microstructure of AKP50, AKP30, A16SG, respectively. Figure 5a shows the pores trapped at grain boundaries typical of densified ceramic materials. The fracture surface of the AKP30 specimen shows the cleavage planes indicating regions of transgranular fracture (Figure 5b). Figure 5c indicates that the fracture mainly occurred by intergranular fracture.

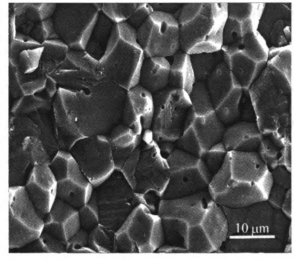

(a)

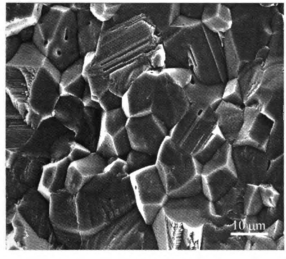

(b)

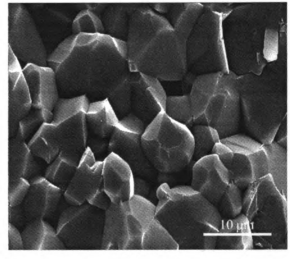

(c)

Figure 5. Fracture surfaces of microwave sintered aluminas: (a) AKP50, (b) AKP30, and (c) A16SG.

3.2. Microwave and Conventional Sintering of Alumina/10wt% Zirconia

The theoretical density of alumina and zirconia (monoclinic) is 3.987 g/cm^3 [25] and 5.82 g/cm^3 [26], respectively, yielding a theoretical density of 4.17 g/cm^3 for the alumina/10wt% zirconia composites. Relative mass densities of the alumina/zirconia composites are given in Table III.

At a sintering temperature of 1150°C, the mass density was 52.3% of theoretical (Table III and Figure 6) for both the specimen sintered in the microwave and the specimen sintered by conventional means. However, as the sintering temperature increased from 1150°C to 1350°C, the density of the microwave heated specimens rapidly increased compared to the densities of the conventionally sintered specimens (Table III and Figure 6). Specimen Al/Zr-3 (microwave-sintered) and CAl/Zr-2 (conventionally

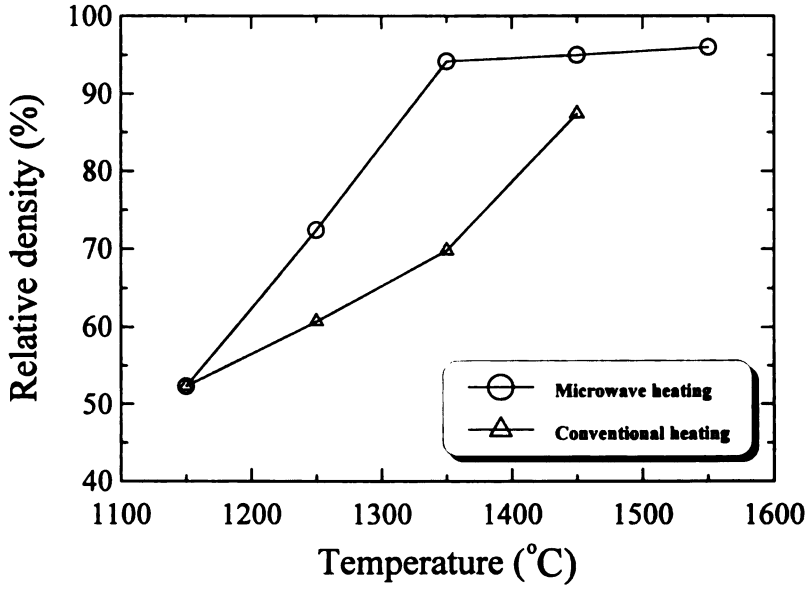

Figure 6. Relative densities of AKP50/10wt% zirconia composites densified by microwave heating and conventional heating as a function of temperature.

sintered) both were sintered at 1350°C for 20 minutes, using heating rates 20°C/minute and 10°C/minute, respectively. Final relative densities of 94.2% for the Al/Zr-3 and 69.8% for the CAl/Zr-2 indicate the improvement in densification afforded by microwave processing the alumina-matrix/zirconia specimens. Specimens Al/Zr-2 and CAl/Zr-1 both were sintered at 1450°C for 20 minutes, but the microwave sintered Al/Zr-2 was well densified (95% of theoretical) while the density of the conventionally sintered CAl/Zr-1 was 87% of theoretical density.

The microstructures for specimens Al/Zr-2 and CAl/Zr-1 showed significant differences (Figures 7b and 7c). The average grain size of Al/Zr-2 was 2.42 μm, while the average grain size of CAl/Zr-1 was 0.77 μm (Table III). The average particle size of the AKP50 alumina powder was 0.23 μm and the particle size for the zirconia powder used in this study was less than 0.4 μm (Experimental Procedure). Specimen CAl/Zr-1 (conventionally sintered at 1450°C) was at the initial stage of sintering at that temperature only three or four particles began to coalesce.

As is typical in both conventional and microwave sintering of ceramics [9], a higher heating rate yields a smaller grain size. The smaller average grain size of specimen Al/Zr-2 compared to specimen Al/Zr-1 (Table III and Figures 7a-7c) likely results from a heating rate of about 22°C/minute for the Al/Zr-2 in contrast to a heating rate of about 10°C/minute for the Al/Zr-1 (Table III and Figures 7a-7c). Microwave sintering can yield smaller grain size than sintering with conventional furnaces due to fast heating and enhanced densification at lower temperature which is so called the 'microwave effect' [1,9,10,16,22]. The well-known and widely-discussed microwave effect results from the direct interaction of the processed material with the microwave field, resulting in internal

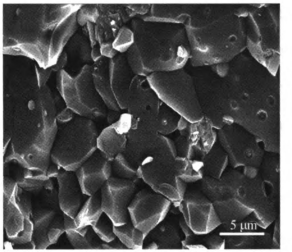

(a)

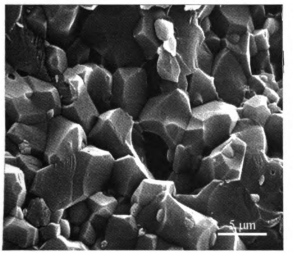

(b)

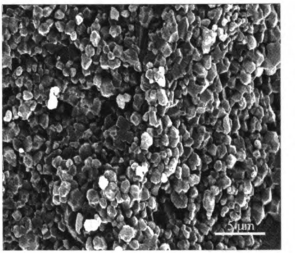

(c)

Figure 7. Fracture surfaces of AKP50/10wt% zirconia sintered (a) by microwave at 1550°C for 20 minutes, (b) by microwave at 1450°C for 20 minutes, and (c) by conventional furnace at 1450°C for 20 minutes.

volumetric heating. The typical loss tangent of alumina is about 0.0001 at ambient temperature and thus does not absorb the microwave energy significantly [27]. However, as the temperature increases to 1000°C, the loss tangent of alumina rapidly increases to about 0.01 [27]. A loss tangent of 0.01 indicates significant interaction with the microwave field. Although we heated the specimens using the casket composed of microwave susceptor (zirconia), at high temperature the alumina itself absorbed the microwave energy, yielding high densification even at the temperature as low as 1350°C (Table III and Figure 6).

The x-ray diffraction pattern for the zirconia powder matched the pattern for

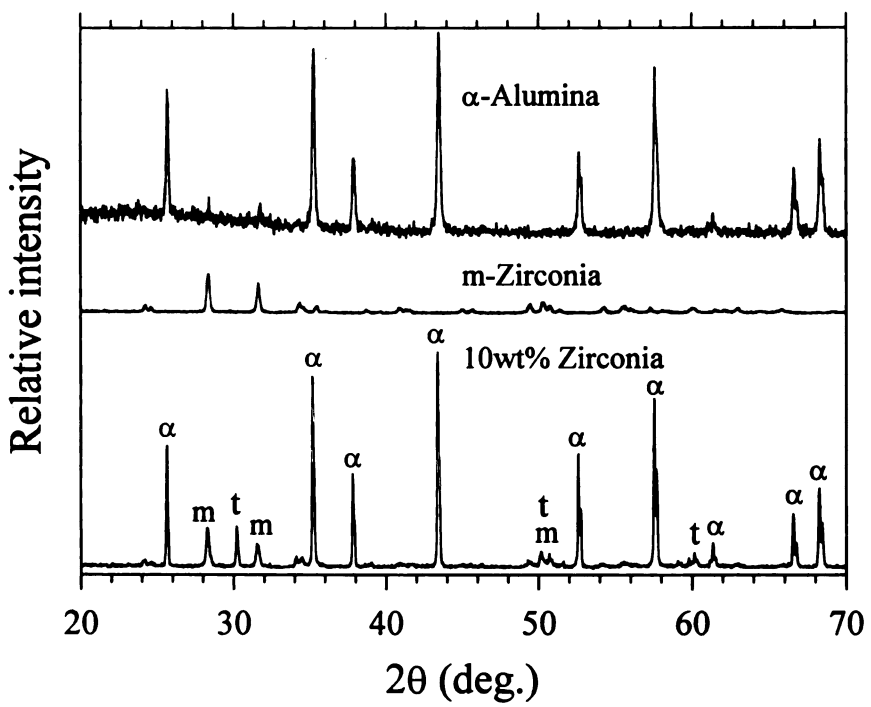

Figure 8. X-ray diffraction patterns of AKP50 alumina powder, zirconia powder, and microwave sintered AKP50/10wt% zirconia.

monoclinic zirconia [26]. The XRD pattern for specimen Al/Zr-1 indicated the presence of both the monoclinic phase and the tetragonal phase of zirconia (Figure 8). The x-ray pattern for tetragonal zirconia was identified based on the original work performed by Ruff and Ebert [28]. Thus a partial transformation from monoclinic to tetragonal phase occurred during microwave heating using the single-mode microwave cavity in this study.

3.3. Grain size and mass density as a function of the cavity mode and the radial position within the AKP30 alumina specimens.

The four Group B AKP30 alumina specimens achieved an average mass density of 96.2% of theoretical with standard deviation of ± 0.6%, as determined for the twelve sections obtained from the four specimens (Table IV). The densities for sections, A, B, and C (Figure 4) of individual specimens sintered in different cavity modes revealed no significant variation in mass density as a function of the radial position within a given specimen (Table IV). Also, from mode to mode the average mass density differed by less than 1%.

Compared to the mass densities, somewhat larger variations in the grain size were observed (Table IV) in terms of both (i) the radial position within a given specimen and (ii) the cavity mode used to sinter the specimen. For the twelve specimen sections examined in this study, the grain size varied from 3.83 μm to 7.72 μm. For the three sections obtained from each of the four individual specimens, the largest standard deviation corresponding to 6.1% of the mean grain size occurred to the specimen densified in TM_{013} mode. Grain sizes averaged over a given cavity mode ranged from

Table IV. Density and grain size measurements for alumina specimens in terms of cavity modes and locations of individual specimens.

Cavity mode	TM_{111}		TE_{112}		TE_{113}		TM_{013}	
Section	Density (%)	Grain size (μm)	Density (%)	Grain size (μm)	Density (%)	Grain size (μm)	Density (%)	Grain size (μm)
A	96.0	7.42 ±0.35	94.9	4.26 ±0.49	96.9	7.72 ±0.48	95.6	6.05 ±0.36
B	97.0	7.35 ±0.35	95.9	3.83 ±0.68	97.0	7.36 ±0.24	96.3	6.23 ±0.39
C	95.6	7.46 ±0.33	96.3	4.06 ±0.75	95.9	7.42 ±0.12	96.5	5.54 ±0.32
Mean density or grain size	96.2 ±0.7	7.41 ±0.06	95.7 ±0.7	4.05 ±0.22	96.6 ±0.6	7.50 ±0.19	96.1 ±0.5	5.94 ±0.36

* Density (%) is relative with respect to the theoretical value of alumina (3.987 g/cm^3) [25].

** Grain sizes were determined by multiplying the average intercept length from the SEM micrographs of fracture surfaces by the stereographic correction factor 1.5 [24].

4.05 μm for the TE_{112} mode to 7.50 μm for the TE_{113} mode (Table IV). We assume relatively large variation in grain size depending on the cavity mode may be due to differences in electromagnetic field strength from mode to mode [23], although similar heating rates, sintering temperatures and times were used for each of the four cavity modes used to heat the four AKP30 alumina specimens (Table II). However, more work needs to be done to clarify this effect.

3.4. Casket-microwave interactions

During this study, we have observed both local hot spots in the ZYC zirconia cylinder wall of the casket and local melting in the SALI refractory board casket end plates. The hot spots in the cylinder wall tend to occur at intermediate temperatures while the local melting occurs near the maximum (sintering) temperature. Both phenomena are associated with strong local microwave-power absorption, which alters the way in which energy is partitioned within the microwave cavity and can lead to transient drops in the specimen temperature. The time-power sequence of the microwave processing was modified to accommodate these absorptions so that despite these perturbations, the alumina and the alumina/zirconia specimens were sintered to high densities.

3.4.1. Local hot spots in the casket wall

For the Group A alumina compacts and the alumina/zirconia composite specimens, the specimen temperature (monitored by an optical pyrometer) began to increase rapidly above 500°C within 11 to 17 minutes after beginning heating in TM_{111} mode (see Experimental Procedure). During each heating run, immediately after the casket began to

heat significantly at a fixed input power of 150 Watts, the reflected microwave power increased, which indicates the cavity had become out of tune. Re-tuning the cavity only (without increasing the input power) raised the specimen temperature from about 500°C to about 800°C (Figures 3a and 3b). At this point, the heating rate control became difficult, apparently due to non-uniform heating of the casket during the initial heating. Thus the input power was held at 150 Watts for about 5 to 10 minutes until the temperature dropped by about 50°C to 60°C and became stable. Then to heat the casket-specimen system to higher temperature, heating was resumed by tuning the cavity and increasing the input power.

However, in each of the heating runs, the increase in microwave input power was accompanied by the development of a red hot spot in the casket wall closest to the power launch probe. The first hot spot appeared with an initial size of about 1 cm diameter at a specimen temperature of about 900°C. The intensity of the hot spot increased until the specimen temperature reached about 1000°C, at which time a second hot spot developed in the opposite wall of the casket. The appearance of the second red spot was accompanied by a decrease in specimen temperature of as much as 30°C despite a 50 watt increase in input power (Figures 3a and 3b). The microwave input power was held at 370 Watts to 430 Watts for 7 minutes to 15 minutes, during which time the first hot spot became less intense and the second hot spot became more intense. When the specimen temperature began to increase again at fixed input power, the input power was increased and tuning the cavity was resumed and continued until the temperature reached the specimen's final densification temperature. Lee et al. [20] previously observed similar temperature changes accompanied by a hot spot in the casket wall during microwave heating of both (i) the casket loaded with

a 2 gram, 2 cm diameter alumina specimen and (ii) the empty casket. The hot spot phenomenon is probably due to non-uniform heating of the zirconia cylindrical casket. In particular, the location of the hot spot may be related to the power launch probe in the "side-feed" microwave cavity used in this study and previous studies [20], although the details of the material-microwave interaction are unknown.

The microwave sintering behavior of the Al_2O_3/ZrO_2 specimens was similar to that of the alumina compacts; at about 1000°C the temperature decreased by as much as 60°C although the heating rates ranged from 10°C/min. to 22°C/min. (Table III, Figures 3a and 3b). For Al/Zr-1 and Al/Zr-2, heated with the average heating rate of 10°C/minute and 22°C/minute, respectively, a temperature drop of 50°C was observed at about 1000°C (Figure 3b illustrates the 50°C temperature drop for specimen Al/Zr-1). Specimen CAl/Zr-1, which was heated in a conventional furnace with a heating rate of 10°C/minute, did not show a temperature drop during heating (Figure 3b). Thus the temperature drop near 1000°C is apparently related to the microwave sintering process rather than some type of endothermic process in the powder compacts themselves.

3.4.2. Local melting in the casket end-plates

The AKP50 powder compact was sintered at 1600°C ± 2°C for 20 minutes by controlling the microwave input power (Table I and Figure 3a). However, the AKP30 specimen temperature decreased to 1535°C within 20 minutes after the temperature reached 1600°C, although during this 20 minute interval the microwave input power was increased by more than 50 Watts. The A16SG specimen's temperature decreased from 1595°C to 1585°C within 20 minutes (Table I and Figure 3a).

The observed decrease in specimen temperature likely was due to local melting in the SALI aluminosilicate refractory boards that formed the top and the bottom casket plates (Figure 2). Local melting of the SALI, which was observed after cooling the casket-specimen system, apparently was caused by the microwave input power being absorbed locally instead of increasing the specimen temperature. The local melting of the SALI boards occurred despite the fact that the specimen temperature as measured by the optical pyrometer was less than 1600°C and the vendor-specified melting temperature of the SALI is 1870°C (SALI's maximum use temperature is specified as 1700°C). For the 5.1 centimeter diameter alumina powder compact specimens used in this study, the melted area of the SALI board was about 4 centimeters in diameter or larger. Local melting of the SALI board also was observed during microwave sintering of 2-gram alumina specimens at 1600°C [20]. The size of melted area was about 2 cm, which was approximately the same diameter or somewhat larger than the size of the alumina specimens. When the SALI of about 7.5 centimeter in diameter and 0.5 centimeter thick was used as a setter material for a processed specimen and the specimen temperature was increased to about 1600°C, severe local melting of the SALI board occurred and ruined the specimen (Figure 9a). In this study we used aluminosilicate fiber (SAFFIL, see Experimental Procedures) as a setter instead of the SALI board. The maximum use temperature and melting temperature of the SAFFIL were 1649°C and 1816°C, respectively, as specified by the vendor. Although the maximum use temperature and the melting temperature of the SAFFIL were lower than the corresponding temperatures of the SALI insulation material, the SAFFIL did not melt. The SAFFIL disc separated the processed specimen from the local melting of the SALI bottom

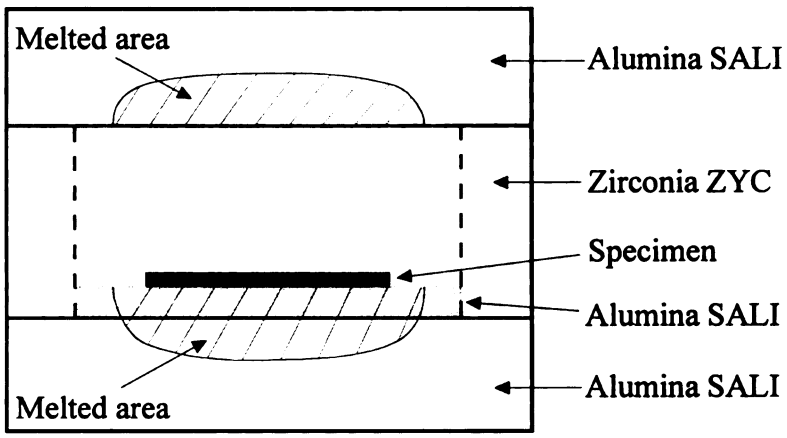

(a)

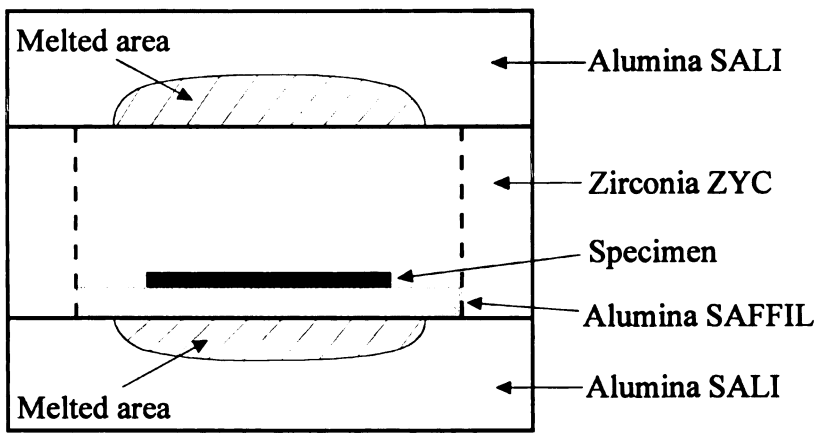

(b)

Figure 9. Schematics of the caskets showing melted area of the SALI insulation (a) when SALI was used as a specimen setter, and (b) when SAFFIL was used as a specimen setter.

plate of the casket, yielding well-densified specimens without either melting or warping (Figure 9b).

Based on the experimental observations of this study for 10 gram alumina specimens and results of a previous study for 2 gram alumina specimens [20], we believe that the local melting of the SALI boards is due to a local thermal runaway [14-16] of the SALI end plates. When the specimen temperature monitored by the pyrometer reaches about 1600°C, the dielectric loss tangent of the SALI probably increases rapidly, resulting in more absorption of the microwave power and increasing the local temperature of the SALI. Finally, the local melting may occur.

For the alumina/zirconia specimens, local melting did not occur in the SALI board, which indicates that a sintering temperature below 1550°C (or corresponding microwave power) was not high enough to cause the local melting. However, in a previous study [21] alumina/zirconia specimens heated to 1600°C resulted in severe local melting in the SALI boards. When a SALI board was used as a specimen setter [21] instead of the SAFFIL fiber insulation used in this study (Figure 2), local melting resulted in a hole about 4 centimeter in diameter in the SALI board and enclosed the specimen in the hole, causing the specimen warping. The local melting confined in the area of the SALI bottom plate under the alumina/10wt% zirconia specimen indicates that a processed specimen, in particular, containing more dielectrically lossy material like zirconia probably promotes the local melting in the SALI board.

4. SUMMARY AND CONCLUSIONS

In this study, relatively large (about 5 centimeter in diameter) disc-shaped alumina and alumina base zirconia composites were successfully densified by a cylindrical single-mode microwave cavity. The three different grades of alumina each about 10 grams sintered in TM_{111} mode showed final densities of about 96% of theoretical with fine grain sizes (Figures 5a-5c) (Table I).

The four Group B AKP30 alumina specimens sintered at 1500°C in the cavity tuned to TM_{111}, TE_{112}, TE_{113}, or TM_{013} modes yielded relatively uniform mass density and grain size in terms of both (i) the radial position within a given specimen and (ii) the cavity mode used to sinter the specimens (Table IV). The four Group B specimens had an average density 96.2% ± 0.6% of theoretical and an average grain size of 6.23 μm ± 1.5 μm. respectively. The small variations in mass density and grain size are likely due to the hybrid effect of the microwave heating and conventional heating using a casket composed of microwave lossy material [11,17].

The advantages of microwave heating over conventional heating have been verified by heating alumina/10wt% zirconia particulate composites. Microwave-sintered composite specimen (Al/Zr-3) reached about 94% theoretical density at a sintering temperature of 1350°C, while a specimen (CAl/Zr-2) conventionally sintered at 1350°C reached only about 70% of theoretical density (Table III). The microstructures of the composite specimens sintered at 1450°C also indicate that microwave heating enhanced the densification over conventional heating (Figures 7b and 7c).

Although a microwave susceptor is required for preheating the specimens at low temperature, a low loss material such as alumina can directly interact with the

microwaves at high temperature, yielding internal, volumetric heating.

ACKNOWLEDGEMENTS

The authors acknowledge the financial support of the Research Excellence Fund of the State of Michigan, provided by the Electronic and Surface Properties of Materials Center, Engineering College, Michigan State University.

REFERENCES

1. M.A. Janney, H.D. Kimrey, "Microwave Sintering of Alumina at 28 GHz," Ceramic Powder Science, II, B, Ceramic Transactions, vol. 1, pp. 919-24, (1988).

2. H.D. Kimrey, J.O. Kiggans, M.A. Janney, and R.L. Beatty, "Microwave Sintering of Zirconia-Toughened Alumina Composites," Mat. Res. Soc. Symp. Proc. vol. 189, 243-256, 1991.

3. J.D. Katz, R.D. Blake, and J.J. Petrovic, "Microwave Sintering of Alumina-Silicon Carbide Composites at 2.45 and 60 GHz," Ceram. Eng. Sci. Proc., 9, 725-34 (1988).

4. M.K. Krage, "Microwave Sintering of Ferrites," Am. Cer. Soc. Bull., 60(11), 1232-34 (1981).

5. K. Bai and H.G. Kim, "Microwave Sintering of $BaTiO_3$ thick Films," Journal of Materials Science Letters, vol.13, p 806-809, 1994.

6. P.A. Haas, "Heating of Uranium Oxides in a Microwave Oven," American Ceramic Society Bulletin, vol.58, No.9, p 873- , 1979.

7. J.F. MacDowell, "Microwave Heating of Nepheline Glass Ceramics," American Ceramic Society Bulletin, vol.63, No.2, p282-286, 1984.

8. L.M. Sheppard, *Am. Cer. Soc. Bull.*, **67**[10], 1656-1661 (1988).

9. Y.L. Tian, D.L. Johnson and M.E. Brodwin, in *Cer. Trans.*, Vol. 1, p. 925-932, The American Ceramic Society Inc., Westerville, Ohio (1988).

10. M.A. Janney and H.D. Kimrey, in *Mat. Res. Soc. Symp. Proc.*, ed. W.B. Snyder, Jr., W.H. Sutton, M.F. Iskander and D.L. Johnson, Vol. 189, p. 215-227, Materials Research Society, Pittsburgh, Pennsylvania (1990).

11. A. De, I. Ahmad, E.D. Whitney, and D.E. Clark, "Microwave (Hybrid) Heating of Alumina at 2.45 GHz: I. Microstructural Uniformity and Homogeneity," Microwaves: Theory and Application in Materials Processing, Ceramic Transactions, vol. 21, pp. 319-28 (1991).

12. C.E. Holcombe, T.T. Meek, and N.L. Dykes, in *Mat. Res. Soc. Symp. Proc.*, ed. W.H. Sutton, M.H. Brooks and I.J. Chabinsky, Vol. 124, p. 227-234, Materials Research Society, Pittsburgh, Pennsylvania (1988).

13. M.C.L. Patterson, P.S. Apte, R.M. Kimber, and R. Roy, in *Mat. Res. Soc. Symp. Proc.*, ed. R.L. Beatty, W.H. Sutton and M.F. Iskander, Vol. 269, p. 301-310, Materials Research Society, Pittsburgh, Pennsylvania (1992).

14. V.K. Varadan, Y. Ma, A. Lakhtakia and V.V. Varadan, in *Mat. Res. Soc. Symp. Proc.*, ed. W.H. Sutton, M.H. Brooks and I.J. Chabinsky, Vol. 124, p. 45-55, Materials Research Society, Pittsburgh, Pennsylvania (1988).

15. S.L. McGill, J.W. Walkiewicz, and G.A. Smyres, in *Mat. Res. Soc. Symp. Proc.*, ed. W.H. Sutton, M.H. Brooks and I.J. Chabinsky, Vol. 124, p. 247-252, Materials Research Society, Pittsburgh, Pennsylvania (1988).

16. V.M. Kenkre, L. Skala, M.W. Weiser, and J.D. Katz, "Theory of Microwave Interactions in Ceramic Materials: the Phenomenon of Thermal Runaway," Journal of Materials Science 26 (1991) 2483-2489.

17. C.E. Holcombe and N.L. Dykes, *J. Matl. Sci. Lett.*, **9**, 425-8 (1990).

18. M.A. Janney, C.L. Calhoun, and H.D. Kimrey, in *Cer. Trans.*, Vol. 21, p. 311-318 (1991).

19. B. Swain, *Adv. Mtls. and Processes*, **134**[3], 76-81 (1988).

20. K.Y. Lee, E.D. Case, J. Asmussen, Jr., and M. Siegel, in *Cer. Trans.*, Vol. 59, pp. 473-480, The American Ceramic Society Inc., Westerville, Ohio (1995).

21. K.Y. Lee, E.D. Case, J. Asmussen, Jr., and M. Siegel, in *Proceedings of the 11th Annual ESD Advanced Composites Conference*, p. 491-503, Ann Arbor, Michigan (1995).

22. Committee on microwave processing of materials: an emerging industrial technology, "Microwave Processing of Materials," National Academy Press, Washington, D.C. (1994).

23. K.Y. Lee, E.D. Case, and J. Asmussen, Jr., to be submitted for publication.

24. E.E. Underwood, A.R. Colcord, and R.C. Waugh, in Ceramic Microstructure, ed. R.M. Fulrath and J.A. Pask, p. 25-52, John Wiley and Sons, New York (1968).

25. National Bureau of Standards (U.S.), Circ. 539, Vol. 9, p. 3 (1959).

26. F. Larson, G. McCarthy, North Dakota State University, Fargo, North Dakota, USA. JCPDS Grant-in-Aid Report (1985).

27. W. B. Westpal and A. Sils, in *Dielectric Constant and Loss Data*, p. 4-37, Massachusetts Institute of Technology, Technical Report AFML-TR-72-39, Air Force Materials Laboratory, Wright- Patterson Air Force Base, Ohio (1972).

28. O. Ruff and F. Ebert, *Zeitschrift fuer Anorganische und Allgemeine Chemie*, **180**, 19-41 (1929).

CHAPTER 2

BINDER BURN-OUT

Part I. MICROWAVE SINTERING OF CERAMIC MATRIX COMPOSITES AND THE EFFECT OF ORGANIC BINDERS ON THE SINTERABILITY[1]

ABSTRACT

A single mode microwave cavity operated at 2.45 GHz and equipped with an automated tuning system has been used to process an alumina matrix, zirconia particulate composites that contained ten weight percent of corn oil binder. This research shows that binder burn-out can be achieved without using a susceptor and can depend greatly on the electromagnetic cavity mode used. For example, nearly 100 percent of the binder was removed from a disc-shaped Al_2O_3/ZrO_2/binder compact using TE_{112} mode, while the TM_{012} mode was quite unsuccessful at removing the binder. When a susceptor material was used, binder burn-out and sintering was successfully performed as a one-step process, yielding a highly densified ceramic composite with uniform, small-grained microstructure after a total processing time of about 3.5 hours.

[1] Ki-Yong Lee, Eldon D. Case, Jes Asmussen, Jr. and Marvin Siegel, Proceedings of the 11th Annual ESD Advanced Composites Conference, ESD, The Engineering Society, Ann Arbor, MI, pp. 491-503 (1995).

1. INTRODUCTION

Microwave processing allows a rapid, uniform and volumetric heating of ceramic materials [1]. Janney and Kimrey densified Al_2O_3 + 0.1 wt% MgO via microwave heating far more rapidly than by conventional heating [2]. Tian et al. [3] achieved rapid densification and ultra-fine microstructures in unreinforced alumina using a single mode microwave applicator.

Once microwaves are produced by a generator, they are guided into a microwave cavity which confines the electromagnetic fields. Upon proper tuning of the cavity, the electromagnetic fields set up a pattern of standing waves (a resonance) within the cavity. If the energy from the microwaves couples efficiently with the material to be processed, then the material may be heated by the microwave energy.

Microwave cavities can be either single mode or multimode [4]. A single mode cavity produces a unique standing wave pattern or mode for a specific cavity dimension. The multimode cavity, such as a kitchen microwave oven, superimposes several fundamental modes to produce a complex pattern of standing waves. Multimode cavities are more commonly used than single mode cavities due to the low cost, ease of construction and adaptability of multimode cavities [5]. However, the nonuniform electric field distributions multimode cavities provide can cause inhomogeneous heating, resulting in low coupling efficiency of microwave energy with materials.

To improve both the coupling efficiency and uniformity of heating, single mode cavities have been designed and used by several researchers [5-10]. Either low loss or lossy materials can couple efficiently with microwaves using an internally tuned single mode cavity [5, 11]. In a single mode cavity, the internal electric field can be maximized at a

location of the processed material by tuning the cavity. Tuning minimizes the reflected power by two adjustments. A sliding short located on a movable top plate of the cylindrical cavity changes the cavity length. A sliding probe located in the microwave power launch assembly (through which the microwaves are fed into the cavity) determines the microwave fields in the region near the probe and the cavity wall. The complex dielectric constants are a function of temperature, thus continuous cavity tuning is required during heating in order to optimize the coupling efficiency, which is a cumbersome job if the tuning is done manually.

Recently Asmussen et al. developed a system for automated tuning of single mode cavities which employs computer-controlled stepper motors to adjust the sliding short position and the power launch probe positions. Using the computer-controlled tuning system for a single mode microwave cavity, Lee and Case [12] demonstrated that repeatable heating schedules can be obtained for sintering various alumina ceramics to high densities.

This study investigates the feasibility of using the automated single mode microwave tuning system to sinter compacts of alumina/zirconia mixed with an organic binder. Several researchers have sintered Al_2O_3-ZrO_2 composites using microwave power [10, 13]. Kimrey et al. [13] have reported that Al_2O_3-10 to 70 wt% ZrO_2 was successfully densified using 2.45 GHz and 28 GHz microwave. Patil et al. [10] sintered Al_2O_3-15 and 23 volume % ZrO_2 powders without binders using a single mode cylindrical cavity operating in the TM_{012} mode.

Ceramic powders are typically compacted into desired shapes by techniques such as pressing, slip casting, and injection molding and then densified at high temperature to obtain strongly bonded components. Such consolidation techniques often rely on organic binders

to play a role as binder, lubricant, plasticizer, and/or sintering aid etc. [14]. If the binders are not removed prior to sintering at higher temperatures, the burn-out of the residual binder at elevated temperature may result in cracking in the final component. Microwave power allows rapid heating rates due to the interaction between electromagnetic fields and material so that careful control of heating is very important to burn out the organic binders without cracking material.

Several researchers [15-18] have removed organic binders from ceramic compacts using multimode microwave cavities. Moore et al. [15, 16] developed a Microwave Thermogravimetric Analyzer (MTGA) to investigate the binder removal mechanism. Using a commercial microwave oven, Harrison et al. [18] fabricated lead zirconate-lead titanate (PZT) and lanthanum containing PLZT ceramics by a series of thermal processing steps including microwave drying, calcining, binder burn-off, and finally sintering at high temperature.

According to Asmussen [11], a cylindrical circular single mode cavity TM_{012} mode is a logical processing mode for a cylindrical billet of material located in the center of the cavity. For a thin slab of material located in the bottom of the cavity [11], either the TE or TM modes may be used to heat the material.

Despite the microwave processing research discussed above, the present authors were not able to find references in the literature to research using a single mode microwave cavity: (1) to remove binder from ceramic compacts, or (2) to sinter ceramics containing a binder phase. This study focuses on microwave binder burn-out and sintering in a single mode cavity.

In this study, two different processing procedures are used. In the first procedure, two adjacent cavity modes, namely TE_{112} and TM_{012} modes, are used to only remove the binder from Al_2O_3-ZrO_2 powder compacts without using a microwave susceptor material. Both fixed and stepped microwave input power levels were used during processing. In this first procedure (without a susceptor) the specimens were not sintered.

In the second procedure for the Al_2O_3/ZrO_2/binder composite specimens, the binder was removed and the specimens were sintered in a one step process. The one-step binder removal/sintering process used TE_{112} and TM_{012} modes with a susceptor (casket) composed of a zirconia microwave absorber.

2. EXPERIMENTAL PROCEDURE

MATERIALS used to fabricate the alumina matrix/zirconia composites were Sumitomo AKP-50 alumina powder and a purified zirconia powder (Fisher Scientific Company). The average particle size for AKP-50, as specified by the vendor, was 0.23 μm. However, the vendor did not specify the particle size for the zirconia powders. Using an SEM (Hitachi, S-2500C), we determined that the average particle size for the zirconia was less than 0.4 μm. A commercial corn oil was used for the organic binder, since it is readily available and non-toxic when removed at high temperature.

The alumina powder, zirconia powder, and the binder were mixed by ball milling. The ball milling also likely reduced the particle size somewhat, but the extent of particle size reduction via ball milling was not determined in this study. All specimens used in the study were approximately 90 wt% alumina and 10 wt% zirconia before adding the corn oil binder.

The ball milling procedure was as follows. First, alumina powder and zirconia powder were mixed in a plastic mill by ball milling for 24 hours using alumina grinding media. The milled alumina/zirconia powder mixture was then heated overnight at 200°C to aid in removing water that may have been absorbed by the powders. After adding ten wt% corn oil, the 81 wt% alumina-9 wt% zirconia-10 wt% binder system was ball milled for another 24 hours. After removing the material from the ball mill, agglomerates were broken-up using a mortar and pestle. The Al_2O_3-ZrO_2 powder/binder material was cold pressed at about 20 MPa into discs approximately 22 mm in diameter and 2 mm thick.

Using an electronic balance (Model EA-1AP, The Torsion Balance Co., Clifton, N.J.) with an accuracy of ± 0.0001 grams, the mass was measured before and after heating the individual specimens. For the twenty seven powder compact specimens used in this study, the mean and standard deviation for the specimen mass before heating was 2.0036 grams and ± 0.0089 grams, respectively. The compacts were stored in a desiccator to reduce the absorption of ambient moisture prior to processing.

EXPERIMENTAL APPARATUS for this study includes the microwave processing system and temperature measurement devices. Continuous wave microwave power was generated by a magnetron (Sairem, Model MWPS 2000, Wavemat Inc., Plymouth, MI) which supplies power from zero to 2000 Watts at 2.45 GHz. A hollow metallic waveguide feeds the microwaves into an internally tunable single mode cavity operated at 2.45 GHz (Model CMPR-250, Wavemat Inc., Plymouth, MI). The cavity was tuned by adjusting a sliding short and a power launch probe to an accuracy of ± 0.1 mm using computer-controller stepper motors (Microstep Drive Sx Series, Compumotor, Fauver, MI) [11, 12].

To reduce contamination of the microwave cavity walls by smoke produced during binder burn-out, a brass tube 5.3 cm in diameter and 24 cm long was affixed to the top, circular plate of the cavity. Also, in some experiments, the elimination of volatiles from the cavity was assisted by a stream of compressed air fed into the cavity through an unused viewing port.

During microwave heating, the specimen temperature was monitored with an accuracy of ± 2°C using a digital thermometer (Accufiber Optical Fiber Thermometer, Model 10, Luxtron Co., Beaverton, Oregon) (Figure 1).

MICROWAVE BINDER BURN-OUT AT BOTH FIXED AND STEPPED INPUT POWER LEVELS, WITHOUT THE USE OF A SUSCEPTOR was performed on the Al_2O_3-ZrO_2/binder specimens. The compact specimens were placed in the center of a disc of alumina insulating board (SALI, Zircar Products Inc.) about 10 cm in diameter and 2 cm thick. No additional insulating or microwave absorbing material was placed around the specimen. The SALI board, with the specimen on it was placed on the bottom plate of the cavity, and centered along the cavity axis. Twenty specimens then were heated one at a time at fixed input power levels of 80 to 150 Watts with the cavity tuned at either the TE_{112} or TM_{012} mode (Table 1 and Figure 2). An additional six specimens also were heated by a stepped power sequence using the input power ranging from 80 to 165 Watts (Table 1 and Figure 4).

IN ADDITION, MICROWAVE BINDER BURN-OUT AND SINTERING WITH THE USE OF A SUSCEPTOR was performed as a one-step process for the

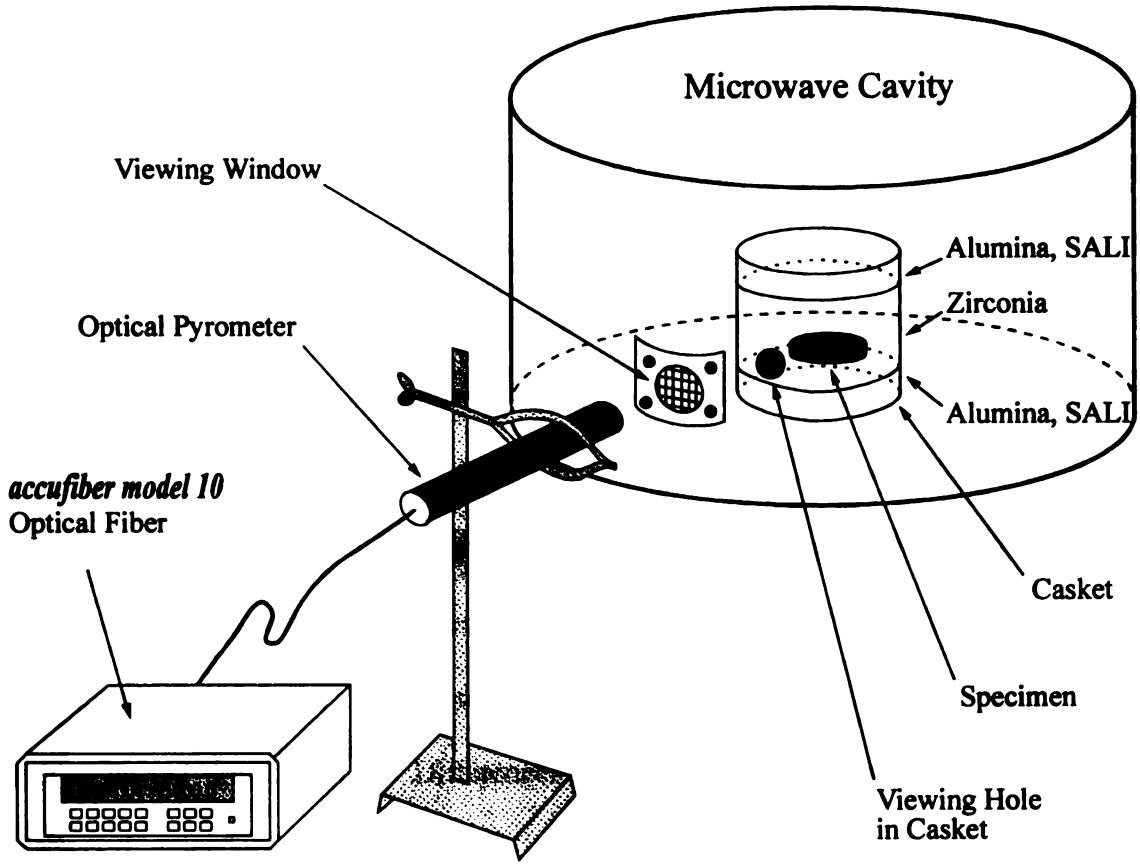

Figure 1. Schematic of the experimental apparatus.

Al_2O_3/ZrO_2/binder specimens. The composite specimens in this study combine a low loss material (alumina, whose room temperature loss tangent values range from 0.0003 to 0.002 [19]) with a relatively lossy material (zirconia, with a typical loss tangent value about 0.01 at room temperature [19]). The nine weight-percent zirconia in the Al_2O_3/ZrO_2/binder specimens does not provide sufficient microwave power absorption to sinter the compacts. Thus in addition to direct coupling with the specimens, heating must be supplemented by radiant heating provided by a casket. The casket is composed of a zirconia cylinder (Type ZYC, Zircar Products Inc.) 3 cm in height, with a 7.62 cm outer diameter and a 5.08 cm inner diameter. Top and bottom discs for the casket were made of alumina insulating board (SALI, Zircar Products Inc.) about 2 cm in thickness. A hole approximately 5 mm in diameter was drilled in the zirconia cylinder wall to allow measurement of the specimen temperature with the optical pyrometer. We employed a 'mode switching' technique to process the alumina/zirconia/binder composite specimens rather than using a single mode, due to differences in the manner in which the two modes (the TE_{112} mode and the TM_{012} mode) heated the specimen. Differences in heating induced by the two modes will be discussed in Section 3.

The rapid mode switching was made possible by the computer control of the sliding short and power launch probe positions. Positions for the sliding short and the power launch probe for the two resonant modes (the TE_{112} mode and the TM_{012} mode) were stored in the computer. During processing, the cavity was quickly switched from mode to mode using the computer-controlled stepper motors.

During binder burn-out and sintering as a one-step process, the heating rate needs to be controlled. Tuning the cavity enhances coupling between the processed material and the

microwave power, yielding a high heating rate. However, rapid heating before complete binder burn-out may crack the specimen. In contrast, detuning reduces the power absorption by the specimen, lowering the heating rate. Thus in this study, we obtained the desired heating rates (which will be discussed in Section 3) at the binder removal stage and at the sintering stage by using the computer-automated system to continuously tune or detune the cavity at a given input power level.

Table 1. Summary of microwave processing done in this study.

Process	Binder burn-out at fixed power level (without susceptor) +					Binder burn-out at stepped power level (without susceptor) ++					Sintering (with susceptor)
Maximum input power level (Watts) and cavity mode	80 *	90 *	120 *	150 *	150 **	80 *	100 *	130 *	150 *	165 *	900 ***
Number of specimens	5	5	4	4	2	2	1	1	1	1	1
Maximum decrease in wt% of specimen	5.86	6.53	7.09	9.5	0.01	3.97	6.03	7.1	7.75	**10.17**	**10.26**

\+ Maximum fixed power level
++ Final power level after a stepped power change
* TE_{112} mode
** TM_{012} mode
*** Switching from TE_{112} mode to TM_{012} mode.

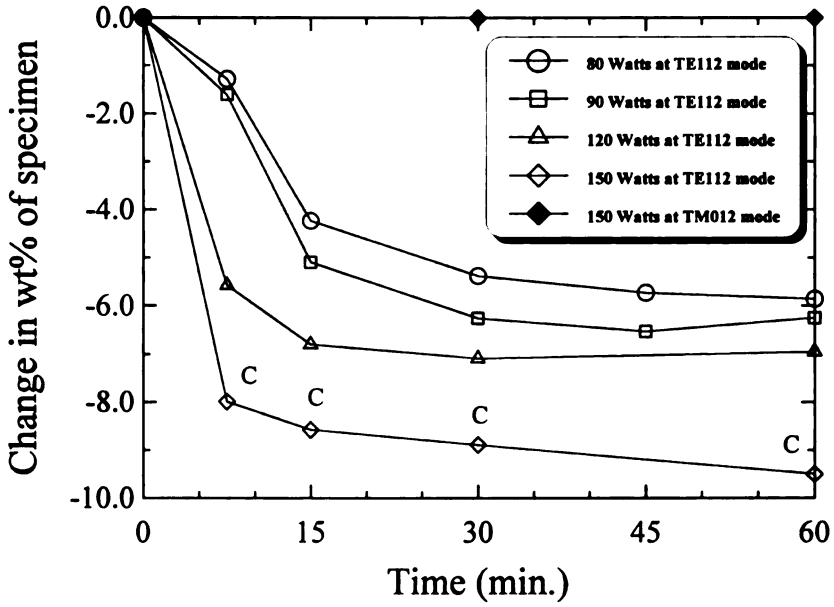

Figure 2. For fixed input power level (without a susceptor), change in wt% of the Al_2O_3/ZrO_2/binder compact specimens as a function of time and input power level. The weight loss corresponds to binder burn-out. The symbol 'C' denotes that the specimen is cracked.

3. RESULTS AND DISCUSSION

MICROWAVE BINDER BURN-OUT AT A FIXED INPUT POWER LEVEL, WITHOUT THE USE OF A SUSCEPTOR was attempted using both the TE_{112} mode and the TM_{012} mode. Using a fixed input power of either 80, 90, 120, and 150 Watts, individual zirconia/alumina/binder compact specimens were heated using TE_{112} mode for time periods of 7.5, 15, 30, 45, or 60 minutes (Table 1 and Figure 2). At each power level, a total of four to five specimens were heated to obtain binder burn-out. At a given input power level the mass of the specimens changed relatively rapidly at the initial stage of heating depending on the power level. After heating for about 15 minutes at the fixed power level, the rate of binder burn-out decreased (Figure 2). For the compact specimens heated at

80, 90, and 120 Watts in the TE_{112} mode, the specimens' mass changed by up to about 7 wt% without cracking (Table 1). For the specimens heated at 150 Watts using the TE_{112} mode, the specimens' mass changed by up to 9.5 wt% (Table 1), however the specimens cracked at the center of the top surface due to rapid binder removal.

Unlike heating in the TE_{112} mode, heating in the TM_{012} mode did not efficiently burn out the binder from the ceramic compact specimens. For the two individual compact specimens heated at 150 Watts input power for 30 and 60 minutes in the TM_{012} mode, the mass decreased by no more than 0.01 weight percent (Table 1). Thus, hardly any binder burn-out occurred during microwave heating using the TM_{012} mode without a susceptor (casket), as shown in Figure 2.

The relative efficiency of binder removal using the TE_{112} and TM_{012} modes may be related to the spatial distribution of electric fields inside a single-mode cylindrical cavity (Figure 3) [5, 11, 20]. For the TE_{112} mode, electric field lines are perpendicular to the cavity axis, thus the electrical field lines are oriented parallel to the disc-shaped powder compact specimen used in this study. In contrast, the TM_{012} mode's electric field lines are parallel to the cavity axis, and thus the electric field lines are oriented perpendicular to the surface of the powder compact specimens. The differing relative orientations of the electric fields may lead to the result that the organic binder was much more readily removed from the alumina/zirconia/binder compacts by heating at TE_{112} mode compared to the TM_{012} mode.

MICROWAVE BINDER BURN-OUT AT A STEPPED INPUT POWER LEVEL, WITHOUT THE USE OF A SUSCEPTOR, can yield more complete binder removal from compact specimens without cracking the specimen (Table 1). Heating was done in the

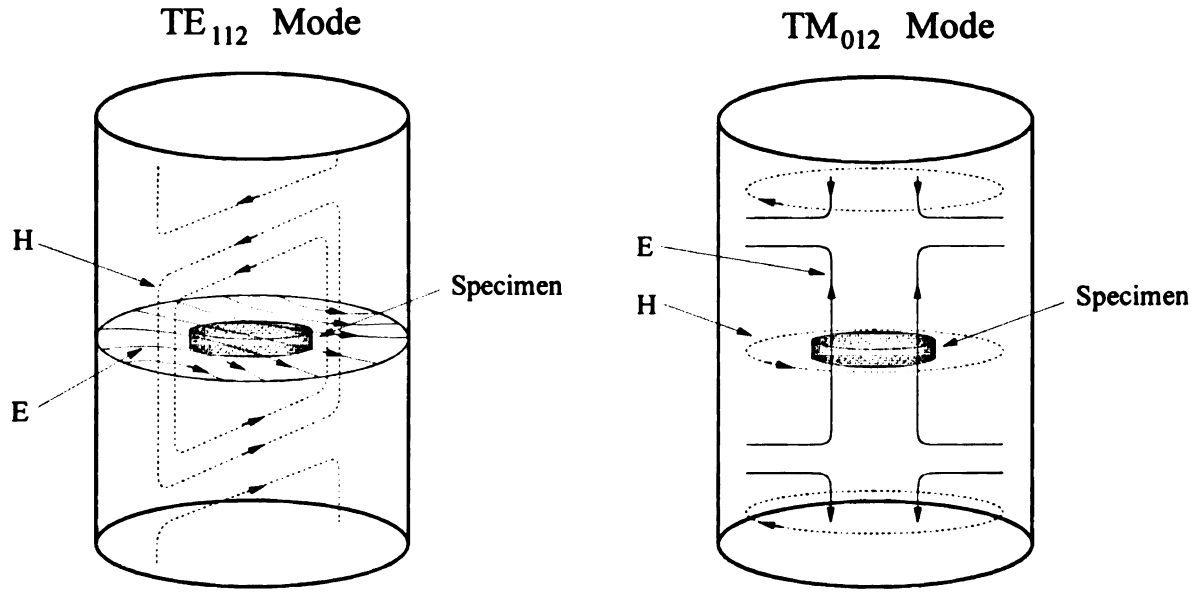

Figure 3. Electromagnetic field distribution for a single mode cylindrical circular cavity [5, 11, 20].

TE_{112} mode using a stepped power sequence (Table 1 and Figure 4). Initially the specimen was heated for 20 minutes at 80 Watts input power. The input power then was increased by 20 to 30 Watts every 10 minutes until the power reached 150 Watts. At about 160 or 165 Watts input power the temperature began to increase rapidly above 500°C. Fast heating at such input power levels caused the binder to burn out too quickly. In one instance, a flame appeared on the specimen surface. The rapid temperature rise induced cracks in the specimens. The binder was burned out when the input power was held at 160 Watts for 40 minutes and subsequently increased to 165 Watts. The maximum temperature obtained at 165 Watts was about 550°C. The mass of a particular compact specimen decreased by as much as 10.17 wt% (Table 1) which was greater than mass fraction of binder initially added

to the compact. The mass decrease in excess of 10 weight percent likely resulted from the loss of water absorbed by the specimen.

To investigate the possibility of binder residue in the specimen that showed the 10.17 weight percent decrease (Table 1 and Figure 4), the specimen first was heated in a conventional furnace at 200°C for 1 hour to eliminate the absorbed water. Then the mass of the specimen dried at 200°C was measured. When the specimen was reheated in the same furnace at 850°C for 8 hours, its mass decreased by 0.1 wt%. Thus, approximately 99 percent of the binder originally added to the alumina/zirconia compact was removed by the microwave heating using a stepped input power sequence in the TE_{112} mode, without using a microwave susceptor (casket).

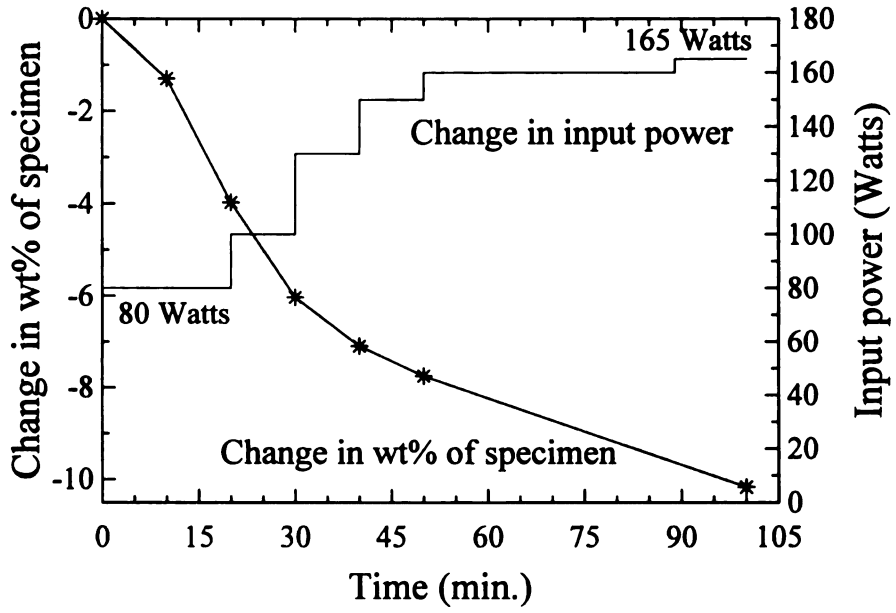

Figure 4. For stepped power levels (with a susceptor), change in wt% of specimens and the input microwave power schedule used to heat the Al_2O_3/ZrO_2/binder specimens. The weight loss corresponds to binder burn-out.

FOR MICROWAVE BINDER BURN-OUT AND SINTERING OF THE ALUMINA/ ZIRCONIA/BINDER SYSTEM USING THE CASKET, we used a mode switching technique for efficient coupling and heating. For the TM_{012} mode, the casket coupled with the microwaves at an input power level of 260 Watts or greater. For the TE_{112} mode, the casket coupled at an input power of 80 Watts or greater. The TM_{012} mode heated the casket better in the temperature range required for sintering. Due to these differences in mode coupling, at the start of the binder burn-out/sintering procedure the microwave cavity was tuned to the TE_{112} resonant mode with 80 Watts input power. A rapid temperature increase (due to the coupling of the zirconia insulation cylinder with the microwaves) occurred within about 12 minutes (Figure 5). When the temperature reached about 620°C at 125 Watts input power, the operating mode was quickly switched from TE_{112} to TM_{012} for further heating. This switch from the TE_{112} mode to the TM_{012} mode is the 'mode switching' referred to in this section and in the Experimental Procedure. Differences in the coupling behavior for the two microwave cavity modes will be explored in a later publication [21].

After coupling, the heating rate was precisely controlled during the entire processing sequence by continuously tuning or detuning the cavity at a given input power level. In the temperature range from 550°C to 850°C the heating rate of about 3.3°C per minute during binder burn off did not crack the specimen (Figure 5). After the binder had burned out, the heating rate was increased to about 9°C per minute. The temperature was held at 1500°C for 20 minutes, during which time final densification occurred. The resulting total processing time was about 3.5 hours.

The mass of a particular sintered Al_2O_3/ZrO_2/binder specimen decreased by 10.26 wt%

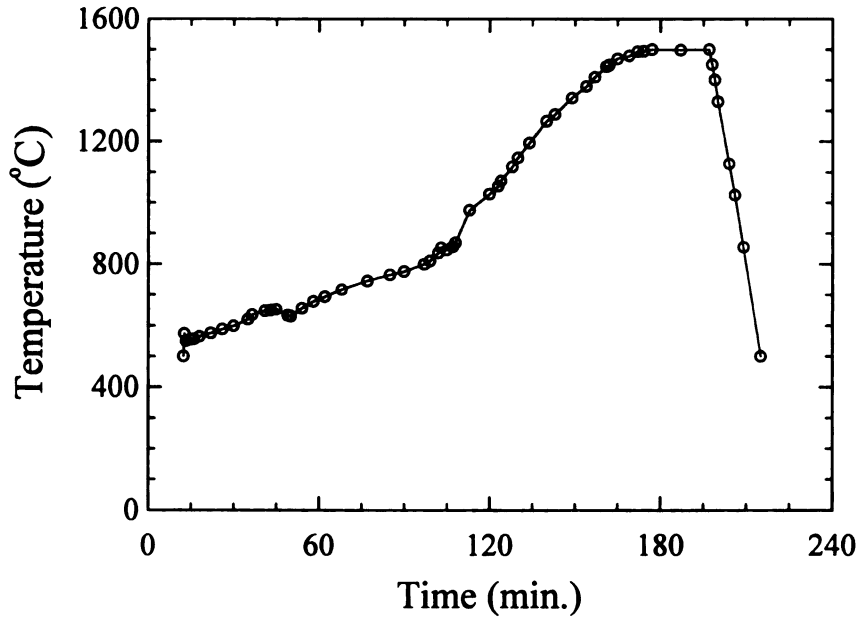

Figure 5. Heating schedule for binder removal and sintering of an Al_2O_3-ZrO_2 ceramic composite using the one-step process discussed in the Experimental Procedure section. In Table 1, this specimen is designated having a 10.26 wt% decrease.

(Table1), giving a final as-sintered density 4.04 g/cm^3, as measured by the Archimedes method. The theoretical densities of alpha alumina and zirconia (monoclinic) are 3.987 g/cm^3 [22] and 5.82 g/cm^3 [23], respectively, yielding a theoretical density of 4.12 g/cm^3 for the 90 wt% Al_2O_3-10 wt% ZrO_2 composite. Thus the measured value of 4.04 g/cm^3 corresponds to 98.1 percent of the theoretical composite density.

The fracture surface of the resulting composite was examined with an SEM (JEOL, JSM 6400V) (Figure 6). The composite has a uniform, small-grain sized microstructure with an average grain size 2.7 μm, as determined by the linear intercept method on SEM micrographs. A stereographic correction factor 1.5 was used to compute the grain size [24].

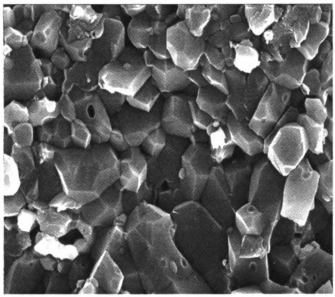

Figure 6. Fracture surface of microwave sintered 90 wt% AKP-50 alumina and 10 wt% zirconia composite (Bar represents a length of one micron). In Table 1, this specimen is designated having a 10.26 wt% decrease.

4. SUMMARY AND CONCLUSIONS

Two processing procedures were used in this study. One procedure only burned out the binder material, without using a susceptor (casket). The second procedure used a casket and combined binder removal and sintering as a one-step process. Both processing procedures were applied to alumina/zirconia/binder compacts consisting of 81 weight percent alumina, 9 weight percent zirconia, and 10 weight percent corn oil binder.

Without using a susceptor material, the first procedure employed the TE_{112} and the TM_{012} cavity modes to attempt binder burn-out only. For example, a fixed input power of 120 Watts in the TE_{112} mode removed about 71 percent of the binder (which corresponds to 7.09 wt% mass decrease, as shown in Table 1) without cracking the specimen. In contrast, the two specimens heated at 150 Watts fixed power level in the TM_{012} mode showed a

maximum binder removal of only 0.01 weight percent (Table 1 and Figure 2). The effectiveness of the TE_{112} mode in binder burn-out was enhanced by changing from a fixed input power to a stepped input power sequence. In particular, nearly 100 percent of the binder was removed using a stepped input power sequence in the TE_{112} mode (Table 1 and Figure 4). Thus, this research shows that for microwave heating the extent of burn-out of an organic binder can differ dramatically from one cavity mode to another. In addition, binder burn-out can be made more complete by using a stepped input power sequence rather than a fixed input power level.

Using a susceptor material, the second procedure employed mode switching from the TE_{112} mode to the TM_{012} mode to burn out the binder and sinter as a one-step process. For an Al_2O_3/ZrO_2/binder powder compact, the binder was removed and the specimen was sintered by the one-step process in a total processing time of 3.5 hours by switching from the TE_{112} mode to the TM_{012} mode and controlling the heating rate (Table 1 and Figure 5). The final sintered alumina/zirconia composite specimen had mass density of 98.1 percent of theoretical with a uniform and fine microstructure with an average grain size 2.7 μm (Figure 6).

REFERENCES

1. W.H. Sutton, "Microwave Processing of Ceramic Materials," Am. Ceram. Soc. Bull. 68[2] pp. 376-386, 1989.

2. M.A. Janney, H.D. Kimrey, "Microwave Sintering of Alumina at 28 GHz," Ceramic Powder Science, II, B, Amer. Cer. Soc., Cer. Trans., vol. 1, pp. 919-924, 1988.

3. Y.L. Tian, D.L. Johnson and M.E. Brodwin, "Ultrafine Microstructure of Al_2O_3 Produced by Microwave Sintering," Ceramic Powder Science II, B, Amer. Cer. Soc., Cer. Trans., vol. 1, pp. 925-932, 1988.

4. J.D. Katz, "Microwave Sintering of Ceramics," Annu. Rev. Mater. Sci., 22:153-70, 1992.

5. J. Asmussen and R. Garard, "Precision Microwave Applicators and Systems for Plasma and Materials Processing," Mat. Res. Soc. Symp. Proc., vol. 124, pp. 347-352, 1988.

6. Y-L. Tian, "Practices of Ultra-Rapid Sintering of Ceramics Using Single Mode Applicators," Microwaves: Theory and Application in Materials Processing, Amer. Cer. Soc., Cer. Trans. vol. 21, pp. 283-300, 1991.

7. B.Q. Tian and W.R. Tinga, "A Wide Range Tunable and Matchable High Temperature Applicator," Microwaves: Theory and Application in Materials Processing, Amer. Cer. Soc., Cer. Trans. vol. 21., pp. 647-654, 1991.

8. J.F. Gerling and G. Fournier, "Techniques to Improve the Performance of Microwave Process Systems Which Utilize High Q Cavities," Microwaves: Theory and Application in Materials Processing, Amer. Cer. Soc., Cer. Trans. vol. 21., pp. 667-674, 1991.

9. H.S. Sa'adaldin, W.M. Black, I. Ahmad and R. Silberglitt, "Coupling with an Adjustable Compound Iris in a Single Mode Applicator," Mat. Res. Soc. Symp. Proc., vol. 269, pp. 91-96, 1992.

10. D.S. Patil, B.C. Mutsuddy, J.Gavulic, and M. Dahimene, "Microwave Sintering of Al_2O_3:ZrO_2 Ceramics," Microwaves: Theory and Application in Materials Processing, Amer. Cer. Soc., Cer. Trans. 21, pp. 565-575, 1991.

11. J. Asmussen, H.H. Lin, B. Manring, and R. Fritz, "Single-mode or controlled multimode microwave cavity applicators for precision materials processing," Rev. Sci. Instrum., 58 [8] 1477-1486, 1987.

12. K.Y. Lee, E.D. Case, J. Asmussen, Jr. and M. Siegel, "Sintering of Alumina Ceramics in a Single Mode Cavity under Automated Control," to be published in Microwaves: Theory and Application in Materials Processing, Amer. Cer. Soc., Cer. Trans., 1995.

13. H.D. Kimrey, J.O. Kiggans, M.A. Janney, and R.L. Beatty, "Microwave Sintering of Zirconia-Toughned Alumina Composites," Mat. Res. Soc. Symp. Proc., vol. 189, pp. 243-256, 1991.

14. D.W. Richerson, Modern Ceramic Engineering, page 170-175, Marcel Dekker, Inc., New York, 1982.

15. E.H. Moore, I. Ahmad, and D.E. Clark, "Microwave Thermogravimetric Analyzer (MTGA)," Microwaves: Theory and Application in Materials Processing, Amer. Cer. Soc., Cer. Trans. 21, pp. 675-681, 1991.

16. E.H. Moore, D.E. Clark, and R. Hutcheon, "Polymethyl Methacrylate Binder Removal from an Alumina Compact: Microwave versus Conventional Heating," Mat. Res. Soc. Symp. Proc., vol. 269, pp. 341-346, 1992.

17. X.D. Yu, F. Selmi, V.V. Varadan and V.K. Varadan, "Binder burn out of tape cast ceramics by microwave energy," Materials Letters 14, 245-250, North-Holland, 1992.

18. W.B. Harrison, M.R.B. Hanson and B.G. Koepke, "Microwave Processing and Sintering of PZT and PLZT Ceramics," Mat. Res. Soc. Symp. Proc., vol. 124, pp. 279-286, 1988.

19. R.C. Buchanan, Ceramic Materials for Electronics, Marcel Dekker, Inc., N.Y., N.Y., pages 4-5, 1986.

20. L.J. Mahoney, The Design and Testing of a Compact Electron Cyclotron Resonant Microwave-Cavity Ion Source, Thesis for the Degree of M.S., Michigan State University, page 36, 1989.

21. K.Y. Lee, E.D. Case, J. Asmussen, Jr., and M. Siegel, to be published.

22. National Bureau of Standards (U.S.), Circ. 539, vol. 9, page 3, 1959.

23. F. Larson, G. McCarthy, North Dakota State University, Fargo, North Dakota, USA. JCPDS Grant-in-Aid Report, 1985.

24. E.E. Underwood, A.R. Colcord, and R.C. Waugh, Ceramic Microstructures, pages 25-52, R.M. Fulrath and J.A. Pask, eds., John Wiley and Sons, New York, 1968.

Part II. BINDER BURN-OUT IN A CONTROLLED SINGLE-MODE MICROWAVE CAVITY[2]

1. INTRODUCTION

Organic binders are added to provide sufficient green strength to an unfired ceramic body to permit handling and machining (1). However, the organic binders must be removed from the ceramic bodies prior to sintering at high temperature. The volatile products produced during binder burn-out can cause cracking if the binder is removed too quickly or if the sintering process (at high temperatures) begins before binder removal is complete.

Several researchers (2-4) have investigated microwave binder burn-out for ceramics. Moore et al. (3) removed PMMA binder from PMMA/alumina compacts using conventional heating, microwave heating and microwave hybrid heating. 100% of the binder was removed from specimens (≤24 grams, containing ≤8wt% binder) heated to 470°C with 3200 Watts of microwave power. Yu et al. (4) completed binder burn-out of tape cast barium strontium titanate ceramics using a single-mode microwave cavity at lower temperature and less time than in a conventional furnace.

This study focuses on microwave binder burn-out of Al_2O_3/binder and Al_2O_3/SiC/binder systems in the single-mode cavity using: (i) fixed input power levels and (ii) stepped input power level sequences.

---

[2] Ki-Yong Lee, Eldon D. Case, Jes Asmussen, Jr. and Marvin Siegel, Scripta Materialia, vol. 35, no. 1, pp. 107-111 (1996).

2. EXPERIMENTAL PROCEDURE

2.1. Materials and Specimen Preparation

The organic binder used in this study was commercial corn oil. Sumitomo AKP-50 alumina powder with a vendor-specified average particle size of 0.23 μm was used for the alumina phase for all specimens. For alumina/silicon carbide composites, AKP-50 alumina powder and silicon carbide platelets (C-Axis Technology, Canada) were used. Prior to fabricating the alumina/binder compacts, the AKP-50 powder was heated overnight at 200°C in a conventional furnace to remove absorbed moisture. The dried alumina powder was ball milled with the corn oil binder for 24 hours. For the alumina/silicon carbide/binder specimens, first 90wt% alumina and 10wt% silicon carbide were ball milled together for 24 hours. The mixture was dried overnight at 200°C in a conventional furnace, then 10wt% of corn oil binder was added and the mixture was ball milled for 24 hours.

Agglomerates created during ball milling were broken-up using a mortar and pestle. Both the alumina/binder and the alumina/silicon carbide/binder specimens were uniaxially pressed at about 20 MPa, resulting in disc-shaped powder compacts approximately 22 mm in diameter and 2 mm thick. The powder compacts were stored in a desiccator to reduce moisture absorption prior to microwave heating.

Before and after heating the specimens in the microwave cavity, the mass of individual compact specimens was measured to an accuracy of ± 0.0001 grams using an electronic balance (Model EA-1AP, The Torsion Balance Co., Clifton, NJ). For the 41 specimens used in this study, the mean mass before microwave heating was 2.0000 grams with a standard deviation 0.0042 grams.

2.2. Experimental Apparatus

Microwave power was produced by a 2000 Watt, 2.45 GHz power supply (Sairem, Model MWPS 2000, Wavemat Inc., Plymouth, MI). The microwaves were guided into a circular cylindrical single-mode cavity 17.78 centimeters in diameter (Model CMPR-250, Wavemat Inc., Plymouth, MI) (5, 6). Cavity tuning via the computer automated system is discussed elsewhere (5, 6). During microwave heating, the specimen temperature was monitored with an accuracy of ± 2°C using an Accufiber optical pyrometer and thermometer (Model 10, Luxtron Co., Beaverton, Oregon).

2.3. Microwave Binder Burn-out

The individual compact specimens were placed in the center of a disc of alumina insulating board (SALI, Zircar Products Inc.) about 10 cm in diameter and 2.5 cm thick. No additional insulating material or microwave susceptor material was used in this study (6). Seventeen alumina/binder specimens were heated using a fixed input power ranging from 70 to 120 Watts (Table 1) (Figure 1), while 50 to 80 Watts of fixed input power heated 14 Al_2O_3/SiC/binder compact specimens (Table 1) (Figure 2). Using a stepped input power level sequence, an additional 5 Al_2O_3/binder specimens were heated by microwave input power ranging from 80 to 150 Watts (Table 1) (Figure 3). Stepped input power between 45 and 130 Watts was used to process 5 Al_2O_3/SiC/binder specimens (Table 1) (Figure 4).

Table 1. Summary of Microwave Binder Burn-Out done in this study

Material	Alumina/binder			Alumina/silicon carbide/binder		
Process	Maximum input power level (Watts)	Number of specimens and cavity mode	Maximum decrease in wt% of specimen	Maximum input power level (Watts)	Number of specimens and cavity mode	Maximum decrease in wt% of specimen
Fixed input power level +	70	4 *	3.48	50	4 *	5.48
	80	4 *	6.31	60	4 *	7.27
	100	4 *	7.21	80	4 *	9.56
	120	3 *	10.35	80	2 **	-0.18
	100	2 **	0.06			
Stepped input power level ++	80	1 *	2.36	45	1 *	2.52
	90	1 *	5.84	55	1 *	4.55
	110	1 *	6.77	75	1 *	6.38
	140	1 *	9.21	105	1 *	8.52
	150	1 *	**10.05**	130	1 *	**10.47**

\+ Maximum fixed input power level
++ Final power level after a stepped input power change
* TE_{112} mode
** TM_{012} mode

3. RESULTS AND DISCUSSION

3.1. Microwave Binder Burn-out Using a Fixed Input Power Level

Individual powder compacts were heated in the TE_{112} mode one at a time for 7.5, 15, 30, and 60 minutes using fixed input power levels of 70, 80, 100, 120 Watts for Al_2O_3/binder and 50, 60, 80 Watts for Al_2O_3/SiC/binder compacts (Table 1) (Figures 1 and 2). For alumina/binder compact specimens heated at input powers of 70 to 100 Watts in the TE_{112} mode, the specimens' mass decreased by up to 7.21wt% without cracking the specimens (Figure 1). An input power of 120 Watts heated both the SALI board setter and the specimen, accelerating the binder burn-out, cracking the specimens, and resulting in a mass decrease of up to 10.35 wt%. This indicates nearly all of binder was removed from the alumina/binder specimens (Figure 1).

At input powers of 100 Watts or less, the SALI did not appear to heat appreciably. However, at 120 Watts, a flame and a red hot zone appeared on the SALI board and the pyrometer temperature rose to a maximum of about 600°C within about 10 minutes. After reaching 600°C, the temperature decreased such that it could no longer be sensed by the pyrometer (the minimum temperature the pyrometer can detect is 500°C). When the input power was 100 Watts or less, the SALI board was discolored after microwave heating. Smoke penetrating into the SALI likely assisted the heating of the SALI board during microwave heating.

The mass decreased by up to 9.56 wt% for the 12 Al_2O_3/SiC/binder compacts heated at powers of from 50 to 80 Watts in the TE_{112} mode (Table 1). Of the eight specimens heated at 60 and 80 Watts, six of them cracked (Figure 2). Unlike the microwave heating

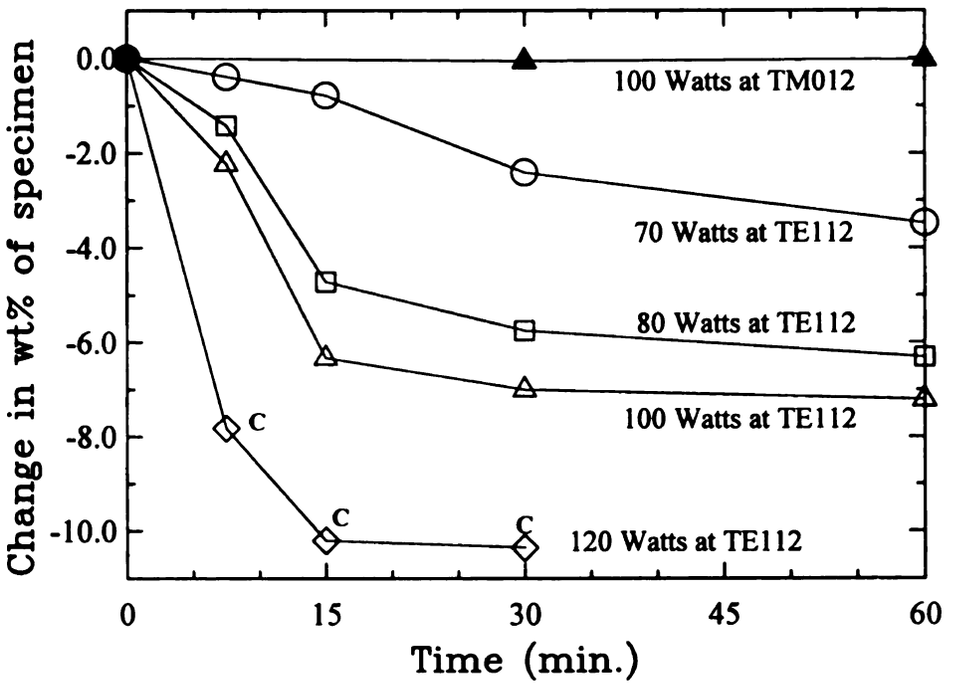

Figure 1. For fixed input power level, change in wt% of the Al_2O_3/binder compact specimens as a function of time and input power level. The weight loss corresponds to binder burn-out. The symbol 'C' indicates that the specimen cracked.

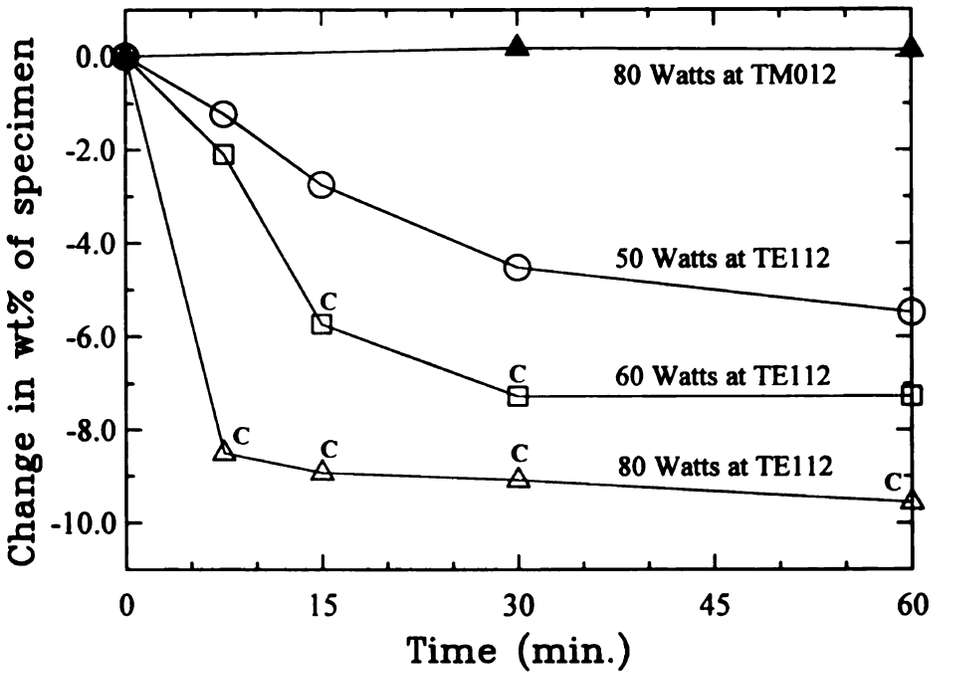

Figure 2. For fixed input power level, change in wt% of the Al_2O_3/SiC/binder compact specimens as a function of time and input power level. The weight loss corresponds to binder burn-out. The symbol 'C' indicates that the specimen cracked.

of the alumina/binder specimens, the temperature during the binder removal process always was below 500°C and there was no indication for heating of the SALI board. An input power of about 50 Watts in the TE_{112} mode was required for approximately 6wt% binder burn-out within one hour for the alumina/silicon carbide/binder composites compared to about 80 Watts in the TE_{112} mode for the alumina/binder compacts. Since the loss tangent of alumina is 0.0003 to 0.002 at room temperature at 1 MHz (7) and the loss tangent of silicon carbides is 0.14 at about 25°C at 8 GHz (8), likely the 81wt% Al_2O_3/9wt% SiC/10wt% binder compacts coupled better with microwave energy at low power than did the 90wt% Al_2O_3/10wt% binder specimens.

An additional 2 specimens each of Al_2O_3/binder and Al_2O_3/SiC/binder systems were heated in the TM_{012} mode using a fixed input power level of 100 Watts for alumina/binder and 80 Watts for alumina/silicon carbide/binder specimens (Table 1) (Figures 1 and 2). The negligible binder burn-out for the TM_{012} mode is likely related to the spatial distributions of electric fields inside a single-mode cavity (6). For the TM_{012} mode the electric fields are parallel to the surface of the disc-shaped powder compacts, whereas for the TM_{012} mode the field lines are perpendicular to the specimen surface.

3.2. Microwave Binder Burn-out Using a Stepped Input Power Level Sequence

Using a fixed input power level, a complete or nearly complete binder burn-out always resulted in cracking the specimens (Section 3.1). However, specimen cracking was avoided when stepped input power sequences in TE_{112} mode was used to heat both the alumina compacts and the alumina/silicon carbide composites. The change in wt% of

individual specimens and the input power sequence (Table 1) are shown in Figures 3 and 4 for the Al_2O_3/binder and the Al_2O_3/SiC/binder specimens, respectively.

Alumina/binder specimen A/B1 was heated for 75 minutes by a stepped input power sequence up to 145 Watts (Figure 3). The input power then was increased to 150 Watts, and the SALI board coupled with microwave energy within 10 minutes. The temperature indicated by the pyrometer stayed at about 550°C for another 15 minutes. After 100 minutes of heating, the specimen's mass decreased by 10.05wt% (Table 1) without cracking the specimen.

For alumina/silicon carbide platelet composite specimen A/S/B1 heated for 105 minutes by a stepped input power level sequence ranging from 45 to 130 Watts, the specimen's mass decreased by 10.47wt% (Table 1) and the specimen did not crack (Figure 4). There was no indication of microwave coupling with the SALI board (the temperature was below 500°C) during heating of the alumina/silicon carbide composites. A final maximum power of 130 Watts removed nearly all of the binder from the Al_2O_3/SiC/binder specimen while 150 Watts was needed to entirely remove the binder from the Al_2O_3/binder compacts. The lower power to complete the binder burn-out for the Al_2O_3/SiC/binder composite specimen is likely due to SiC's higher loss tangent (Section 3.1).

For specimen A/B1 (alumina/binder specimen, Figure 3) and specimen A/S/B1 (alumina/SiC/binder composite, Figure 4), we quantitatively determined the amount of binder residue left in each specimen after microwave heating. Following microwave binder burn-out (Figures 3 and 4), the specimens were heated at 200°C for one hour in a conventional furnace. The dry mass of each specimen was measured, then the specimens

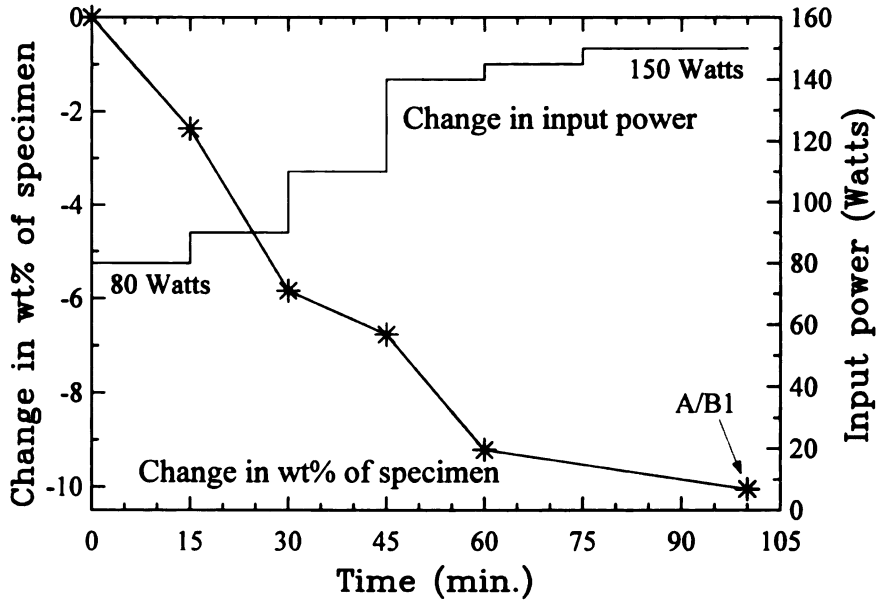

Figure 3. For stepped power levels, change in wt% of specimens and the input microwave power schedule used to heat the Al_2O_3/binder specimens. The weight loss corresponds to binder burn-out.

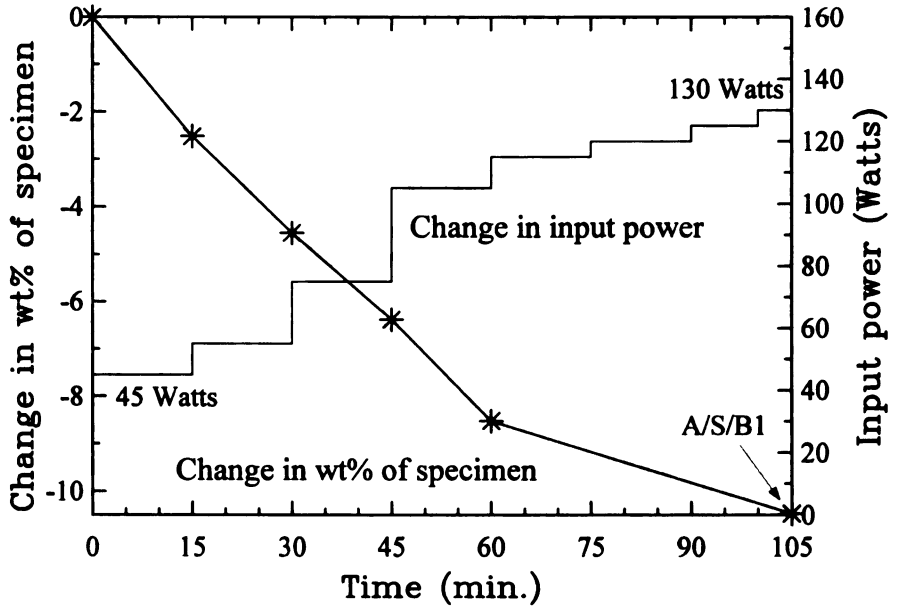

Figure 4. For stepped power levels, change in wt% of specimens and the input microwave power schedule used to heat the Al_2O_3/SiC/binder specimens. The weight loss corresponds to binder burn-out.

were heated at 850°C in the conventional furnace for 8 hours. After the burn-out in the conventional furnace, the mass of the two specimens decreased by 0.11wt% with respect to the dry mass. Therefore, approximately 99% of the binder originally added to the alumina powder and the alumina/silicon carbide platelet compact was removed by the microwave heating using stepped input power in the TE_{112} mode.

4. CONCLUSIONS

This study attempted corn-oil binder removal from alumina/binder and the alumina/silicon carbide/binder compacts by microwave heating in the TE_{112} and the TM_{012} mode of a computer controlled single-mode cavity. In the TE_{112} mode when the fixed input power level was relatively high, the binder removal was nearly complete but the specimens cracked due to the rapid binder removal. The fixed input power level required to decrease the specimens' mass by about 6wt% was 50 Watts for the Al_2O_3/SiC/binder specimens compared to 80 Watts for the Al_2O_3/binder specimens (Table 1). The Al_2O_3/SiC/binder composite compacts coupled better with the microwave energy due to the high loss tangent of the silicon carbide itself. In contrast to heating in the TE_{112} mode, almost no binder burned out in the TM_{012} mode for any of the Al_2O_3/binder or the Al_2O_3/SiC/binder specimens heated (Figures 1 and 2).

A stepped input power level sequence burned out in the TE_{112} mode almost 100 percent of the binder from both the alumina/binder and the alumina/silicon carbide/binder systems without cracking the specimens (Table 1) (Figures 3 and 4). For the Al_2O_3/binder specimens, microwave coupling with the SALI board at 150 Watts assisted the binder removal. In contrast, the alumina/SiC/binder compacts coupled better with the

microwave energy, completing the binder burn-out at an input power low enough (130 Watts) that the microwave heating of the SALI board was apparently negligible.

ACKNOWLEDGEMENT

This study was financially supported by the Research Excellence Fund of the state of Michigan.

REFERENCES

1. D. W. Richerson, Modern Ceramic Engineering, p. 170, Marcel Dekker Inc., NY (1982).

2. W. B. Harrison, M. R. B. Hanson and B. G. Koepke, Microwave Processing of Materials, Materials Research Society, 124, p. 279, Pittsburgh, Pennsylvania (1988).

3. E. H. Moore, D. E. Clark and R. Hutcheon, Microwaves: Theory and Application in Materials Processing II, Ceramic Transactions, 36, p. 325, The American Ceramic Society Inc., Columbus, Ohio (1993).

4. X. D. Yu, F. Selmi, V. V. Varadan and V. K. Varadan, Materials Letters 14, p. 245 (1992).

5. K. Y. Lee, E. D. Case, J. Asmussen, Jr. and M. Siegel, accepted for publication in Microwaves: Theory and Application in Materials Processing, Ceramic Transactions, The American Ceramic Society Inc., Columbus, Ohio (1995).

6. K. Y. Lee, E. D. Case, J. Asmussen, Jr. and M. Siegel, Proceedings of the 11th Annual ESD Conference on Advanced Composites, p.491, ESD-The Engineering Society, Ann Arbor, MI (1995).

7. R. C. Buchanan, Ceramic Materials for Electronics, p. 4, Marcel Dekker Inc., NY (1986).

8. R. D. Hollinger, V. V. Varadan, V. K. Varadan and D. K. Ghodgaonkar, Microwaves: Theory and Application in Materials Processing, Ceramic Transactions, 21, p. 243, The American Ceramic Society Inc., Columbus, Ohio (1991).

Part III. MICROWAVE BINDER BURN-OUT FOR BATCH PROCESSING OF Al_2O_3, Al_2O_3/SiC PLATELET, AND Al_2O_3/ZrO_2 PARTICLE POWDER COMPACTS[3]

ABSTRACT

A cylindrical 2.45 GHz single-mode microwave cavity was used for organic binder burn-out of batch processed ceramic compacts. The burn-out was accomplished without enclosing the specimens in a microwave susceptor material. Strategies are discussed for controlling cavity mode and input power to avoid specimen cracking during burn-out.

1. INTRODUCTION

Organic binders are often used in industrial processing of ceramics. The binders add green strength to ceramic powder compacts, reducing the damage induced by handling the compacts prior to sintering [1]. However, the binders must be burned out (eliminated) from the powder compacts prior to densification. The binder burn-out process may take up to 24 hours, thus the time needed for binder burn-out of large parts can exceed the sintering time.

In this study, a 2.45 GHz single-mode microwave cavity was used to burn organic binder from ceramic powder compacts processed in a batch process mode (six to seven specimens processed simultaneously). The results of previous studies done by the present authors on binder burn-out of individually-processed specimens [2,3] will be

[3] Ki-Yong Lee, Eldon D. Case, Jes Asmussen, Jr., Microwaves: Theory and Application in Materials Processing V, Cer. Trans. vol. 80, pp. 539-546, Edited by D.E. Clark, W.H. Sutton, and D.A. Lewis, American Ceramic Society, Westerville, Ohio (1997).

compared with this batch processing study.

2. EXPERIMENTAL PROCEDURE

To facilitate comparison with a previous binder-burn-out study done by the current authors for individually-processed specimens [2,3], this binder-burn-out study for batch processed specimens employed specimens of the same composition and binder type as the study of individually processed specimens 2,3]. Materials used for both the batch-processed and individually-processed specimens were Al_2O_3, Al_2O_3/SiC platelet, and Al_2O_3/ZrO_2 particle with 10 wt% corn oil binder in each compact. Identical processing methods, including the ball milling and dry pressing were used for both studies. Furthermore the dimensions and mass of the specimens were nominally identical. In both studies, the same 2.45 GHz single-mode microwave cavity and power supply were used for binder burn-out.

For the two composite compositions (Al_2O_3/SiC platelet and Al_2O_3/ZrO_2 particle) the ratio of reinforcing phase to the Al_2O_3 matrix was 1:9 after binder burn-out. Sumitomo AKP50 powder, having an average particle size of 0.23 μm (as specified by the manufacturer) was used as the Al_2O_3 phase in every specimen in this study. SEM examination revealed that the ZrO_2 particles (Fisher Scientific Company) were approximately equiaxed, with a mean diameter of about 0.4 microns, while the SiC platelets (C-Axis Technology, Canada) were about 2 microns thick with irregular shapes.

The Al_2O_3/ZrO_2 particle and Al_2O_3/SiC platelet powders were mixed by dry ball milling for 24 hours. No dry ball milling was done for the monophase Al_2O_3 specimens. Each of the three compositions then were ball milled with 10 wt% corn oil for 24 hours.

The specimens were uniaxially hard-die pressed at 32 MPa, yielding disc-shaped compacts about 22 mm in diameter with an average thickness of about 2 mm. Each specimen mass was measured before and after microwave heating by an electronic balance (Model EA-1AP, The Torsion Balance Co., Clifton, NJ) with an accuracy of ± 0.0001 grams. Prior to binder burn-out, the specimens' mean mass and standard deviation were 1.9988 grams and ± 0.0068 grams, respectively, for a total of 269 specimens included in this study.

The 2.45 GHz single-mode microwave cavity and the microwave power supply are described in detail elsewhere [2,4,5]. A brass tube 5.3 cm in diameter and 24 cm long attached to the movable short plate of the cavity allowed smoke generated during binder burn-out to exit the cavity into a fume hood. This avoided contamination of the cavity wall and allowed better monitoring of the specimen through a viewing port in the microwave cavity.

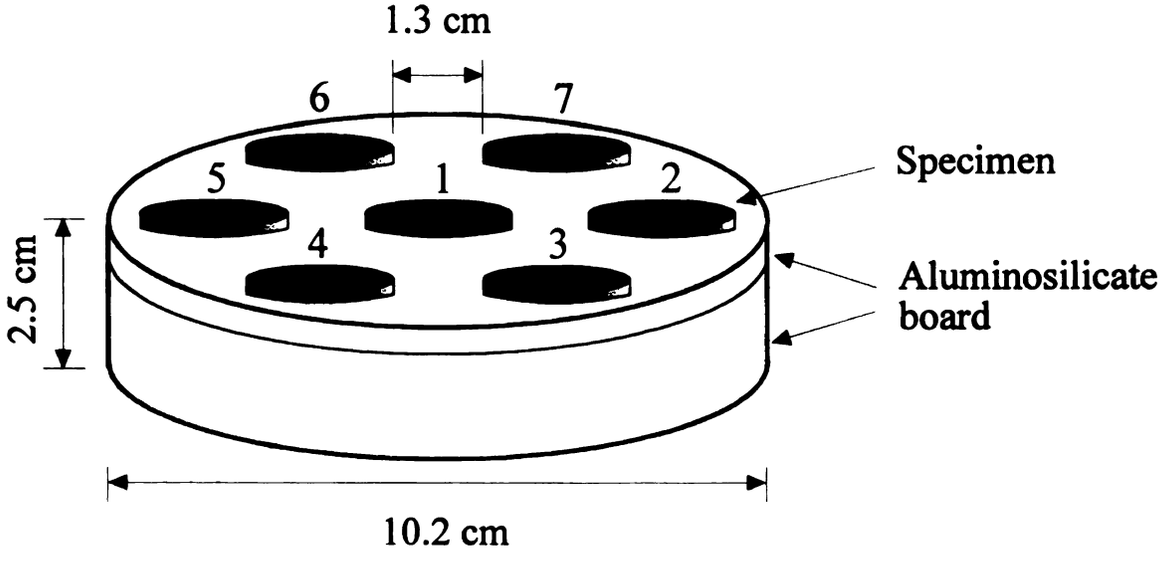

Figure 1. Schematic showing the setter material for binder burn-out and the seven positions for powder/binder compact specimens.

The batch-processed powder compacts were placed on disc-shaped SALI or SALI-2 aluminosilicate (Zircar Products, Inc.) refractory board setters (Figure 1). No further insulation was placed around the specimens, and the specimens were not enclosed in a "casket" of susceptor material.

Microwave power level was controlled by one of two protocols [2,3]: (1) fixed microwave power or (2) stepped microwave power. The fixed input power levels ranged from 50 Watts to 150 Watts depending on the material composition.

The stepped power procedure involved microwave power increments δP (where $\delta P \leq 50$ Watts) made at 5 to 15 minute intervals. For both the fixed power and the stepped power protocols, binder burn-out was monitored as a function of heating time (Figures 2 and 3) by heating a series of initially nominally identical powder/binder compacts for successively longer times. For example, for the Al_2O_3 compacts heated at a fixed input power of 80 Watts, a total of three batches of seven specimens each were heated (Figure 2).

The processing temperatures, measured via an optical pyrometer system (Accufiber Optical Fiber Thermometer, Model 10, Luxtron Co., Beaverton, OR), were obtained by sighting on the side of the central specimen when seven specimens were present or on the central region of the refractory setter disk when six specimens were present. (When six specimens were used, the central specimen was removed.) The pyrometer is capable of measuring temperatures ranging from 500°C to 1900°C with an accuracy of ± 2°C.

The persistent differential heating between the central specimen and six circumferential specimens lead us to attempt binder burn-out using only six specimens, omitting the central specimen. Each of the three types of powder compacts was heated

using six-specimen batches. Four sets each of Al_2O_3/binder and Al_2O_3/ZrO_2/binder specimens were heated by increasing the input power from 70 Watts to 460 Watts in increments of 10 to 20 Watts every 5 minutes. At an input power of about 300 Watts the center region of the setter began to heat above 500°C. Three batches of alumina/SiC/binder powder compacts (six specimens per batch) were heated using a stepped input power that was increased from 40 Watts to 250 Watts in increments of 10 or 20 Watts every 5 minutes.

In addition to the microwave heating, an electrical resistance furnace (Eurotherm Limited, England) was used for conventional heating and binder burn-out of seven alumina/SiC/binder compacts (Figure 3b). The furnace temperature was increased from room temperature to 545°C at a heating rate of 5°C/minute. In order to determine the weight % binder burn-out, one specimen was removed from the furnace every 15 minutes during conventional heating.

3. RESULTS AND DISCUSSION

During this batch processing study and the individual specimen burn-out study [2,3], the principal microwave parameters that were found to be important to binder burn-out are: (1) the electromagnetic cavity mode, (2) the magnitude of the microwave power, (3) the control of microwave power level (fixed or stepped input power) during the processing, and (4) the cavity "load", including the mass of material being processed and its dielectric nature.

3.1. Binder Removal using Fixed Input Power

For both individually [2,3] and batch processed powder compacts, the choice of electromagnetic mode can greatly affect the burn-out results. For each of the three types of ceramic compacts (Al_2O_3/binder, Al_2O_3/ZrO_2/binder, and Al_2O_3/SiC/ binder), the individually processed specimens [2,3] showed a maximum binder burn-out of only 0.6 wt% after heating at 100 to 150 Watts (fixed power) for 1 hour in TM_{012} mode. For the batch-processed specimens, the maximum binder burn-out was 1.4 ± 0.4 wt% in the TM_{012} mode at 150 Watts and a heating time of one hour. In contrast to the TM_{012} mode, we were able to achieve essentially complete binder burn-out using the TE_{112} mode. Therefore, the remainder of the experimentation performed in this study with both fixed and stepped power levels was done using the TE_{112} mode.

For low microwave input power (80 Watts, TE_{112} mode) the average percentages of the binder burned out after 60 minutes during batch processing were 22.6 wt% for the Al_2O_3/binder specimens, 20.9 wt% for Al_2O_3/ZrO_2/binder specimens, and 40.1 wt% for alumina/SiC/binder specimens (Figure 2). Each batch for each material included seven specimens, where the relative specimen locations are illustrated in Figure 1. In each case (Figure 2) little additional binder burns out during the elapsed time interval from 30 minutes to 60 minutes. The trends for the individually processed specimens are quite similar to the trends for the batch processed specimens, except that the overall binder burn-out is higher for the individually processed specimens than for the batch processed specimens (Figure 2). When the microwave input power was increased from 80 Watts to 150 Watts, the mean binder burn-out for a given batch increased by up to a factor of five.

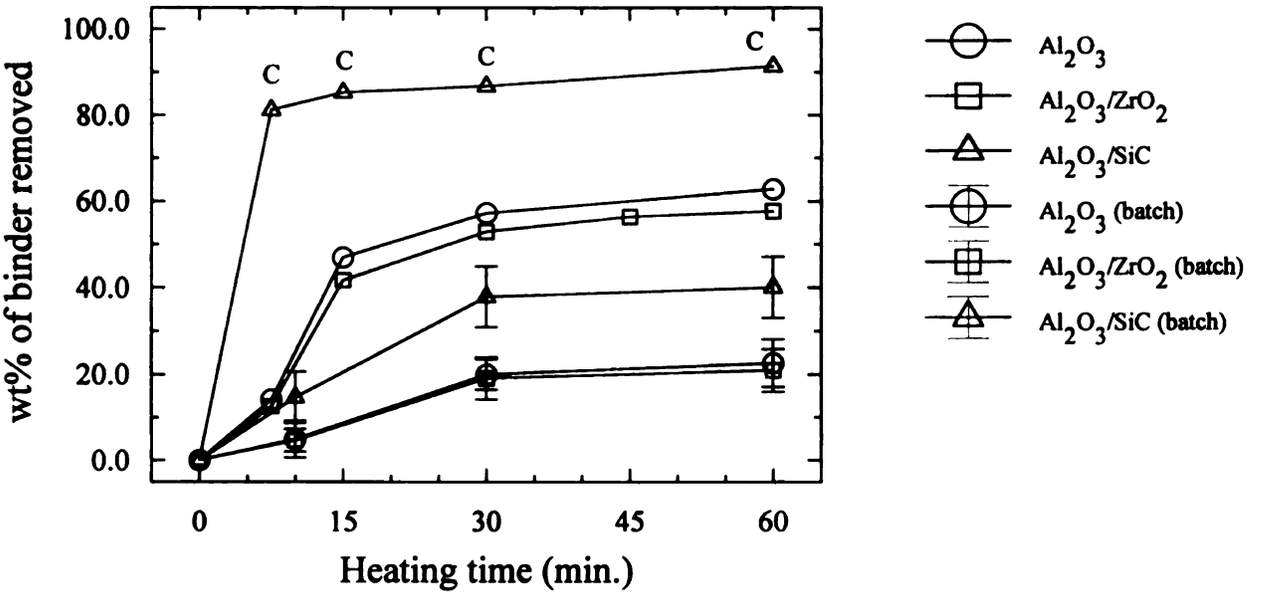

Figure 2. Wt% of binder removed as a function of heating time using 80 Watts fixed input power in TE_{112} mode for both singly-processed specimens [2,3] and batch-processed specimens. The symbol 'C' denotes that the specimen cracked.

The extent of binder burn-out is similar for the alumina/binder and the alumina/zirconia/binder systems (Figures 2 and 3a). The low temperature (monoclinic) form of zirconia is not a susceptor, while the high temperature (above about 1000°C) tetragonal form of zirconia is a susceptor material [6]. Since binder removal is mostly done below 800°C, zirconia does not aid binder removal.

3.2. Binder Removal using Stepped Input Power

Using a stepped input power sequence, five batches of alumina/SiC/binder were heated (7 specimens per batch) using SALI refractory board setters. At about 150 Watts the setter temperature rapidly rose to about 600 to 700°C. Typically the center specimen and three to four of the other six specimens cracked during binder burn-out.

Due to the local melting, the SALI refractory board was replaced with a SALI-2 refractory board, which has higher temperature capabilities. Using SALI-2, five batches of alumina/zirconia/binder compacts (with 7 specimens per batch) were heated using stepped input power. For the two experimental runs for which the final input power was ≥ 240 Watts, the central region of the setter heated above 500°C and the central specimen cracked. For the central specimen nearly all of the binder burned out, while only about 68 wt% of the binder burned out from the other circumferential specimens (Figure 1). However, in the stepped-power experimentation on each of the three types of ceramic compacts, when the center specimen was removed and the SALI-2 refractory was used, we were able to achieve nearly complete binder burn-out without cracking the specimens (Figure 3), in contrast to the partial burn-out achieved for fixed input power (Figure 2).

Although the microwave heating burned out the binder immediately after the power was applied, the conventional heating did not burn out the binder until the temperature reached about 175°C at heating time of 30 minutes (Figure 3b). At 545°C, about 90 wt% of the binder was removed by the conventional heating, while the microwave heating burned out about 95 wt% of the binder at 250 Watts.

Although in this study, no "casket" of susceptor material surrounded the specimens, the authors have successfully removed corn oil binder in a one-step process in which the binder was burned out in a casket, then the microwave power was increased and the specimens were sintered [2]. Also, batch-sintering alumina specimens using a casket and the same microwave cavity as in this study resulted in specimens of relatively uniform grain size, mass density, fracture toughness, and hardness [7]. Especially at high

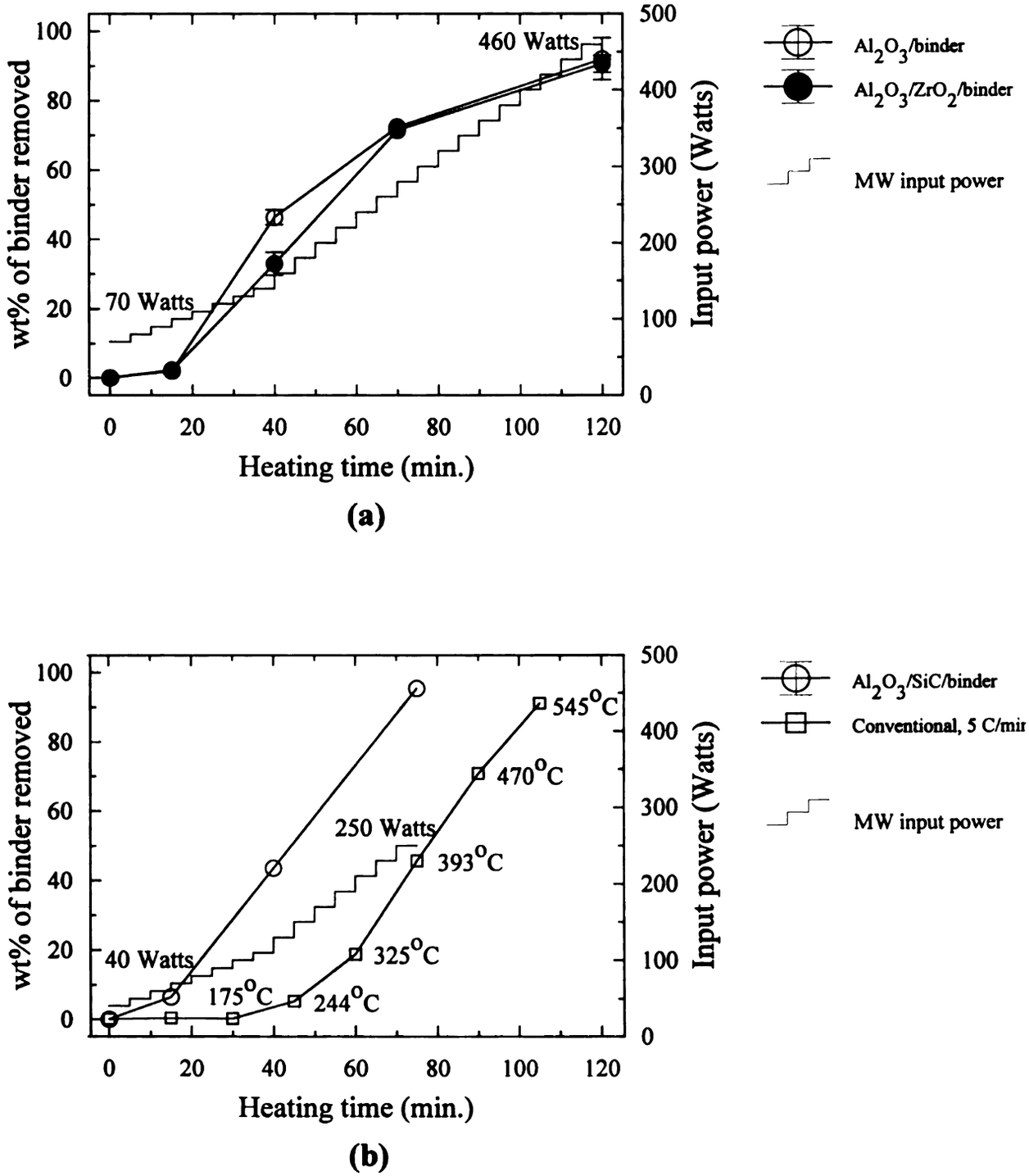

Figure 3. For a stepped input power sequence, average fraction of the binder removed in wt% for six-specimen batches as a function of power and heating time for (a) Al_2O_3/binder and Al_2O_3/ZrO_2 binder specimens and (b) for Al_2O_3/SiC/binder specimens. For those data points without error bars, the symbol size exceeds the standard deviation. Figure (b) also includes data for Al_2O_3/SiC/binder specimens for which the binder was removed by conventional heating.

temperatures, the radiant heating and insulating qualities of the casket likely reduce temperature gradients. However, an advantage of not using a refractory casket for binder removal may be related to the level of residual carbon in the specimens after binder burn-out. Moore et al. [8] found that for removal of polymethly methacrylate binder from alumina compacts, there was 2 to 3 times more residual carbon in the microwave heated specimens than in conventionally heated specimens. Moore et al. attributed the differences in residual carbon to the oxygen-poor environment within the insulating casket that enclosed the specimens [8]. Thus, binder removal without the use of microwave casket may lead to more complete burn-out.

4. CONCLUSIONS

For both the singly processed specimens [2,3] and the batch processed specimens, the extent of binder burn-out can vary widely with the electromagnetic mode. For example, heating via the TM_{012} mode resulted in very little binder burn-out, while in comparison, nearly complete binder burn-out was achieved in the TE_{112} mode (Figures 2-3).

For both the individually-processed specimens [2,3] and the batch-processed specimens (this study), a stepped input power sequence burned out the binder more completely than a fixed input power without cracking the specimens. Among the three types of ceramic compacts processed (Al_2O_3/ZrO_2 composites, Al_2O_3/SiC platelet composites, and Al_2O_3) the binder burned out at lower power for the Al_2O_3/SiC platelet specimens, under both fixed and stepped power conditions. This may have been due to differing dielectric properties of the specimens.

For a given batch, the centrally-located specimens exhibited the most complete binder burn-out. Thermally-sensitive paper indicated that (for low powers) the highest temperatures on the specimen setter were at the central-specimen position, which agrees with the binder burn-out results for low power (80 Watt) and higher power (440 Watt) binder burn-out. Thus the temperatures (and likely the electromagnetic fields) were highest along the cavity axis.

In this batch-processing study, no microwave casket enclosed the specimens (Figure 1). Future work should directly compare the residual carbon left in specimens as a function of processing temperature for binder burn-out with and without a microwave casket enclosing the specimens.

ACKNOWLEDGEMENTS

The authors acknowledge the financial support of the Michigan Research Excellence Fund provided through the Electronic and Surface Properties of Materials Center, Michigan State University.

REFERENCES

1. D.W. Richerson, Modern Ceramic Engineering, 2nd edition, p. 496-497, Marcel Dekker, Inc., New York (1992).

2. K.Y. Lee, E.D. Case, J. Asmussen, Jr., and M. Siegel, Proc. 11th ESD Advanced Composites Conf., Ann Arbor, MI, pp.491-503 (1995).

3. K.Y. Lee, E.D. Case and J. Asmussen, Scripta Mat., 35[1]: 107-111 (1996).

4. K.Y. Lee, E.D. Case, J. Asmussen, Jr., and M. Siegel, Cer. Trans., Vol. 59, Amer. Cer. Soc., Columbus, OH, pp. 473-480 (1995).

5. J. Asmussen and R. Garard, Mat. Res. Soc. Proc. 124: 347-352 (1988).

6. P. S. Apte, R. M. Kimber, A. Pant, R. Roy, D. N. Mitchell, United States Patent 5,072,087, December 10 (1991).

7. K. Y. Lee, L. Cropsey, B. Tyszka, and E. D. Case, accepted for publication, Materials Research Bulletin.

8. E. H. Moore, D. E. Clark, and R. Hutcheon, Mat. Res. Soc. Symp. Proc., 269: 341-346 (1992).

CHAPTER 3

JOINING

Part I. MICROWAVE JOINING AND REPAIR OF CERAMICS AND CERAMIC COMPOSITES[1]

1. INTRODUCTION

The application of ceramics and ceramic composites is limited in part by the difficulty in processing components with complex geometries. However, the processing difficulties could be reduced considerably if the components were formed from subcomponents of simpler geometries. This paper first briefly overviews some ceramic joining techniques and then discusses work done on microwave joining of ceramics. Although ceramics may be joined as green (unfired) billets [1], both literature review (Section 2) and the experimental results of this paper will deal with joining of densified ceramics. Also, to address the repair of ceramics, this study includes experimentation on the healing of Vickers indentation cracks via microwave heating.

[1] Ki-Yong Lee, Eldon D. Case, and Donnie Reinhard, Ceramic Engineering and Science Proceedings, vol. 18, no. 4, pp. 543-550 (1997).

2. CERAMIC-CERAMIC JOINING: BACKGROUND

2.1. Ceramic-Ceramic Joining using conventional heating

Various researchers have utilized brazing techniques for ceramic-ceramic joining. In the metallurgical context, brazing is defined as "a joining process in which a filler metal and a flux are sandwiched between the workpieces" [2]. Subsequent heating of the component converts the filler metal/flux system into a liquid that wets the joined surfaces. Ceramic-ceramic joining via brazing uses oxide and oxynitride glasses as bonding media as well as slurries of metal particles or metal layers between the ceramic pieces to be joined [3]. Using zero applied stress, oxide glasses can bond alumina [4,5] and oxynitride glasses can join silicon nitride [6]. However, the glass layer formed during such joining leads to relatively low fracture toughness and poor high temperature properties for the joined component [3,5] since the glass layers themselves tend to have low fracture toughness and soften at elevated temperatures.

Sandage et al. used Ba-Al-Si metal tape, 200 microns thick, to join 1.0 cm x 0.5 cm mullite plates [3]. Heating at 1230°C in air for 5 hours oxidized the Ba-Al-Si metallic tape, converting it to a $BaAl_2Si_2O_8$-rich layer that also contained crystalline alumina, mullite, barium aluminate, and a glassy aluminosilicate phase [3].

Diffusion bonding joins materials at high temperatures and pressures, ideally via solid state diffusion of atoms across the joined interface, although interlayers can be added which promote local melting and hence enhance the mass diffusion rates [3,7]. Diffusion bonding is enhanced when the stresses and temperature are high enough to induce creep [8,9].

2.2. Ceramic-Ceramic Joining via microwave processing

Ceramic/ceramic joining via microwave heating has been done for simple cross-sectional geometries including bars [10], rods [11], discs [12], and tubes [13]. Applied external loads have ranged from about 0.6 MPa to 9.0 MPa for joining mullite, alumina, and silicon nitride [13], to 3 MPa for alumina (in air) and silicon nitride (in nitrogen gas) [11], to no external load for plasma sprayed Si coated SiC disks [13].

When ceramic-ceramic joining is done without the use of an interlayer, the bonding typically takes place via an intergranular glassy layer already present in the ceramic; such intergranular phases can become viscous at elevated temperatures [11,13]. As an example of the role of intergranular phases in microwave joining, Fukushima et al. [11] joined alumina with 92 to 96 percent purity using microwave heating, but failed to directly join specimens of 99 percent alumina, although inserting a sheet of the lower purity alumina between the 99 percent purity alumina components gave a successful bond.

3. EXPERIMENTAL PROCEDURE

3.1. Materials and Specimen Preparation

Two materials (sintered polycrystalline alumina and a commercial mica platelet reinforced glass ceramic) were used in the joining experiments. Coors ADS-995, a commercial polycrystalline alumina, was used for the Vickers indentation crack healing experiments.

The flurophlogopite mica platelet reinforced glass ceramic used was MaCor™, a machinable glass ceramic (Corning Code 9658) in the system SiO_2-Al_2O_3-MgO-K_2O-F. As

received MaCor billets 7.8 cm x 7.8 cm x 0.18 cm were sectioned into specimens roughly 1 cm X 2 cm using a low speed diamond saw and polished prior to joining.

Sumitomo AKP50 powder alumina discs were uniaxially hard-die pressed at 32 MPa, giving powder compacts about 22 mm in diameter and about 2 mm thick, weighing about 2.0 gm. The alumina discs were sintered using a 2.45 GHz single-mode microwave cavity with an automated sliding short and launch probe position controls [14]. Seven alumina powder compacts were sintered simultaneously at 1500°C for 20 minutes in a zirconia refractory casket using the TM_{111} cavity mode. After sintering, the alumina disks were polished with a series of grit sizes, ending with 1 micron diamond paste.

3.2. Microwave Joining and Crack Healing

After polishing, both the alumina and the glass ceramic specimens were coated with silica film (Emulsitone Company, Whippany, New Jersey) by spinning on a substrate spinner at 3000 rpm for 20 seconds. The coatings were then cured by two methods: (1) heating in a conventional furnace for 1 hour at 200°C or (2) heating in the microwave cavity at low power.

The coated specimens were joined in the microwave cavity using a zirconia casket and the TM_{111} microwave cavity mode with a stepped input power sequence typically starting at 100 Watts and increasing to about 1200 Watts in steps of 100 Watts every 3 minutes. During both the sintering (Section 3.1) and joining, the specimen temperatures were measured via an optical pyrometer system (Accufiber Optical Fiber Thermometer, Model 10, Luxtron Co., Beaverton, OR). The pyrometer is capable of measuring temperatures ranging from 500°C to 1900°C with an accuracy of ± 2°C.

The joined specimens were sectioned and polished, with the cuts oriented normal to the specimen interface. The polished surfaces were examined both by optical microscopy and scanning electron microscopy.

4. RESULTS AND DISCUSSION

The as-microwave-sintered AKP-50 alumina disks had a mean mass density of about 99% of theoretical and a mean grain size of about 6.3 microns. Alumina discs joined at 1625°C had a mean grain size of 16.4 microns (Figure 1).

For the AKP-50 alumina specimens, the crack path near the joint was determined since crack deflections at an interface can indicate the relative magnitude of the interfacial fracture energy compared to the matrix fracture energy [15]. As reviewed by Lee et al. [15], crack deflection at interfaces can occur for interfacial fracture energies < 0.25 the matrix fracture energy [15]. If defects located at the interface extend before the primary crack reaches the interface, then a crack approaching the interface will deflect if the interfacial fracture energy is less than about 60 percent of the matrix fracture energy [15]. Three joined AKP-50 alumina specimens were selected for Vickers indentation, in which a series of 49 N and 98 N indentation cracks were placed across the specimen surface, where the radial crack systems were oriented approximately normal to the joined interface. Except when a series of pores were present at the interface, the indentation cracks were undeflected at the joint, indicating a strong interface.

One of the joined alumina specimens (with an as-joined thickness of 4.2 mm) was fractured by loading in bend. SEM examination of the joined region of the fractured specimen shows no evidence of cracking or microcracking near the joint (Figure 1); thus the

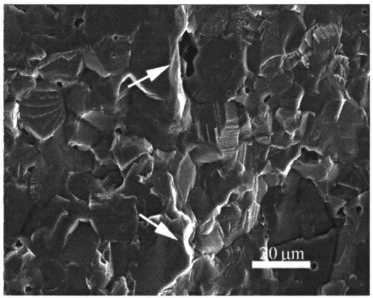

Figure 1. SEM micrograph of fracture surface of alumina discs joined at 1625°C for 10 minutes. Arrows indicate the joined interface.

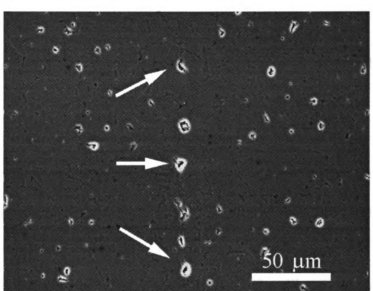

Figure 2. SEM micrograph of polished surface of joined alumina discs heated at 1625°C for 10 minutes. Arrows indicate the joined interface.

macrocrack that fractured the specimen apparently did not damage the joint, again indicating a very strong interface. Also, the grain structure near the joint does not differ from the grain structure in the bulk of the specimen (Figure 1), indicating that the process of generating the joint does not greatly perturb the specimen's microstructure, at least on a micron-size scale. Future research should include a detailed TEM examination of the joint to analyze the phases present.

Polished surfaces of the alumina-alumina joint region also show the continuity of the microstructure (Figures 2 and 3, where arrows included in the micrographs mark position of the interface). An elemental map generated by the SEM EDS facility shows a homogeneous distribution of aluminum ions through the joined region (Figure 4).

The region of the joint covered by the elemental map of aluminum ions in Figure 4 is identical to the area shown in Figure 3. An x-ray line scan across the joint also shows a constant concentration of alumina ions across the joint.

For the coated and joined AKP-50 alumina specimens, the nature of the joint is related to the silica-alumina phase diagram. For alumina fractions below about 60 mole percent, the silica-alumina equilibrium phase diagram has an eutectic at 1587°C ± 10°C. Between about 15 and 60 mole percent alumina, mullite and a 95% silica-5% alumina liquid are the equilibrium phases from the eutectic temperature up to about 1800°C. For the temperatures at which joining was successful (1605 to 1665°C), the silica and alumina should react, and as the reaction continues, the alumina/silica ratio should increase and shift the equilibrium to the alumina-mullite side of the phase diagram [17]. The siliceous liquid present is likely very viscous in the joining temperature range, which might aid the joining process by helping to hold the opposing faces together.

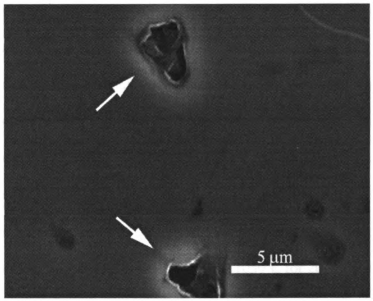

Figure 3. SEM micrograph of polished surface of joined alumina discs heated at 1625°C for 10 minutes. Arrows indicate the joined interface.

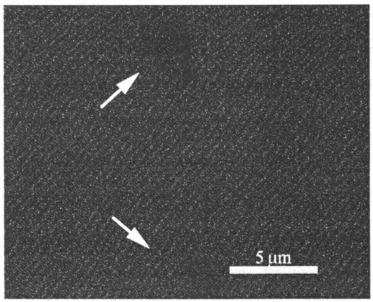

Figure 4. An elemental map showing the position of aluminum ions near the joint for joined alumina discs.

Polished and coated pairs of MaCor™ specimens failed to join when microwave-heated for 20 minutes at temperatures of 1000°C and 1025°C. Additional polished and coated specimens partly joined when heated at 1075°C for 20 minutes and for one hour. Polished and uncoated specimens were heated together with the joined specimens at temperatures between 1000°C and 1075°C but the uncoated MaCor™ specimens did not join during microwave heating. Coated and polished specimens joined at 1150°C but the MaCor™ specimens warped at that temperature (the maximum recommended working temperature for MaCor™ is 1000°C). A pair of specimens with coated but as-received (unpolished) surfaces joined weakly when heated at 1050°C for 20 minutes.

In addition to the joining experiments, a 1 cm x 1 cm square of polished Coors ADS-995 polycrystalline alumina was indented at 49 Newtons and 98 Newtons using a Vickers indenter. The indented specimen was aged for 48 hours in laboratory air to stabilize against slow crack growth, then the specimen was heated in the microwave
cavity for 1 hour at 1500°C. Both the 98 Newton cracks (12 radial cracks) and 48 Newton indents (6 radial cracks) healed completely, leaving only the indent impression to mark to indent locations (Figure 5). In contrast, for conventional heating of 48 Newton Vickers indents in ADS-995 under the same conditions (one hour at 1500°C), the change in relative crack length was only 45.4% ± 7.9% for six radial cracks [16].

5. CONCLUSIONS

While nearly all of the ceramic-ceramic joining described in the literature involves externally applied pressure, the present research involves only ambient pressure. Microwave-sintered alumina discs were polished, coated with a silica film, and joined using

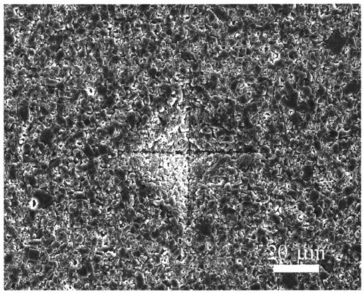

Figure 5. Micrograph showing Vickers indentation impression for 98 Newton Vickers indent, microwave-heated at 1500°C for 1 hour. Radial cracks have healed.

microwave heating at temperatures between about 1605°C and 1665°C. Under SEM examination, the best joints were essentially indistinguishable from the bulk material, except for occasional small pores. Specimens of a mica platelet reinforced glass ceramic composite also were polished, coated, and joined at 1075°C.

In order to explore the repair of ceramic components, Vickers indentation cracks were placed in polished surfaces of Coors ADS-995 polycrystalline alumina (no coating was applied to the indented surfaces). The dramatic healing observed in the indentation crack healing experiment likely indicates an enhanced mass diffusivity, either via the "microwave effect" or possibly by intense local heating caused by the interaction of the microwave fields and the "air gap" formed by the crack. Due to the microscopic scale of the crack opening displacement, the pyrometer used to measure the specimen temperature would likely be

insensitive to such local heating. This phenomena and its origins merits further study, since during both joining and repair of ceramics, small air gaps would occur at the interface.

ACKNOWLEDGEMENTS

Funding was provided by the Electronic and Surface Properties of Materials Center and Composite Materials and Structure Center, Michigan State University.

REFERENCES

1. C. H. Bates, M. R. Foley, G. A. Rossi, G. J. Sundberg, and F.J. Wu, Amer. Ceram. Soc. Bull., 69[3]: 350-56, 1990.

2. J. P. Schaffer, A. Saxena, S. D. Antolovich, T. H. Sanders, Jr., and S. B. Waner, pp. 718-720 in The Science and Design of Engineering Materials, Irwin Press, Chicago, 1995.

3. K. H. Sandhage, H. J. Schmutzler, R. Wheeler, and H. L. Fraser, J. Am. Ceram. Soc., 79[7]: 1839-1850, 1996.

4. A. J. Moorhead, Adv. Ceram. Mater., 2:159-166, 1987.

5. W. A. Zdaniewski, P. M. Shah, and H. P. Kirchner, Adv. Ceram. Mater., 2: 204-208, 1987.

6. M. L. McCartney, R. Sinclair, and R. E. Loehman, J. Amer. Ceram. Soc., 68: 472-488, 1985.

7. M. Santella, Am. Ceram. Soc. Bull., 71:947-54, 1992.

8. G. Elssner, W. Diem, and J. S. Wallace, pp. 629-639 in Surfaces and Interfaces in Ceramic and Ceramic-Metal Systems, Edited by J. Pask and A. G. Evans, Plenum Press, New York, 1981.

9. W. D. Kingery, H. K. Bowen, and D. R. Uhlmann, pp. 744-54, Introduction to Ceramics, Second Ed., Wiley, New York, 1976.

10. J. C. Xiao-ming, L.-W. Zhang, X. Li, Y. Tian, T. Chen, and J. Guo, J. Am. Ceram. Soc.,77: 1090-1092, 1994.

11. H. Fukushima, T. Yamanaka, and Matsui, J. Mater. Res., 5[2]: 397-405, 1990.

12. D. Palaith and R. Silberglitt, Ceramic Bulletin, 68 [9]: 1601-1606, 1989.

13. R. Silberglitt, D. Palaith, W. M. Black, H. S. Sa'adaldin, J. D. Katz and R. D. Blake, Ceram. Trans., **21**: 473-480, Amer. Ceram. Soc., Columbus, OH, 1991.

14. K.Y. Lee, E.D. Case, J. Asmussen, Jr., and M. Siegel, Scripta Mat. 107-111, 1996.

15. W. Lee, S. J. Howard, and W. J. Clegg, Acta Mater. 44[10]: 3905-3922, 1996.

16. B. A. Wilson and E. D. Case, unpublished data

17. Pages 304-307 in reference 9.

Part II. MICROWAVE AND CONVENTIONAL JOINING OF CERAMIC COMPOSITES USING SPIN-ON MATERIALS[2]

ABSTRACT

Polycrystalline alumina, glass ceramic composites reinforced by mica platelets (MaCor™), and alumina/zirconia composites were joined using a commercial spin-on material which is also used as a passivation layer in semiconductor processing. The film thickness was controlled by varying spin speed, spin time, and temperature for heat treatment. Curing a coated specimen at 200°C produced a film thickness ranging from about 0.2 micron to about 0.6 micron. Joining was performed in both a conventional electrical resistance furnace and a single-mode 2.45 GHz cylindrical microwave cavity. Effects of film thickness, joining temperature, and heating time on the joining of the materials will be discussed.

1. INTRODUCTION

Ceramic components with complex geometric shapes are difficult to process. Intricately shaped components are of interest in high temperature heat exchanger and engine applications. Complex structures, however, can be fashioned by joining ceramic components of simpler shape. Joining simpler ceramic subcomponents assists quality control as well, by allowing flawed subcomponents to be rejected prior to joining.

Using conventional (radiant) heating, ceramic components have been brazed via oxide

[2] Kiersten N. Seiber, Ki-Yong Lee, and Eldon D. Case, Proceedings of the 12th Annual Meeting of the American Society for Composites, pp. 941-949 (1997).

or oxinitride glasses, slurries of metal particles, and metal layers (Sandage et al., 1996). Oxide glasses have been shown to join alumina (Moorhead, 1987; Zdaniewski, Shah, and Kirchner, 1987) and oxinitride glasses have been used to join silicon nitride (MeCartney, Sinclair, and Loehman, 1985). Diffusion bonding has also been utilized to join ceramic components under high applied pressures and temperatures (Santella, 1992).

Ceramic-ceramic joining using the microwave system typically involves externally applied pressures. An applied load of 3 MPa has been utilized to join alumina (in air) and silicon nitride (in nitrogen gas) (Silberglitt et al., 1991), while loads ranging from 0.6 MPa to 9 MPa have been used to join alumina, mullite, and silicon nitride. (Fukushima,Yamanaka, and Matsui, 1990). The objectives of this study were to 1) join the subcomponents with the use of a spin-on film and 2) to use ambient or low externally applied pressures in the joining process. A low external pressure, provided by dead weight loading, avoided the use of loading systems (such as those using a piston and load cell) which can be awkward and interfere with the microwave fields. In this study, a total of 15 pairs of MaCor™ specimens, five pairs of alumina specimens and 1 pair of alumina/zirconia composite specimens were joined.

2. EXPERIMENTAL PROCEDURE

MaCor™, polycrystalline alumina specimens, and alumina/zirconia particulate composite specimens were joined in this study. MaCor™ is a machineable glass ceramic reinforced by mica platelets (Corning code 9658). The MaCor™ specimens were cut from as received billets of the material into 1 cm x 1 cm components using a low speed diamond saw.

To fabricate the alumina specimens, about 2 grams of alumina powder was hard-die pressed at about 32 GPa from Sumitomo AKP-30 powders, resulting in a disc-shaped powder compact of about 2.2 cm diameter and 2 mm thick. The specimens were sintered at 1550°C for 20 minutes using a 2.45 GHz single-mode microwave cavity (Lee et al., 1996; Lee, Case, and Reinhard, 1997; Lee, Case, and Asmussen, 1997). The average grain size of the sintered alumina specimens was about 8.6 μm after multiplying the average intercept size by a stereographic factor of 1.5 (Fullman, 1953). The density determined by Archimedes technique was about 3.806 g/cm^3, which is about 95% of theoretical density of alumina (National Bureau of Standards, 1959).

For alumina/zirconia particulate composite specimens, AKP30 alumina powder was mixed with 15wt% of zirconia powder (Fisher Scientific Co.). The mixture was ball-milled with alumina grinding media in a plastic container for 48 hours.

Approximately 2 grams of the Al_2O_3/15wt% ZrO_2 powder mixture (pressed using conditions identical to those used for the alumina compacts) was sintered at 1550°C for 20 minutes in the microwave cavity.

Using an automatic polisher (LECO Corporation, St. Joseph, MI), alumina and alumina/zirconia particulate specimens were polished using a series of grits; 25, 17, 10, 6 and 1 μm diamond paste. MaCor™ specimens were polished using 17, 10, and 1 μm diamond paste. After polishing, selected specimens of MaCor™, alumina, and alumina/zirconia were coated with silica film by placing ten drops of the silica film (Silicafilm, Emulsitone Co., Whippany, NJ) onto the specimens and spinning the specimens on a substrate spinner. The specimens were spun for 20 minutes at spinning rates ranging

from 500 rpm to 2000 rpm. Curing the film in a conventional oven for 20 minutes at 200°C yielded a high purity silica coating.

Notches were made in five MaCor™ specimens and four alumina specimens with a stationary sonic mill (Sonic-Mill, Rio Grande Jewelers Supply Inc., Albuquerque, NM). A razor blade tool was made by silver soldering a commercial razor blade to a standard flat sonic-mill screw. The sonic mill vibrated the razor blade tool in a slurry of boron carbide particles, which in turn vibrated the boron carbide particles contacting the razor blade tool. The specimen was cut (notched) by the vibration of the boron carbide media itself.

A portion of the specimen containing the notch was then sectioned and reserved for scanning electron microscope (SEM) analysis, in order to examine the notch prior to joining (Figure 1). The remaining section was used in the joining experiment.

Microwave heating was done in a single-mode, 2.45 GHz microwave cavity using the TM_{111} mode (Lee et al., 1996; Lee, Case, and Reinhard, 1997; Lee, Case, and Asmussen, 1997).

The specimens were positioned in a refractory casket (Figure 2) that was centered along the microwave cavity axis. The refractory casket acted as a thermal insulator that coupled well with the microwaves at low temperatures. Sintered alumina discs about 4 grams (approximately 1.8 cm in diameter and 4 mm thick) and 20 grams (approximately 4.1 cm in diameter and 4 mm thick) were used as dead weights (Figure 2). A total of 0 to 60 grams of dead weight was applied to the specimens. The microwave input power, initially set at 100 Watts, was increased by 100 Watts every 3 minutes until the desired temperature was reached, providing a heating rate of approximately 40°C/min. The temperature in the microwave system was measured

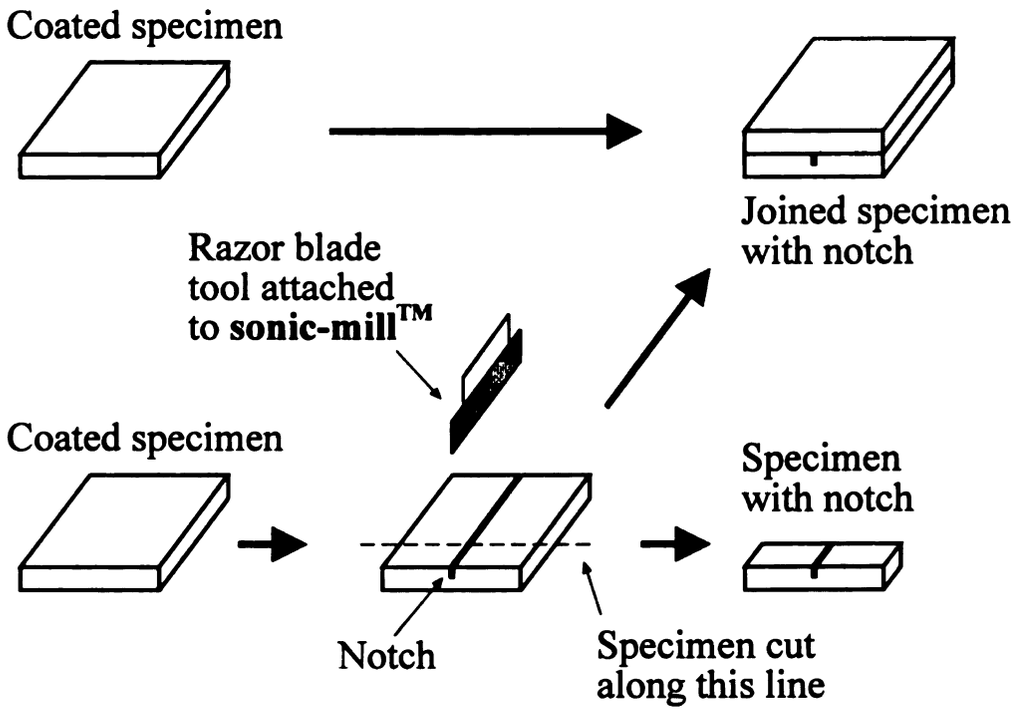

Figure 1. Schematic showing notched specimen preparation.

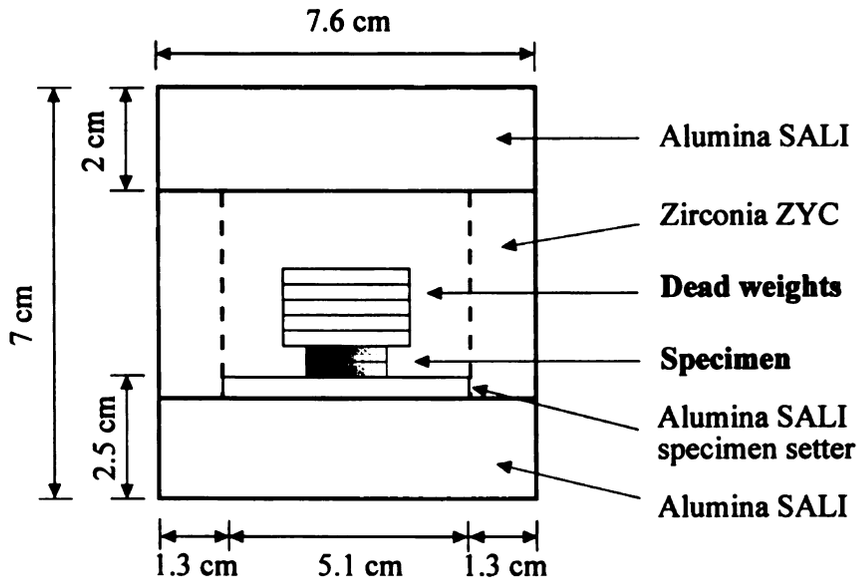

Figure 2. Schematic for refractory casket used for microwave heating, showing dead weights placed on the specimen for joining.

using an optical pyrometer (Accufiber Optical Fiber Thermometer, Model 10, Luxtron Co., Beaverton, OR).

Conventional heating was performed using an electric box furnace (C·M Inc.) with $MoSi_2$ heating elements. The specimens to be joined were placed on an alumina (Coors high alumina) setter and covered with an inverted cylindrical alumina crucible (Coors high alumina) 60 mm in height, 10 mm in diameter, and a wall thickness of 1 mm. The temperature was sensed by a K-type thermocouple placed in contact with the crucible. The heating rate was approximately 30-40°C/min. The crucible protected the specimens from contamination by material from the furnace elements and insulation.

3. RESULTS AND DISCUSSION

Four MaCor™ specimens and four alumina specimens were coated using spinning rates between 500 rpm and 2000 rpm. The specimens were then cured at 200°C for 20 minutes. The silica film thickness was a function of the spinning rate, such that the coating thickness decreased with increasing spinning rate (Figures 3 and 4, Table I). For example, an alumina specimen spun at 500 rpm had a coating thickness of approximately 0.61 microns (Figure 3a), while another alumina specimen spun at 2000 rpm had a coating thickness of about 0.20 microns (Figure 3b). Over the range of spinning rates used in this study, the as-cured silica film thicknesses for the MaCor™ and alumina specimens agreed to within ± 9% (TABLE I).

Ten pairs of MaCor™ specimens were joined in the microwave cavity using 20 gram dead weight loading at temperatures of 1050°C and 1075°C with an approximate joining

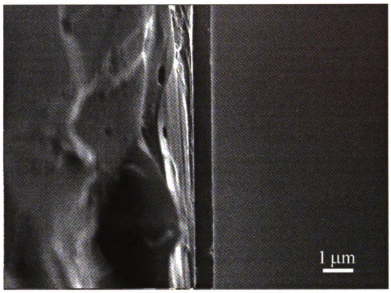

(a)

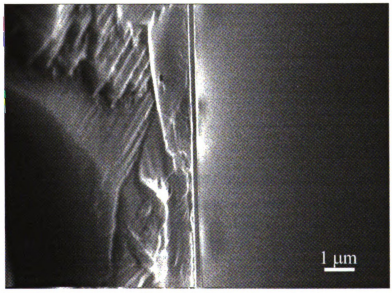

(b)

Figure 3. SEM images of silica film spun on alumina specimens at (a) 500 rpm and (b) 2000 rpm.

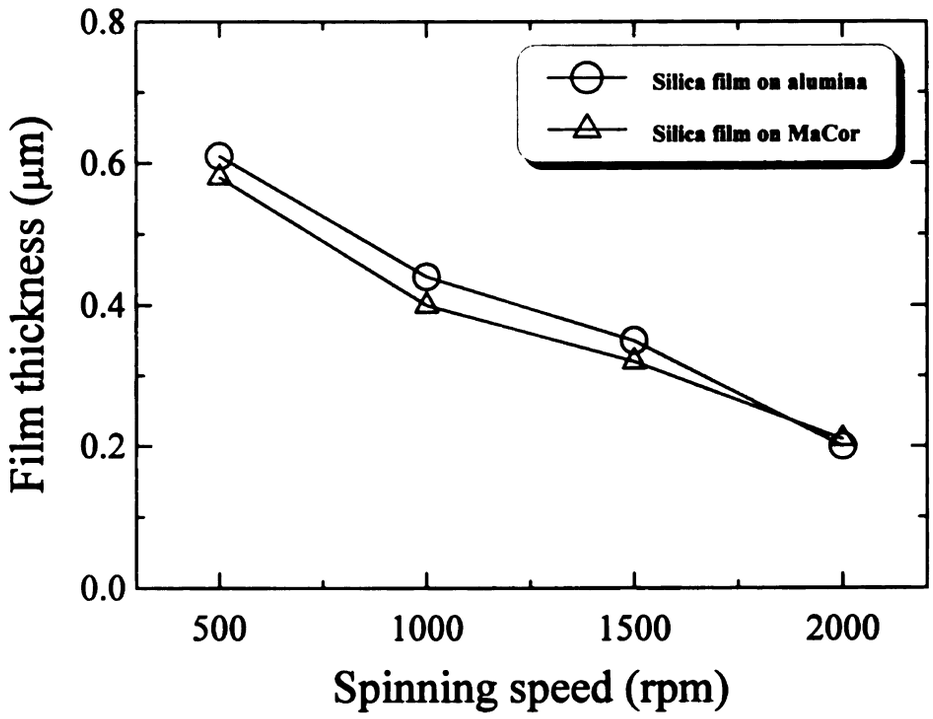

Figure 4. Silica film thickness as a function of spinning speed.

Table I. Thickness of the as-cured silica film as a function of spinning speed.

Spinning speed	500 rpm	1000 rpm	1500 rpm	2000 rpm
Silica film on alumina (μm)	0.61	0.44	0.35	0.20
Silica film on MaCor™ (μm)	0.58	0.40	0.32	0.21

time of 20 minutes. Conventionally, five pairs of MaCor™ specimens were joined at 1050°C with no externally applied load and with 20 gram dead weight loading, using an approximate joining time of 20 minutes. Initial results indicated that heating times shorter than 20 minutes may not be sufficient to join MaCor™ specimens. For example, one pair of MaCor™ specimens was tested with a joining temperature of 1050°C, a joining time of 10 minutes, and a 20 gram dead weight loading. The 10 minute heating time failed to join the MaCor™ specimens.

The width and depth of notches in the MaCor™ specimens changed by less than 5.7 percent during joining (Figure 5, Table II), while for the alumina specimens the notch width and depth changed by less than 4.1 percent (Figure 6, Table II). Note that the dimensional stability observed for the notch geometries holds for a range of notch sizes (Table II).

For five alumina and for five MaCor™ specimens, the fraction of the interface that included pores was evaluated by SEM observations, where F_P is defined as

$$F_P = \frac{\text{total length of porous regions along specimen interface}}{\text{total length of specimen interface}} \qquad (1)$$

The fraction of F_P is a function of the silica film thickness (Figure 7) for both the MaCor™ and alumina specimens. However, the functional dependence of F_P is quite different for alumina and MaCor™ specimens (Figure 7). One pair of microwave heated, polished, and coated MaCor™ specimens was compared to a conventionally heated, polished and coated MaCor™ specimen. Both the microwave and the conventionally heated specimens were processed at a maximum temperature of 1050°C for 20 minutes, with a 20 gram dead-weight

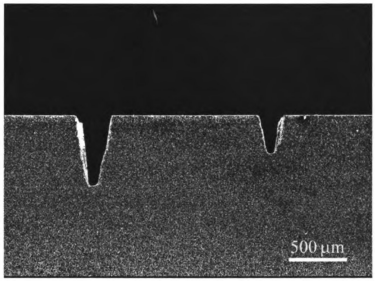

(a)

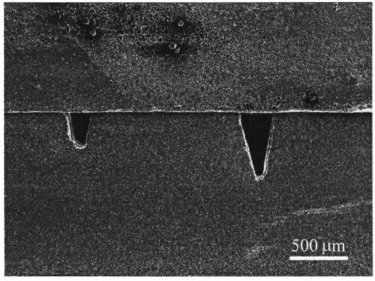

(b)

Figure 5. SEM images of notch made in MaCor™ specimen (a) before and (b) after joining.

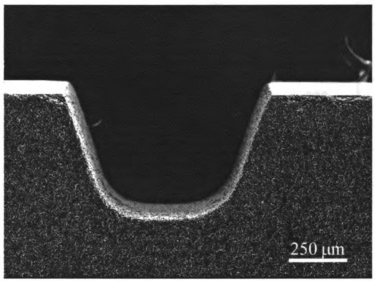

(a)

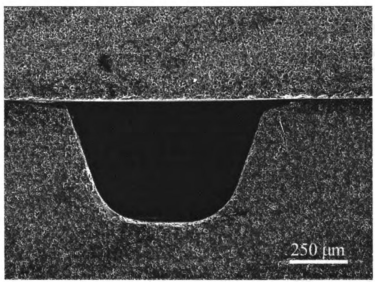

(b)

Figure 6. SEM images of notch made in alumina specimen (a) before and (b) after joining.

Table II. Dimensions of notches before joining and after joining.

Material	MaCor™				Alumina	
Dimension	Depth (μm)	Width (μm)	Depth (μm)	Width (μm)	Depth (μm)	Width (μm)
Before joining	619	321	331	228	531	907
After joining	585	312	314	215	528	870
% difference	-5.5	-2.8	-5.1	-5.7	-0.6	-4.1

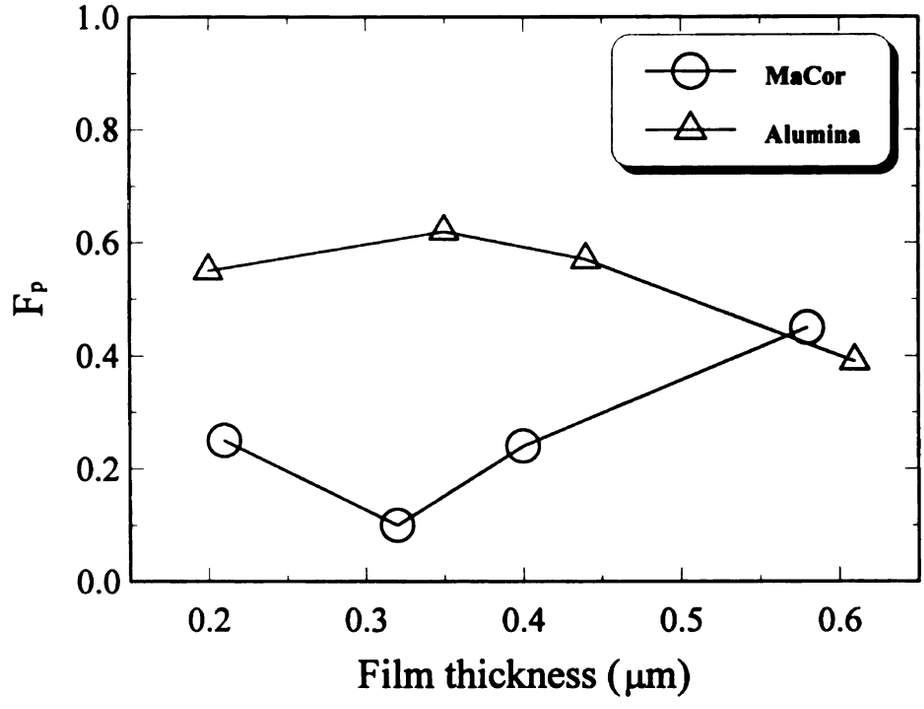

Figure 7. Total fraction of pores along the joint interface in joined MaCor™ and alumina specimens as a function of film thickness.

load. The coatings for both specimens were spun at 2000 rpm and cured for 20 minutes at 200°C. The F_P values were 0.14 and 0.25 for the conventional and microwave heated specimens, respectively.

4. SUMMARY AND CONCLUSIONS

A total of five pairs of alumina specimens, fifteen pairs of MaCor™ specimens and one pair alumina/zirconia particulate composite specimens were successfully joined with low externally applied pressure. The joining temperature for alumina was 1575°C with a joining time of 20 minutes in the microwave system. The MaCor™ specimens were joined using both conventional and microwave heating techniques for approximately 20 minutes at 1050°C and 1075°C. The quality of the joins was assessed using F_P (equation 1). Figure 7 shows the functional dependence of F_P on the film thickness.

Notches in MaCor™ specimens changed dimension by less than 5.7% in width and depth during joining (Figure 5, Table II). Alumina specimens changed by less than 4.1% in width and depth (Figure 6, Table II). Notch shape retention indicates that ceramic components with intricate features, such as small holes and channels, could maintain their complex geometry during joining. Also for the MaCor™ specimens, the constancy of notch geometry indicates a lack of wide-scale viscous flow.

Additional work needs to be done to compare the quality of the joins as a function of the join temperature, time, coating thickness, and heating mode (microwave versus conventional heating). Also, future research might include mechanical testing of the joined region using techniques, such as compressive shear tests using a variety of loading

techniques. Transmission electron microscopy (TEM) analysis of phases present near the joined region should also be investigated.

ACKNOWLEDGEMENTS

We acknowledge the financial support from the Electronic and Surface Properties of Materials Center and the Composite Materials and Structure Center at Michigan State University. We also acknowledge the use of the electron microscopes at the Center for Electron Optics, Michigan State University.

REFERENCES

Fukushima, H., T. Yamanaka, and M. Matsui. 1990. "Microwave Heating of Ceramics and Its Application to Joining," *J. Mater. Res.*, 5 (2): 397-405, 84.

Fullman, R. L. 1953. "Measurements of particle sizes in opaque bodies," *Trans. Met. Soc.* AIME 197(3): 447-452.

Lee, K. Y., E. D. Case, J. Asmussen, Jr., and M. Siegel. 1996. "Binder Burnout in a Controlled Single-Mode Microwave Cavity," *Scripta Materialia*, 35(1):107-111.

Lee, K. Y., E. D. Case, and D. Reinhard. 1997. "Microwave Joining and Repair of Ceramics and Ceramic Composites," *Ceramic Eng. and Sci. Proc.* vol. 18.

Lee, K. Y., E. D. Case, and J. Asmussen, Jr. 1997. "Microwave Binder Burn-out for Batch Processing of Al_2O_3, Al_2O_3/SiC Platelet, and Al_2O_3/ZrO_2 Particle Powder Compacts," *Cer. Trans.*, 80:539-546.

Mecartney, M. L., R. Sinclair, and R. E. Loehman. 1985. "Silicon Nitride Joining," *J. Amer. Ceram. Soc.*, 68:472-488.

Moorhead, A. J. 1987. "Direct Brazing of Alumina Ceramics," *Adv. Ceram. Mater.* 2:159-166.

National Bureau of Standards (U.S.). 1959. *Circ. 539*, 9:3.

Sandage, K. H., H. J. Schmutzler, R. Wheeler, and H. L. Fraser.1996. "Mullite Joining by Oxidation of Malleable, Akaline-Earth-Metal-Bearing Bonding Agents," *J. Am. Ceram. Soc.*, 79(7): 1839-50.

Santella, M. 1992. "A Review of Techniques for Joining Advanced Ceramics," *Am. Ceram. Soc. Bull.*, 71:947-54.

Silberglitt, R., D. Palaith, W. M. Black, H. S. Sa'adaldin, J. D. Katz and R. D. Blake. 1991. "Investigation of interlayer Materials for the Microwave Joining," *Ceram. Trans.*, 21:487-495.

Zdaniewski, W. A., P. M. Shah, and H. P. Kirchner, 1987. "Crystallization Toughening of Ceramic Adhesives for Joining Alumina," *Adv. Ceram. Mater.*, 2:204-208.

CHAPTER 4

CRACK HEALING

Part I. DIFFUSIVE CRACK HEALING BEHAVIOR IN POLYCRYSTALLINE ALUMINA: A COMPARISON BETWEEN MICROWAVE ANNEALING AND CONVENTIONAL ANNEALING[1]

ABSTRACT

Crack healing experiments via both conventional heating and microwave heating were performed on Vickers-indented specimens of polycrystalline alumina (Coors ADS-995). For the entire temperature range included in this experiment (1510 K to 1742 K), the crack healing rate was enhanced for microwave heating compared to conventional heating. The microwave crack-healing data was described well by a diffusive mass transport model given by Stevens and Dutton.

1. INTRODUCTION AND BACKGROUND

Distributed damage due to microcracking can be induced by crystallographic phase transformation [1], thermal expansion anisotropy (TEA) [2-7], thermal shock and thermal

[1] B.A. Wilson, K.Y. Lee and E.D. Case, Materials Research Bulletin, vol. 32, no. 12, pp. 1607-1616 (1997).

fatigue [8-14], mechanical fatigue [15-19], particulate impact [20], and machining damage [21]. Also, microcracks affect a wide range of material properties, including Young's modulus, shear modulus [2-5,7,9,10], Poisson's ratio [22], fracture surface energy [23], thermal diffusivity [6], thermal conductivity [24] and thermal expansion [7,25], and strength [7,26-29].

Since microcracking occurs for a variety of mechanisms and since microcracking can in turn affect a broad spectrum of material properties, there is interest in microcrack "healing", that is, reversing to some extent the effects of microcracking by reducing the size/number density of microcracks. While crack healing occurs near room temperature in humid environments for glass [30,31] and in mica [32], microcrack healing is typically accomplished by thermal annealing in conventional furnaces [33]. For example, conventional heating has resulted in strength increases for a number of studies of microcracked ceramics [7,26-29]. Also, there have been direct observations of a crack length decrease as a function of thermal annealing time and temperature [34-37], again for annealing in conventional furnaces.

During microwave processing, a number of researchers, beginning with Janney and Kimrey [38], report an enhanced sintering rate compared to the sintering rate obtained by heating in a conventional furnace, and other authors have reported an increase in grain and diffusivity during microwave heating, compared to conventional heating. However, the present authors are not aware of a published study of crack healing in a microwave furnace, except for a preliminary study of crack healing in alumina by two of the present authors [39]. This study employs Vickers indentation cracks as model microcrack systems [40-44].

2. EXPERIMENTAL PROCEDURE

Crack healing experiments were performed on commercial polycrystalline alumina (Coors ADS-995) specimens. The cutting, polishing, and indentation was done in the same manner for all specimens included in the study. The specimens were cut to nominal dimensions of 10 mm x 10 mm x 1 mm using a high speed cutting saw (K.O. Lee Slicer/Dicer) and then polished using an automatic polisher (Leco VP-50 12" Wheel Polisher with an AP-50 Auto Polishing Attachment). To mark specimen orientation, one or two circular holes, 1.5 mm in diameter and about 0.4 mm deep (Figure 1), were milled in a specimen corner using an ultrasonic milling machine (Sonic Mill Co., Stationary Sonic Mill). The specimens then were ultrasonicated in a de-ionized water bath for 10 to 15 minutes to remove debris produced by the polishing or the milling procedures.

Six indents per specimen, three at 49 N load and three at a 98 N load (Figure 1) were made with a 70 microns/second loading rate and a loading time of 15 seconds. After indentation, all specimens were aged for 24 hours in laboratory air to allow for slow crack growth saturation of the indentation cracks [45]. Following the aging in air, the specimens were thermally annealed either (i) in air in a conventional tube furnace or (ii) in air in a single-mode microwave cavity. For both the conventional and the microwave anneals, the specimens were heated to a maximum temperature between 1510 K and 1742 K, held for 60 minutes at the maximum temperature, and then cooled to room temperature.

Conventional heating was performed in a tube furnace (MRL Thermtec Horizontal Tube Furnace) with a heating and cooling rate of 10°C per minute. The time-temperature

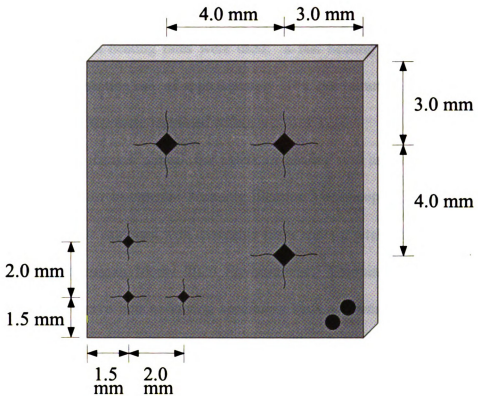

Figure 1. Schematic of indented alumina specimens used for both the conventional and the microwave heating experiments. The indentation crack lengths are exaggerated.

history for conventional heating was determined from a chart recording of an R-Type thermocouple which was placed next to the specimens.

Microwave heating was done using a 2.45 GHz single-mode microwave cavity (Wavemat CMPR250) with an automated sliding short and launch probe position controls. Details of the microwave cavity and power supply are given elsewhere [46,47]. During annealing, specimens were placed in a refractory casket consisting of a zirconia cylinder 3 cm high with an outer diameter of 7.6 cm and two aluminosilicate end plates, each 7.6 cm in diameter and 2 cm thick. The specimens were heated using a TM_{111}

electromagnetic microwave cavity mode. All microwave-annealed specimens were heated from room temperature to about 1000°C in 8 - 9 minutes. For temperatures above 1000°C, two different heating rates were used: a fast heating rate of about 75°C per minute and a slow heating rate of approximately 10°C per minute. During the one hour dwell period, the temperature remained within ± 2°C of T_{max}.

Following the thermal anneal, the extent of healing was assessed using an optical microscope and an Environmental Scanning Electron Microscope (ESEM). The optical microscope used was equipped with moveable filars and a digital length readout to ± 0.1 micron. An Electroscan Model 2020 Environmental Scanning Electron Microscope allowed one to observe nonconducting specimens such as ceramics without applying a conductive coating to the specimen surface [34,48].

3. RESULTS AND DISCUSSION

The observed crack healing rates (Figure 2) are functions of the dwell temperature, T_{max}, heating mode, and the applied indentation load. For the three heating modes used in this study: (i) conventional heating with a ramp rate of 10°C/min. (CV), (ii) microwave heating with a "slower" ramp rate of 10°C/min. (MWS), and (iii) microwave heating with a "faster" ramp rate of 75°C/min. (MWF), the crack healing rate $\Delta a/\Delta t$ was very similar at about 1510 K (Figure 2). However, the healing rate curves diverge with increasing temperature, such that for both the 49 N and 98 N indentation cracks, $\Delta a/\Delta t$ is at least double for microwave annealing MWS compared to conventional annealing CV (Figure 2). The healing rate $\Delta a/\Delta t$ (Figure 2) was evaluated as $\Delta a/\Delta t = (a_f - a_i)/\Delta t$, where a_f = the final crack length (after annealing), a_i = the initial crack length (after aging the

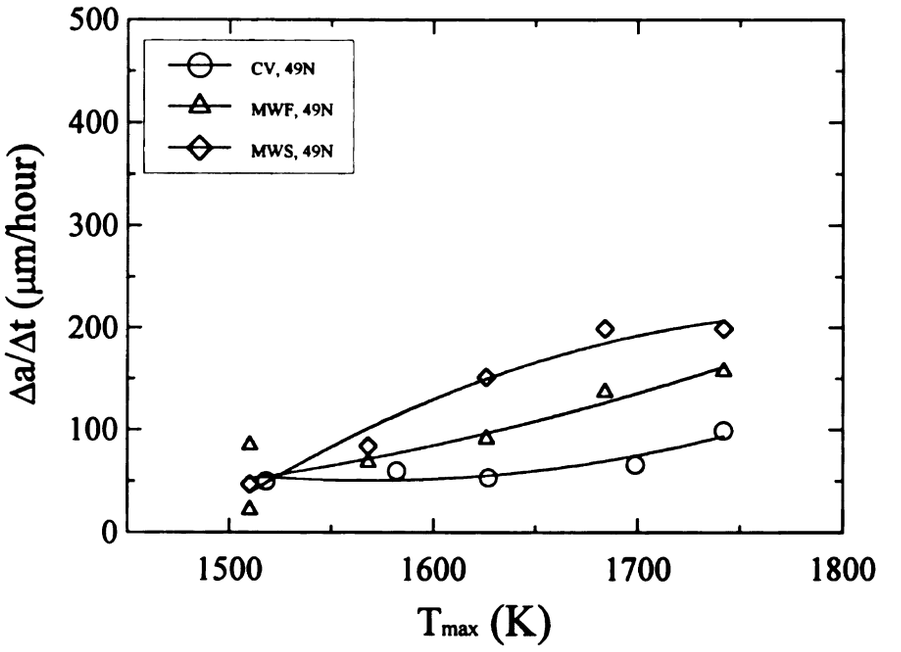

(a)

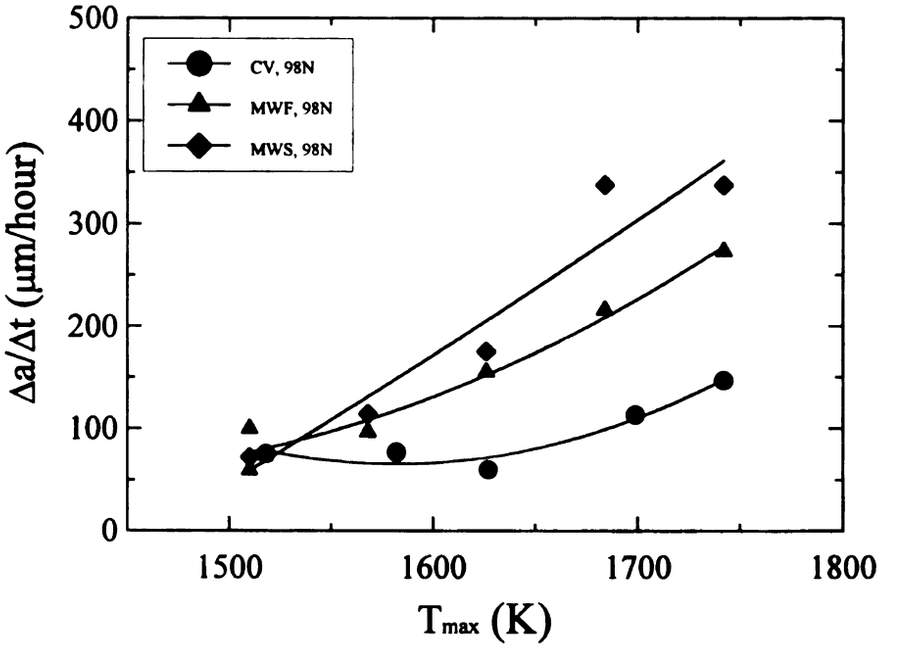

(b)

Figure 2. The crack healing rates $\Delta a/\Delta t$ for polycrystalline alumina specimens with (a) 49 N and (b) 98 N indentation cracks, annealed by (i) microwave heating, with a ramp rate of 75°C/min. (MWF), (ii) microwave heating, with a ramp rate of 10°C/min. (MWS), (iii) conventional heating, with a ramp rate of 10°C/min. (CV). The solid lines represent a least-squares fit to quadratic polynomial of the form $\Delta a/\Delta t = a + bT_{max} + cT^2_{max}$, where T_{max} is the dwell temperature for each annealing treatment.

indentation crack in air, but before annealing), and Δt = 1 hour = time at T_{max}. In this study the initial crack length was about 200 μm and 350 μm for 49 N and 98 N indentation cracks, respectively.

With increasing temperature, the "slower" microwave ramp rate heating, MWS, (10°C/min) shows higher crack healing rates compared to the "faster" microwave ramp rate heating, MWF (75°C/min), despite the fact that all microwave and conventionally annealed specimens were held at T_{max} for one hour (Figure 2). At 1742 K, the MWS heating gives $\Delta a/\Delta t$ values that are higher than the MWF heating $\Delta a/\Delta t$ values by a factor of 1.27 for the 49 N indentation cracks and a factor of 1.24 for the 98 N indentation cracks. The increased $\Delta a/\Delta t$ values observed for the MWS anneals may be due to differences in the time-averaged diffusivity for the two anneals. For the integral [49]

$$\int_0^t D(t)dt = \overline{Dt} \tag{1}$$

a slower heating rate is equivalent to a longer anneal time at T_{max}. Consider a time-temperature history "A" with a heating ramp rate H from an initial temperature T_{int} up to a maximum temperature T_{max} which is held for time $t_{dwell, A}$ and then cooled with rate H to T_{int}. Let time-temperature history B be an idealized step-function change from T_{int} to the same maximum temperature T_{max}, which is held for time $t_{dwell, B}$, followed by a step-function drop to temperature T_{int}. If $t_{dwell, A} = t_{dwell, B}$, then by equation 1 $\overline{Dt}$ for history A will be somewhat greater than $\overline{Dt}$ for history B. The difference in $\overline{Dt}$ between the two histories would increase as the ramp rate H decreases.

Equation 1 is consistent with the general trends observed in the crack healing rate data (Figure 2). For a T_{max} of 1510 K, the crack healing rate is low, hence the diffusivities are

low for both the "faster" and "slower" microwave heating rates. Given the Arrhenius nature of the temperature dependence of D, the time spent in the ramp portion of the heating curve < 1510 K will add little to $\overline{Dt}$. However, as T_{max} increases the ramp portion of the heating curve will include increasingly significant contributions to $\overline{Dt}$. However, the time dependence of the crack healing rate has not been studied.

Differences between $\Delta a/\Delta t$ for the 49 N indentation cracks and the 98 N indentation cracks may be due to differences in the crack geometry or due to differences in residual stress states resulting from the differing indentation loads. A diffusive mass transport model by Stevens and Dutton [50] provides a framework for both understanding a possible source of crack geometry- $\Delta a/\Delta t$ relations along with providing a link between $\Delta a/\Delta t$ data and activation energies for crack healing. For the case of zero applied external stress, Stevens and Dutton's model [50] may be rewritten as [35]

$$\frac{\partial a}{\partial t} = \frac{C}{T}\exp\left(-\frac{Q}{kT}\right) \tag{2}$$

where $\partial a/\partial t$ = the crack healing rate

T = temperature in Kelvin

Q = activation energy for diffusion

k = Boltzmann's constant

The constant C in equation 2 is in turn given by [35]

$$C = \frac{\pi D_o \gamma \Omega}{R^2 k \ln(L_o / R)} \tag{3}$$

where D_o is the pre-exponential factor for the diffusivity D, γ is the surface free energy, Ω is the atomic volume, R is the equilibrium crack tip radius of curvature and L_o is the distance from the crack edge to the external bulk surface [50]. For each alumina

specimen included in this study, the average $\partial a/\partial t$ was evaluated as $\Delta a/\Delta t$ (Figure 2). Equation 2 can be rewritten as

$$\ln[T_{\max}\Delta a] = \ln(C\Delta t) - \frac{Q}{kT_{\max}}. \quad (4)$$

The healing data show different activation energies, Q, for each of three heating modes used in this study (Figure 3 and Table 1). Note that the activation energy, Q, is significantly higher for microwave heating compared to conventional heating (Table 1), and the intercepts are higher for microwave heating. For each heating mode, the healing curves for the 49 N indentation cracks and the 98 N indentation cracks are approximately parallel (Figure 3), giving activation energies, Q, which are not significantly different for the two crack sizes (Table 1), indicating that the Q for healing is not a sensitive function of crack size or applied load for the range of the crack size, indentation load, and temperature employed in this study. In each case, the curves for the 98 N data were displaced upward from the 49 N data (Figure 3, parts a-c), which may be related to the crack geometry term $R^2\ln[L_o/R]$ in the denominator of the expression for the constant C (equation 3). A careful electron microscopic study of the effective equilibrium crack tip radii, R, as a function of crack size (indentation load) and temperature should be done to quantitatively determine whether or not Stevens and Dutton's [50] crack geometry term can explain the observed effect of crack size upon healing rate (Figure 2).

If we assume that R and L_o are not sensitive functions of heating mode, heating time, and temperature, then from equation 3, we can use the C values (Table 1) to calculate the ratios of D_o's between two different heating modes by

$$\frac{D_{o(MWS)}}{D_{o(CV)}} = \frac{C_{MWS}}{C_{CV}} \quad (5)$$

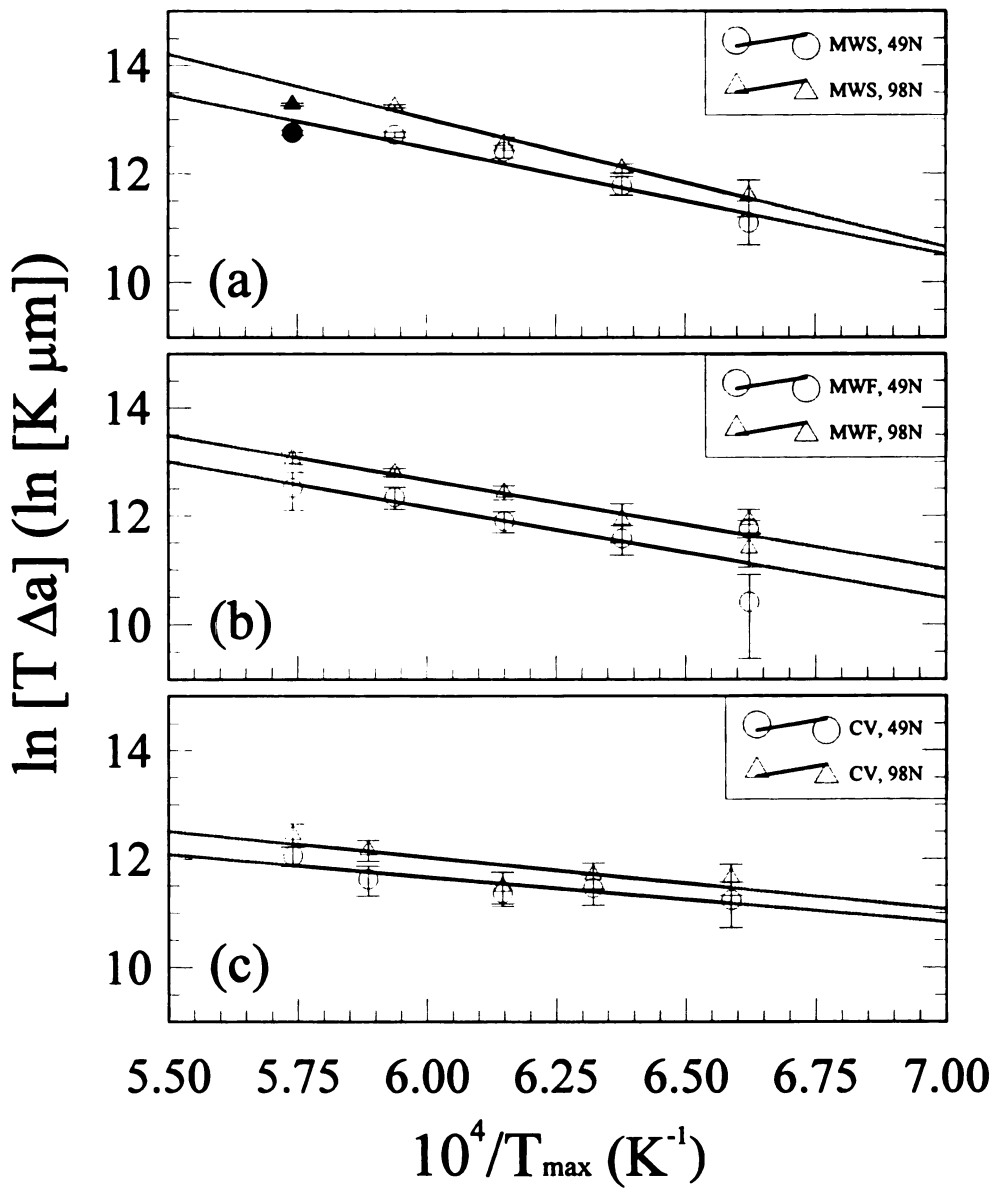

Figure 3. A modified Arrenhius plot of $\ln[T_{max}\Delta a]$ versus $1/T_{max}$ (equation 4 [35, 49]) for polycrystalline alumina specimens annealed by (a) microwave heating, with a ramp rate of 10°C/min. above 1000°C, (b) microwave heating, with a ramp rate of 75°C/min. above 1000°C, (c) conventional heating, with a ramp rate of 10°C/min. The solid lines represent a least-squares fit to equation 4.

Table 1. For each of the three heating modes used in this study, the activation energy, Q, and constant C (equations 2-4) calculated from the slopes and intercepts of the curves in Figure 3.

Heating mode	Indentation load	Q (kJ/mol)	C (m·K/sec)
Conventional	49N	69 ± 21	0.005
(10°C/min., CV)	98N	80 ± 34	0.014
Microwave	49N	140 ± 49	1.29
(75°C/min., MWF)	98N	137 ± 20	1.76
Microwave	49N	193 ± 16	101
(10°C/min., MWS)	98N	197 ± 17	190

for the particular example of the MWS and CV heating modes. In general, the diffusivity D can be written as

$$D = D_o \exp\left(-\frac{Q}{kT}\right). \tag{6}$$

Thus, combining equation 5 and equation 6 gives the diffusivity ratio D_{MWS}/D_{CV} as

$$\frac{D_{MWS}}{D_{CV}} = \frac{C_{MWS}}{C_{CV}} \cdot \frac{\exp(-Q_{MWS}/kT)}{\exp(-Q_{CV}/kT)}. \tag{7}$$

The other diffusivity ratios were calculated (Figure 4) in a similar manner. In analogy with Figure 2, the calculated diffusivity ratios for each heating mode are approximately equal to 1 at low temperature (1510 K), implying that the effective diffusivities are approximately equal for microwave and conventional heating. At higher temperatures (1742 K) the diffusivity ratios increase, ranging from about 1.7 for D_{MWS}/D_{MWF} to 4.1 for D_{MWS}/D_{CV} (Figure 4).

The microwave enhancement of crack healing rates for the specimens included in this study imply that mass transport via diffusion is enhanced during the microwave annealing of the indented specimens. Although the literature does not include other studies of microwave-enhanced crack healing in ceramics, there are numerous examples of microwave heating enhancement of sintering and grain growth [38,51-53]. A recent study by Nightingale et al [53] compared microwave and conventional processing for 3 mol% yttria zirconia specimens: (i) sintered at maximum temperatures, T_{max}, of 1573 K to 1773 K with no dwell time at T_{max} and (ii) grain growth at 1773 K for 1 - 15 hours. Microwave heating enhanced densification for T_{max} = 1573 K, but the enhancement

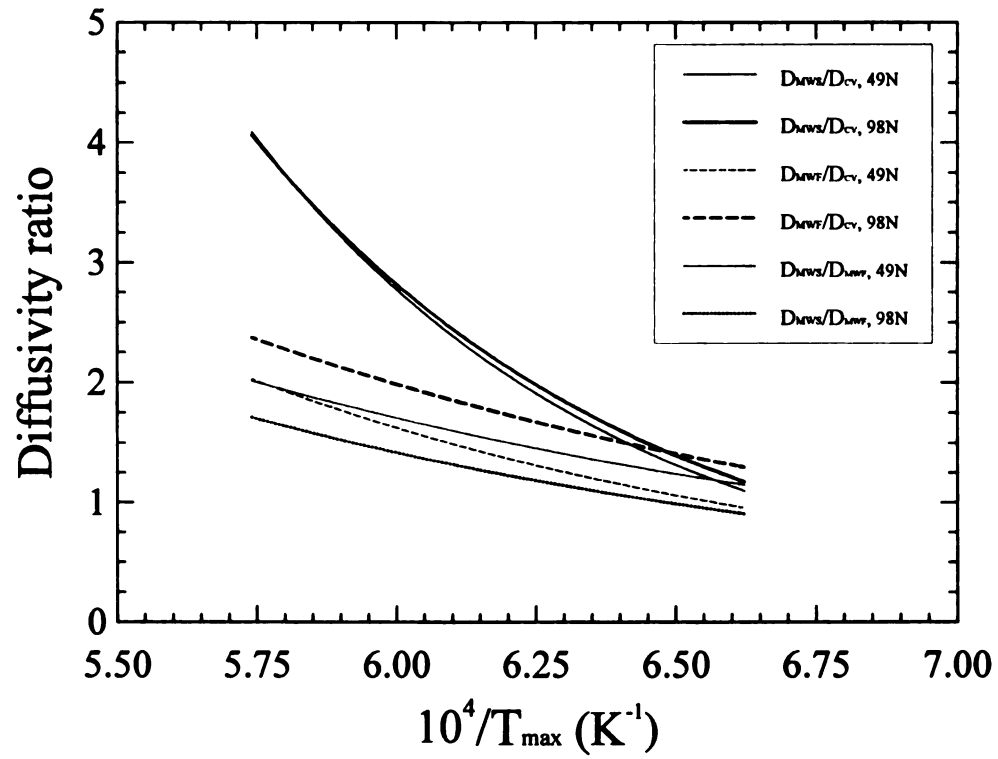

Figure 4. The calculated diffusivity ratios (equation 7) based on the values of activation energies Q and constants C given in Table 1 for each of the heating modes.

decreased as temperature increased such that at T_{max} = 1773 K the densities were essentially the same for microwave and for conventional heating. Also, there was a modest increase in grain growth for microwave-heated specimens compared to conventional heating. From analysis of the grain size-density trajectories of the yttria zirconia specimens, Nightingale et al [53] inferred that microwave heating tends to enhance lattice diffusion more than it enhances surface and grain boundary diffusion. Thus Nightingale et al [53] found that the relative microwave enhancement for the sintering process was a function of temperature, but the importance of grain boundary, surface, and lattice diffusion changes as the sintering process evolves so that detailed comparisons between the temperature dependence of sintering and the temperature dependence of crack healing may be difficult.

At 1473 K, for alpha alumina powders doped with 0.21 wt% MgO, the ratio of diffusivities $D_{(microwave)}$ / $D_{(conventional)}$ for microwave and conventional heating was 3, based on linear shrinkage kinetics during sintering [51]. However, an analysis based on sintering rates is not able to determine whether the net change in diffusivity D stems from a change in D_o, a change in Q, or changes in both D_o and Q. Katz et al [54] studied diffusion in microwave-heated chromia/alumina diffusion couples. The diffusion couples were prepared from dense polycrystalline alumina plasma-sprayed with a 30 micron-thick chromia layer. Comparison with chromia/alumina diffusion data from the literature [55,56] showed the interdiffusivity for chromium in alumina was about 3 times higher for microwave heating that for conventional heating. However, the slopes of the Arrenhius plots of logD versus 1/T were approximately parallel for conventional- and microwave-heated specimens, indicating that while the activation energies were similar for

microwave and conventional heating, $D_{o(microwave)}$ was three times higher than $D_{o(conventional)}$. Katz et al [54] argued that the apparent increase in D_o may result from microwave-induced changes in the correlation factor and/or the entropy for defect formation and ion movement.

The results of this study are roughly consistent with the results of Cheng [51] and Katz et al [54], in that the apparent diffusivity due to microwave heating can be larger than that for conventional heating by about a factor of up to about three or four (Figure 4), and that microwave heating can induce changes in D_o (Table 1 and equations 5 - 7). However, the changes in D_o are far larger in this study compared to Katz et al's work [54].

4. SUMMARY AND CONCLUSIONS

In this study, Vickers-indented specimens of a commercial polycrystalline alumina (Coors ADS-995) were annealed both via microwave heating and by conventional (radiant) heating for one hour at maximum temperatures ranging form 1510 K to 1742 K. The crack healing data was analyzed using equation 4, which is based on a diffusive mass transport model by Dutton and Stevens [50]. The activation energies for crack healing were significantly lower for conventional heating than for microwave healing (Figure 3 and Table 1). However, based on the experimentally determined Q values (Table 1) and the D_o ratios calculated from the C values (Table 1), the net diffusivities inferred from the healing data show that the microwave heating increased the diffusivities by a factor of about 1 to 4 over the range of the temperature used in this study (Figure 4). Regardless of the inferred diffusivities, the net crack healing rate for microwave annealed indentation cracks was considerably higher than annealing by

conventional furnaces (Figure 2).

This research has observed differences between the crack healing rates $\Delta a/\Delta t$ based on (i) indentation load (crack size) and (ii) heating ramp rate for microwave annealing, and mechanisms for each effect has been identified. The possible mechanism for the indentation load/crack size effect is the geometric factor $R^2\ln[L_o/R]$ in the denominator of equation 3, which arises in the Stevens and Dutton model [50]. A mechanism for the heating rate effect is the time-averaged diffusivity (equation 1 [49]). Additional work needs to be done to gather the data that allow one to quantitatively compare the effects of these mechanisms with the crack healing rate data.

The microwave-enhanced healing rates observed for the Vickers indentation cracks included in this study imply that for a microcracked specimen annealed for a given temperature and time, the recovery of strength, elastic modulus, etc. would occur more rapidly via microwave annealing than for conventional thermal annealing. Additional research should be done to investigate such effects. In addition, although this study was limited to the healing of microcracks (Vickers indentation cracks), further work should be done to determine whether the microwave enhancement also applies to healing of macrocracks.

ACKNOWLEDGEMENTS

The authors acknowledge the financial support of the Electronic and Surface Properties of Materials Center and the Composite Materials and Structure Center, Michigan State University.

REFERENCES

1. E.D. Case and C. Glinka, J. Mater. Sci. **9**, 2962 (1984).

2. S.L. Dole, O. Hunter, Jr., F.W. Calderwood, and D.J. Bray, J. Amer. Ceram. Soc. **61**, 486 (1978).

3. E.D. Case, J.R. Smyth, and O. Hunter, Mater. Sci. and Eng. **51**, 175 (1984).

4. E.D. Case, J.R. Smyth, and O. Hunter, J. Nuclear Mater. **102**, 135 (1981).

5. J.J. Cleveland and R.C. Bradt, J. Amer. Ceram. Soc. **61**, 478 (1978).

6. J.J. Siebeneck, D.P.H. Hasselman, J.J. Cleveland, and R.C. Bradt, J. Amer. Ceram. Soc. **60**, 336 (1977).

7. Y. Ohya, Z.E. Nakagawa, and K. Hamano, J. Amer. Ceram. Soc. **71**, c232 (1988).

8. J.C. Coppola and R.C. Bradt, J. Amer. Ceram. Soc. **56**[4], 214 (1973).

9. W.J. Lee and E.D. Case, Mater. Sci. and Eng. **A119**, 113 (1989).

10. W.J. Lee and E.D. Case, J. Mater. Sci. **25**, 5043 (1990).

11. W.J. Lee and E.D. Case, Mater. Sci. and Eng. **A154**, 1 (1992).

12. E.D. Case, Y. Kim, and W.J. Lee, *24th International SAMPE Technical Conference,* SAMPE, Covina, CA, p 1123 (1992).

13. E.D. Case, Y. Kim, and W.J. Lee, *Thermal Shock Behavior and Thermal Fatigue of Advanced Ceramics*, G.A. Schneider and G. Petzow, Editors, Kluwer Academic Publishers, the Nederlands, p 393 (1993).

14. E.D. Case, *Proc. 1995 SEM Spring Conference on Experimental Mechanics*, Soc. for Experimental Mechanics, Inc., Bethel, CN, p 264 (1995).

15. M.J. Reece, F. Guiu, and M.F.R. Sammur, J. Amer. Ceram. Soc. **72**, 348 (1989).

16. R.H. Dauskardt, M.R. James, J.R. Porter, and R.O. Ritchie, J. Amer. Ceram. Soc. **75**[4], 759 (1992).

17. S.Y. Liu and I.W. Chen, J. Amer. Ceram. Soc. **75**[5], 1191 (1992).

18. B.A. Wilson and E.D. Case, 1993, *Proc. 9th Annual Advanced Composites Conf.*, The Engineering Society, Ann Arbor, MI, p 518 (1993).

19. B.A. Wilson and E.D. Case, Scripta Mater. **28**, 1571 (1993).

20. E.D. Case, K.M. Louie, and A.G. Evans, J. Mater. Sci. Letters **10**, 879 (1984).

21. D.B. Marshall, *Fracture in Ceramic Materials: Toughening Mechanisms, Machining Damage, Shock*, A. G. Evans, editor, Noyes Press, Park Ridge, New Jersey, p 190 (1984).

22. E.D. Case, J. Mater. Sci. **11**, 3702 (1984).

23. E.D. Case, and J.R. Smyth, J. Mater. Sci. **16**, 3215 (1981).

24. D.P.H. Hasselman, J. Comp. Mat. **3**, 403 (1978).

25. W.R. Manning, O. Hunter, F.W. Calderwood and D.W. Stacey, J. Amer. Ceram. Soc. **55**, 342 (1972).

26. F.F. Lange and K.C. Radford, J. Amer. Ceram. Soc. 53, 420 (1970).

27. T.K. Gupta, J. Amer. Ceram. Soc. **59**[5-6], 259 (1976).

28. A.G. Evans and E.A. Charles, Acta Met. **25**, 919 (1977).

29. G. Bandyopadhyay and C.R. Kennedy, J. Amer. Ceram. Soc. **59**[9-10] (1977).

30. T.A. Michalske and E.R. Fuller, Jr., J. Amer. Ceram. Soc. **68**, 586 (1985).

31. M.K.C. Holden and V.D. Frechette, J. Amer. Ceram. Soc. **72**[11], 2189 (1989).

32. R.B. Leonesio, J. Amer. Ceram. Soc. **55**[9], 437 (1972).

33. E.D. Case, J.R. Smyth, and O. Hunter, *Fracture Mechanics of Ceramics*, vol. 5, edited by R. C. Bradt, A.G. Evans, D.P.H. Hasselman, and F.F. Lange, Plenum Press, New York, p 507 (1983).

34. B.A. Wilson and E.D. Case, J. Mater. Sci. **32**, 3163 (1997).

35. Z. Wang, Y.Z. Li, M.P. Harmer, and Y.T. Chou, J. Amer. Ceram. Soc. **75**[6], 1596 (1992).

36. R. Raj, W. Pavinich, and C.N. Ahlquist, Acta Metall. **23**, 399 (1975).

37. J. Rodel and A.M. Glaser, J. Amer. Ceram. Soc. **73**, 592 (1990).

38. M.A. Janney and H.D. Kimrey, Ceramic Transactions, Vol. **1**, 919 (1988).

39. K.Y. Lee, E.D. Case, and D.K. Reinhard, Cer. Eng. Sci. Proc. **18**, 543 (1997).

40. E.D. Case and Y. Kim, J. Mater Sci. **28**, 1885 (1993).

41. Y. Kim, E.D. Case and S. Gaynor, J. Mater. Sci. **28**, 1910 (1993).

42. Y. Kim and E.D. Case, J. Mater. Sci. **28**, 1901 (1993).

43. B.R. Lawn, Fracture Mechanics of Ceramics, vol 5., edited by R.C. Bradt, A.G. Evans, D.P.H. Hasselman, and F.F. Lange, Plenum Press, New York, p 1 (1983).

44. D.B. Marshall and B.R. Lawn, J. Mater. Sci., 14, 2001 (1979).

45. W.S. Kim and E.D. Case, Proc. 11th Annual Advanced Composites Conference, The Engineering Society, Ann Arbor, MI, p 505 (1995).

46. K.Y. Lee, E.D. Case, J. Asmussen, Jr., and M. Siegel, Cer. Trans., Vol. 59, Amer. Cer. Soc., Columbus, OH, p 473 (1995).

47. K.Y. Lee, E.D. Case, J. Asmussen, Jr., and M. Siegel, *Proc. 11th ESD Advanced Composites Conf.*, ESD, The Engineering Society, Ann Arbor, MI, p 491 (1995).

48. S.F. Flegler, J.W. Heckman JR., K.L. Klomparens, *Scanning and Transmission Electron Microscopy: An Introduction*, W.H. Freeman and Company, New York, N.Y. (1993).

49. P. Shewmon, Diffusion in Solids, Second Edition, The Minerals, Metals, & Materials Soc., Warrendale, PA, p 37 (1989).

50. R.N. Stevens and R. Dutton, Mater. Sci. Eng. **8**, 220 (1971).

51. J. Cheng, J. Qiu, J. Zhou, and N. Ye, p 323 in Mat. Res. Soc. Symp. Proc., Vol. 269, Microwave Processing of Materials II, Materials Research Society (1992).

52. R. Wroe and A.T. Rowley, J. Mater. Sci. **31**, 2019 (1996).

53. S.A. Nightingale, D.P. Dunnie, and H.K. Worner, J. Mater. Sci. **31**, 5039 (1996).

54. J.D. Katz, R.D. Blake, and V.M. Kenkre, Cer. Trans. Vol. 21, Amer. Cer. Soc., Westerville, Ohio, p. 95 (1991).

55. V.S. Stubican and J.W. Osenbach, Advances in Ceramics, **10**, 406 (1984).

56. Y. Oishi and W.D. Kingery, J. Chem. Phys. **33**, 905 (1960).

CHAPTER 5

EFFECTS OF CASKET GEOMETRY AND MICROWAVE POWER ON MICROWAVE HEATING

Part I. THE STEADY-STATE TEMPERATURE AS A FUNCTION OF CASKET GEOMETRY FOR MICROWAVE-HEATED REFRACTORY CASKETS[1]

ABSTRACT

This study demonstrates experimentally that for a fixed microwave input power, the steady-state temperature for microwave "caskets" (specimen enclosures) can vary significantly as the casket geometry changes. Also, the steady-state casket temperatures are very similar for caskets with and without an included specimen, as long as the specimen's volume and mass are small compared to the casket's volume and mass. In addition to the experimental work, a simple model is presented that describes the variation in steady-state temperature as a function of casket geometry. The model also describes how the steady-state casket temperature scales with microwave input power level. For the single-mode microwave cavity operated at 2.45 GHz that is used in this study, the steady-state casket temperature at 600 Watts of input power ranged from

1 K.Y. Lee and E.D. Case, and J. Asmussen, Jr, Materials Research Innovation, vol. 1, no. 2, pp. 101-116 (1997).

1112°C to 1519°C as the casket geometry changed for caskets composed of porous zirconia cylinders with aluminosilicate end plates.

1. INTRODUCTION

At room temperature, only a few ceramic materials such as silicon carbide and zirconia couple well with microwave energy. Typically the dielectric losses increase with increasing temperature, so that materials that do not couple well at low temperatures can couple well at elevated temperatures. For example, alumina does not couple well at room temperature, where the loss tangent is less than 0.001 for frequencies between 3.15 GHz and 4.13 GHz [1]. However, alumina does couple well at temperatures between 900°C to 1300°C, where the dielectric loss tangent increases to 0.01 for the same frequency range [1].

The difficulty in heating many ceramics with microwaves (at least at low temperatures) leads to the practice of hybrid heating, where the specimen to be heated is enclosed in a "casket" consisting of thermal insulation and/or microwave susceptor material. The casket typically serves the dual functions of (i) absorbing microwave power, thereby heating the specimen via radiant heating and (ii) thermally insulating the specimen [2]. The radiant heat supplied by microwave heating of the susceptor can in turn boost the dielectric loss of the ceramic specimens and allow the specimens to directly couple with the microwave energy.

2. RELATION TO PREVIOUS WORK

2.1. Caskets and Insulation Used in Ceramic Processing

A variety of casket/insulation materials and geometries have been used in microwave processing of ceramics. Insulation or casket materials used during microwave processing include alumina [3-8], boron nitride [2,9,10], zirconia [10-17], and alumina-silica [11,18,19]. Typical casket geometries include prismatic boxes [20] or cylindrical crucibles [2-4,7,9,10]. Within the caskets, some researchers use powder beds containing mixtures of insulating/susceptor materials, such as silicon nitride, silicon carbide, or yttria [7,10,20,21].

Susceptor materials to provide hybrid heating also have been incorporated into the casket via SiC rods inserted into the insulating materials, and the insulating materials often are in turn surrounded by a box or cylindrical refractory fiberboard enclosure [6,13,22-24]. Alternatively, cylindrical susceptors, such as porous zirconia cylinders [12-17] act both as insulators and susceptor materials. Thus, despite the variety in casket geometry and material, typical casket design elements include (i) a cylindrical geometry and (ii) inclusion of susceptor materials to provide hybrid heating. The caskets included in this study consist of porous zirconia cylinders and aluminosilicate end plates, and the systematic changes in the steady-state inner wall temperature are measured as a function of casket geometry. In addition, we develop a simple model to describe this functional dependence of steady-state casket temperature on casket geometry. Therefore, we shall briefly survey the literature that deals with thermal modeling of microwave heating.

2.2. Thermal Modeling of Microwave Heating

In the literature, thermal runaway has received the most attention in terms of thermal modeling of microwave processing of materials. Thermal runaway during microwave heating has been explained in terms of a specimen temperature which is a multivalued function of the absorbed microwave power density p_{abs} (or, alternatively the magnitude of the local electric field strength), so that an instability develops during heating [24-28]. When a critical temperature is exceeded, the instability allows the specimen temperature to "jump" from the stable low-temperature branch to the stable high-temperature branch of the temperature-p_{abs} curve. (An unstable branch of the temperature-p_{abs} curve connects the two stable branches).

In addition to modeling thermal runaway, a number of authors have used finite difference calculations to model the electromagnetic fields and the temperature distribution within loaded cavities during microwave processing [24,29-35]. Johnson and co-workers [34,35] used finite difference techniques to calculate temperature distributions and thermal stability for microwave-heated ceramic specimens with a convection/radiation condition along a vertical wall. For cylinders of alumina, Johnson et al. determined the temperature gradients in the radial direction for varying thicknesses of insulation surrounding a long cylindrical specimen [34]. Johnson et al. [34,35], thus focused on the temperature distribution within the specimen and the thermal stability of the specimen.

Tucker et al. [30,31] used a Finite-Difference Time-Domain (FDTD) technique to model heating in a multimode rectangular waveguide for a cylindrical specimen encased in insulating material. SiC rods inserted in the insulator acted as a susceptor material.

The absorbed power density in the specimen and the surrounding insulation was calculated using a 3-dimensional finite-difference time-domain code, then the temperature distribution was solved via a finite-difference heat transfer code [31]. Since the dielectric properties of the specimen and insulation were functions of temperature, the temperature distribution results were input to the absorbed power density, and the process was continued iteratively. The field pattern in the cavity and the temperature distribution in the specimen was computed with and without the insulation, and with the SiC rods in various configurations.

While Tucker et al. [30,31] modeled susceptor materials in terms of SiC rods, Skamser and Johnson [36] used a finite difference technique to model a cylindrical bundle of alumina fibers surrounded by a cylinder consisting of a lossy susceptor material. The electric field and temperature distributions were then calculated for the specimens.

Jackson et al. [24,32,33] modeled heating a lossy dielectric sphere in a rectangular resonant microwave cavity. The finite difference computations simultaneously solved Maxwell's equation and the heat balance equation using dielectric constants and thermal conductivity that were temperature dependent (thus equations were mathematically nonlinear). The sphere was modeled with homogeneous thermal and dielectric properties in a given thin shell, but thermal and dielectric properties varied from shell to shell, resulting in properties that changed as a function of the radial coordinate. In addition to the assumed symmetry for the material properties of the sphere, the mode (TM_{354} rectangular waveguide mode), the cavity dimensions, and the placement of the sphere were selected to give an isotropic electric field near the sphere. Despite the simplifying

assumptions of material-property symmetry, isotropic local electric field, etc., the calculations became extremely complex when the dielectric and thermal properties were allowed to change as a function of temperature, as is highlighted by Jackson's statement that "Even with these simplifications, part of the calculations required the use of a Cray computer" [24].

Thus, most of the effort in thermal modeling has been aimed at transient temperature distributions including thermal runaway and temperature distributions as a function of time for a given susceptor/specimen system. For the calculation of transient or steady-state temperature fields in microwave-heated specimens and caskets, the computational complexity of the thermal modeling has led most researchers to employ numerical calculation techniques, such as finite difference or finite element. In this study we concentrate on predicting the steady-state temperature of the inner wall of empty (no specimens included with the casket) caskets. Steady-state temperatures are much easier to model than transient temperatures, yet steady-state temperature conditions are often employed in sintering, binder burnout, and joining.

2.3. Key Innovations and Differences from Previous Work

For a fixed microwave input power, the steady-state inner wall casket temperature, T_i, for an empty casket can vary dramatically as a function of casket geometry. In this study, at a fixed input power of 600 Watts, we observed T_i to change by more than 400°C as the casket geometry changed. This study presents a set of simple heat transfer equations that describe well this geometrical dependence of T_i. In addition, we also show how T_i scales with changes in the microwave input power, and the experimental

observations of this scaling agree well with the heat transfer equations given in this paper. The authors were unable to find work in the literature that describes either the dependence of T_i on casket geometry or on scaling of T_i with microwave input power.

In contrast to many other studies, this study focuses on the heating behavior of empty caskets (no specimens included within the casket). Since the casket material often has a relatively large volume and mass compared to the specimen volume and mass, if the dielectric losses in the casket are high, the casket will dominate the heating process (equations 1 - 6 in Section 4). In order to relate the heating behavior of the empty caskets to the microwave processing of the ceramics, we performed additional experiments in which we compared the inner wall temperature and the absorbed power for caskets with and without a specimen present in the casket. When the specimen's volume and mass was small compared to the casket's volume and mass, the inner wall casket temperature was nearly the same for both the empty casket and the casket with the specimen inside.

The simple and approximate models developed in this paper describe well the dependence of T_i, the steady-state inner wall casket temperature as a function of casket geometry. As discussed in Section 2.2, other researchers have modeled casket temperatures using finite element techniques, but such techniques can be cumbersome. Parametric studies could potentially describe the dependence of the steady-state temperature upon casket geometry, but even if the numerical modeling was successful, one still would need to distill the functional dependence of the geometrical parameters from the numerical results. The models presented here give analytical results which form a basis for the rational design of microwave caskets, and the tools for such a casket design strategy are not found now in the literature.

The computer database Compendex was searched using the following keywords: microwave heating, microwave processing, microwave cavity, microwave sintering for the years 1991-1996. The following keywords were searched by the Compendex as a group: microwave, cylinder (cylinders, cylindrical), and ceramic (ceramics). In addition, references were taken from the authors' files of microwave heating and processing papers.

3. EXPERIMENTAL PROCEDURE

3.1. Materials

In this study, the refractory caskets that were microwave-heated were nominally identical to caskets used by the authors [14-16] for hybrid heating of ceramics and ceramic composites. Each casket used for this research (Table 1 and Figure 1) was made of aluminosilicate board end plates (SALI, Zircar) and zirconia cylinders (ZYC, Zircar). The approximate compositions (as specified by the vendor) of the aluminosilicate refractory boards and the zirconia cylinders are given in Table 2 [38].

The caskets were divided into three groups. Caskets in Group 1 (Caskets 1 - 4) included a disc-shaped aluminosilicate (SALI) specimen setter (Figure 1) similar to those setters used by the authors for microwave sintering and joining of ceramic materials [14-16]. The specimen setters had a radius equal to the inner radius of the zirconia cylinder. The setter thickness was 0.5 cm for Caskets 1, 2, and 3, and 1.5 cm for Casket 4.

Group 2 (Caskets 5, 6, 7, and 8) and Group 3 (Caskets 9, 10, 11, and 12) included only SALI end plates and zirconia cylinder; no specimen or specimen setter was included. For Group 2, the b/a ratio (outer radius/inner radius) was fixed at 1.5 and the

Table 1. Volume and dimensions of each casket used in this study.

Group	Casket	Outer radius, b (cm)	Inner radius, a (cm)	b/a	L_{Zr} [b] (cm)	L_{SA} [b] (cm)	V^{Zr} [c] (cm^3)	V^{SA} [c] (cm^3)	Total volume of casket (cm^3)
1	Casket 1	5.08	3.81	1.33	3	4	106	347	453 [d]
	Casket 2	3.81	2.54	1.50	3	4	76	193	269 [d]
	Casket 3	5.08	2.54	2.00	3	4	182	334	516 [d]
	Casket 4	5.08	3.81	1.33	5	2	177	231	408 [d]
2	Casket 5[a]	3.81	2.54	1.50	2	2	51	91	142
	Casket 6	3.81	2.54	1.50	3	2	76	91	167
	Casket 7	3.81	2.54	1.50	4	2	101	92	193
	Casket 8	3.81	2.54	1.50	5	2	127	91	218
3	Casket 5[a]	3.81	2.54	1.50	2	2	51	91	142
	Casket 9	5.08	3.81	1.33	2	2	71	162	233
	Casket 10	5.08	2.54	2.00	2	2	122	162	284
	Casket 11	3.81	3.00	1.27	2	2	35	91	126
	Casket 12	5.08	3.00	1.69	2	2	106	162	268

[a] Same heating data for the casket used in analysis.
[b] L_{Zr} and L_{SA} are length of zirconia cylinder and total thickness of SALI end plates, respectively.
[c] V^{Zr} and V^{SA} are volume of zirconia cylinder and volume of SALI, respectively.
[d] Volume included the volume of specimen setter (SALI) inside each casket in Group 1.

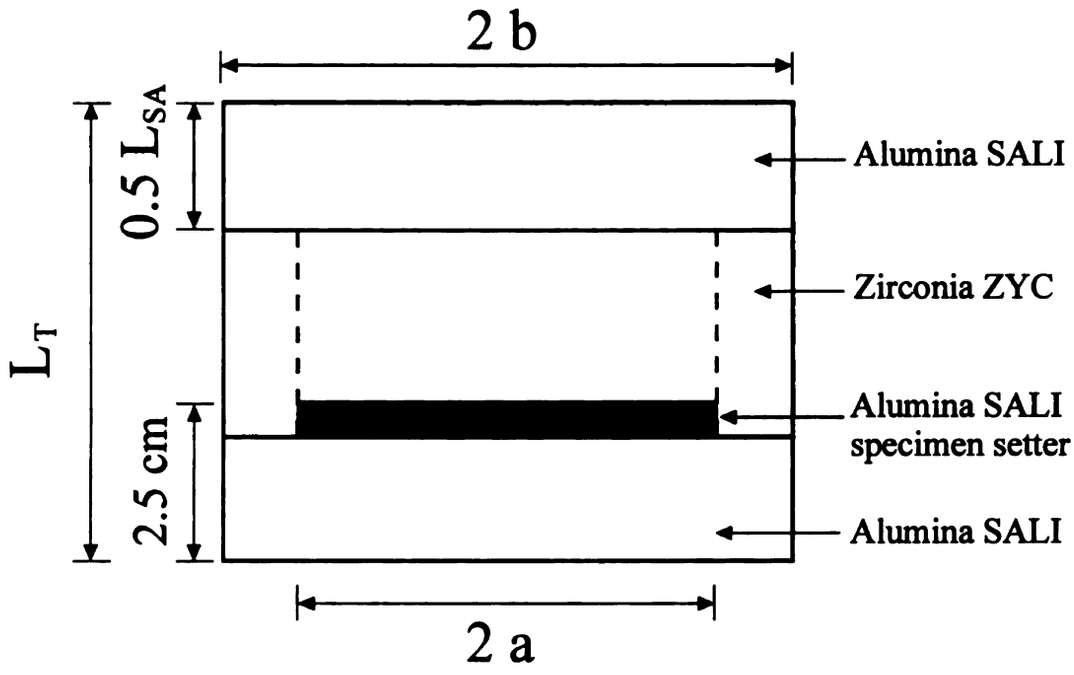

Figure 1. Schematic of the casket (specimen enclosure) used in this study. The aluminosilicate (SALI) specimen setter was included in Caskets 1-4.

Table 2. Composition, density, and porosity of the insulation used for caskets in this study [38].

Refractory	Composition, wt%	Density (g/cm^3)	Porosity (%)
Aluminosilicate, SALI	80% Al_2O_3 - 20% SiO_2	0.48	84
Zirconia, ZYC	87% ZrO_2 - 8% Y_2O_3 - 5% SiO_2	0.48	91

total casket length ranged from 4 cm to 7 cm. For Group 3, the casket length was fixed at 4 cm (2 cm zirconia cylinder height and 2 cm total aluminosilicate board thickness), but the b/a ratio ranged from $1.27 \leq b/a \leq 2.0$ (Table 1).

In addition to heating the empty caskets, Casket 6 (Group 2) and Casket 9 (Group 3) were reheated with a powder compact specimen added to the caskets. A 2 gram alumina-15 wt% zirconia powder compact and a 20 gram alumina powder compact were heated in Caskets 6 and 9, respectively, to compare the steady-state temperatures at 600 Watts to the temperatures of the corresponding caskets without specimens at the same microwave input power. The materials used for the 2 gram powder compact specimen were Sumitomo AKP50 and zirconia powder (Fisher Scientific Company). For the 20 gram specimen, Sumitomo AKP30 was used. Both the specimens were uniaxially pressed (the 2 gram specimen at 32 MPa and the 20 gram specimen at 4 MPa), yielding a 2 gram disc-shaped Al_2O_3-15 wt% ZrO_2 powder compact, 2.2 cm in diameter and about 2 mm thick and a 20 gram disc-shaped Al_2O_3 powder compact, 5.1 cm in diameter and 5.5 mm thick.

3.2. Refractory Casket Construction

The caskets were prepared from as-received billets of aluminosilicate board and from as-received zirconia cylinders (Zircar SALI and ZYC, respectively). The boards and cylinders were cut to the desired dimensions using a commercial saw. The cut surfaces were finished by abrading the zirconia cylinder with a sheet of notebook paper to reduce possible thermal losses from the gaps between the casket end plates and the zirconia cylinder.

For each casket, the total casket height (zirconia cylinder plus the aluminosilicate

board end plates) ranged from 4 cm to 7 cm (Table 1 and Figure 1). The cylindrical zirconia refractory was available in two types. One had 10.16 cm (4 inch) OD and 7.62 cm (3 inch) ID, while the other had 7.62 cm (3 inch) OD and 5.08 cm (2 inch) ID. The caskets having b/a ratio equal to 1.3333 (Casket 1, 4, 9) or 1.5 (Casket 2, 5, 6, 7, 8) were prepared from the as-received 10.16 cm OD or 7.62 cm OD cylinders, respectively (Table 1). Caskets 3 and 10 having a b/a ratio of 2.00 were made by inserting a 7.62 cm OD cylinder into a 10.16 cm OD (7.62 cm ID) cylinder. For Casket 11, a b/a ratio of 1.27 was obtained by reaming a casket of an original inner diameter of 5.08 cm to a final inner diameter of 6 cm. For Casket 12, a b/a ratio of 1.69 was obtained by inserting a casket having an inner diameter of 5.08 cm into a casket having an inner diameter of 7.62 cm and then reaming the inner diameter from 5.08 cm to a final inner diameter of 6 cm. (Table 1). Therefore, each casket had an outer radius of either 3.81 cm or 5.08 cm and an inner radius of either 2.54 cm, 3 cm, or 3.81 cm. The dimensions of the 12 caskets constructed for this study are listed in Table 1.

A maximum casket length of 7 cm was used in this study because the tuned microwave cavity height varies from a lower limit of 7.3 cm to an upper limit 21.95 cm. During heating, the cavity was tuned by adjusting the cavity height and launch probe position. A casket height equal to or smaller than 7 cm avoids possibly crushing the casket by the top plate of the microwave cavity.

3.3. The Microwave Cavity, Power Supply, and Associated Apparatus

The microwave cavity used in this study was an internally tunable, cylindrical single-mode cavity operated at 2.45 GHz (CMPR-250, Wavemat, Plymouth, MI, Figure

2) [14-17,39,40-42]. Continuous microwave power ranging from 0 Watts to 2 kWatts generated by a magnetron power supply (Sairem MWPS2000, Wavemat, Plymouth, MI) was transmitted to the cavity by a rectangular metallic hollow waveguide with approximate internal dimensions of 7.2 cm by 3.4 cm (Figure 2). The power was fed into the cavity through a power launch probe which determines the field distribution around the cavity wall (Figure 3). The microwave cavity was tuned using two computerized stepper motors which change the probe and short positions with an accuracy of ±0.01 cm (Figures 2 and 3) [14-17,41,42].

P_r, the reflected power was measured by a Hewlett-Packard power meter (HP435B). The total power, P_T, absorbed by the cavity system was calculated from $P_T = P_i - P_r$, where P_i is the microwave input power.

The temperature at the inner wall of the casket was measured via an optical pyrometer system (Accufiber Optical Fiber Thermometer, Model 10, Luxtron Co., Beaverton, OR) (Figures 2 and 4) capable of measuring temperatures ranging from 500°C to 1900°C with an accuracy of ± 2°C. For every casket used in this study, a 5 mm diameter hole was drilled in the casket wall (Figures 2 and 4) [14,15] to allow the temperature measurement. The hole was positioned 2.5 cm above the cavity bottom plate during microwave heating of the caskets to allow the hole to be aligned with the microwave cavity viewport A, which in turn permitted pyrometer observation (Figures 2 and 4).

In addition to the temperature measurement of the casket inner wall, the outer wall temperature was measured for the caskets in Groups 2 and 3 (Table 3). Using cavity viewport B (Figure 2), the outer casket wall temperature was measured by sighting the

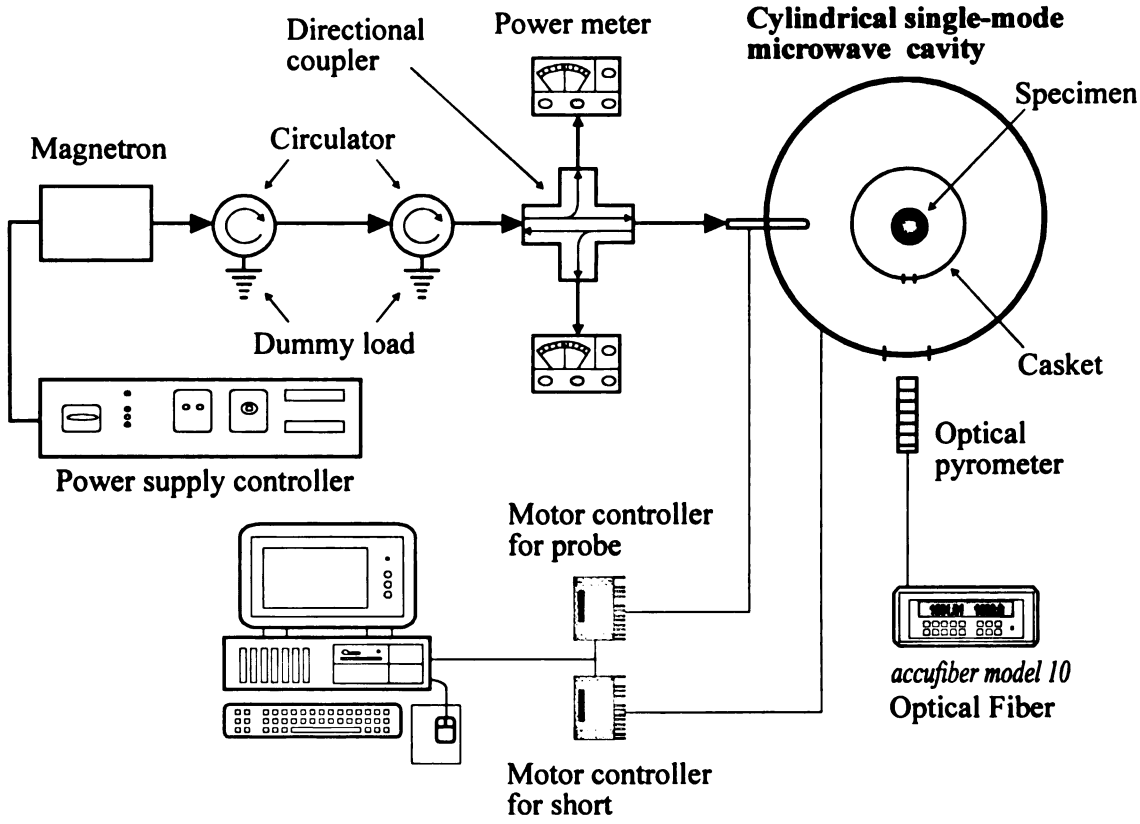

Figure 2. Apparatus for microwave heating using a cylindrical single-mode cavity.

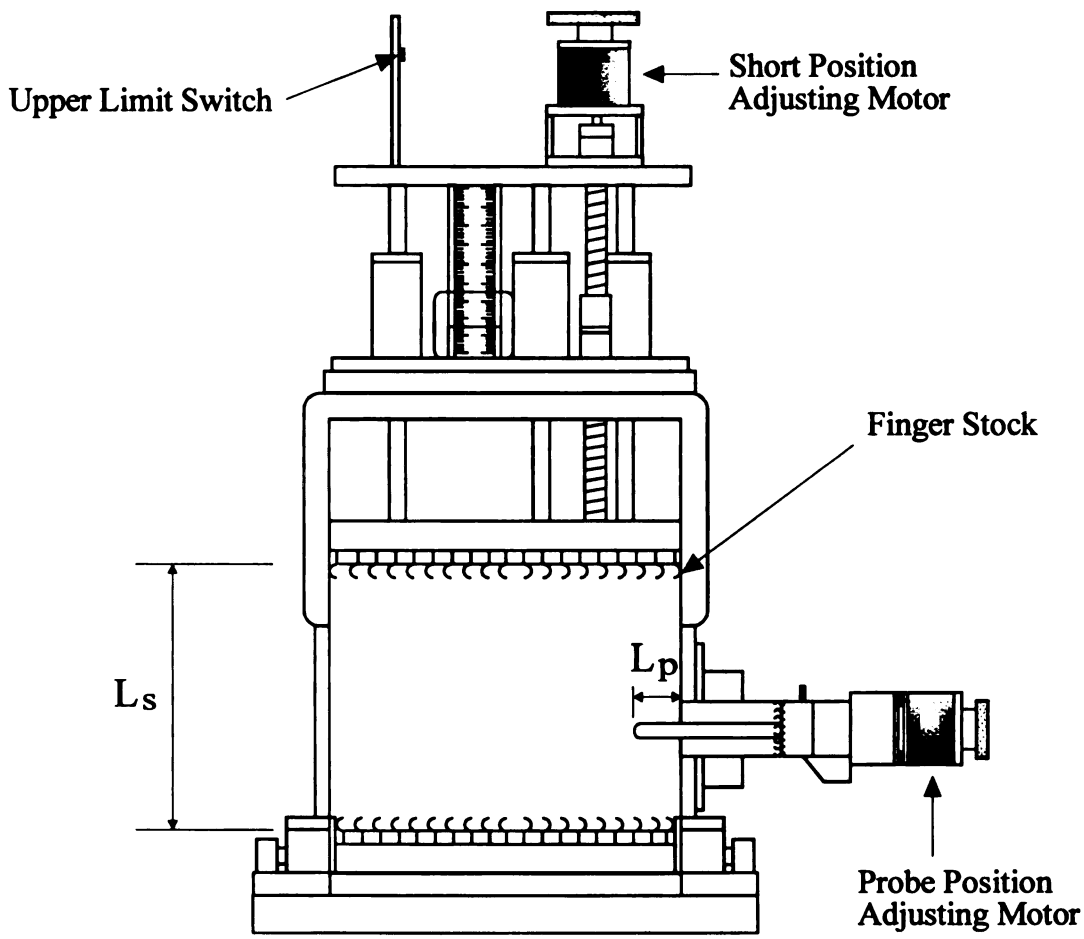

Figure 3. Schematic of cylindrical single-mode microwave cavity. The short position, L_s (cavity height) and the probe position, L_p are illustrated.

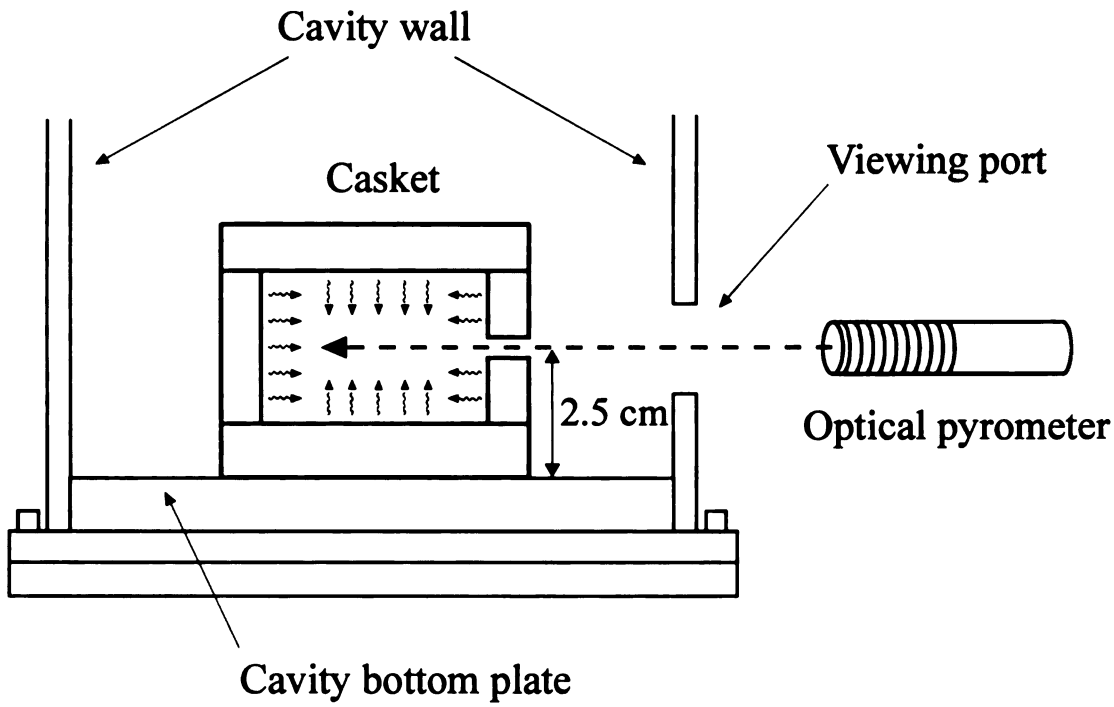

Figure 4. Schematic showing the measurement of the temperature of the casket's inner wall. The optical pyrometer is sited through cavity viewport A and through a 5 mm hole in the casket wall.

Table 3. Measured outer casket wall temperature, T_o, for caskets 5 - 12.

Casket #	5	6	7	8	9	10	11	12
Measured T_o (°C)	906	865	835	804	937	759	873	975

optical pyrometer on the casket's cylindrical outer surface. The outer wall temperature was measured when the inner casket wall temperature reached a steady-state at 600 Watts. Unlike the inner wall temperature measurement, where the pyrometer was sighted through the 5 mm hole in the casket wall, the curved outer surface of the casket made temperature measurement difficult. The uncertainty in outer wall temperature was estimated as about ± 50°C. In addition, the microwave cavity was set up in a fume hood which made it difficult to maneuver the optical pyrometer near viewport B as it was being sighted on the casket outer wall, but there was no similar space problem involved in aligning the pyrometer near viewport A through which the inner wall temperature was measured.

3.4. Heating of Microwave Caskets

The heating experiments were done in two stages. First, the caskets were heated to 500°C using a fixed power ranging from 100 to 130 Watts. After the casket temperature reached 500°C, the microwave input power was increased by 30 Watts every three minutes up to a maximum power of 600 Watts. This rate of power increase resulted in a relatively slow heating rate ranging from 8°C/min. to 22°C/min. for the temperature range from 500°C to the maximum temperature.

The caskets in Group 1 were heated in various cavity modes (Mode 1 - Mode 9 described in Table 4) [37]. The caskets in Groups 2 and 3 were heated in the cavity tuned to Mode 3. The reason for identifying the cavity modes used in this study with a simple one-digit label is as follows. For an empty cavity, ideally there are a set of pure TE and TM electromagnetic cavity modes. When the cavity is loaded with a lossy dielectric, the

Table 4. Summary for the cavity short position (i.e. cavity height), L_s, as a function of the electromagnetic resonance cavity mode, determined at a microwave input power of 50 Watts.

Mode	L_s (cm) for ideal 7" cylindrical empty cavity (mode)	L_s (cm) for empty cavity	L_s (cm) for casket 1	L_s (cm) for casket 2	L_s (cm) for casket 3	L_s (cm) for casket 4
Mode 1	7.21 (TM_{011})	7.66	[a]	[a]	[a]	[a]
Mode 2	8.24 (TE_{211})	8.43	7.72	8.15	7.47	7.65
Mode 3	11.29 (TM_{111})	11.62	9.77	10.32	9.45	9.50
Mode 4	13.38 (TE_{112})	13.60	12.83	12.96	12.52	12.80
Mode 5	14.41 (TM_{012})	15.13	14.43	14.63	14.30	14.35
Mode 6	15.71 (TE_{311})	16.63	15.31	16.26	15.10	15.35
Mode 7	16.48 (TE_{212})	17.19	16.20	16.71	16.00	16.17
Mode 8	20.07 (TE_{113})	20.46	19.79	19.92	19.49	19.70
Mode 9	21.62 (TM_{013})	[a]	21.76	[a]	21.34	21.68

[a] Could not determine, outside the range of the adjustable cavity height.

electric field distribution can be greatly modified, so that a simple TE or TM mode designation is no longer appropriate [43]. For example, the TE modes can be distorted to include z (axial) field components. Table 4 lists the corresponding designations for the ideal cylindrical empty cavity mode and the short positions for the actual empty cavity and for the cavity loaded with Caskets 1 - 4.

When Caskets 6 and 9 were reheated with a specimen present, the powder compact specimens were placed at the center on the casket bottom plate without a specimen setter. The caskets with each specimen were heated in the microwave cavity by the same heating procedure used for heating the corresponding empty caskets. As was the case for the temperature measurements for the empty caskets, the casket inner wall temperature was monitored by the pyrometer through cavity viewport A and the 5 mm hole in the casket wall (Figures 2 and 4).

4. MODEL FOR THE DEPENDENCE OF STEADY-STATE CASKET TEMPERATURE UPON CASKET GEOMETRY

The power dissipated per unit volume of microwave absorbing material is given by p_{abs}, which is related to the dielectric properties of the material by

$$p_{abs} = 2\pi f \varepsilon_o \varepsilon_r'(\vec{r},T)\tan\delta(\vec{r},T)\left|E(\vec{r})\right|^2 \qquad (1)$$

where f = frequency of the incident microwave energy in Hz

ε_o = 8.854×10^{-12} F/m

= permittivity of free space

$\varepsilon_r'(\vec{r},T)$ = relative dielectric constant as a function of position vector, $\vec{r}$, and temperature, T

$\tan\delta(\vec{r},T)$= loss tangent as a function of $\vec{r}$ and T

$E(\vec{r})$ = magnitude of internal electric field in V/m as a function of $\vec{r}$.

The total power, P_T, absorbed by the cavity loaded with a casket and a specimen is equal to the difference between the input power, P_I, and the reflected power, P_R, which can be expressed as

$$P_T = P_I - P_R = P_W + P_C + P_S \tag{2}$$

where P_W = power dissipated by the cavity wall

P_C = power absorbed by the casket

P_S = power absorbed by a processed specimen.

In turn, P_C and P_S can be expressed in terms of power density

$$P_C = < p_{abs}^C > V^C \tag{3}$$

$$P_S = < p_{abs}^S > V^S \tag{4}$$

where $< p_{abs}^C >$ = spatial average for power density within a casket of volume V^C

(heat energy per unit time per unit volume)

$< p_{abs}^S >$ = spatial average for power density within a specimen of

volume V^S.

For microwave heating performed with the casket alone (no specimen) then the total power absorbed by the specimen becomes

$$P_T = P_W + P_C . \tag{5}$$

The caskets used in this study consisted of zirconia cylinders with aluminosilicate refractory board end plates which are very lossy materials [23]. In this study, at 600 W input power the measured reflected power was 0.1% to 1.4% of the input power for the

caskets of various geometries included in this study (Table 5) so that the power is nearly totally absorbed by the cavity system (the cavity walls and the casket). From equation 2, since the measured reflected power is very small, the total absorbed power, P_T, is well approximated by the input power, P_i for 600 Watts. In fact, we observed experimentally that P_T is very nearly equal to P_i over the entire range of input power from about 500 Watts to 600 Watts.

For lossy casket materials, $P_W << P_C$ the wall losses can be neglected in this case and we can approximate P_T by [43]

$$P_T \approx P_C = < p_{abs}^C > V^C \tag{6}$$

which is the heat per unit time generated within the cylindrical casket (due to microwave heating), thus $P_C \approx$ the total absorbed power P_T.

We shall now develop a simple model for the steady-state thermal energy balance for the microwave heated casket. This energy balance will consider the thermal energy per unit time generated in the casket as a function of microwave heating and thermal energy per unit time that flows out from the cavity walls. At steady-state, the energy fluxes must balance.

For the steady-state flow of heat energy in a hollow infinite cylinder of inner radius a and outer radius b subject to the boundary conditions that

$$\text{(i)} \qquad \text{At r = a,} \quad T = T_{inside} = T_i \tag{7}$$

$$\text{(ii)} \qquad \text{At r = b,} \quad \frac{dT}{dr} = h(T_i - T_o) = 0 \ . \tag{8}$$

Carslaw and Jaeger give [44] the outward radial heat flux per unit length of cylinder as

$$J' = \frac{2\pi k(T_i - T_o)Hb}{1 + Hb\ln(b/a)} \tag{9}$$

Table 5. Input power, P_i reflected power, P_r, and power density, p_{abs}, for various caskets at a fixed input power of 600 Watts.

Group	Casket	Reflected power, P_r (Watts)	$\frac{P_i - P_r}{P_i} \times 100$ (%)	p_{abs} (W/m^3)
1	Casket 1	1.54	99.7	5.65
	Casket 2	3.38	99.4	7.85
	Casket 3	8.21	98.6	3.25
	Casket 4	6.15	99.0	3.36
2	Casket 5 [a]	3.08	99.5	4.21
	Casket 6	1.54	99.7	3.58
	Casket 7	0.51	99.9	3.11
	Casket 8	0.51	99.9	2.75
3	Casket 5 [a]	3.08	99.5	4.21
	Casket 9	0.51	99.9	2.57
	Casket 10	1.03	99.8	2.11
	Casket 11	2.05	99.7	2.23
	Casket 12	4.10	99.3	4.73

[a] Casket 5 is included in both Group 2 and Group 3.

where in equations 7 - 9

T_i = temperature at inner wall of hollow cylinder

T_o = temperature at outer wall of hollow cylinder

H = h/k and

h = surface heat transfer coefficient for the cylinder

k = thermal conductivity of the cylinder.

For a total length L_T of the cylinder, the flux J is thus given by

$$J = J'L_T = \frac{2\pi k(T_i - T_o)HbL_T}{[1 + Hb\ln(b/a)]} \quad (10)$$

Given units of watts/m °C for k, watts/m^2 °C for h, and meters for the dimensions a, b, L_T, then H has units of m^{-1} and J has units of watts (joule/sec). Thus J measures the heat energy per unit time that flows through a length L of the cylinder wall.

At steady-state, the production of heat energy per unit time with the cylindrical casket will be balanced by the outflow of energy (equation 10) so that

$$P_T = < p_{abs}^C > V^C = \frac{2\pi k(T_i - T_o)HbL_T}{[1 + Hb\ln(b/a)]} \quad (11)$$

where for a length of zirconia cylinder, L_{Zr}, and a total thickness of SALI end plates (Figure 1), the total length of the cylindrical casket is

$$L_T = L_{Zr} + L_{SA}.$$

If we include in the volume of the casket, V^C, the volume of the SALI end plates and the volume of the zirconia cylinder then

$$P_T = < p_{abs}^C > \left[\pi(b^2 - a^2)L_{Zr} + \pi b^2 L_{SA}\right]. \quad (12)$$

Upon solving for T_i from equation 5 we obtain

$$T_i = \frac{P_T}{2\pi k} \cdot \frac{[1 + Hb\ln(b/a)]}{HbL_T} + T_o \tag{13}$$

Using the measured T_i data as the independent variable, with four dependent variables (three measured geometrical parameters, b, a, and L_T, along with P_T, the measured total absorbed microwave power) we can use the following candidate equation to fit the data.

$$T_i = \frac{C_1' P_T [1 + C_2' b\ln(b/a)]}{bL_T} + C_3'. \tag{14}$$

In theory, the fitted coefficients (Table 6) should correspond to

$$C_1' = \frac{1}{2\pi kH} = \frac{1}{2\pi h} \tag{14a}$$

$$C_2' = H = \frac{h}{k} \tag{14b}$$

$$C_3' = T_o. \tag{14c}$$

If for the casket, the inner radius a, the outer radius b, and the total length L_T are fixed, then equation 14 reduces to

$$T_i = \frac{D_1}{L_T} + D_2 \tag{15}$$

where L_T = the total cylinder length and D_1 and D_2 are fitted constants of the caskets in Group 2 (Table 7). Referring to equation 13, D_1 is given by

$$D_1 = P_T \cdot \frac{[1 + Hb\ln(b/a)]}{2\pi kHb} \tag{16}$$

and $D_2 = T_o$.

In the case that the geometric variables b, b/a, and L_T are fixed, and the material parameters H and k are fixed, then the coefficient D_1 in equation 16 should vary linearly with P_T.

Table 6. Least-squares coefficients and coefficient of determination (R^2) determined by fitting the casket heating data of the caskets in Group 1, 2, and 3 to equation 14.

Group	C_1' ($m^2 \cdot °C/W$)	C_2' (m^{-1})	C_3' (°C)	R^2
1	0.0052	17.2	26	0.999
2	0.1238	-64.3	1149	0.999
3	0.0025	10.8	342	0.997
1, 2, and 3	0.0006	13.5	1128	0.196

Table 7. Least-squares coefficients and coefficient of determination (R^2) determined by fitting the casket heating data of the caskets in Group 2 to equation 15.

Input power (Watts)	D_1 ($m \cdot °C$)	D_2 (°C)	R^2
600	12.9	1149	0.999
570	12.0	1121	0.972
540	11.4	1095	0.942

Thus the observed casket temperature results from a balance of the power absorbed (which is a function of casket volume) and the heat losses (which is a function of the casket surface area). Therefore, the volume and surface area of the caskets, as well as the dielectric properties of the casket, will be important in determining the casket temperature. When the volume and mass of the casket is large compared to the volume and mass of the microwave-heated specimens, and the dielectric losses of the casket and specimen materials are comparable, the casket should dominate the heating process (equations 1 - 6, Section 5.2, and Figure 5). If the casket dominates the steady-state casket temperature, then the casket geometry will have an important impact on the processing of ceramics and ceramic composites, since often materials are processed at a steady-state temperature.

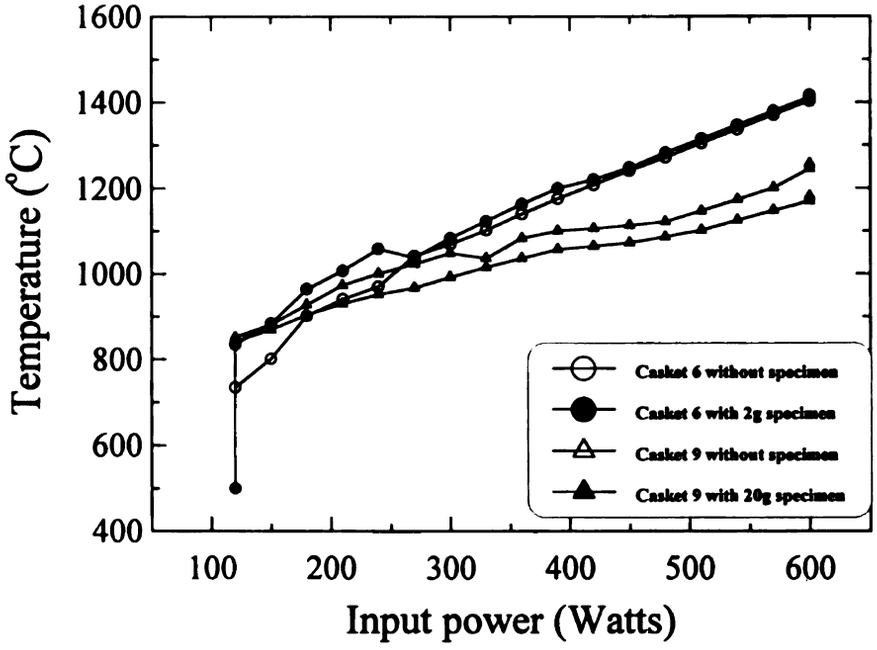

Figure 5. Temperature versus microwave input power for microwave heating of caskets with and without specimens.

Equation 14 considered the microwave-generated heat within the casket and convective heat losses from the casket's outer surface, resulted in amazingly high values of the coefficients of determination, R^2, when the caskets within a given Group (Group 1, Group 2, and Group 3) were modeled (Table 6). However, for the full set of 12 empty caskets (that is, Groups 1, 2 and 3 taken together), the R^2 value was 0.196, indicating that the entire data set can not be appropriately described by equation 14. The low R^2 value obtained from equation 14 led us to include the top and bottom surface areas of the caskets' aluminosilicate end plates.

For a plane wall of thickness L, the flux per unit area is expressed as [44]

$$J' = \frac{k(T_i - T_o)}{L} .$$

Then for a surface of area, A, the flux is

$$J = J'A = \frac{k(T_i - T_o)}{L} A \qquad \text{A = area of end plates} \tag{17}$$

$$J = \frac{k(T_i - T_o)\pi b^2}{L} \tag{18}$$

For a circular cylindrical casket used in this study, the thickness of each end plate is 0.5 L_{SA}. Thus the flux from two end plates of the casket is

$$J = 2 \cdot \frac{k(T_i - T_o)\pi b^2}{0.5 L_{SA}} = \frac{4k(T_i - T_o)\pi b^2}{L_{SA}} \tag{19}$$

From equations 10 and 19, a total heat flux for the circular cylinder with end plates,

$$J_{Total} = \frac{2\pi k(T_i - T_o)HbL_T}{1 + Hb\ln(b/a)} + \frac{4\pi k(T_i - T_o)b^2}{L_{SA}} \tag{20}$$

Thus at steady-state, the production of heat energy per unit time with the circular cylindrical casket with end plates will be balanced by the outflow of energy so that

$$2\pi k(T_i - T_o) = \left[\frac{HbL_T}{1 + Hb\ln(b/a)} + \frac{2b^2}{L_{SA}}\right] = p_{abs}V = P_T \tag{21}$$

Solving for T_i gives

$$T_i = \frac{P_T}{2\pi k} \cdot \frac{L_{SA}[1 + Hb\ln(b/a)]}{HbL_T L_{SA} + 2b^2[1 + Hb\ln(b/a)]} + T_o \tag{22}$$

where $L_T = L_{SA} + L_{Zr}$.

On multiplying by 1/H in both the nominator and denominator, then we obtain

$$T_i = \frac{P_T}{2\pi k} \cdot \frac{L_{SA}[\frac{1}{H} + b\ln(b/a)]}{bL_T L_{SA} + 2b^2[\frac{1}{H} + b\ln(b/a)]} + T_o \tag{23}$$

Using the measured T_i data as the independent variable, with five dependent variables (four measured geometrical parameters, b, a, L_{Zr}, and L_{SA} along with P_T, the measured total absorbed microwave power) we can use the following candidate equation to fit the data.

$$T_i = \frac{P_T L_{SA}[C_1 + C_2 b\ln(b/a)]}{bL_T L_{SA} + fb^2[C_3 + b\ln(b/a)]} + C_4 \tag{24}$$

where $$C_1 = \frac{1}{2\pi kH} = \frac{1}{2\pi h} \tag{24a}$$

$$C_2 = \frac{1}{2\pi k} \tag{24b}$$

$$C_3 = \frac{1}{H} = \frac{k}{h} \tag{24c}$$

$$C_4 = T_o. \tag{24d}$$

In equation 24, the factor f corresponds to the dimensionless coefficient 2 in the term $2b^2[C_3+b\ln(b/a)]$ in the denominator of equation 23. During the least-squares

fitting, f was also varied. The value of f equal to 0.1728 gave an optimal least-squares fit of equation 24 to the data for the 12 empty caskets (Table 8).

Equation 14 or 24 can be generalized by replacing the expression for the heat flow per unit length in a hollow cylinder (equation 9) with the following equation for the heat flow per unit length in a composite cylinder composed of a series of n coaxial cylindrical shells where the i_{th} shell has thermal conductivity k_i, such that [44,45,47]

$$J' = 2\pi(T_i - T_o)\cdot\left[\sum_{r=1}^{n}\frac{\ln(a_{r+1}/a_r)}{k_r} + \sum_{r=1}^{n+1}\frac{R_r}{a_r}\right]^{-1} \tag{25}$$

where T_1, T_2, T_3, ... are the temperatures at the radii a_1, a_2, a_3, ... and T_i equals the temperature inside the composite cylinder and T_o is the temperature outside the composite cylinder. R_i is the contact resistance per unit area for the cylindrical surface located at radius a_i.

Equation 25 could be applied to composite casket systems described in the literature, such as coaxial aligned crucibles with fiber or powder insulation between the inner and outer crucibles [3,7]. If we let a_{n+1} equal the outer radius of the composite cylinder and a_1 equal the inner radius of the composite cylinder, then in the limit as

Table 8. Least-squares coefficients and coefficient of determination (R^2) determined by fitting the casket heating data of the caskets in Group 1, 2, and 3 to equation 24.

Group	C_1 ($m^2 \cdot {}^oC/W$)	C_2 ($m \cdot {}^oC/W$)	C_3 (m)	C_4 (^oC)	R^2
1, 2, and 3 [a]	0.0036	0.106	0.203	747	0.993

[a] Casket 1 was not included.

$a_{n+1}/a_1 \rightarrow 1$, the casket walls become infinitely thin while in the limit $a_{n+1}/a_1 \rightarrow \infty$, the casket approaches a solid cylinder. For a_{n+1}/a_1 large, equation 25 might be applied to the case of a cylindrical casket filled with a powder bed [2,10]. In this particular study, we shall not pursue the composite cylinder model further, although it could likely be applied to a variety of caskets described in the literature [2,3,7,10].

This model (equations 14, 15, and 24) ignores the temperature and spatial dependencies of both the thermal and dielectric properties of the casket material. For the zirconia cylinders and aluminosilicate (SALI) refractory board used to construct the caskets in this study, Figure 6 gives the temperature dependence of the thermal conductivities as specified by the vendor (Zircar Inc. [38]). The solid curves fitted through the data was fitted by the authors to a quadratic function of temperature.

In addition to the thermal properties of the material, the surface heat transfer coefficient h, is a measure of the transport of thermal energy across the interface between the casket and the ambient air, and in this case the surface heat transfer coefficient for free convection should be appropriate for the heated caskets in this study. However, h is a function of temperature, and h varies from point to point on a surface, and the form of h varies considerably for vertical as opposed to horizontal surfaces [45-47].

Information on the temperature dependence of the dielectric properties of the casket materials was not available from the vendor. However, Figure 7 shows the temperature variation of ε' and tan δ as a function of temperature for several different aluminas [1]. The temperature dependence for ε' and tan δ for zirconia is broadly similar to that of alumina [48]. In this study, we did not attempt to estimate the temperature dependence of ε' and tan δ since P_T was measured directly. (For the caskets, $P_T = < p_{abs}^C > V^C$ where p_{abs}

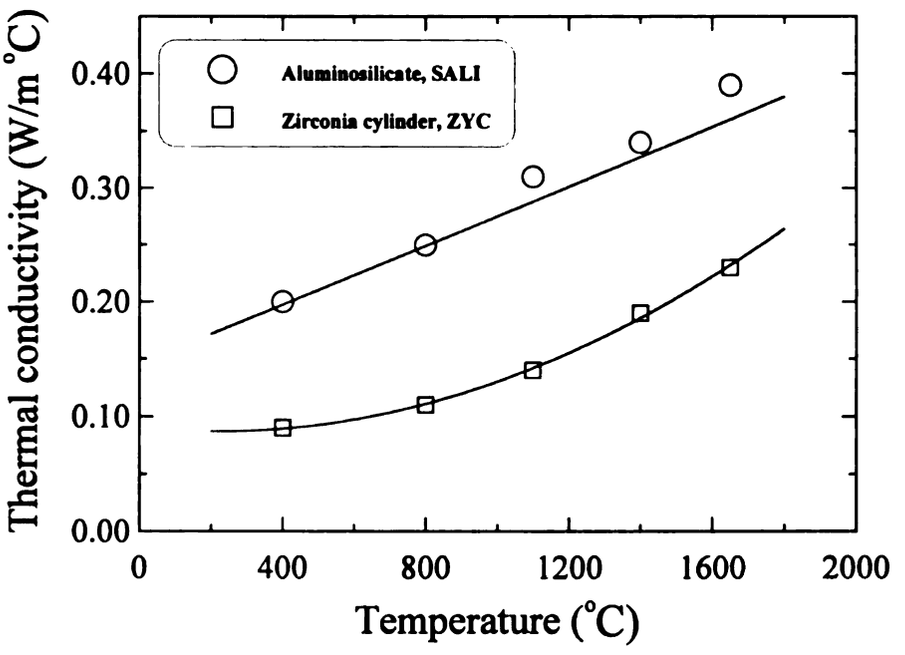

Figure 6. The temperature dependence of the thermal conductivities of the zirconia cylinders (ZYC) and aluminosilicate refractory board (SALI) as specified by the vendor (Zircar, data taken from ref. [38], curve fit done by the authors).

is a function of ε' and tan δ, as shown in equations 1 - 6.)

Since the thermal conductivity, k, the surface heat transfer coefficient, h, and the dielectric properties ε' and tan δ all are functions of temperature, and since the temperature changes as a function of position through the casket walls, then k, h, ε', and tan δ also will depend on position within the casket. In addition, material inhomogeneities in the casket material will contribute thermal local perturbations in the thermal and dielectric properties of the casket.

Also, the model presented here ignores radiative losses from the outer surface of the casket. The heat flow due to radiation goes as the fourth power of the surface temperature, and the details of the heat flow involves shape factors (not included in our

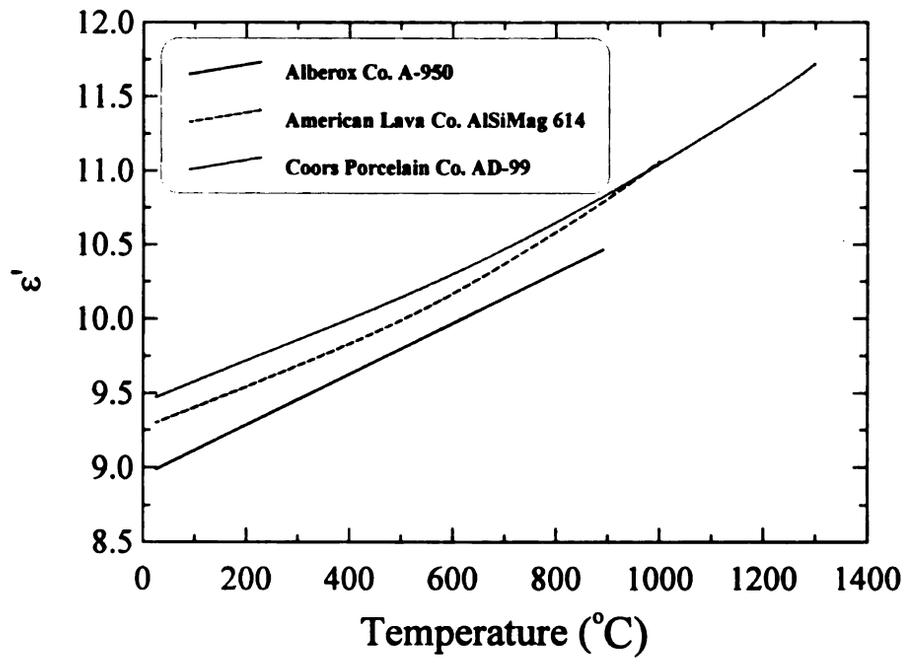

(a)

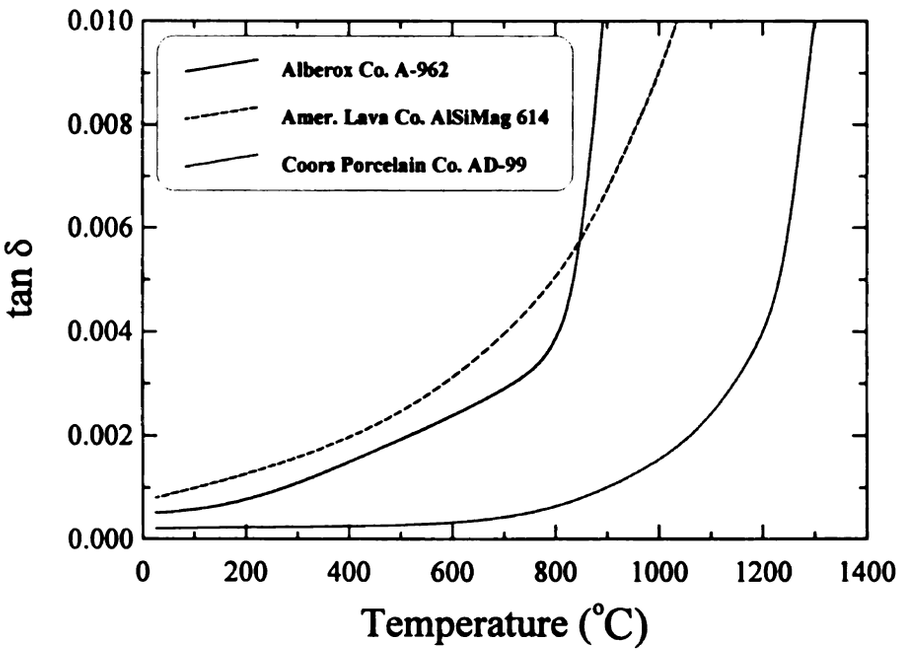

(b)

Figure 7. For various aluminas, ε′ (a) and tan δ (b) as a function of temperature (after [1]).

analysis) that are functions of the geometry of the radiating body [45].

Including the temperature dependence of the thermal or dielectric properties would make the problem mathematically nonlinear. Also, the problem becomes nonlinear if the radiative heat transfer is included. If the temperature and spatial dependencies k, h, ε', and tan δ were treated fully, along with the radiative heat transfer, the problem would be analytically intractable and numerical techniques would be required. By treating the problem in a very approximate and simplified fashion, we were still able to capture the geometric dependence of the steady-state inner wall temperature, T_i, for the cylindrical caskets included in this study.

5. RESULTS AND DISCUSSION

5.1. Dependence of the Steady-State Casket Temperature on Casket Geometry

The steady-state temperature T_i measured at the inner wall of the zirconia cylinder in the casket (Figure 8) changes as the casket geometry changes (Figures 9-11), but the trends in T_i versus geometry are not immediately obvious based on a parametric study alone. In particular, T_i is not correlated well with either the total casket volume (Figure 9) or with the ratio of total volume/total surface area of the casket (Figure 10). A plot of T_i versus the outer surface area of the casket (Figure 11) shows somewhat less scatter than T_i versus volume or T_i versus volume/surface area, although T_i versus the outer surface area shows considerable scatter. Clearly, any dependence of T_i upon casket geometry is not merely a function of only the total volume, the total surface area, or the volume/surface ratio. However, the simple heat transfer model presented in Section 4 of this paper can relate the temperature T_i to the casket geometry.

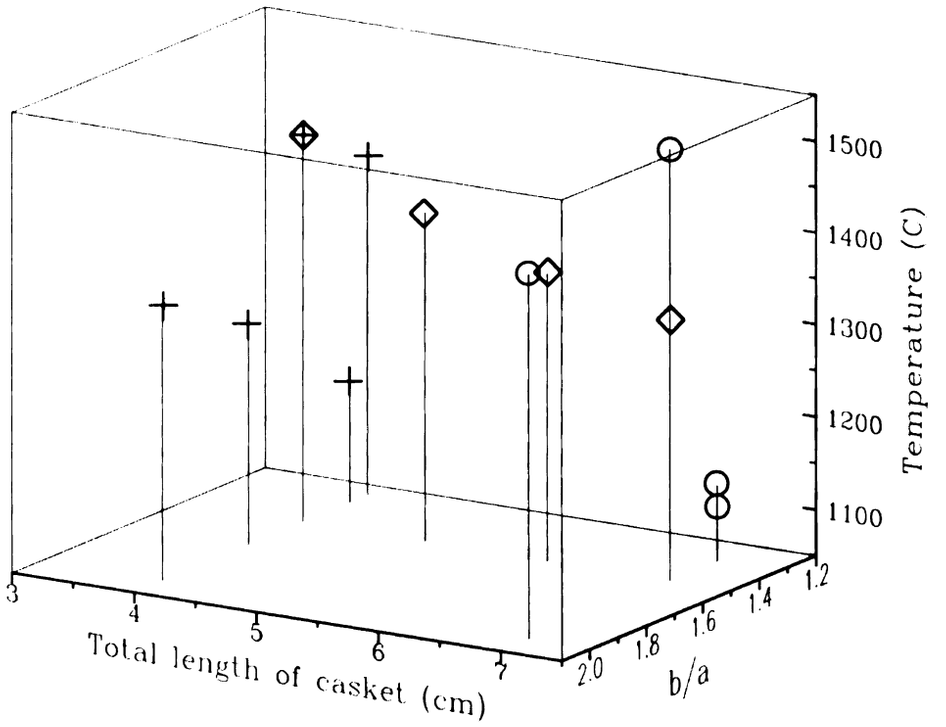

Figure 8. A three-dimensional plot of the steady-state temperature T_i measured at the inner wall of the caskets' zirconia cylinder as a function of total casket length and the radius ratio b/a.

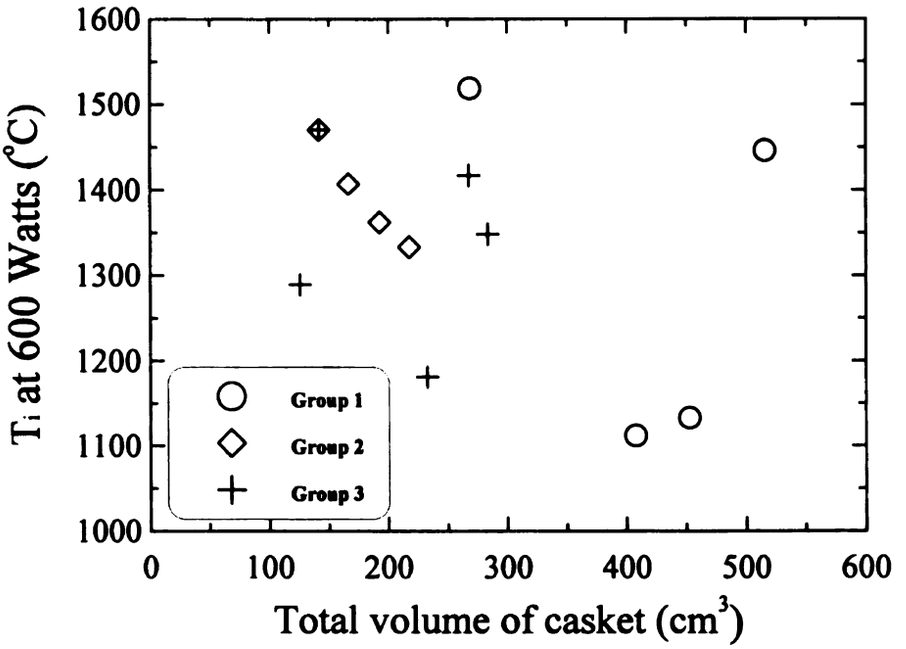

Figure 9. Measured T_i versus the total volume of each casket included in this study. Note the lack of correlation between T_i and the total volume.

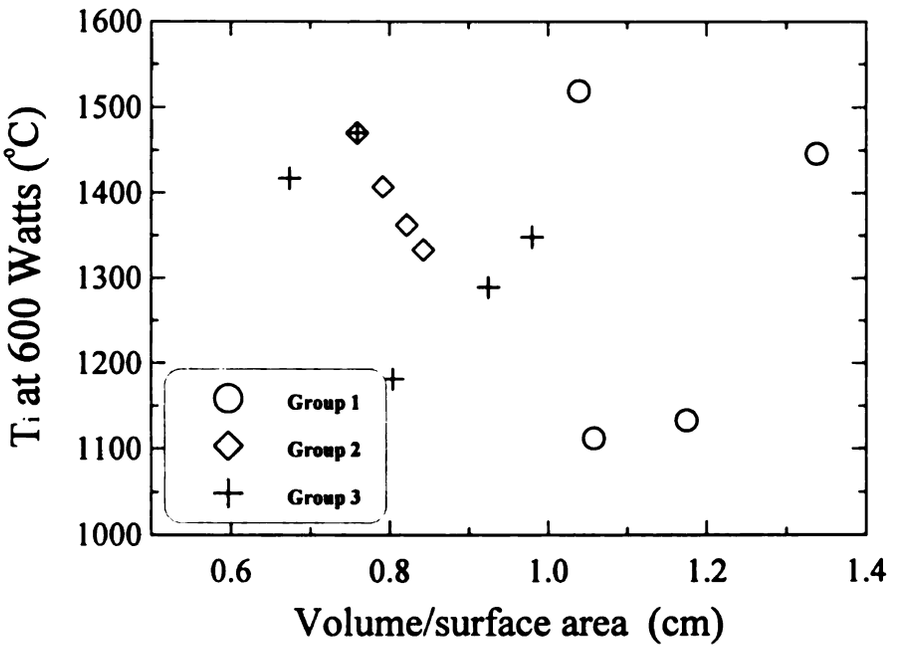

Figure 10. Measured T_i versus the ratio of total volume/total surface area of the casket. Note the lack of correlation between T_i and the volume/surface area ratio.

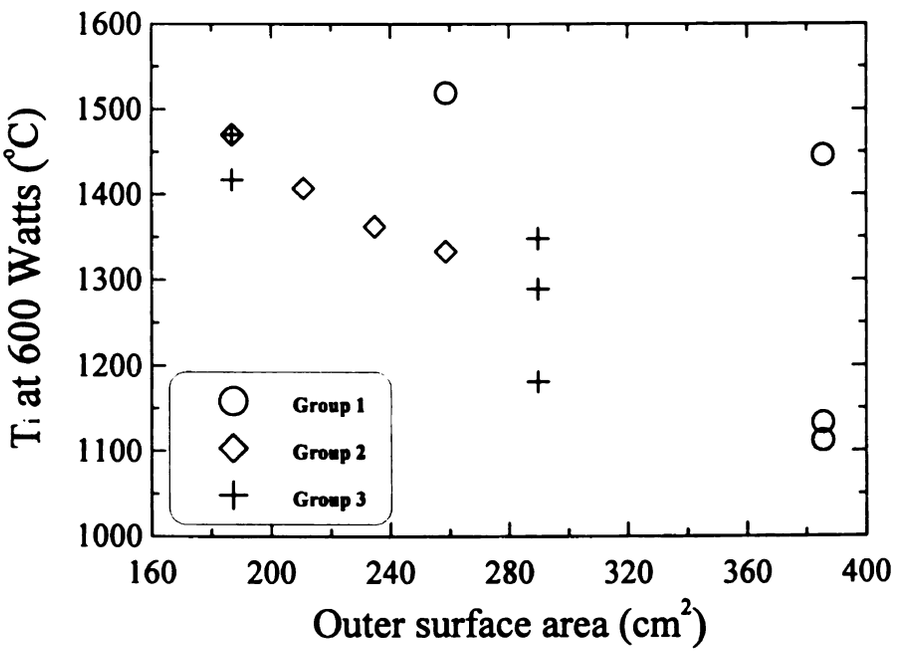

Figure 11. Measured T_i versus the outer surface area of the casket. Note the lack of correlation between T_i and the outer surface area.

For the caskets in Group 1 (Caskets 1 - 4, Table 1) the total length, L_T, was fixed at 7 cm and b/a ranged from 1.33 to 2.0. Caskets 1 - 3 had a total aluminosilicate end plate thickness, L_{SA}, equal to 4.0 cm and zirconia cylinder length, L_{Zr}, equal to 3.0 cm. For Casket 4, L_{SA} was 2.0 cm and L_{Zr} was 5.0 cm. A least-squares fit of the steady-state temperature, T_i to equation 14 for the Group 1 caskets gave a coefficient of determination, R^2, value of 0.999 (Table 6, Figure 12). In Figure 12, the lower curve was plotted setting the outer casket radius, b, equal to 0.0508 meter and the upper curve was plotted setting b equal to 0.0381 meter. Thus, although Figure 12 shows two solid curves, both curves were obtained from a single set of fitted coefficients (Table 6).

For equation 14, the independent variable is the steady-state temperature, T_i and the four dependent variables are b, a, L_T, and P_T (outer casket radius, inner casket radius, total casket length, and the measured total absorbed microwave power, respectively). For equation 24, the independent variable is T_i and there are five experimentally determined dependent variables b, a, L_{SA}, L_{Zr}, and P_T (where L_{SA} = the total thickness of the aluminosilicate end plates and L_{Zr} = the length of the zirconia cylinder). For the four caskets in Group 1, only three caskets had a fixed value of L_{SA} so that if equation 24 was used to fit the data, we could only include three data points in the least-squares fit, and equation 24 has four fitted coefficients. Thus we could not use equation 24 to attempt to fit the Group 1 data. However, for equation 14, we can use each of the four data points in Group 1 since equation 14 (which has three fitted coefficients) only requires that the total casket length, L_T, is fixed. Therefore, we used only equation 14 (Figure 12 and Table 6) to fit the Group 1 data.

Consider the caskets in Group 3 (Table 1), which includes caskets with fixed values

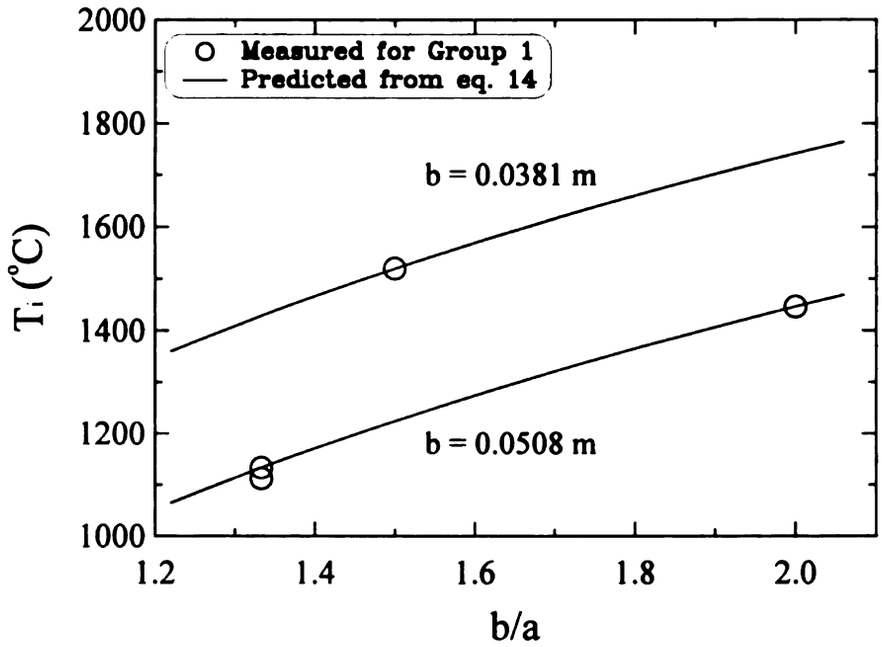

Figure 12. The inner wall temperature, T_i as a function of the ratio b/a (b = outer radius of zirconia cylinder, a = inner radius of zirconia cylinder). The least-squares fit to equation 14 describes the data well for the Group 1 caskets.

of L_T = 4.0 cm, L_{SA} = 2.0 cm, P_T = 600 Watts. The caskets include five different b/a ratios, ranging from 1.27 to 2.0, which includes the entire range of b/a ratios included in this study. A least-squares fit to equation 14 (solid curves) and to equation 24 (dashed curves) to the casket heating data shows good agreement between the measured T_i and predicted T_i values for both equations (Figure 13, Tables 6 and 8). In addition, the two equations predict very similar values of T_i over the plotted range of b/a ($1.2 < b/a < 2.0$). To illustrate the functional dependence of equation 24 on the b/a ratio, Figure 14 shows the predicted values of steady-state temperature as a function of b/a for $1 \leq b/a \leq 5$ and several values of outer radius b, given L_T = 4 cm, L_{SA} = 2.0 cm, and a fixed input power of 600 Watts.

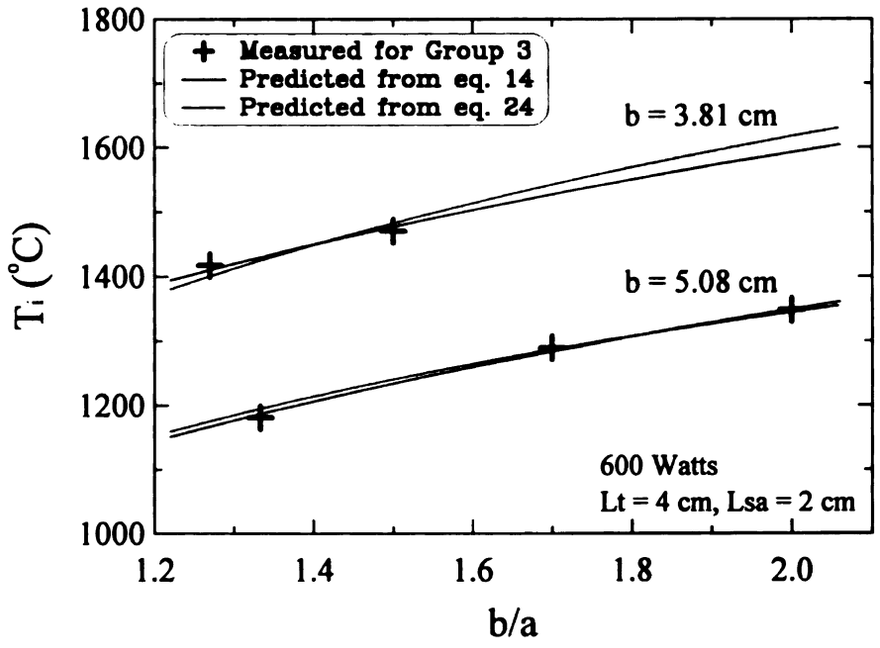

Figure 13. The inner wall temperature T_i as a function of the ratio b/a (b = outer radius of zirconia cylinder, a = inner radius of zirconia cylinder). The least-squares fit to equation 14 (solid curves) and to equation 24 (dashed curves) both describe the data well for the Group 3 caskets.

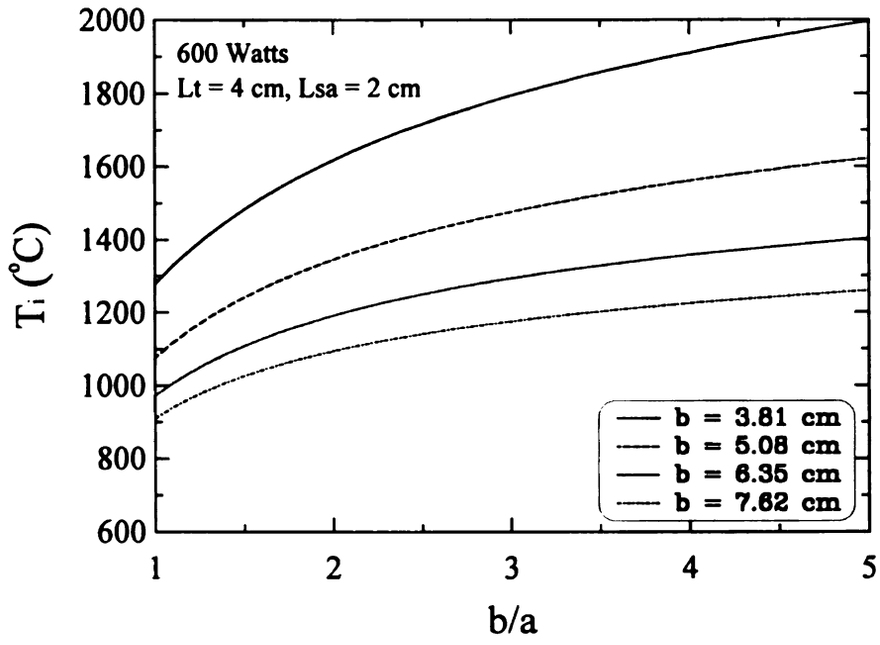

Figure 14. Using equation 24 for several different b values, the predicted values of casket steady-state temperature as a function of b/a for several values of casket outer radius b, given L_T = 4 cm, L_{SA} = 2.0 cm, and a fixed input power of 600 W.

For the caskets in Group 2, the b/a ratio is fixed at 1.5, the SALI thickness is fixed at 2.0 cm, the input power is fixed at 600 W, and the length of the zirconia cylinder ranges from 2 to 5 cm in 1 cm increments, giving a total casket length ranging from 4.0 cm to 7.0 cm (Table 1). For the Group 2 data, decrease in the steady-state temperature T_i as a function of $1/L_T$ is described very accurately by equation 15 (Table 7), corresponding to the solid curve in Figure 15. The least-squares fit of the Group 2 data to equation 24 is shown as the dashed line in Figure 15.

During the microwave heating of the Group 2 caskets, the temperature was recorded after incrementing the input power by 30 Watts, up to the maximum input power of 600 Watts. The temperature as a function of casket length for input powers of 540 W, 570 W, and 600 W are shown in Figure 16, along with a least-squares fitted line to equation 15 for each of the three different power levels. Although the heating conditions are at steady-state for the 600 W case, steady-state may not have been achieved for the measurements taken at input powers less that 600 W. For an input power, P_i, of 600 Watts, the reflected power, P_r, was only about 0.1% to 1.4% of P_i (Table 5). Thus the total power absorbed, P_T, is nearly identical to the input power, P_i (equation 2). Also, we found experimentally that P_T is very nearly equal to P_i for input powers between about 500 Watts to 600 Watts. Thus in Figure 17, we plotted the D_1 coefficients as a function of P_i rather than P_T, since for each curve in Figure 16 there are four slightly different values of P_T (one for each casket) for each of the three input power levels, but all of the P_T values are nearly the same as P_i. The fitted coefficients D_1 show a linear trend as a function of input power for 600 W, 570 W and 540 W (Figure 17). The linear trend between the coefficients D_1 and P_T (where $P_T \approx P_i$) is consistent with the predictions of

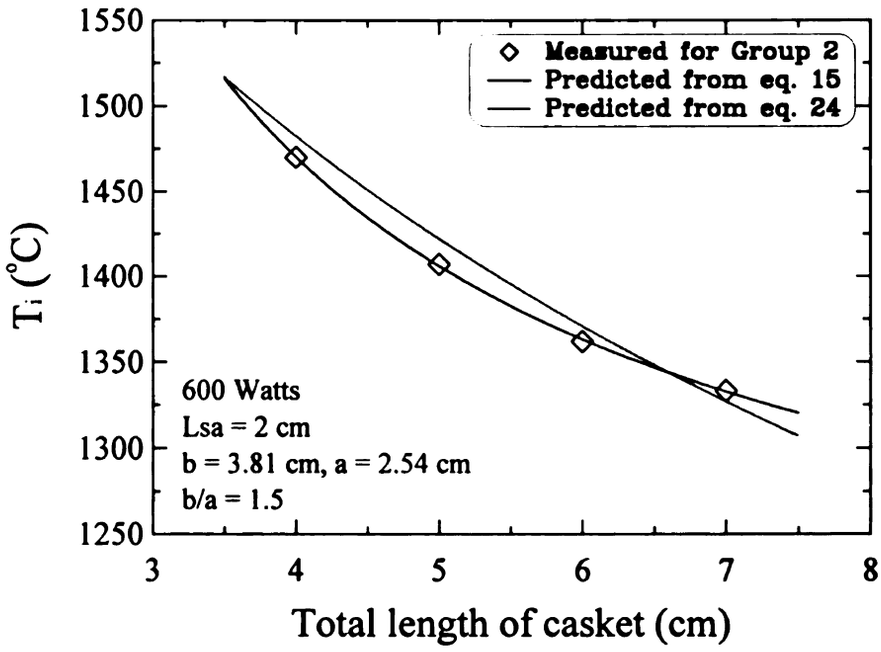

Figure 15. The steady-state temperature, T_i, as a function of the total casket length for Group 2 caskets, for which the b/a ratio is fixed at 1.5, the SALI thickness is fixed at 2.0 cm, and the input power is fixed at 600 Watts.

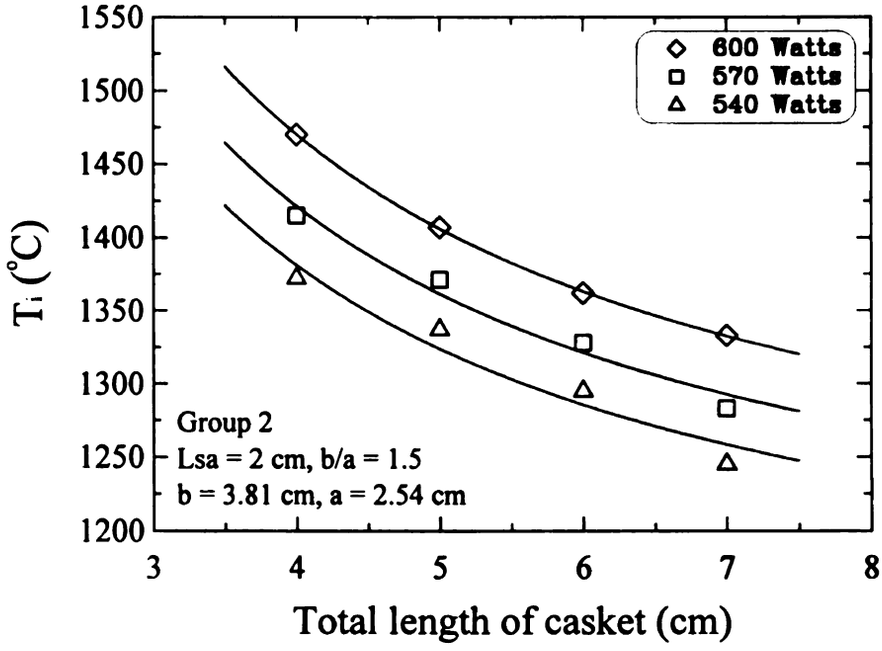

Figure 16. For the Group 2 caskets, the temperature T_i as a function of casket length for three different input power levels: 540 W, 570 W, and 600 W.

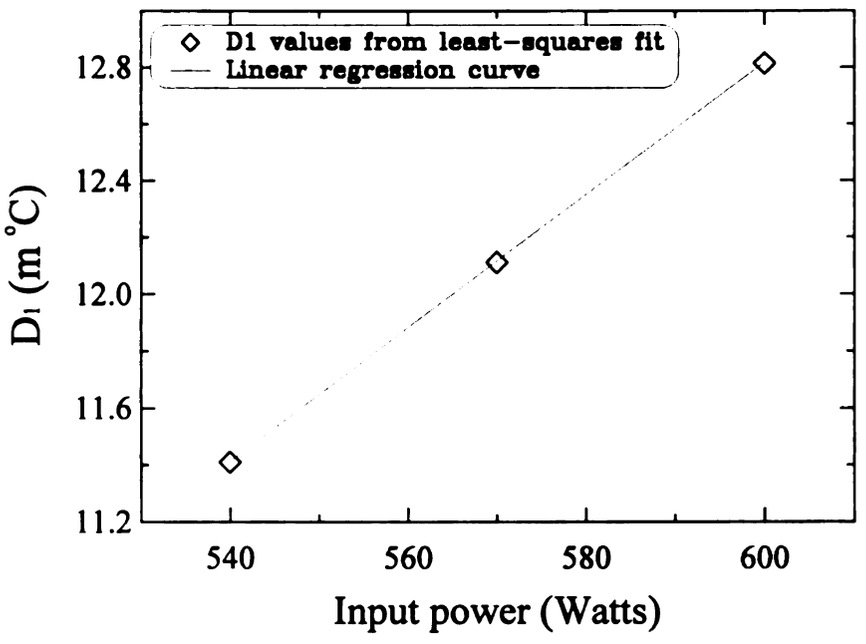

Figure 17. The D_1 versus input power, where the D_1 values were obtained by fitting the data in Figure 16 to equation 15.

equation 16.

The fitting coefficients C_1', C_2' (obtained for equation 14) and C_1, C_2, C_3 (obtained for equation 24) are functions of thermal conductivity, k, and surface heat transfer coefficient, h (equations 14a - 14b, 24a - 24c). However, the numerical values of these fitting coefficients do not agree with values calculated from our estimates of k_{eff} and <h>, the caskets' effective thermal conductivity and average surface heat transfer coefficient, respectively.

The surface heat transfer coefficient for free convection in air ranges from about 5 to 15 $W/m^2\ ^\circ C$ [49]. We chose a value of 10 $W/m^2\ ^\circ C$ for our estimate of <h> the mean value of the surface heat transfer coefficient.

To estimate the effective thermal conductivity, k_{eff}, for the caskets, we used the

relationship [50]

$$k_{eff} = k_{SA} V_{SA} + k_{Zr} V_{Zr} \quad (26)$$

where k_{SA} = thermal conductivity of the aluminosilicate (SALI) end plates

V_{SA} = volume fraction of the aluminosilicate end plates

k_{Zr} = thermal conductivity of the porous zirconia cylinders

V_{Zr} = volume fraction of the porous zirconia cylinders,

assuming that the heat flow takes place primarily parallel to the interfaces between the end plates and the cylinder. Mean values of k_{SA} = 0.30 W/m °C and k_{Zr} = 0.15 W/m °C were selected from Figure 6 for the temperature range from about 800°C to 1400°C. The values of V_{SA} and V_{Zr} were calculated from the casket dimensions (Table 1). The values of k_{eff} for the twelve caskets included in this study, as estimated from equation 26, ranged from 0.213 W/m °C to 0.265 W/m °C, with a mean value of 0.242 W/m °C.

From equation 24a, $C_1 = 1/2\pi h$. Using the <h> value of 10 W/m^2 °C, C_1 should be 0.016 m^2 °C/W, but for equation 24 the least-squares fit to the data for the full set of the twelve caskets gave a C_1 value of 0.0036 m^2 °C/W (Table 8). Thus the value of coefficient C_1 obtained from the least-squares fit of equation 24 differs by a factor of 4.4 from the estimate of C_1 based on <h> = 10 W/m^2 °C. The coefficient $C_2 = 1/2\pi k$ (equation 24b) has a value of 0.65 m °C/W based on our estimate of the caskets' k_{eff}, while C_2 obtained from the least-squares fitting was 0.106. These two values of C_2 disagree by a factor of about 6.1. The coefficient $C_3 = k/h$ (equation 24c), but the value of C_3 obtained from the least-squares fit is different by a factor of about 8.4 from the value obtained using k_{eff} and <h>. The lack of agreement likely is related to this study's exclusion of the temperature and spatial variations for the thermal and dielectric

properties. Nevertheless, the value of the coefficient C_4 obtained for equation 24 was 747°C, where C_4 corresponds to T_o the outside casket wall temperature (equation 24d). This value of C_4 is in rough agreement with the average outer wall temperature of 869°C obtained for eight caskets in Groups 2 and 3 (Table 3).

Despite the discrepancy between the fitted and the estimated coefficients, the least-squares fit of equation 24 corresponds well with T_i data. For the entire set of 12 empty caskets included in this study (Table1), the overall correlation between the measured T_i data and the T_i predictions based on equation 24 is relatively good (Table 9 and Figure 18). Eleven of the twelve data points in Figure 18 lie very close to the straight line, where the straight line corresponds to perfect agreement between the measured and predicted values.

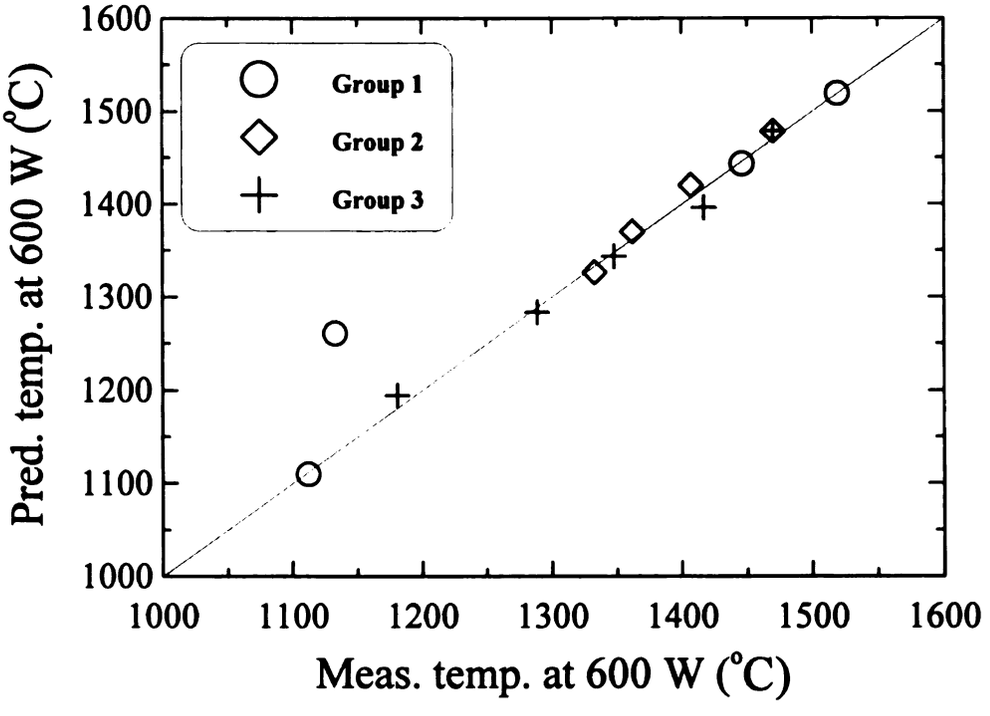

Figure 18. The measured T_i values versus the T_i values predicted on the basis of equation 24.

Table 9. Average heating rate, measured temperatures, temperatures predicted by equation 24, and residuals for the least-squares fit to the data for the entire set of empty caskets.

Group	Casket	Average heating rate from 500°C to temp. at 600 Watts (°C/min.)	Measured temp., T_m (°C)	Predicted temp., T_p (°C)	Residual, $T_m - T_p$, (°C)	$\frac{T_m - T_p}{T_m} \times 100$ (%)
1	Casket 1	12.2	1133	1261	-128	-11.3
	Casket 2	19.8	1519	1519	0	-0.0
	Casket 3	18.9	1446	1443	3	0.2
	Casket 4	12.1	1112	1110	2	0.2
2	Casket 5[a]	18.8	1470	1479	-9	-0.6
	Casket 6	18.2	1407	1420	-13	-0.9
	Casket 7	17.2	1362	1370	-8	-0.6
	Casket 8	16.4	1333	1326	7	0.5
3	Casket 5[a]	18.8	1470	1479	-9	-0.6
	Casket 9	13.5	1181	1194	-13	-1.1
	Casket 10	16.3	1348	1343	5	0.3
	Casket 11	15.5	1289	1284	5	0.4
	Casket 12	18.0	1417	1396	21	1.5

[a] Casket 5 is included in both Group 2 and Group 3.

5.2. Comparison of Steady-State Temperature and Heating Rate for Empty Casket and Casket with a Processed Material

In Section 5.1, the T_i data that is fit to equations 14, 15, and 24 corresponds to: (i) Group 1 caskets, which include an aluminosilicate refractory board setter and no specimen and (ii) Groups 2 and 3 caskets, which do not include either a specimen or a specimen setter. By reheating caskets 6 and 9 with powder compact specimens present, we seek to determine how the steady-state casket temperature, T_i differs for the empty casket case compared to the casket loaded with specimens.

For Casket 6, the steady-state inner casket wall temperature T_i for the empty casket was 1407°C, while T_i was 1416°C for reheating Casket 6 loaded with a 2.0 gram alumina/15 wt% zirconia specimen (Table 10 and Figure 5). Furthermore, the heating rate from 500°C to T_i was very similar for Casket 6, with and without the 2.0 gram specimen present (Table 10). Thus for Casket 6, where the specimen-to-casket volume ratio was 0.005 and the specimen-to-casket mass ratio was 0.02, the specimen did not greatly perturb the value of T_i from that obtained for the empty casket (Table 10). However, for Casket 9, the steady-state inner casket wall temperature T_i for the empty casket was 1181°C, while T_i was 1257°C for reheating Casket 9 loaded with a 20 gram alumina specimen (Table 10 and Figure 5). Also, the heating rate from 500°C to T_i was somewhat higher when Casket 9 was loaded with the 20 gram alumina specimen (Table 10). For Casket 9, where the specimen-to-casket volume ratio was 0.03 and the specimen-to-casket mass ratio was 0.16, the 20 gram specimen did significantly perturb the value of T_i from that obtained for the empty casket (Table 10).

Table 10. Comparison of the heating characteristics for two empty caskets and the same two caskets with specimens.

System		Casket volume (cm^3)	Volume ratio of specimen to casket	Casket mass (g)	Mass ratio of specimen to casket	Total absorbed power, P_T (Watts)	Heating rate from 500°C to temp. at 600 W (°C/min.)	Steady-state temp. at 600 W (°C)
Casket	Without specimen	167.2	[a]	84	[a]	598.5	18.2	1407
6	With specimen	168.0	0.005	86	0.02	599.0	18.0	1416
Casket	Without specimen	233.1	[a]	129	[a]	599.5	13.5	1181
9	With specimen	240.3	0.03	149	0.16	596.4	15.1	1257

[a] Not available

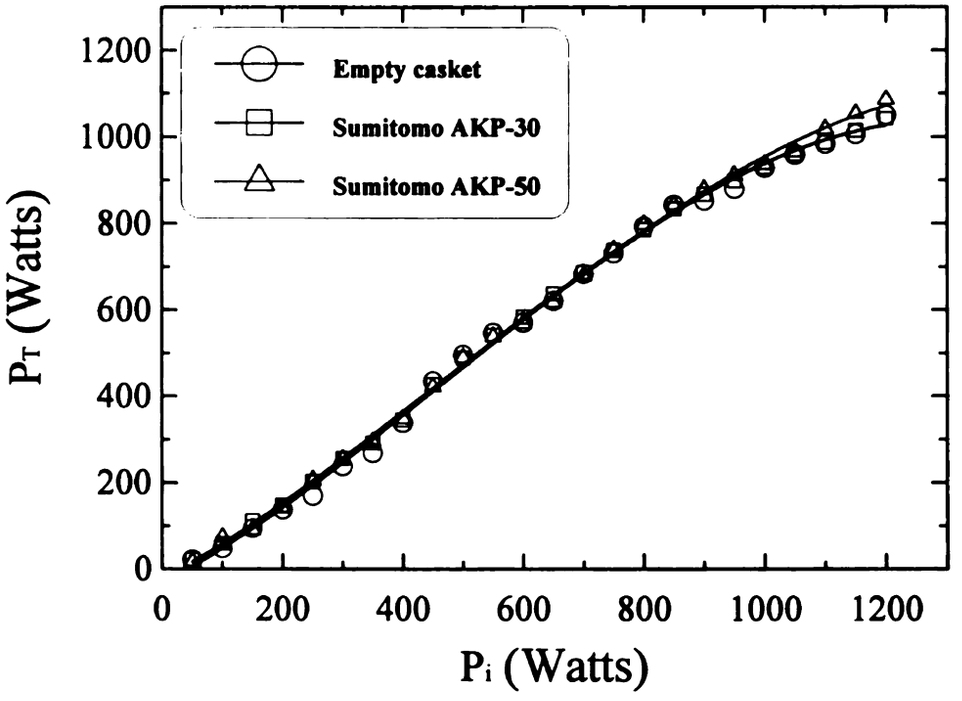

Figure 19. The total power absorbed, P_T, versus the input power for two sintering runs for Sumitomo AKP30 and AKP50 alumina in Casket 1, compared to a heating run for Casket 1 with no specimen included.

In addition, in separate sintering experiments using Casket 1, two microwave sintering runs were done, each including either a single 2 gram specimen of Sumitomo AKP30 or a single 2 gram specimen of Sumitomo AKP50. The absorbed power versus input power for the two sintering experiments were each nearly identical to the absorbed power versus input power for a heating run done for an empty Casket 1 (no specimen present) (Figure 19). For the two sintering runs and the empty casket, a steady-state temperature of 1575°C was achieved with a 1200 Watts input power for AKP30 sintering experiment and the empty casket, and with 1225 Watts input power for the AKP50 specimen. Thus in these sintering experiments where the specimen mass and volume is small compared to the casket mass and volume, the steady-state inner wall casket temperature, T_i, is essentially identical whether or not a specimen is present. This is important, since if we can predict T_i for an empty casket, then we can also predict the steady-state (i.e. the sintering) temperature for caskets that include processed specimens.

Therefore, although the total absorbed microwave power may be partitioned between the casket and the specimen, the casket can play a dominate role in microwave hybrid heating. The effect of specimen mass or volume on microwave hybrid heating should be studied further.

5.3. Dependence of Heating Characteristics on Microwave Cavity Modes

Since every microwave cavity resonance mode has a unique electromagnetic field pattern [51, 52], and because p_{abs} and P_T are functions of the local electric field strength (equations 1 - 6), microwave heating using different cavity modes might give different steady-state temperatures. To explore this effect [37], the authors heated Caskets 1, 2, 3,

and 4 using eight different cavity modes, corresponding to eight different resonance lengths (cavity lengths) (Table 4). For example, with Casket 1 heated at 600 Watts, the steady-state inner casket wall temperature ranged from 1055°C to 1186°C for the entire set of eight modes, which corresponds to a maximum difference of 131°C in the steady-state temperature for heating in the various cavity modes. However, for the 12 caskets included in this study (which were heated in a single mode) the differing casket geometry resulted in a maximum difference of 407°C in the steady-state temperature. Thus the temperature differences induced by changing modes for a fixed casket geometry can be much less than the temperature differences induced by changing the casket geometry. Details of the difference in heating behaviors as a function of changing the electromagnetic mode will be discussed in a forth-coming paper by the present authors [37].

6. CONCLUSIONS

Using simple heat transfer concepts, we have developed a model that captures the geometric dependence of the steady-state inner casket wall temperature T_i as a function of casket geometry.

For a fixed microwave input power, the steady-state temperature T_i for microwave "caskets" (specimen enclosures) can vary significantly as the casket geometry changes. For an input power of 600 Watts, the steady-state temperature ranged from 1112°C to 1519°C for caskets composed of porous zirconia cylinders with aluminosilicate end plates.

Knowing that (1) the absorbed microwave power is proportional to the volume of

the dielectric material (equation 1 and references 34, 35, 44) and that (2) the heat flow out from the cylindrical casket is proportional to the surface area of the casket [34, 35, 44] is not sufficient to describe the geometrical dependence of the steady-state temperature, as demonstrated by Figures 9 - 11, where T_i does not correlate well with the surface area, volume, or volume/surface area of the caskets. However, equations 14, 15, and 24 in Section 4.0 can describe the geometric dependence of T_i (Figures 12, 13, 15, 16, and 18) and the manner in which T_i scales with input power (Figure 17).

At a fixed input power of 600 Watts, (Figures 12, 13, 15 and Table 6) equation 14 fits the data very well for Group 1 (L_T fixed, L_{SA}, L_{Zr}, and b/a vary), Group 2 (b/a fixed, L_T varies), and Group 3 (L_T, L_{SA}, and L_{Zr} fixed, b/a varies). Equation 15, which is a simplified version of equation 14 (Section 4), fits well the Group 2 casket data for the case where three different values of input power were used. Also, the coefficients D_1 obtained by fitting the data for the Group 2 caskets heated at three different input power levels, follows the linear trend with P_T predicted by equation 16 (Figure 18). Thus, this analysis shows how the steady-state casket temperature scales with input power.

Although equation 14 fails to describe the entire dependence of T_i on casket geometry for the entire data set of empty caskets where each of the geometric variables (L_T, L_{ZR}, L_{SA}, a, b, and b/a can vary), equation 24 does describe the full data set well (Table 9 and Figure 18).

In addition to presenting experimental evidence for the dependence of steady-state temperature on casket geometry and developing simple equations to describe that dependence, we have shown that for the lossy dielectric casket materials used in this study, the casket temperature was only slightly perturbed by the presence of a specimen

with a volume and mass that was small compared to the casket volume and mass. However, for a relatively "large" specimen, whose mass was about 0.16 of the casket mass, the temperature perturbation was significant. The steady-state empty casket temperature was 1181°C and the steady-state temperature of the casket plus the large specimen was 1257°C, which was a specimen-induced steady-state temperature shift of 76°C.

The simple models presented in this study ignore the temperature and spatial dependencies of k, h, ε', and tan δ along with ignoring the radiative heat losses. An equation for heat flow in an infinite hollow cylinder (equation 9) was the starting point of the analysis, thus end effects due to the finite cylinder length are neglected for the equations given in Section 4. Also, the coefficients obtained from the least-squares fitting of the T_i data do not agree with the value of the coefficients calculated from our estimates k_{eff} and <h> (Section 5.1). The lack of agreement likely stems, at least in part, from neglecting the spatial and temperature dependencies of the thermal and dielectric parameters. However, treating these dependencies in detail would require numerical techniques, which lack advantage of providing a straightforward analytical expression for the functional dependence of T_i.

ACKNOWLEDGEMENTS

The authors acknowledge the financial support of the Michigan Research Excellence Fund provided through the Electronic and Surface Properties of Materials Center, Michigan State University.

REFERENCES

1. Westphal WB and Sils A (1972) Dielectric Constant and Loss Data, Technical Report AFML-TR-72-39, Massachusetts Institute of Technology, Cambridge, MA.

2. Holcombe CE and Dykes NL (1990) J. Matl. Sci. Lett. 9:425.

3. Janney MA, Kimrey HD, Schmidt MA, and Kiggans JO (1991) J. Am. Ceram. Soc. 74[7]:1675.

4. McGill SL, Walkiewicz JW, and G.A. Smyres (1988) The Effect of Power Level on the Microwave Heating of Selected Chemical Minerals. In: Sutton WH, Brooks MH and Chabinsky IJ (eds) Microwave Processing of Materials, Mat. Res. Soc. Proc., vol. 124, Materials Research Society, Pittsburgh, Pennsylvania, pp. 247-252.

5. Patil DS, Mutsuddy BC, Gavulic J, and Dahimene M (1991) Microwave Sintering of Alumina Ceramics in a Single Mode Applicator. In: Clark DE, Gac FD, and Sutton WH (eds) Microwaves: Theory and Application in Materials Processing, Cer. Trans. vol. 21, Amer. Cer. Soc., Westerville, Ohio, pp. 301-309.

6. Kimrey HD, Kiggans JO, Janney MA, and Beatty RL (1990) Microwave Sintering of Zirconia-Toughned Alumina Composites. In: Snyder WB, Jr., Sutton WH, Iskander MF and Johnson DL (eds) Microwave Processing of Materials II, Mat. Res. Soc. Symp. Proc. vol. 189, Materials Research Society, Pittsburgh, Pennsylvania, pp. 243-256.

7. Lorenson CP, Patterson MCL, Risto G, and Kimber R (1992) The Effect of Particle Size on Microwave Heated Carbon and The Subsequent Crystallite Growth. In: Beatty RL, Sutton WH and Iskander MF (eds) Microwave Processing of Materials III, Mat. Res. Soc. Symp. Proc. vol. 269, Materials Research Society, Pittsburgh, Pennsylvania, pp. 129-136.

8. Boch Ph, Lequeux N, and Piluso P (1992) Reaction Sintering of Ceramic Materials by Microwave Heating. In: Beatty RL, Sutton WH and Iskander MF (eds) Microwave Processing of Materials III, Mat. Res. Soc. Symp. Proc. vol. 269, Materials Research Society, Pittsburgh, Pennsylvania, pp. 211-216.

9. Holcombe CE and Dykes NL (1991) Ultra High-Temperature Microwave Sintering. In: Clark DE, Gac FD, and Sutton WH (eds) Microwaves: Theory and Application in Materials Processing, Cer. Trans. vol. 21, Amer. Cer. Soc., Westerville, Ohio, pp. 375-386.

10. Patterson MCL, Apte PS, Kimber RM, and Roy R (1992) Batch Process for Microwave Sintering of Si_3N_4. In: Beatty RL, Sutton WH and Iskander MF (eds) Microwave Processing of Materials III, Mat. Res. Soc. Symp. Proc. vol. 269, Materials Research Society, Pittsburgh, Pennsylvania, pp. 291-300.

11. Katz JD, and Blake RD (1991) Amer. Cer. Soc. Bull. 70[8]:1304.

12. Agrawal DK, Fang Y, Roy DM, and Roy R (1992) Fabrication of Hydroxyapatite Ceramics by Microwave Processing. In: Beatty RL, Sutton WH and Iskander MF (eds) Microwave Processing of Materials III, Mat. Res. Soc. Symp. Proc. vol. 269, Materials Research Society, Pittsburgh, Pennsylvania, pp. 231-236.

13. Fang Y, Agrawal DK, Roy DM and Roy R (1991) Rapid Sintering of Hydroxyapatite Ceramics by Microwave Processing. In: Clark DE, Gac FD, and Sutton WH (eds) Microwaves: Theory and Application in Materials Processing, Cer. Trans. vol. 21, Amer. Cer. Soc., Westerville, Ohio, pp. 349-356.

14. Lee KY, Case ED, Asmussen J, Jr., and Siegel M (1995) Sintering of Alumina Ceramics in a Single Mode Cavity under Automated Control. In: Microwaves: Theory and Application in Materials Processing III, Cer. Trans., vol. 59, Amer. Cer. Soc., Westerville, OH, pp. 473-480 .

15. Lee KY, Case ED, Asmussen J, Jr., and Siegel M (1995) Microwave Sintering of Ceramic Matrix Composites and the Effect of Organic Binders on the Sinterability. In: Proceedings of the 11th Annual ESD Advanced Composites Conference, Ann Arbor, MI, pp. 491-503.

16. Lee KY, Cropsey L, Tyszka B, and Case ED (1997) Materials Research Bulletin 32[3]:287.

17. Lee KY, Case ED, and Asmussen J, Jr. (1997) Microwave Binder Burn-out for Batch Processing of Al_2O_3, Al_2O_3/SiC Platelet, and Al_2O_3/ZrO_2 Particle Powder Compacts. In: Microwaves: Theory and application in materials processing, IV, Cer. Trans., vol 80, Amer. Cer. Soc., Westerville, OH, pp. 539-546.

18. Meek TT, Blake RD, and Petrovic JJ (1987) Microwave Sintering of Al_2O_3 and Al_2O_3-SiC Whisker Composites. In: Cer. Eng. Sci. Proc. vol. 8 [7-8], pp. 861-71.

19. Cheng J, Qiu J, Zhou J, and Ye N (1992) Densification Kinetics of Alumina During Microwave Sintering (1992). In: Beatty RL, Sutton WH and Iskander MF (eds) Microwave Processing of Materials III, Mat. Res. Soc. Symp. Proc. vol. 269, Materials Research Society, Pittsburgh, Pennsylvania, pp. 323-328.

20. Kiggans JO, Jr., and Tiegs TN (1992) Characterization of Sintered Reaction-Bonded Silicon Nitride Processed by Microwave Heating (1992). In: Beatty RL, Sutton WH and Iskander MF (eds) Microwave Processing of Materials III, Mat. Res. Soc. Symp. Proc. vol. 269, Materials Research Society, Pittsburgh, Pennsylvania, pp. 285-290.

21. Tiegs TN, Kiggans JO, Jr., and Kimrey HD, Jr. (1990) Microwave Processing of Silicon Nitride. In: Snyder WB, Jr., Sutton WH, Iskander MF and Johnson DL (eds) Microwave Processing of Materials II, Mat. Res. Soc. Symp. Proc. vol. 189, Materials Research Society, Pittsburgh, Pennsylvania, pp. 267-272.

22. Janney MA, Calhoun CL, and Kimrey HD (1991) Microwave Sintering of Zirconia-8 mol % Yttria. In: Clark DE, Gac FD, and Sutton WH (eds) Microwaves: Theory and Application in Materials Processing, Cer. Trans. vol. 21, Amer. Cer. Soc., Westerville, Ohio, pp. 311-318.

23. Janney MA, Calhoun CL, and Kimrey HD (1992) J. Am. Cer. Soc. 75[2]:341.

24. Jackson HW, Barmatz M, and Wagner P (1993) Transient Temperature Behavior of a Sphere Heated by Microwaves. In: Clark DE, Tinga TR, and Laia JR, Jr. (eds) Microwaves, Theory and Applications in Materials Processing II, Cer. Trans. vol 36, Amer. Cer. Soc., Westerville, OH, pp. 189-199.

25. Kriegsmann GA (1991) Microwave Heating in Ceramics. In: Clark DE, Gac FD, and Sutton WH (eds) Microwaves: Theory and Application in Materials Processing, Cer. Trans. vol. 21, Amer. Cer. Soc., Westerville, Ohio, pp. 177-183.

26. Kriegsmann GA (1992) Thermal Runaway and its Control in Microwave Heated Ceramics (1992). In: Beatty RL, Sutton WH and Iskander MF (eds) Microwave Processing of Materials III, Mat. Res. Soc. Symp. Proc. vol. 269, Materials Research Society, Pittsburgh, Pennsylvania, pp. 257-264.

27. Kriegsmann GA (1993) J. Appl. Phys. 71:1960.

28. Reimbert CG, Minzoni AA, and Smyth NF (1996) IMA Journal of Applied Mathematics 57:165.

29. Chapman B, Iskander MF, Smith RL, and Andrade OM (1992) Simulation of Sintering Experiments in a Single-Mode Cavity (1992). In: Beatty RL, Sutton WH and Iskander MF (eds) Microwave Processing of Materials III, Mat. Res. Soc. Symp. Proc. vol. 269, Materials Research Society, Pittsburgh, Pennsylvania, pp. 53-59.

30. Tucker J, Smith R, Iskander MF, and Andrade CM (1992) Dynamic Model for Calculating Heating Patterns During Microwave Heating (1992). In: Beatty RL, Sutton WH and Iskander MF (eds) Microwave Processing of Materials III, Mat. Res. Soc. Symp. Proc. vol. 269, Materials Research Society, Pittsburgh, Pennsylvania, pp. 61 - 67.

31. Tucker J, Iskander MF, and Huang Z (1994) Calculation of heating patterns in microwave sintering using a 3D finite-difference code. In: Iskander MF, Lauf RJ and Sutton WH (eds) Microwave Processing of Materials IV, Mat. Res. Soc. Symp. Proc. vol. 347, Materials Research Society, Pittsburgh, Pennsylvania, pp. 353-362.

32. Jackson HW and Barmatz M (1991) J. Appl. Phys. 70:5193.

33. Barmatz M and Jackson HW (1992) Steady State Temperature Profile in a Sphere Heated by Microwaves (1992). In: Beatty RL, Sutton WH and Iskander MF (eds) Microwave Processing of Materials III, Mat. Res. Soc. Symp. Proc. vol. 269, Materials Research Society, Pittsburgh, Pennsylvania, pp. 97 - 103.

34. Johnson DL, Skamser DJ, and Spotz MS (1993) Temperature Gradients in Microwave Processing: Boon and Bane. In: Clark DE, Tinga WR, and Laia JR, Jr. (eds) Microwaves, Theory and Applications in Materials Processing II, Cer. Trans. vol 36, Amer. Cer. Soc., Westerville, OH, pp. 133-146.

35. Spotz MS, Skamser DJ, and Johnson DL (1995) J. Am. Ceram. Soc. 78[4]:1041.

36. Skamser DJ and Johnson DL (1994) Simulation of Hybrid Heating. Iskander MF, Lauf RJ, and Sutton WH (eds) Microwave Processing of Materials IV, Mat. Res. Soc. Symp. Proc. vol 347, Materials Research Society, Pittsburgh, Pennsylvania, pp. 325-330.

37. Lee KY, Case ED and Asmussen J, Jr., to be pulished.

38. Zircar Fibrous Ceramics Catalog (December, 1995) Zircar Products Inc., Florida, New York.

39. Asmussen J and Garard R (1988) Precision Microwave Applicators and Systems for Plasma and Materials Processing. In: Sutton WH, Brooks MH and Chabinsky IJ (eds) Microwave Processing of Materials, Mat. Res. Soc. Proc., vol. 124, Materials Research Society, Pittsburgh, Pennsylvania, pp. 347-352.

40. Asmussen J., Lin HH, Manring B, and Fritz R (1987) Rev. Sci. Instrum. 58[8]:1477.

41. Lee KY, Case ED, Asmussen J, Jr., and Siegel M (1996) Scripta Materialia 35[1]:107.

42. Lee KY, Case ED, and Reinhard D (1997) Microwave Joining and Repair of Ceramics and Ceramic Composites. In: Cer. Eng. and Sci. Proc. 18:543-550.

43. Mak P and Asumssen J (1997) J. Vac. Sci. Technol. A15(1):154-168.

44. Carslaw HS and Jaeger JC (1959) Conduction of Heat in Solids, 2nd ed., Oxford University Press, Fair Lawn, NJ, pp. 19, 188-190.

45. Kreith F (1972) Chapters 2, 5, and 7 in Principles of Heat Transfer, Third Edition, International Textbook Company, Scranton, PA,.

46. Beck JV, Blackwell B, and Clair CR, Jr. (1985) Inverse Heat Conduction, Wiley-Interscience, New York, pp. 281-300 .

47. Gebhart B (1993) Heat Conduction and Mass Diffusion, McGraw-Hill, New York, pp. 48-52, 64-71, 139-144.

48. Binner J, Cross T and Greenacre N (1997). In: Abstract Book for First World Congress on Microwave Processing, Lake Buena Vista, Florida, pp. 47.

49. Karlekar BV and Desmond RM (1977) Engineering Heat Transfer, West Publishing Co., New York, pp. 8, 14.

50. Kingery WD, Bowen HK, and Uhlmann DR (1991) Introduction to Ceramics, 2nd edition, John Wiley & Sons, Inc., New York, pp. 634-637, 822.

51. Liao SY (1990) Microwave Devices and Circuits, 3rd ed., Prentice Hall, New Jersey, pp. 136-138.

52. Pozar DM (1990) Microwave Engineering, Addison-Wesley Publishing Company, Inc., New York, pp. 348-353.

Part II. STEADY-STATE TEMPERATURE OF MICROWAVE-HEATED REFRACTORIES AS A FUNCTION OF MICROWAVE POWER AND REFRACTORY GEOMETRY[2]

ABSTRACT

Using a simple energy balance model developed in a previous paper, this study presents an improved least-squares fitting equation that relates T_i (the steady-state inside wall temperature for hollow cylindrical refractory caskets) to microwave input power and to casket geometry parameters. For microwave input power ranging from 200 Watts to 700 Watts, we measured 132 new casket/input power combinations, adding to the authors' earlier data characterizing twelve different casket geometries at a fixed input power of 600 Watts. When such caskets are used for the microwave processing of ceramic materials, T_i is very significant since it approximates the processing temperature within the casket.

1. INTRODUCTION

1.1. Background

The authors and co-workers have measured and modeled steady-state temperatures for refractory caskets heated in a single-mode microwave cavity [1]. Such refractory caskets are widely used as insulation and/or susceptor materials for the microwave processing of ceramics. While the previous study investigated trends in steady-state temperature mainly as a function of casket geometry [1], this paper considers both geometrical effects and the

2 K.Y. Lee and E.D. Case, submitted for publication, Materials Science & Engineering A (1998).

microwave input power level effects on the steady-state casket temperature. From this point on in this paper, we shall refer to this previous study [1] as Paper 1.

The authors and co-workers have used refractory caskets consisting of porous zirconia cylinders with refractory fiberboard end plates (Figure 1) for various types of microwave ceramic processing, including sintering, joining, crack healing, thermal etching, and binder burn-out of ceramics [2-12]. For example, the authors and co-workers have microwave-sintered various aluminas [2,6], alumina/zirconia particulate composites [3], and yttria stabilized zirconia [10] using such refractory caskets (Figure 1). In addition, the authors have studied ceramic-ceramic joining for alumina [7,8], MaCor [7,8], and zirconia [10] as well as crack healing behavior in alumina [7,9] and thermal etching in polycrystalline alumina [11,12]. During binder burn-out studies for alumina and alumina/zirconia powder compacts, the present authors and co-workers used refractory caskets [3], but subsequent binder burn-out work on Al_2O_3, Al_2O_3/SiC platelets, and Al_2O_3/ZrO_2 particle powder compacts was done without a casket [4,5]. (Not using a refractory casket during binder burn-out allows volatiles generated during burn-out to escape more effectively than when a casket is used [4,5].) Other researchers have also used porous zirconia cylinders for refractory casket materials during microwave sintering of ceramics [13,14].

1.2. Authors' Previous Analytical Model for Refractory Casket Heating

In Paper 1 [1], a simple model for the steady-state temperature inside a microwave-heated refractory casket was obtained by balancing the total power absorbed by the casket and the thermal energy per unit time that flows out from the casket walls. This section briefly summarizes that model [1].

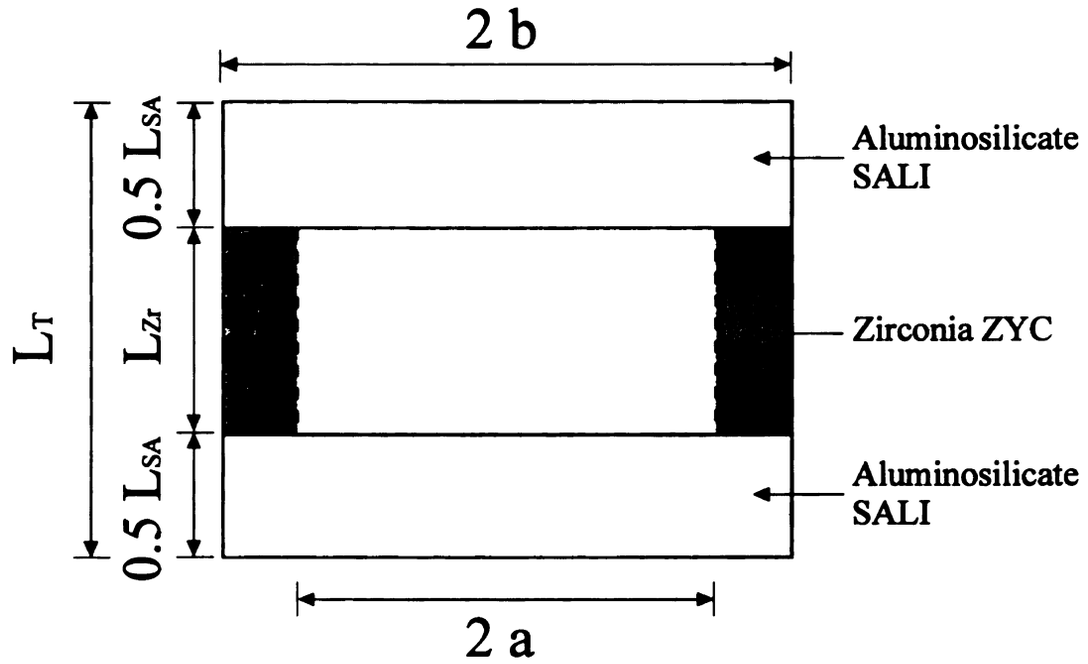

Figure 1. Schematic of a refractory casket, showing a cross-sectional view of the hollow ZYC cylinder and the aluminosilicate disk-shaped end plates [1]. The symbols a, b, L_{SA}, L_{Zr}, and L_T are as defined in equation 5.

For a microwave cavity, the cavity "load" may be defined as those materials or objects added to an ideal empty cavity that absorbs microwave energy (an ideal empty cavity would not absorb energy even at the cavity wall). For a system consisting of a microwave cavity loaded with a lossy refractory casket and a lossy ceramic specimen, the total power, P_T, absorbed by the system is [1]

$$P_T = P_I - P_R = P_W + P_C + P_S \tag{1}$$

where P_I = microwave input power

P_R = reflected microwave power

P_W = power dissipated by the cavity wall

P_C = power absorbed by the casket

P_S = power absorbed by a processed specimen.

If we define p_{abs} as an absorbed energy per unit volume, then P_C and P_S are the spatial averages of p_{abs} integrated over the appropriate material volumes, such that

$$P_C = \int_{V_C} p_{abs} dV \tag{2a}$$

$$P_S = \int_{V_S} p_{abs} dV \tag{2b}$$

where in the above integrals, V_C represents the casket volume and V_S represents the specimen volume. For a dielectrically lossy cavity load, most of the microwave input power is absorbed by the casket plus specimen combination, such that P_W can be neglected.

When no specimen is present in the cavity, the total microwave power absorbed by the casket alone may be approximated as

$$P_T = P_W + P_C . \tag{3}$$

If the relative wall loss << the power absorbed by the casket for the entire range of the microwave input power, then the microwave power absorbed by the casket during heating at a given input power level is

$$P_C \approx P_T . \tag{4}$$

During microwave heating, a steady-state refractory casket temperature is achieved when the power absorbed by the casket, P_C, is balanced by the outflow of thermal energy, such that

$$P_C = 2\pi k(T_i - T_o)\left[\frac{HbL_T}{1 + Hb\ln(b/a)} + \frac{2b^2}{L_{SA}}\right] \tag{5}$$

where k = thermal conductivity

T_i = temperature at inner wall of hollow cylinder

T_o = temperature at outer wall of hollow cylinder

H = h/k

h = surface heat transfer coefficient for the cylinder

$L_T = L_{SA} + L_{Zr}$ = total length of the casket, where

L_{Zr} = length of zirconia cylinder

L_{SA} = total thickness of the end plates

b = outer radius of the cylinder

a = inner radius of the cylinder.

In this paper we assumed that $P_C = P_I - P_R$. Rewriting equation 5 gives [1]

$$T_i = \frac{P_C}{2\pi k} \cdot \frac{L_{SA}\left[\frac{1}{H} + b\ln(b/a)\right]}{bL_T L_{SA} + 2b^2\left[\frac{1}{H} + b\ln(b/a)\right]} + T_o \qquad (6)$$

Equation 6 was derived using a number of simplifying assumptions [1]. For example, the heat flow expression from Carslaw and Jaeger [15] used to derive equation 6 assumed an infinite hollow cylinder with heat generated within the cylinder wall. The actual caskets are of finite length. Also, the heat flow through the end plates was modeled in terms of a simple linear addition of terms describing heat flow through a plate.

In addition to the simplifications involving the heat flow equations [1], equation 6 ignores that k, h, and the dielectric properties of the casket are each function of temperature and position. (Since k is a function of temperature and since the casket temperature varies in a radial direction through the casket wall, k also will vary as a function of spatial coordinates.) Also ignored are the radiation losses at the outer casket

wall which are functions of T^4 and are expressed in terms of shape factors that are functions of the geometry of the radiating body [16].

There are a number of physical and mathematical problems involved in directly using equation 6 to predict the steady-state temperature T_i. For example, the heat transfer coefficients for convective heat transfer and for radiative heat transfer are difficult to measure and to model [16-19]. The derivation of equation 6 used an expression for heat flow through the wall of an infinite hollow cylinder [1]. Real refractory caskets are finite so that equation 6 neglects complicated end effects that may be expressed in terms of infinite series of Bessel functions [15]. Even more important is the fact that the temperature and spatial dependence of h, k and the radiative heat loss makes the problem mathematically nonlinear. In fact, the temperature dependence of any one of the three factors (h, k, radiative heat loss) is sufficient to make the problem nonlinear [20]. Such nonlinear problems generally can be solved only by numerical techniques.

Given the nonlinearity and the other mathematical difficulties discussed above, the refractory casket heating problem is analytically intractable. On the other hand, even numerical solutions of such problems are extremely complex [21,22,23]. For problems involving a large number of parameters (here 4 geometric variables and P_C, the power dissipated in the casket) it can be difficult to distill trends from a collection of numerical solutions. In Paper 1 [1], we chose to use a simple linear model (equation 6, which treats h and k as constants) as the candidate function for a least-squares regression of the data. T_o fit the measured steady-state casket temperatures to the model (equation 6) we rewrite equation 6 as [1]

$$T_i = \frac{P_C L_{SA}[C_1' + C_2' b \ln(b/a)]}{bL_T L_{SA} + fb^2[C_3' + b\ln(b/a)]} + C_4' \tag{7}$$

where

$$C_1' = \frac{1}{2\pi kH} = \frac{1}{2\pi h} \tag{7a}$$

$$C_2' = \frac{1}{2\pi k} \tag{7b}$$

$$C_3' = \frac{1}{H} = \frac{k}{h} \tag{7c}$$

$$C_4' = T_o \,. \tag{7d}$$

For the least-squares fitting procedure, equation 6 was modified in the following ways: (1) the free parameters C_1', C_2', C_3', and C_4' replaced functions of k, h, and T_O as defined in equations 7a-7d, and (2) the factor f in equation 7 replaces the numerical coefficient 2 in the term $2b^2[1/H+b\ln(b/a)]$ in the denominator of equation 6. In addition to allowing C_1', C_2', C_3', and C_4' to vary during fitting, f also varied [1]. For the 12 empty caskets included in Paper 1 [1], the best least-squares fit of the data was obtained for f = 0.1728.

The data fitted to equation 7 in Paper 1 [1] consists of 12 ordered sextuples of the form (T_i, P_I, L_{SA}, b, b/a, and L_T). Although the casket geometry differed from casket to casket in Paper 1 [1] (Table 1), P_I was 600 Watts for each sextuple [1].

2. EXPERIMENTAL PROCEDURES

2.1. Casket Construction

The refractory caskets used in this study (Figures 1 and 2) consisted of as-received aluminosilicate boards (SALI, Zircar Products Inc.) and partially stabilized zirconia cylinders (ZYC, Zircar Products Inc.). Using a commercial saw, the SALI board end plates

Table 1. Dimensions of the individual refractory caskets used in Paper 1 [1]. b, a, L_T, L_{SA}, L_{Zr}, L_{Zr} are as defined in equation 5. V_{SA} and V_{Zr} are the volume of the SALI aluminosilicate end plates and the volume of the zirconia cylinder, respectively.

Group	b/a	b (cm)	a (cm)	L_T (cm)	L_{SA} (cm)	L_{Zr} (cm)	V_{SA} (cm^3)	V_{Zr} (cm^3)
	1.33	5.08	3.81	7	4	3	347	106
Group 1	1.50	3.81	2.54	7	4	3	193	76
	2.00	5.08	2.54	7	4	3	334	182
	1.33	5.08	3.81	7	2	5	231	177
	1.50	3.81	2.54	4	2	2	91	51
Group 2	1.50	3.81	2.54	5	2	3	91	76
	1.50	3.81	2.54	6	2	4	91	101
	1.50	3.81	2.54	7	2	5	91	127
	1.50	3.81	2.54	4	2	2	91	51
	1.33	5.08	3.81	4	2	2	162	71
Group 3	2.00	5.08	2.54	4	2	2	162	122
	1.27	3.81	3.00	4	2	2	91	35
	1.69	5.08	3.00	4	2	2	162	106

were cut into disks either 3.81 cm or 5.08 cm in radius with a fixed thickness of 1cm (Figure 2). In a given casket, the top and bottom plates were identical in dimension. The ZYC cylinders were cut to a length of 2 cm, 3 cm, 4 cm, or 5 cm. The cut surfaces of the ZYC cylinders were finished by abrading the cylinders with a sheet of notebook paper, in order to planarize the cut cylinder surfaces and in turn reduce possible thermal losses due to the gaps between the ZYC cylinder and the end plates.

The as-received ZYC cylinders available for this study were either (1) 2.54 cm ID and 3.81 cm OD, or (2) 3.81 cm ID and 5.08 cm OD, giving a b/a ratio of the outer radius, b, to the inner radius, a, of the 1.33 and 1.50. In addition, caskets of b/a = 2.00 were prepared by inserting the smaller cylinders into the larger cylinders, yielding cylinders with a 2.54 cm ID and a 5.08 cm OD.

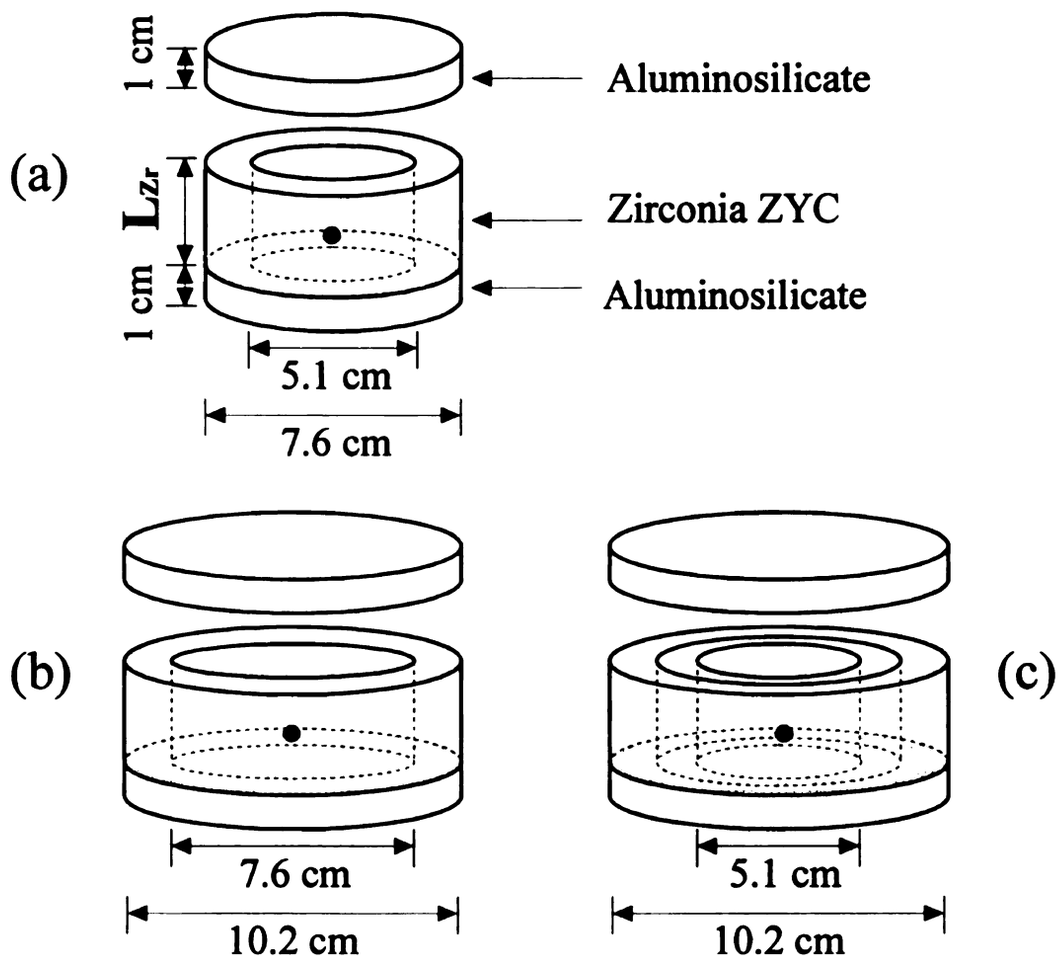

Figure 2. Schematic showing caskets with differing b/a ratios for inner radius, a, and outer radius, b [after 1]. In this study, the length of zirconia cylinder, L_{Zr}, ranged from 2 cm to 5 cm.

Depending on the total casket length L_T, the caskets used in this study were divided into four groups; L_T = 7 cm for Group 4, L_T = 6 cm for Group 5, L_T = 5 cm for Group 6, and L_T = 4 cm for Group 7 (Table 2). The SALI thickness, $0.5L_{SA}$, was 1 cm for each of the two endplates for each casket included in the present study (Figure 2).

2.2. Microwave Processing Apparatus

A 2.45 GHz single-mode cylindrical microwave cavity [1-9] heated the refractory caskets. The cavity was internally tuned by two stepper motors, each interfaced to a computer. The stepper-motor tuning adjusted the launch probe and the cavity short positions to within an accuracy of ±0.1 millimeter. A Sairem power supply generated continuous microwave power of 0 to 2 kWatts at 2.45 GHz. The microwave cavity and the power supply is further described elsewhere [1-9].

Table 2. Dimensions of individual refractory caskets used in this study, where b, a, L_T, L_{SA}, L_{Zr}, L_{Zr} are as defined in equation 5. V_{SA} and V_{Zr} are the volume of the SALI aluminosilicate end plates and the volume of the zirconia cylinder, respectively.

Group	b/a	b (cm)	a (cm)	L_T (cm)	L_{SA} (cm)	L_{Zr} (cm)	V_{SA} (cm^3)	V_{Zr} (cm^3)
Group 4	1.33	5.08	3.81	**7**	2	5	162	177
	1.50	3.81	2.54	**7**	2	5	91	127
	2.00	5.08	2.54	**7**	2	5	162	304
Group 5	1.33	5.08	3.81	**6**	2	4	162	142
	1.50	3.81	2.54	**6**	2	4	91	101
	2.00	5.08	2.54	**6**	2	4	162	243
Group 6	1.33	5.08	3.81	**5**	2	3	162	106
	1.50	3.81	2.54	**5**	2	3	91	76
	2.00	5.08	2.54	**5**	2	3	162	182
Group 7	1.33	5.08	3.81	**4**	2	2	162	71
	1.50	3.81	2.54	**4**	2	2	91	51
	2.00	5.08	2.54	**4**	2	2	162	122

2.3. Microwave Heating of Caskets and Temperature Measurements

Individual caskets were centered on the bottom plate of the microwave cavity. The initial microwave input power was set to 100 Watts, and then the cavity was tuned to an "apparent" TM_{111} cavity mode (Appendix A, Figure A1). When the microwave input power level was increased to 200 Watts, the casket temperature rapidly increased above 500°C. An optical thermometry system capable of measuring temperatures between 500°C to 1900°C [1-9] monitored the casket's inner wall temperature (Figure 3). In order to view the inner casket wall, a hole, approximately 5 mm in diameter was drilled 2.5 cm from the bottom endplates' top surface (Figure 3). Aligning the hole with the optical pyrometer and one of the cavity's view ports allowed measurement of the inner casket wall temperature, T_i

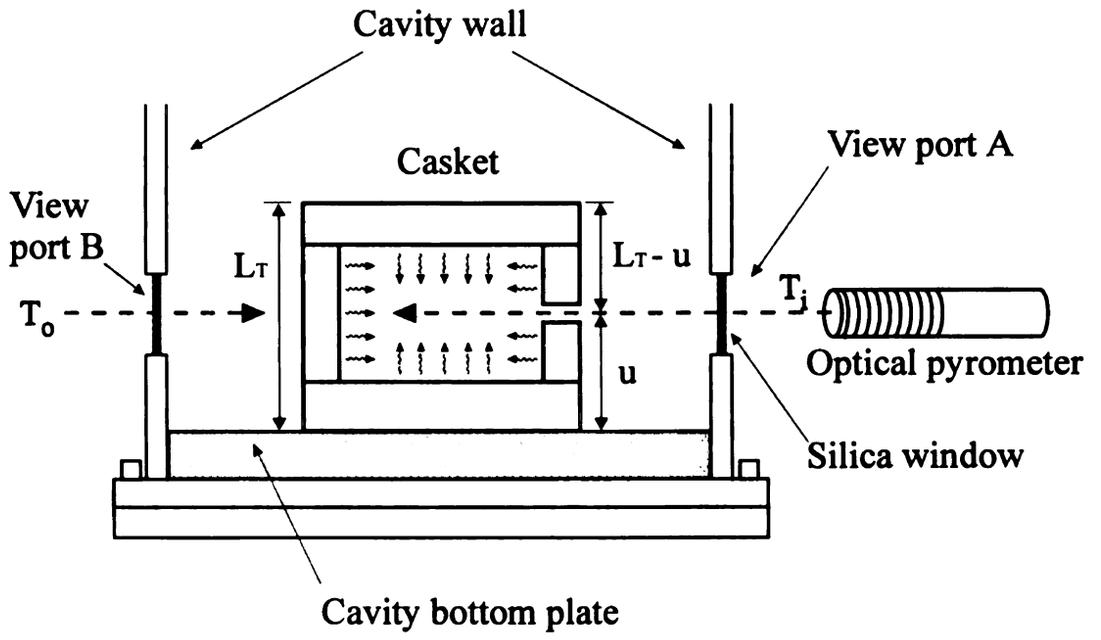

Figure 3. Schematic of measurement of the casket inner wall temperature T_i and the outer wall temperature T_o by an optical pyrometer. The distance, u, from the bottom plate of the cavity to the center of the hole made in the casket wall, is fixed at 2.5cm [after 1].

(Figure 3). The outer casket-wall temperate, T_o, was measured by the same optical pyrometer used for the inner casket wall measurements, but through another cavity view port (Port B, Figure 3). For outer casket wall temperature measurements no additional holes were made in the casket wall.

Immediately after the casket began to heat, the cavity was tuned by changing the launch probe position and the cavity short position. The steady-state inside wall and outside wall temperatures were measured at microwave input power levels ranging from 200 Watts to 700 Watts with 50 Watts power increments. The microwave input power level was changed, the cavity was retuned, and within about 10 to 15 minutes after reaching a given microwave power level, the inner wall casket temperature reached steady state. Once the inner casket temperature reached a steady-state temperature, both the inner and outer casket temperatures were measured.

3. RESULTS AND DISCUSSION

3.1. The Inner and Outer Wall Steady-State Casket Temperatures

This paper includes a vastly expanded data set compared to Paper 1 [1], with 132 new octuple data items (T_i, P_I, P_R, L_{SA}, b, b/a, L_T, T_o) where P_I for the new data set ranges from 200 Watts from 700 Watts. For Paper 1, the data set consisted of 12 ordered sextuples, (T_i, P_I, L_{SA}, b, b/a, and L_T), where P_I = 600 Watts for all data [1]. Unlike Paper 1 [1], in this study we measured both (1) the steady-state casket outer wall temperatures, T_o (Figure 4), and (2) the steady-state casket inner wall temperatures, T_i (Figure 5). In Paper 1, only limited T_o data was obtained [1].

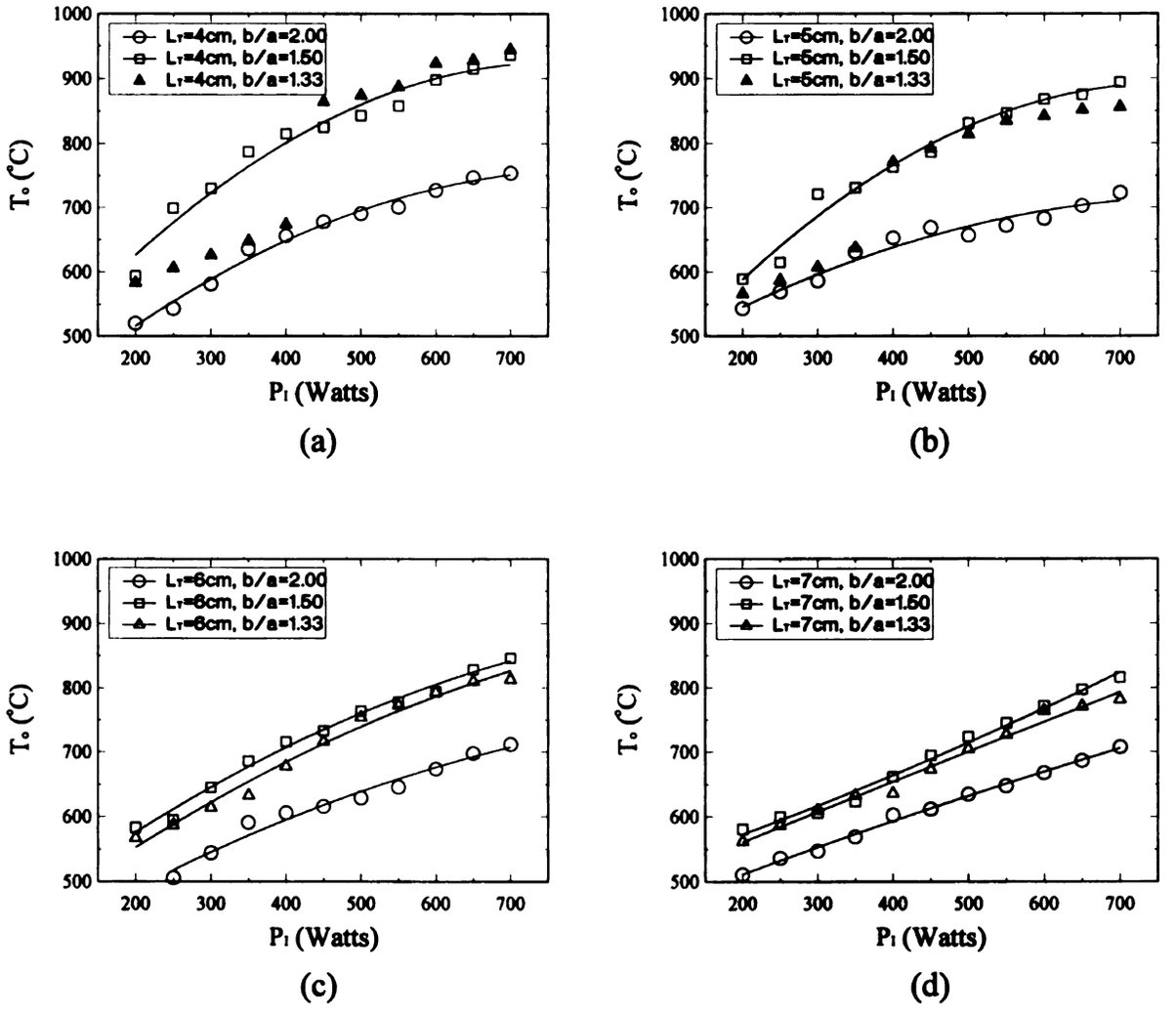

Figure 4. Measured outside casket wall temperature, T_o, as a function of microwave input power level, P_I. Trends in the T_o versus P_I data are highlighted by the solid curves that represent the least-squares best fit to the empirical quadratic equation for T_o versus P_I (equation 8b). Note that in Figures (a) and (b), the data for b/a = 1.33 is not fit to equation 8b, due to the "jump" in T_o at $P_I \approx 350$ - 450 Watts, as discussed in Section 3.1.

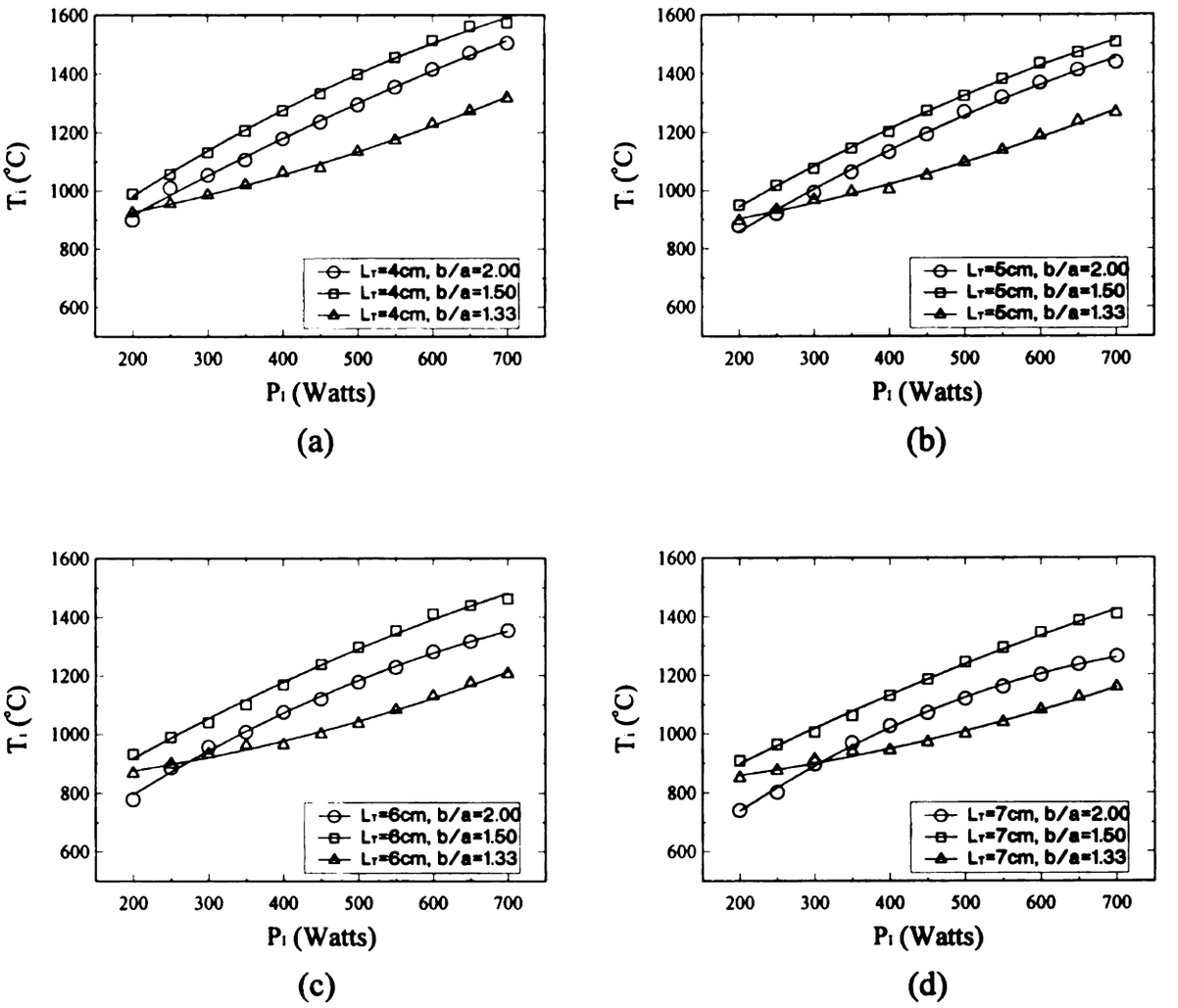

Figure 5. Measured casket inside wall temperature, T_i, as a function of microwave input power level, P_I. Trends in the T_i versus P_I data are highlighted by the solid curves that represent the least-squares best fit to the empirical quadratic equation for T_i versus P_I (equation 8a).

Recall that we can express the refractory heating problems in terms of four geometric variables, L_{SA}, b, b/a, and L_T, where L_{SA} is fixed at 2 cm in this study. In a 2-dimensional plot it is impossible to simultaneously represent T_i, P_I, and four geometric variables (although a fixed value of L_{SA} makes the effective number of geometric variables equal to three).

The T_i versus P_I plots (Figures 5a-5d) display two categories of geometric data, namely (1) an outer radius b of 5.08 cm for b/a values of 1.33 and 2, and (2) an outer radius b of 3.81 cm for b/a values of 1.5. For caskets with b = 5.08 cm, b/a = 1.33 or 2, the trends of T_i versus P_I are very similar for a fixed L_T value (L_T is 4 cm, 5 cm, 6 cm, and 7 cm in Figures 5a-5d, respectively). Caskets with b = 3.81 cm and b/a = 1.5 show slightly different trends. For example, for L_T = 5, 6, and 7 cm, the T_i curves for b/a = 2.0 and b/a = 1.33 cross at about 250 to 300 Watts. However, the T_i versus P_I plots are 2-dimensional "surfaces" cutting through a 6-dimensional space (T_i, P_I, and four geometric variables), thus it is difficult to visualize the multidimensional surfaces over which the b = 5.08 cm and b = 3.81 cm data is distributed. This difficulty underscores the need for a theoretical model to help us understand the interdependence of geometry, temperature, and power in the refractory casket heating problem.

Before fitting the inner and outer wall steady-state casket temperatures to a theoretical model, we first consider the raw data trends in terms of (1) T_i versus P_I and (2) T_o versus P_I. Both the T_i versus P_I and T_o versus P_I data (grouped according to L_T and b/a values) are described well by the empirical quadratic equations 8a and 8b, respectively (Figures 4 and 5)

$$T_i = \alpha_i + \beta_i P_I + \gamma_i P_I^2 \quad (8a)$$

$$T_o = \alpha_o + \beta_o P_I + \gamma_o P_I^2 \quad (8b)$$

where α_i, β_i, γ_i, α_o, β_o, and γ_o are least-squares fitted constants. Trends in T_i versus P_I were discussed above. The T_o data (again grouped according to L_T and b/a values) changes smoothly as a function of P_I, except that for L_T = 4cm (b/a = 1.33) and 5cm (b/a = 1.33), T_o jumps by about 150°C to 200°C between P_I = 350 Watts and P_I = 450 Watts (Figure 4). These jumps in T_o likely are due to inhomogeneous heating (hot spots) that occur in the casket. (Hot spots have been frequently observed during the microwave heating of ceramics [24-27].) The observed differences in uniformity between the inside and outside wall temperatures (T_i and T_o, respectively) may be related in part to emissivity differences between the inside and outside of the casket, as discussed in Section 3.2.

3.2. Further Development of the Refractory Casket Heating Model

In addition to generating 132 new data items, this study presents an improved form of model in equation 9 (Section 3, Results and Discussion) which uses only three free parameters (C_1, C_2, and C_3) instead of 5 free parameters used in equation 7 (C_1', C_2', C_3', C_4', and f). Also, in Paper 1, we considered only the microwave input power P_I, while in this study, we use P_I and reflected power, P_R, to compute the energy dissipated by the casket P_C by $P_C = P_I - P_R$.

Although it was not discussed in Paper 1 [1], the emissivity, ϵ, is also a function of temperature. Since the microwave casket is a closed cylindrical region with a single, small (5 mm) hole in the casket wall (Figures 2 and 3), the volume inside the casket should approximate a black body, so that $\epsilon \approx 1$ within the casket. (In the Second edition

of his textbook Optics [28], E. Hecht notes that "Generally, one approximates a blackbody in the laboratory by a hollow insulated enclosure... with a hole in one wall", which is a very good description of the refractory caskets used in this study.) In contrast, the casket outer wall is not a black body and thus (as is the case for ceramics generally [29]) the emissivity, $\epsilon(T)$, for the outer wall can vary considerably as a function of temperature [29].

Changes in the emissivity of the outer casket wall as a function of temperature mean that T_i and T_o are measured under differing thermal radiation conditions, thus further complicating the task of modeling T_o as a function of power and geometry variables. However, T_i the steady-state inside wall casket temperature is by far the most important temperature of the two temperatures (T_i and T_o) to model. In terms of ceramic processing, the black-body environment inside the closed refractory casket means that T_i should approximate the steady-state specimen temperature.

3.3. Least-Squares Fitting of the Steady-State Temperatures to the Extended Model

In this study, the data for: the steady-state inner casket wall temperature, T_i, the power dissipated in the casket, P_C ($P_C = P_I - P_R$), and four geometric variables b, b/a, L_T, and L_{SA}, were least-squares fit to equation 9 (Figure 6)

$$T_i = \frac{P_C L_{SA}[C_1 + C_2 b \ln(b/a)]}{bL_T L_{SA} + 2b^2[C_1/C_2 + b\ln(b/a)]} + C_3 \tag{9}$$

where

$$C_1 = \frac{1}{2\pi kH} = \frac{1}{2\pi h} \tag{9a}$$

$$C_2 = \frac{1}{2\pi k} \tag{9b}$$

$$\frac{C_1}{C_2} = \frac{1}{H} = \frac{k}{h} \tag{9c}$$

$$C_3 = T_o . \tag{9d}$$

For the least-squares fitting to equation 9, the coefficient of determination, R^2, was greater than 0.984 for four individual data groups (Group 4-7, Table 3). For the entire 132-item new data set obtained in this study (not grouped) the R^2 value was 0.957 (Table 3). The R^2 value was 0.954 for 144-item data set including the 12 data points at 600 Watts from Paper 1 [1] and 132 data items from this study (Table 3). For the individual data groups for L_T = 4, 5, 6, and 7cm, the mean of the residuals for the T_i residuals ranged from 16°C to 21°C for the thirty three data points in each group (Figure 6).

Thus, equation 9 captures well the trends in the steady-state inner casket wall temperature T_i as a function of P_C, the microwave power dissipated in the casket and the four geometric variables (L_{SA}, b, b/a, L_T) that describe the refractory caskets used in this study. However, according to the simple energy balance model (Paper 1 [1] and equation 6 of this study, the fitted parameters C_1, C_2, and C_3 should correspond to $C_1 = 1/2\pi h$, $C_2 = 1/2\pi k$ and $C_3 = T_o$, where h = surface heat transfer coefficient, k = thermal conductivity, and T_o = outer wall temperature. The effective thermal conductivity, k_{eff}, for the caskets over the temperature range included in this study, is roughly 0.21 W/m·°C - 0.26 W/m·°C [1], based on the vendor-specified temperature-dependent k values for the casket materials. The k_{eff} values computed from the fitted C_2 values are about 0.45 W/m·°C - 0.54 W/m·°C (Table 3), or about a factor of two different than the k_{eff} calculated from the vendor data.

In Paper 1 [1], we estimated h for free convection to range from very roughly from 5 W/m^2·°C to 15 W/m^2·°C, although that number is based on free convection. The actual h

Table 3. Least-squares fitted constants C_1, C_2, and C_3, and the coefficients of determination, R^2, values obtained by fitting the T_i, P_C and geometry data from this study and from Paper 1 [1] to equation 9.

Group	Number of data used for fitting	C_1 ($m^2 \cdot °C/W$)	C_2 ($m \cdot °C/W$)	C_3 (°C)	R^2
Group 4	33	0.0021	0.2923	677.1	0.967
Group 5	33	0.0006	0.3267	693.1	0.977
Group 6	33	-0.0010	0.3519	729.4	0.984
Group 7	33	-0.0015	0.3569	745.9	0.988
Group 4 - 7	132	-0.0003	0.3426	705.8	0.957
Group 1 - 7	144	-0.0004	0.3396	711.3	0.954

value may be much larger than the free convection h, due to radiative contributions to h. From C_1, we obtain h values ranging from ~75 $W/m^2 \cdot °C$ to ~265 $W/m^2 \cdot °C$ for the Group 4 and Group 5 caskets (Table 3). However, the negative values of C_1 associated with Groups 6 and 7 are clearly unphysical. The mean of the measured T_o values for the caskets in this study ranges from about 600°C to 800°C which roughly corresponds to T_o as inferred from C_3.

Thus the values of k and T_o obtained by fitting the T_i, P_C, L_{SA}, b, b/a, and L_T to equation 9 correspond roughly to experimental values of k and T_o. In contrast, the h values obtained from fitting the data to equation 9 is sometimes unrealistic, especially for negative values of C_1. However, equation 9 does an excellent job in describing the trends in T_i as a function of power and casket geometry, given the complex six-dimensional functional space (T_i, P_C, L_{SA}, b, b/a, L_T) being fitted and given the nonlinear nature of the problem (Sections 1.2 and 3.2).

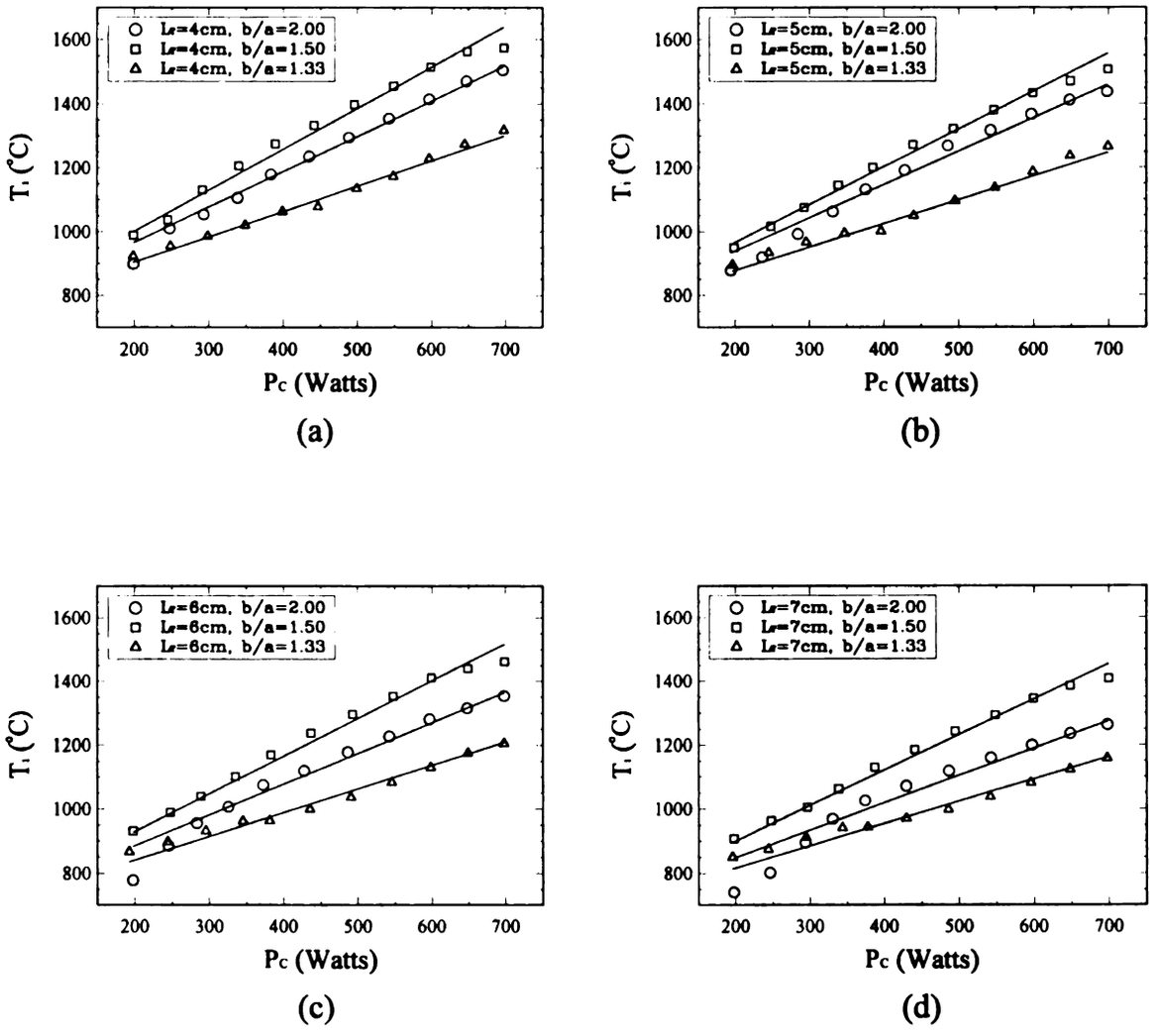

Figure 6. Measured casket inside wall temperature, T_i, as a function of total absorbed microwave power, P_C. The curves represent the least-squares best fit of the data T_i, P_C, L_{SA}, b, b/a, and L_T in Group 4-7 to equation 9.

4. SUMMARY AND CONCLUSIONS

In this study, we measured 132 new octuple data items (T_i, P_I, P_R, L_{SA}, b, b/a, L_T, T_o) for microwave heating of ceramic refractory caskets of varying geometry (Figure 2 and Table 2), where T_i = steady-state inner wall casket temperature, P_I = microwave input power, P_R = reflected microwave power, L_{SA} = thickness of SALI end plates, b = outer radius of the casket, b/a = ratio of the outer casket radius/inner casket radius, L_T = total casket length, and T_o = steady-state outer wall casket temperature. Unlike Paper 1 [1], where the data was taken almost exclusively at P_I = 600 Watts, in this study the microwave input power ranged from 200 to 700 Watts. The data set for this study also includes T_o measurements for every casket/input power combination but Paper 1 included only very few T_o measurements.

Even more important than the expanded data set is the fact that equation 9, the fitting equation introduced in this study (equation 9), represents a significant improvement over equation 7, the fitting equation presented in Paper 1 [1]. While equation 7 involves five free parameters, the new equation (equation 9) has three free parameters. In addition, equation 7 employed microwave input power P_I in describing the energy balance relationship while in equation 9 we used $P_C = P_I - P_R$ instead of P_I. The P_R term in P_C accounts for the measured microwave energy that is reflected during microwave heating, which brings the model closer to physical reality. Using P_C and the larger data set still results in an improved least-squares fit to the data compared to Paper 1 [1].

Paper 1 discussed the numerous simplifications and assumptions involved in simple energy balance model developed in that paper [1], where the final form of that model is given here as equation 6. In addition to reviewing the simplifications noted in Paper 1, we

have also discussed difficulties in modeling the steady-state outside casket wall temperature, T_o. One of the chief difficulties in integrating T_o data into the fitted equation (equation 9) likely is that the radiative heat transfer at the inner wall and at the outer wall are subject to different emissivity conditions.

The energy balance model [1] (equation 6) ignores many of the details of the temperature dependence of material properties and thermal radiation. Nevertheless when the model is used as a candidate equation for least-squares fitting (equation 9), the high values of R^2 obtained (Table 3) indicate that it describes very well the dependence of the steady-state inner wall temperature, T_i, on the power dissipated in the casket and the geometry of heated refractory caskets (Figure 6).

It is important to note that the most crucial temperature to measure is T_i since inside the refractory casket T_i likely approximates the specimen processing temperature. Thus for practical applications such as sintering and joining of ceramics, equation 9 provides the means for a rational design of microwave caskets of the type discussed here.

Future Work

Finite element and/or finite difference methods will be used to analyze both the steady-state and transient heating behaviors for refractory caskets. We will attempt to integrate the numerical results with the model that was given in Paper 1 [1] and extended in this study. In collaboration with the present authors, a colleague has begun a finite element analysis of the refractory caskets included in this study. In addition, the authors will investigate microwave heating using other casket materials and geometries, including powder filled caskets.

ACKNOWLEDGMENTS

The authors acknowledge the financial support of the Electronic and Surface Properties of Materials Center, Michigan State University.

Appendix A. Differences between the resonant electromagnetic field patterns for loaded and unloaded microwave cavities

An empty cavity mode refers to a resonant electromagnetic field pattern for an unloaded microwave cavity (Figure A1). By "unloaded" we mean that there is no external object within the cavity [A1]. When the microwave cavity is loaded with a dielectric material, the presence of the dielectric perturbs the electromagnetic field pattern, so that at the resonant condition the electromagnetic field pattern for the loaded cavity case is different than for an unloaded cavity [A2]. The magnitude of the difference between the electromagnetic field pattern for the unloaded and the loaded cavities increases as the volume of the load (dielectric material added to the empty cavity) increases. The perturbation is also a function of the complex dielectric constants of the load.

As the temperature of the dielectric material increases due to microwave heating, the complex dielectric constants also change with temperature. As the complex dielectric constants change during heating, the electromagnetic nature of the cavity load changes also, so that the cavity must be retuned to maintain the resonance condition. The microwave cavity is retuned by adjusting the cavity height and the probe position to minimize the reflected microwave power.

References for Appendix

A1. S.Y. Liao, Microwave Devices and Circuits, 3rd ed., Prentice Hall, New Jersey, pp. 136-138 (1990).

A2. P. Mak and J. Asumssen, "Experimental Investigation of the Matching and Impressed Electric Field of a Multipolar Electron Cyclotron Resonance Discharge," J. Vac. Sci. Technol. A15[1]: 154-168 (1997).

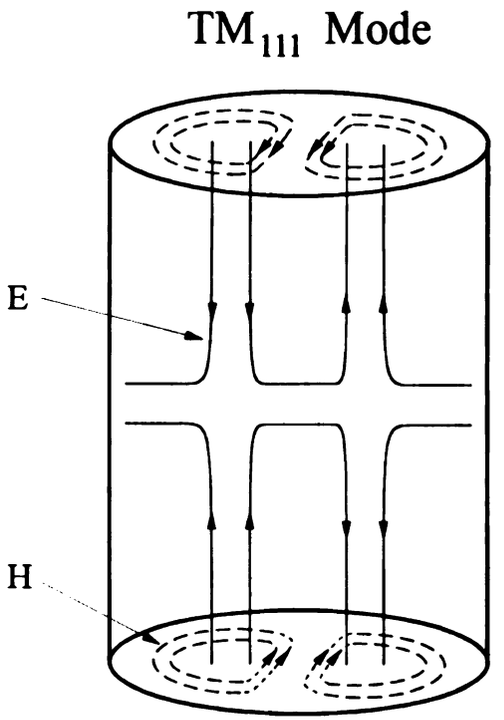

Figure A1. Schematic for electromagnetic field distributions of unloaded TM_{111} resonance microwave cavity mode.

REFERENCES

1. K.Y. Lee, E.D. Case, and J. Asmussen, Jr., "The Steady-State Temperature as a Function of Casket Geometry for Microwave-Heated Refractory Caskets," Mat. Res. Innovat. 1[2]: 101-116 (1997).

2. K.Y. Lee, E.D. Case, J. Asmussen, Jr., and M. Siegel, "Sintering of Alumina Ceramics in a Single Mode Cavity under Automated Control," Cer. Trans., vol. 59, Amer. Cer. Soc., pp. 473-480 (1995).

3. K.Y. Lee, E.D. Case, J. Asmussen, Jr., and M. Siegel, "Microwave Sintering of Ceramic Matrix Composites and the Effect of Organic Binders on the Sinterability," Proceedings of the 11th Annual ESD Advanced Composites Conference, ESD, The Engineering Society, Ann Arbor, MI, pp. 491-503 (1995).

4. K.Y. Lee, E.D. Case, J. Asmussen, Jr., and M. Siegel, "Binder Burn-out in a Controlled Single-Mode Microwave Cavity," Scripta Materialia, 35[1]: 107-111 (1996).

5. K.Y. Lee, E.D. Case, and J. Asmussen, Jr., "Microwave Binder Burn-out for Batch Processing of Al_2O_3, Al_2O_3/SiC Platelet, and Al_2O_3/ZrO_2 Particle Powder Compacts," Cer. Trans. vol. 80, pp. 539-546 (1997).

6. K.Y. Lee, L.C.G. Cropsey, B.R. Tyszka, and E.D. Case, "Grain Size, Density and Mechanical Properties of Alumina Batch-Processed in a Single-Mode Microwave Cavity," Mat. Res. Bull., 32[3]:287-295 (1997).

7. K.Y. Lee, E.D. Case, and D. Reinhard, "Microwave Joining and Repair of Ceramics and Ceramic Composites," Ceramic Engineering and Science Proceedings, vol. 18, pp. 543-550 (1997).

8. K.N. Seiber, K.Y. Lee, and E.D. Case, "Microwave and Conventional Joining of Ceramic Composites Using Spin-On Materials," Proceedings of the American Society for Composites, 12th Technical Conference, Dearborn, MI, pp. 941-949 (1997).

9. B.A. Wilson, K.Y. Lee, and E.D. Case, "Diffusive Crack Healing Behavior in Polycrystalline Alumina: A Comparison Between Microwave Annealing and Conventional Annealing," Mat. Res. Bull., 32[12]:1607-1616 (1997).

10. J.G. Lee and E.D. Case, "Microwave Joining of Zirconia by using Spin-On Materials," to be submitted, Materials Research Bulletin (1998).

11. K.Y. Lee and E.D. Case, "An AFM Study of Thermally-Induced Grain-Boundary Grooving in Polycrystalline Alumina: Part I, Groove Profile, Width, and Depth," to be submitted, Journal De Physique III (1998).

12. K.Y. Lee, E.D. Case, and J.G. Lee "An AFM Study of Thermally-Induced Grain-Boundary Grooving in Polycrystalline Alumina: Part II, Groove Angle, Surface Energy, Surface Diffusivity," to be submitted, Journal De Physique III (1998).

13. D.K. Agrawal, Y. Fang, D.M. Roy, and R. Roy, "Fabrication of Hydroxyapatite Ceramics by Microwave Processing," R.L. Beatty, W.H. Sutton and Iskander MF (eds) Microwave Processing of Materials III, Mat. Res. Soc. Symp. Proc. vol. 269, Materials Research Society, Pittsburgh, Pennsylvania, pp. 231-236 (1992).

14. Y. Fang, D.K. Agrawal, D.M. Roy and R. Roy, "Rapid Sintering of Hydroxyapatite Ceramics by Microwave Processing," D.E. Clark, F.D. Gac, and W.H. Sutton (eds) Microwaves: Theory and Application in Materials Processing, Cer. Trans. vol. 21, Amer. Cer. Soc., Westerville, Ohio, pp. 349-356 (1991).

15. H.S. Carslaw and J.C Jaeger, Conduction of Heat in Solids, 2nd ed., Oxford University Press, Fair Lawn, NJ, pp. 19, 188-190 (1959).

16. F. Kreith, Chapters 2, 5, and 7 in Principles of Heat Transfer, Third Edition, International Textbook Company, Scranton, PA, (1972).

17. J.V. Beck, B. Blackwell, and C.R. Clair, Jr., Inverse Heat Conduction, Wiley-Interscience, New York, pp. 281-300 (1985).

18. B. Gebhart, Heat Conduction and Mass Diffusion, McGraw-Hill, New York, pp. 48-52, 64-71, 139-144 (1993).

19. B.V. Karlekar and R.M. Desmond, Engineering Heat Transfer, West Publishing Co., New York, pp. 8, 14 (1977).

20. M.N. Ozisik, Finite Difference Methods in Heat Transfer, Boca Raton, CRC Press, pp. 1-18, 61-65 (1994).

21. H.W. Jackson, M. Barmatz, and P. Wagner, "Transient Temperature Behavior of a Sphere Heated by Microwaves," D.C. Clark, T.R. Tinga, and J.R. Laia, Jr. (eds), Microwaves: Theory and Applications in Materials Processing II, Cer. Trans. vol 36, Amer. Cer. Soc., Westerville, OH, pp. 189-199 (1993).

22. H.W. Jackson and M. Barmatz, "Microwave Absorption by a Lossy Dielectric Sphere in a Rectangular Cavity," J. Appl. Phys. 70:5193-5204 (1991).

23. M. Barmatz and H.W. Jackson, "Steady State Temperature Profile in a Sphere Heated by Microwaves," R.L. Beatty, W.H. Sutton and M.F. Iskander (eds), Microwave Processing of Materials III, Mat. Res. Soc. Symp. Proc. vol. 269, Materials Research Society, Pittsburgh, Pennsylvania, pp. 97-103 (1992).

24. G.A. Kriegsmann, "Microwave Heating in Ceramics," D.E. Clark, F.D. Gac, and W.H. Sutton (eds), Microwaves: Theory and Application in Materials Processing, Cer. Trans. vol. 21, Amer. Cer. Soc., Westerville, Ohio, pp. 177-183 (1991).

25. G.A. Kriegsmann, "Thermal Runaway and its Control in Microwave Heated Ceramics," R.L. Beatty, W.H. Sutton and M.F. Iskander (eds), Microwave Processing of Materials III, Mat. Res. Soc. Symp. Proc. vol. 269, Materials Research Society, Pittsburgh, Pennsylvania, pp. 257-264 (1992).

26. D.L. Johnson, D.J. Skamser, and M.S. Spotz, "Temperature Gradients in Microwave Processing,: Boon and Bane," D.E. Clark, W.R. Tinga, and J.R. Laia, Jr. (eds), Microwaves: Theory and Applications in Materials Processing II, Cer. Trans. vol. 36, Amer. Cer. Soc., Westerville, OH, pp. 133-146 (1993).

27. M.S. Spotz, D.J. Skamser, and D.L. Johnson, "Thermal Stability of Ceramic Materials in Microwave Heating," J. Am. Ceram. Soc. 78[4]: 1041-1048 (1995).

28. E. Hecht, Optics, Second Edition, Addison-Wesley Publishing Company, Reading, Massachusetts, pp. 539 (1990).

29. Y.S. Touloukian, ed., Thermophysical Properties of High Temperature Solid Materials, Volume 4: Oxides and Their Solutions and Mixtures, The Macmillan Company, New York, pp. 28-31 (1967).

CONCLUSIONS

1. SINTERING

This study demonstrated that a cylindrical single-mode microwave cavity equipped with computer controlled tuning system can be used to provide repeatable heating schedules and successfully densify alumina ceramics and alumina matrix zirconia composites. For the specimens densified at 1500°C to 1600°C, the mass density as determined by Archimedes was about 96% up to nearly 100% of theoretical density.

The advantages of microwave heating over conventional heating have been verified by heating alumina/10wt% zirconia particulate composites. Microwave-sintered composite specimen reached about 94% theoretical density at a sintering temperature of 1350°C, while a specimen conventionally sintered at 1350°C reached only about 70% of theoretical density. The microstructures of the composite specimens sintered at 1450°C also indicate that microwave heating enhanced the densification over conventional heating.

In addition, in this study the variations in the density, grain size, and/or hardness, fracture toughness of microwave-sintered ceramics were examined in terms of (i) the radial position within individually-processed specimens, (ii) the specimen position within the zirconia casket for the batch-processed specimens, and (ii) the operating microwave cavity mode.

For alumina specimens sintered at 1500°C in the cavity tuned to four different cavity modes, mass density and grain size examined in terms of both the radial position within a given specimen and the cavity mode were relatively uniform with an average density 96.2% ± 0.6% of theoretical density and an average grain size of 6.23 μm ± 1.5 μm, respectively.

For batch-processed alumina specimens, the variation in mass density in terms of both the specimen position and the cavity mode was negligible, which was less than 0.6% of theoretical density. However, the mean grain size ranged from 6 μm up to 8 μm depending on the operating cavity mode and for the specimens processed in a batch (i.e. same cavity mode) the standard deviation was less than 1 μm. The average hardness determined by Vickers' indentation was 16 GPa and the calculated toughness was about 2.70 $MPa \cdot m^{1/2}$. The average hardness and fracture toughness values for the specimens heated at the same position but in different batches (i.e. different cavity modes) differed by no more than 2.6% and 5.3%, respectively, from position to position. However, depending on the modes used to sinter specimens in batches, the variations in mean hardness and toughness values were somewhat large, which were about 6.6% and 15.9%, respectively.

Therefore, based on the obtained results, this sintering study revealed that the microwave casket (specimen enclosure) used in this study can act to homogenize the temperature field, such that the grain size, density, hardness, and fracture toughness can be relatively uniform in terms of position within a given specimen and/or position of specimens batch-processed within the casket.

2. BINDER BURN-OUT

The objectives of binder burn-out study was to burn out organic binders utilizing three processing procedures; (i) binder burn-out and sintering as a one step process using a casket, (ii) fixed input power sequence without using a casket, and (iii) stepped input power sequence without using a casket. These three procedures were applied to burn out the corn oil binder from the individual powder compacts or the powder compacts in a batch. The materials used for the binder burn-out study were alumina, alumina/10wt% zirconia, alumina/10wt% silicon carbide powders mixed with 10wt% corn oil binder.

Using a susceptor material, the binder was successfully burned out and sintered as a one step process by controlling heating rate by cavity tuning control, microwave power control, and mode switching. The total processing time was relatively short, about 3.5 hours. The final sintered alumina/zirconia composite specimen had mass density of 98.1 percent of theoretical density with a uniform and fine microstructure with an average grain size 2.7 μm.

In literature, binder burn-out studies which were performed by microwave energy using caskets enclosing specimens to be heated have been reported but few reported on binder burn-out without a casket. This study attempted to burn out the binder without using any insulation material enclosing specimens. This study revealed that for both the individually- and the batch-processed specimens, the extent of binder burn-out can vary widely with the electromagnetic mode. For example, heating via the TM_{012} mode resulted in very little binder burn-out, while in comparison, nearly complete binder burn-out was achieved in the TE_{112} mode. In particular, for both the individually-processed specimens and the batch-processed specimens, a stepped input power sequence burned

out the binder more completely than a fixed input power without cracking the specimens. Among the three types of ceramic compacts processed (Al_2O_3/ZrO_2 composites, Al_2O_3/SiC platelet composites, and Al_2O_3) the binder burned out at lower power for the Al_2O_3/SiC platelet specimens, under both fixed and stepped power conditions. This may have been due to differing dielectric properties of the specimens.

3. JOINING

Compared to typical ceramic-ceramic joining by conventional heating which requires relatively high applied stress of several MPa's, this study employed no or very low applied stress ranging from 0 to 6 kPa to join alumina ceramics and glass ceramics with spin-on film materials by using microwave energy.

Without a dead weight, alumina components were joined by heating at 1625°C for 10 minutes in a single-mode microwave cavity. SEM examination of the joined region of the fractured alumina specimen showed no evidence of cracking or microcracking near the joint. That is, the macrocrack that fractured the specimen apparently did not damage the joint. This observation indicates that the joint is a very strong interface. Also, the grain structure near the joint does not differ from the grain structure in the bulk of the specimen, indicating that the process of generating the joint does not greatly perturb the specimen's microstructure, at least on a size scale of a few microns.

The maximum hold temperature for ceramic joining could be apparently lowered by using dead weights. For example, alumina-alumina joining with dead weights of 60 grams (about 2 kPa) lowered the joining temperature from 1625°C (corresponding to temperature without a dead weight) down to 1575°C. For joining of MaCor™ specimens, the joining

temperature was lowered from 1150°C (corresponding to temperature without a dead weight) to 1050°C by using dead weights of 60 grams (about 6 kPa).

Dimensional changes in notches made in alumina specimens or MaCor™ glass ceramics were examined before and after joining. Alumina specimens heated at 1575°C for 20 minutes changed notch dimensions by less than 4.1% in width and in depth. Notches in MaCor™ specimens changed dimension by less than 5.7% in width and in depth during joining at a maximum hold temperature of 1050°C for 20 minutes. Notch shape retention indicates that ceramic components with intricate features, such as small holes and channels, could maintain their complex geometry during joining. Also for the joined MaCor™ specimens, the constancy of notch geometry indicates a lack of wide-scale viscous flow which might be a potential disadvantage for using spin-on silica or silicate film.

4. CRACK HEALING

Crack healing study for both conventional heating and microwave heating was performed on Vickers-indented specimens of polycrystalline alumina (Coors ADS-995) for the temperatures ranging from 1510 K to 1742 K. The crack healing rates were studied as a function of i) heating mode, ii) dwell temperature, and iii) applied indentation load.

The heating modes used in this study were i) conventional heating with a heating rate of 10°C/min., ii) microwave heating with a "slower" heating rate of 10°C/min., and iii) microwave heating with a "faster" heating rate of 75°C/min.. For the three heating modes, the crack healing rate $\Delta a/\Delta t$ was very similar at about 1510 K. However, for both the 49 N and 98 N indentation cracks, $\Delta a/\Delta t$ was at least double for microwave annealing

(slower heating rate) compared to conventional annealing with increasing the dwell temperature, indicating that microwave heating considerably enhanced the crack healing rate.

The crack healing data analyzed based on a diffusive mass transport model by Dutton and Stevens revealed that the activation energies for crack healing were significantly lower for conventional heating than for microwave healing. However, the net diffusivities inferred from the healing data showed that the microwave heating increased the diffusivities by a factor of about 1 to 4 over the range of the temperature used in this study.

The microwave-enhanced healing rates observed for the Vickers indentation cracks included in this study imply that for a microcracked ceramic material, microwave heating may recover mechanical properties such as the strength, elastic modulus, etc. faster than conventional heating.

5. EFFECTS OF CASKET GEOMETRY AND MICROWAVE POWER ON MICROWAVE HEATING

This study demonstrated that the steady-state inner-wall temperature of a casket which is used to process ceramic materials by microwave energy, can vary significantly as a function of casket geometry. For example, the steady-state casket temperature at 600 Watts of microwave input power ranged from 1112°C to 1519°C as the casket geometry changed for caskets composed of porous zirconia cylinders with aluminosilicate end plates. However, the variation of the steady-state casket temperature could not be described by a function of only simple geometric variables such as volume, surface area,

etc. Based on thermal balance between the heat generated within the casket by microwave energy and the heat dissipated from the outer surface of the casket, a simple model equation was developed to describe the variation in steady-state temperature as a function of casket geometry. The model also described well the dependence of the steady-state casket temperature on the microwave power level.

This study also revealed that the steady-state temperature of the dielectrically lossy casket was only slightly perturbed by the presence of a specimen with a volume and mass that was small compared to the casket volume and mass.

APPENDICES

APPENDIX A. PHOTOS OF MICROWAVE PROCESSING APPARATUS.

Figure A-1. Photo of microwave processing apparatus.

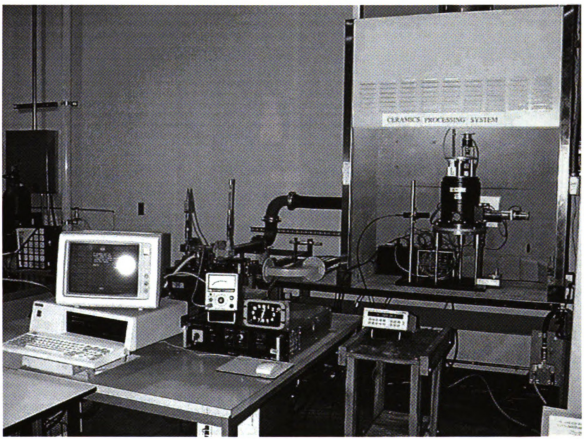

Figure A-2. Photo of cylindrical single-mode microwave cavity.

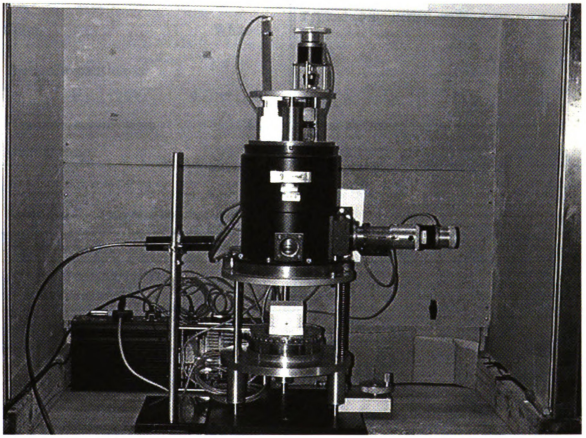

APPENDIX B. PROPERTIES OF REFRACTORY MATERIALS USED FOR MICROWAVE PROCESSING[1]

Appendix B-1. Zirconia Insulating Cylinder, Type ZYC

Table B-1-1. General characteristics and properties

Property	Data	Property	Data
Density	0.48 (gm/cm^3)	Moisture and organic content	Nil
Porosity	91 (%)	Outgassing in vacuum	Nil
Color	White	Typical composition, wt%	
		ZrO_2	87
Thermal expansion for		Y_2O_3	8
RT-1425°C	9×10^{-6} (1/°C)	SiO_2	5
Maximum service temp.	1650 (°C)	Linear shrinkage isothermal	
Melting temp.	2200 (°C)	soak for 24 hrs at 1650°C	4% max.

Table B-1-2. Thermal conductivity

Mean temperature (°C)	400	800	1100	1400	1650
Thermal conductivity, k (Watts/m·K)	0.09	0.11	0.14	0.19	0.23

[1] Catalog (1995) from Zircar Products Inc.,
110 North Main Street - P.O. BOX 458, Florida, New York 10921-0458
TEL: 914-651-4481, FAX: 914-651-3192
Internet: www.zircar.com, e-mail: zircarsa@zircar.com

Table B-1-3. Properties of zirconia fibers contained in Type ZYC

Property	Data	Property	Data
Diameter	4 - 6 (μm)	Stabilizer (Yttria)	4.5 (wt%)
Density (92-97% dense)	5.6 - 5.9 (gm/cm^3)	Composition ($ZrO_2+HfO_2+Y_2O_3$)	99+ (%)
Surface area (N_2 BET)	< 1.0 max. (m^2/gm)	Melting point	2590 (°C)

Appendix B-2. Alumina Insulating Board, Type SALI

Table B-2-1. General characteristics & properties

Property	Data	Property	Data
Typical composition, %		Linear Shrinkage, %	
Al_2O_3	80	24 hrs at 1650°C	1
SiO_2	20	24 hrs at 1700°C	3
Moisture & organic content, %	0	Flexural strength	2.07 (MPa)
Bond	Silica	Compressive strength at 10% compression	1.31 (MPa)
Density	0.48 (gm/cm^3)	SAG/Distortion, 152mm×25.4mm×25.4mm,	
Open porosity	84 (%)	127mm Span,	
Maximum use temp.	1700°C	% after 24 hrs. at 1650°C	2
Melting temp.	1870°C	Thermal expansion	
Color	White	for RT-1000°C	5.0×10^{-6}/°C

Table B-2-2. Thermal conductivity

Mean temperature (°C)	400	800	1100	1400	1650
Thermal conductivity, k (Watts/m·K)	0.20	0.25	0.31	0.34	0.39

Appendix B-3. Alumina Insulating Board, Type SALI-2

Table B-3-1. Characteristics & properties

Property	Data	Property	Data
Typical composition, %		Linear Shrinkage, %	
Al_2O_3	80	24 hrs at 1650°C	0
SiO_2	20	24 hrs at 1700°C	3.5
Moisture & organic content, %	0	Flexural strength	2.14 (MPa)
Bond		Compressive strength at 10% compression	1.04 (MPa)
Density	0.51 (gm/cm^3)	SAG/Distortion, 125mm×25.4mm×25.4mm,	
Open porosity	84 (%)	100mm Span,	
Maximum use temp.	1800°C	% after 24 hrs. at 1700°C	2
Melting temp.	1870°C	Thermal expansion coefficient	
Color	White	for RT-1000°C	6.0×10^{-6}/°C

Table B-3-2. Thermal conductivity

Mean temperature (°C)	400	800	1100	1400	1650
Thermal conductivity, k (Watts/m·K)	0.15	0.20	0.25	0.34	0.39

APPENDIX I. SINTERING.

Figure I-1. Sem Images of Fracture Surface of Alumina Specimens Batch-Processed in Various Microwave Cavity Modes.

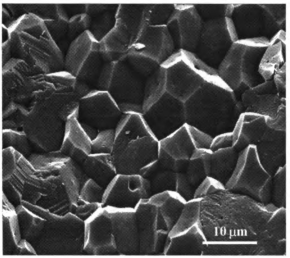

(a) TM_{111} mode (position 3)

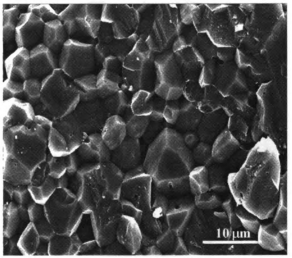

(b) TE_{112} mode (position 2)

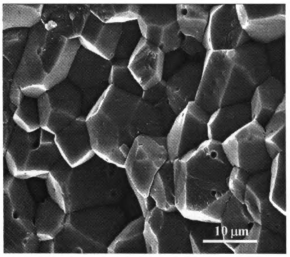

(c) TE_{113} mode (position 2)

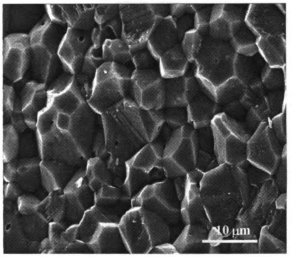

(d) TM_{013} mode (position 5)

Figure I-2. Heat Distribution inside Empty Casket as Determined by Thermally Sensitive Paper. The casket was heated in each cavity mode (a) for 15 minutes at 80 Watts, (b) for 7 minutes at 90 Watts, (c) for 15 minutes at 150 Watts, and (d) 5 minutes at 90 Watts. The dark areas in (a)-(d) indicate regions of microwave heating.

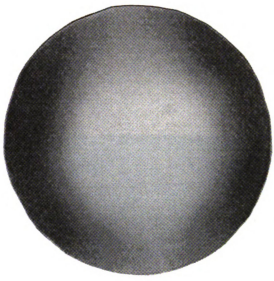

(a) TE_{211} mode

(b) TE_{112} mode

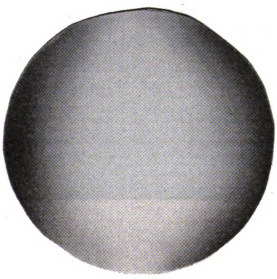

(c) TM_{012} mode

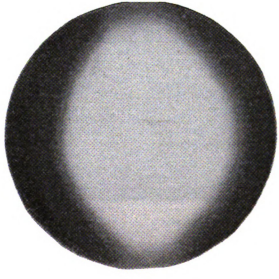

(d) TE_{212} mode

APPENDIX II. CERAMIC/BINDER COMPACT SPECIMENS HEATED IN A MICROWAVE CAVITY.

Figure II-1. Photo of Al_2O_3/binder compact specimens heated by microwave heating.

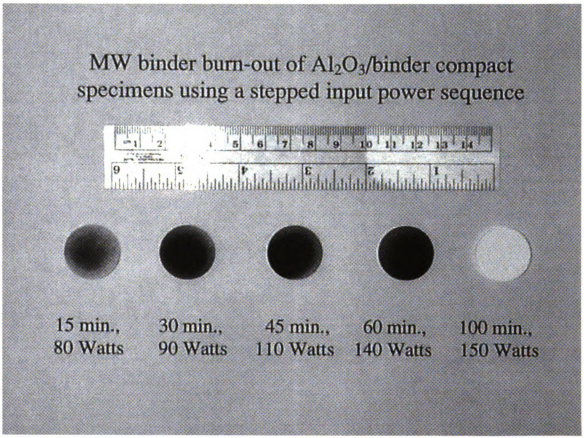

Figure II-2. Photo of Al_2O_3/SiC/binder compact specimens heated by microwave heating.

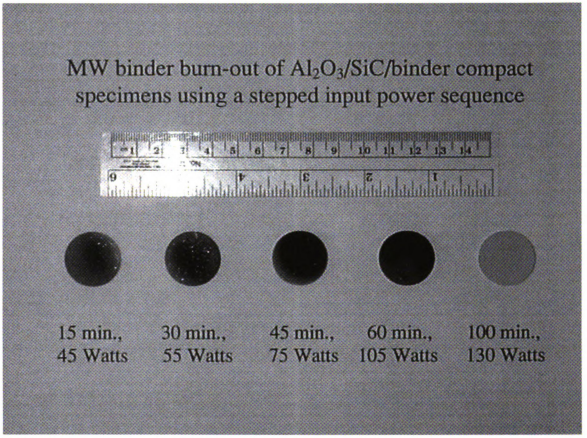

Figure II-3. Photo of Al_2O_3/ZrO_2/binder compact specimens heated by microwave heating.

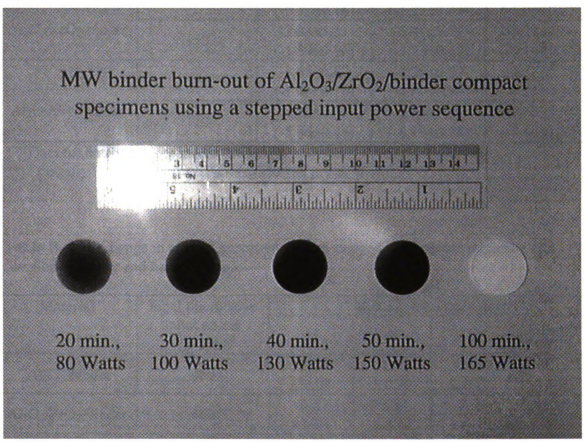

Appendix II-4. Raw Data for Batch-Processed Binder Burn-Out

Table II-4-1. Change in wt% of specimen using a fixed input power sequence as a function of power and heating time.

Material	Microwave input power (Watts)	Heating time (minutes)		
		10	30	60
Al_2O_3/binder	80	-0.50±0.44* (-0.33±0.04)**	-2.03±0.36 (-1.90±0.13)	-2.30±0.56 (-2.10±0.21)
	150	-2.70±3.48 (-1.40±0.43)	-5.50±2.19 (-4.68±0.34)	-6.74±1.62 (-6.13±0.30)
Al_2O_3/ZrO_2/binder	80	-0.47±0.27 (-0.39±0.16)	-1.93±0.49 (-1.82±0.43)	-2.12±0.50 (-1.95±0.21)
	150	-2.84±3.31 (-1.59±0.16)	-6.40±1.77 (-5.73±0.17)	-6.72±1.56 (-6.14±0.30)
Al_2O_3/SiC/binder	80	-1.65±0.67 (-1.40±0.16)	-4.26±0.79 (-4.00±0.39)	-4.51±0.79 (-4.23±0.32)
	120	-6.26±1.25 (-5.86±0.76)	-6.64±1.39 (-6.19±0.78)	-7.69±1.54 (-7.44±1.52)

* Data for batches of seven specimens.
** Centrally located specimens not considered in calculation.

Table II-4-2. Change in wt% of specimen using a stepped input power sequence as a function of power and heating time.

Material	Final microwave input power (Watts)	Heating time (minutes)			
		15	40	70*	120
Al_2O_3/binder	460	-0.20 ± 0.04	-4.72 ± 0.22	-7.36 ± 0.17	-9.36 ± 0.62
Al_2O_3/ZrO_2/binder	460	-0.23 ± 0.04	-3.34 ± 0.34	-7.24 ± 0.16	-9.18 ± 0.25
Al_2O_3/SiC/binder	250	-0.73 ± 0.04	-4.90 ± 0.16	-10.73 ± 0.10	

* For Al_2O_3/SiC/binder, the heating time was 75 minutes.

APPENDIX III. JOINING

Figure III-1. SEM images of (a) mw-sintered AKP30 Al_2O_3 , (b) MgF_2, (c) MaCor, and (d) mw-sintered TZ-3Y ZrO_2.

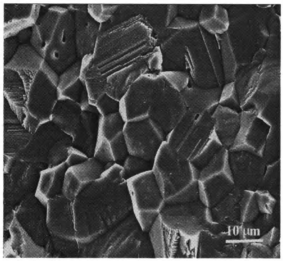

(a)

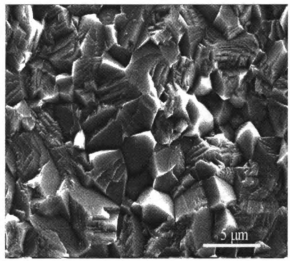

(b)

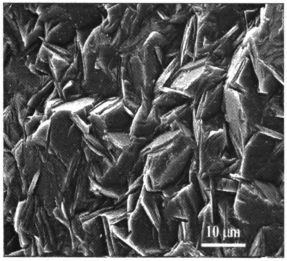

(c)

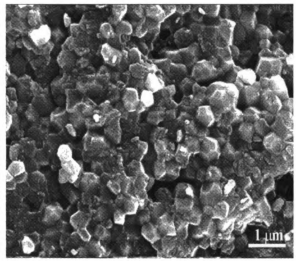

(d)

APPENDIX IV. CRACK HEALING.

Table IV. Raw data for crack healing study. Anneal time is fixed at 1 hour.

Annealing process	Anneal temp. (°C)	Anneal temp. (K)	Change in crack length, dC (μm)	
			49N indentation crack	98N indentation crack
Conventional (10°C/min.)	1245	1518	50.0 ± 19.7	75.5 ± 21.0
	1309	1582	59.9 ± 16.1	77.0 ± 18.1
	1354	1627	53.3 ± 9.5	60.1 ± 18.3
	1426	1699	66.0 ± 17.5	113.5 ± 21.8
	1469	1742	99.0 ± 17.9	146.8 ± 31.7
Microwave (75°C/min.)	1237	1510	22.0 ± 14.2	59.2 ± 17.6
	1295	1568	68.3 ± 18.3	96.4 ± 33.5
	1353	1626	91.0 ± 17.7	155.3 ± 20.1
	1411	1684	136.9 ± 27.8	216.0 ± 16.4
	1469	1742	157.1 ± 53.2	273.0 ± 30.6
Microwave (10°C/min.)	1237	1510	46.9 ± 17.7	72.1 ± 23.4
	1295	1568	84.1 ± 14.4	114.3 ± 9.0
	1353	1626	151.5 ± 17.7	175.6 ± 21.8
	1411	1684	199.1 ± 10.1	338.0 ± 9.2
	1469	1742	199.1 ± 9.2	337.9 ± 8.8

APPENDIX V. DATA FOR REFRACTORY HEATING STUDY AND ADDITIONAL STUDY

Appendix V-1. Additional Raw Data for Refractory Heating Study

Table V-1-1. The inner casket wall temperature, T_i, and the casket outer wall temperature, T_o, measured as a function of microwave input power level, P_i, for refractory caskets which has **b/a = 1.33**. L_T is the total casket length.

P_i	L_T = 4 cm		L_T = 5 cm		L_T = 6 cm		L_T = 7 cm	
(Watts)	T_i (°C)	T_o (°C)	T_i (°C)	T_o (°C)	T_i (°C)	T_o (°C)	T_i (°C)	T_o (°C)
200	924	583	895	566	867	567	850	562
250	955	606	934	587	898	587	875	587
300	986	626	967	607	932	614	911	610
350	1021	648	995	637	962	633	941	633
400	1063	674	1002	771	963	678	943	636
450	1078	864	1050	792	999	716	970	673
500	1135	874	1096	814	1036	754	998	705
550	1173	987	1137	835	1083	773	1038	727
600	1229	923	1187	842	1130	793	1081	764
650	1274	928	1237	852	1175	810	1124	771
700	1318	944	1266	856	1205	813	1158	782

Table V-1-2. The inner casket wall temperature, T_i, and the casket outer wall Temperature, T_o, measured as a function of microwave input power level, P_i, for refractory caskets which has **b/a = 1.50**. L_T is the total casket length.

P_i	L_T = 4 cm		L_T = 5 cm		L_T = 6 cm		L_T = 7 cm	
(Watts)	T_i (°C)	T_o (°C)	T_i (°C)	T_o (°C)	T_i (°C)	T_o (°C)	T_i (°C)	T_o (°C)
200	989	594	949	589	931	583	908	581
250	1037	699	1017	615	989	595	963	600
300	1131	730	1075	721	1039	645	1005	606
350	1206	787	1145	731	1101	686	1062	624
400	1275	815	1201	763	1169	716	1130	662
450	1333	825	1272	786	1238	733	1185	695
500	1398	843	1323	831	1297	764	1243	724
550	1456	858	1381	847	1353	778	1293	745
600	1514	898	1434	868	1411	794	1345	772
650	1562	915	1471	875	1440	828	1386	797
700	1574	936	1507	894	1462	846	1409	816

Table V-1-3. The inner casket wall temperature, T_i, and the casket outer wall Temperature, T_o, measured as a function of microwave input power level, P_i, for refractory caskets which has **b/a = 2.00**. L_T is the total casket length.

P_i	L_T = 4 cm		L_T = 5 cm		L_T = 6 cm		L_T = 7 cm	
(Watts)	T_i (°C)	T_o (°C)	T_i (°C)	T_o (°C)	T_i (°C)	T_o (°C)	T_i (°C)	T_o (°C)
200	899	520	878	543	778	*	740	511
250	1010	543	920	569	885	506	802	536
300	1054	581	993	586	956	544	896	547
350	1106	636	1063	631	1007	591	969	569
400	1179	656	1132	653	1075	606	1026	603
450	1236	678	1192	669	1120	616	1071	612
500	1295	691	1269	657	1178	629	1119	635
550	1355	701	1318	672	1228	646	1160	648
600	1415	727	1368	683	1281	674	1200	668
650	1471	747	1412	703	1316	698	1236	687
700	1505	754	1438	723	1354	712	1263	708

Appendix V-2. ELECTROMAGNETIC MODE IDENTIFICATION AND HEATING CHARACTERISTICS OF CASKETS IN VARIOUS MICROWAVE MODES IN A CYLINDRICAL SINGLE-MODE MICROWAVE CAVITY

Two methods were used to identify the particular electromagnetic modes present in the cylindrical resonant cavity, namely: (1) reflected power measurements and (2) electric field probe measurements. Mode identification was done on a microwave cavity loaded with caskets of various dimensions (Table V-2-1) as well as on an empty cavity.

1. REFLECTED POWER MEASUREMENTS AT LOW AND HIGH INPUT POWER

The reflected power was measured as a function of cavity height under (a) low power conditions (50 Watts), and (b) higher power conditions, during the microwave heating of the caskets.

For the low power measurements, the reflected power versus cavity height was determined at a fixed microwave input power of 50 Watts and with the launch probe position fixed at 1 cm from the inner wall of the cavity (Figure 1). The input power of 50 Watts were selected for the low power measurements since at 50 Watts the caskets used in this study did not heat above 500°C. At higher input power levels, the caskets couple with microwave energy and heat above 500°C depending on the cavity height, accompanied by the rapid change of dielectric properties of the insulation materials. Thus as the cavity height changes from the lower limit to the upper limit of the cavity height, the temperature of the casket rapidly increases and decreases repeatedly. This

Table V-2-1. Geometry and composition of the zirconia/aluminosilicate caskets employed in this study

Casket	Casket 1	Casket 2	Casket 3	Casket 4
Outer Diameter (cm)	10.16	7.62	10.16	10.16
Inner Diameter (cm)	7.62	5.08	5.08	7.62
Thickness of zirconia cylinder (cm)	1.27	1.27	2.54	1.27
Height of zirconia cylinder (cm)	3	3	3	5
Volume of zirconia (cm^3)	106	76	182	177
Volume of SALI (cm^3)	347	193	334	231
Total volume (cm^3)	453	269	516	408
Outer surface area (cm^2)	386	259	386	386
Inner surface area (cm^2)	151	80	80	187

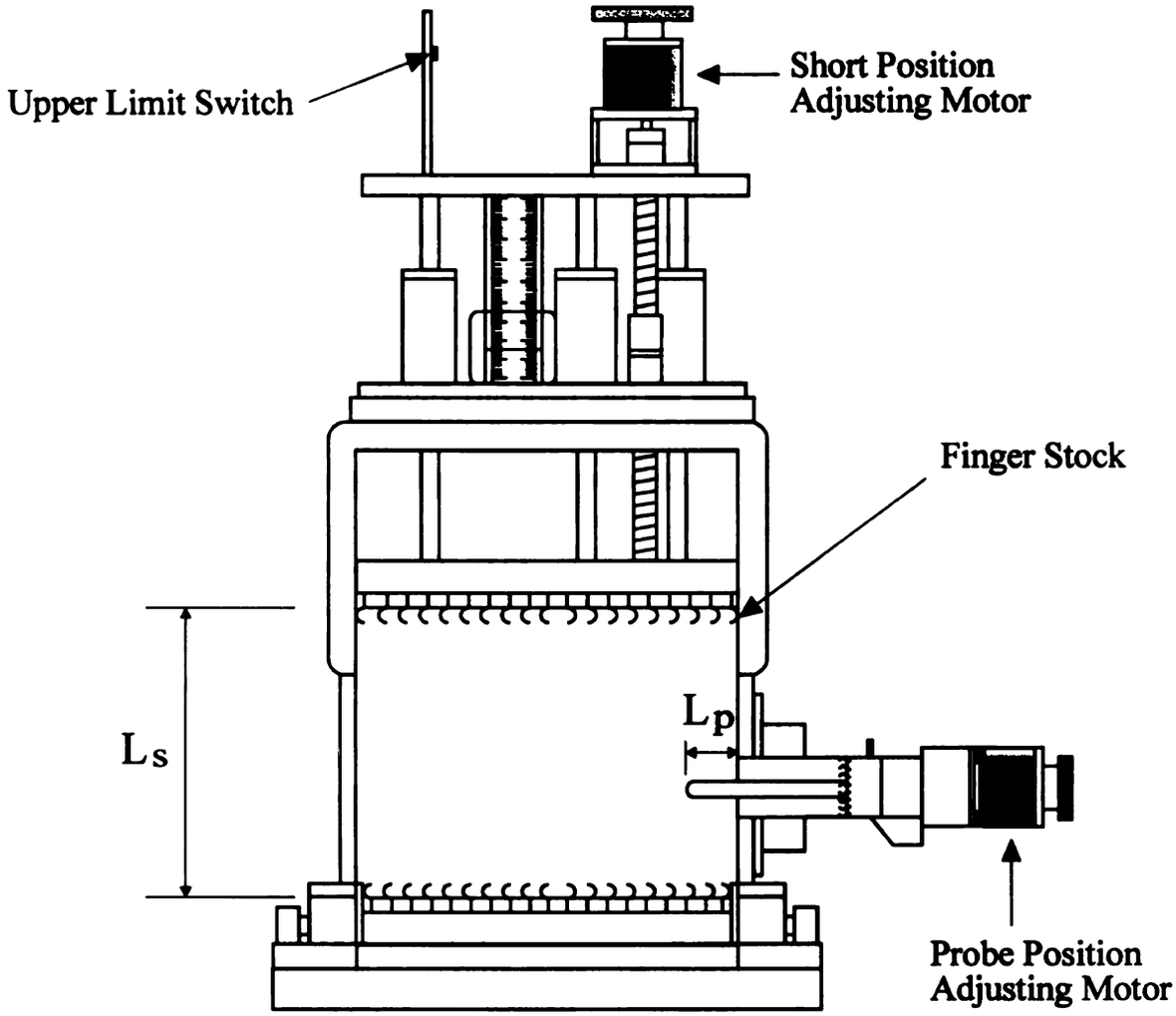

Figure V-2-1. Schematic of a cylindrical single-mode microwave cavity defining the cavity height, L_s, (short position) and probe position, L_p.

rapid change of properties will make the uniform measurement of the reflected power difficult as a function of cavity height to determine the resonance length of the cavity modes available in the cavity. The cavity height was increased by 0.4 mm from 7.3 cm to 21.95 cm by using a computer-controlled stepper motor to displace the moveable top plate of the microwave cavity.

A minimum reflected power reading corresponds to a maximum power absorption by the cavity walls and (when it was present) the casket. The cavity heights corresponding to reflected power minima were compared to theoretical resonance lengths of the cylindrical single-mode cavity at 2.45 GHz.

For an ideal cylindrical cavity (no load and no wall losses) with cavity radius, α, and cavity height, d, the theoretical resonance frequencies, f_o, can be calculated for various modes using an equation expressed as [1, 2]

$$(f_o)_{nml} = \frac{v}{2\pi}\sqrt{\left(\frac{P_{nm}}{\alpha}\right)^2 + \left(\frac{l\pi}{d}\right)^2} \qquad \text{for } TM_{nml} \text{ modes} \qquad (1)$$

where v = speed of light in a medium

= 2.998×10^8 m/sec in free space

P_{nm} = m_{th} x value at which $J_n(x) = 0$

J_n = Bessel function of the First Kind of order n

n = number of periodicity in ϕ direction (n = 0,1,2,3...)

m = number of zero fields in radial direction (m =1,2,3...)

l = number of half-waves in axial direction (l = 0,1,2,3...)

and

$$(f_o)_{nml} = \frac{v}{2\pi}\sqrt{\left(\frac{Q_{nm}}{\alpha}\right)^2 + \left(\frac{l\pi}{d}\right)^2} \qquad \text{for } TE_{nml} \text{ modes} \qquad (2)$$

Q_{nm} = m_{th} x value at which $J_n'(x) = 0$

n = number of periodicity in ϕ direction (n = 0,1,2,3...)

m = number of zero fields in radial direction (m = 1,2,3...)

l = number of half-waves in axial direction (l = 1,2,3,4...).

Using equations 1 and 2, one can construct a mode chart (Figure V-2-2) which gives the theoretical cavity lengths for a range of frequencies, including 2.45 GHz. For an empty (no caskets or other material loaded into the cavity) 7 inch single-mode cavity operated at 2.45 GHz, there are eight or nine expected cavity modes, namely TE_{211}, TM_{111} (TE_{011}), TE_{112}, TM_{012}, TE_{311}, TE_{212}, TE_{113}, and TM_{013} (Table V-2-2 and Figure V-2-2). The TM_{111} mode and TE_{011} mode have the same resonance frequency for a given cavity size, which are called "degenerated modes."

Reflected power measurements at high input power was done during microwave heating. As the casket was heated, the short position, L_s, (i.e. cavity height) was adjusted every 2-3 minutes during the entire heating cycle. In every case, the short position was adjusted to give a minimum reflected power.

2. ELECTRIC FIELD PROBE MEASUREMENTS

An electric field probe was made by soldering a small SMA semi-rigid coaxial cable about 8.5 cm long and 2 mm in diameter to a SMA connector with RG58C/U 50Ω coaxial cable (Pasternack Enterprises, Irvine, CA). The probe was used to determine the

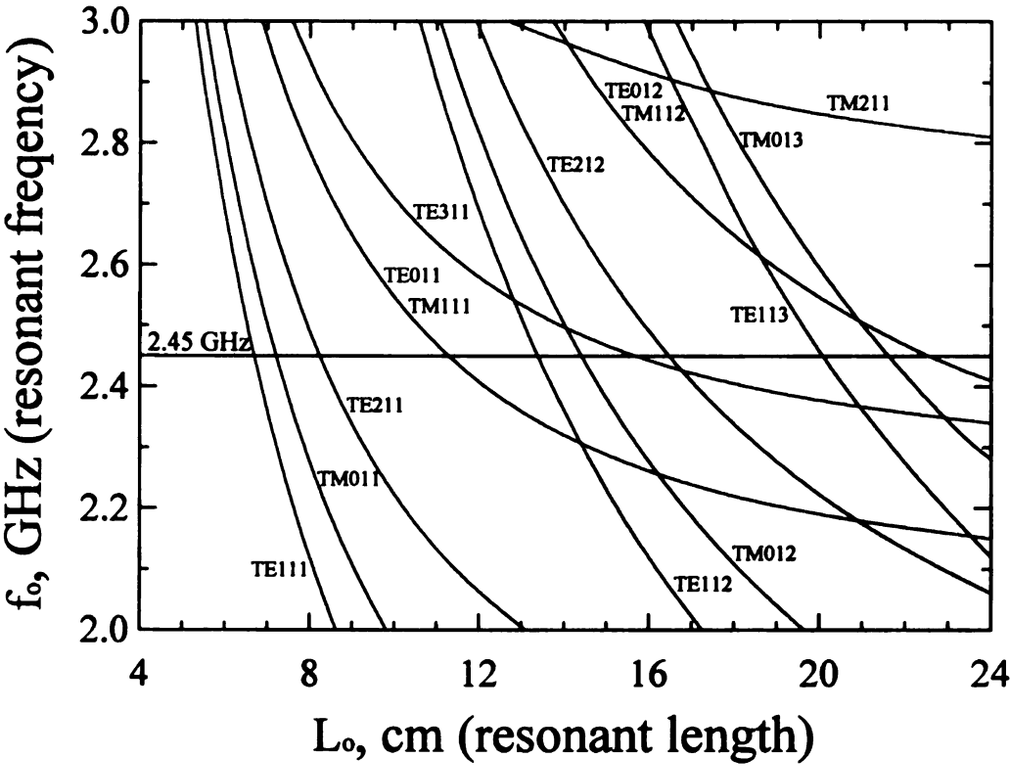

Figure V-2-2. Mode diagram for ideal 7 inch cylindrical single-mode microwave cavity.

Table V-2-2. Summary for the cavity short position (i.e. cavity height), L_s, as a function of the electromagnetic resonance cavity mode, determined at a microwave input power of 50 Watts.

Mode	L_s (cm) for ideal 7" cylindrical empty cavity	L_s (cm) for empty cavity	L_s (cm) for casket 1	L_s (cm) for casket 2	L_s (cm) for casket 3	L_s (cm) for casket 4
TM_{011}	7.21	7.66	*	*	*	*
TE_{211}	8.24	8.43	7.72	8.15	7.47	7.65
TM_{111}	11.29	11.62	9.77	10.32	9.45	9.50
TE_{112}	13.38	13.60	12.83	12.96	12.52	12.80
TM_{012}	14.41	15.13	14.43	14.63	14.30	14.35
TE_{311}	15.71	16.63	15.31	16.26	15.10	15.35
TE_{212}	16.48	17.19	16.20	16.71	16.00	16.17
TE_{113}	20.07	20.46	19.79	19.92	19.49	19.70
TM_{013}	21.62	*	21.76	*	21.34	21.68

* Could not determine, outside the range of the adjustable cavity height

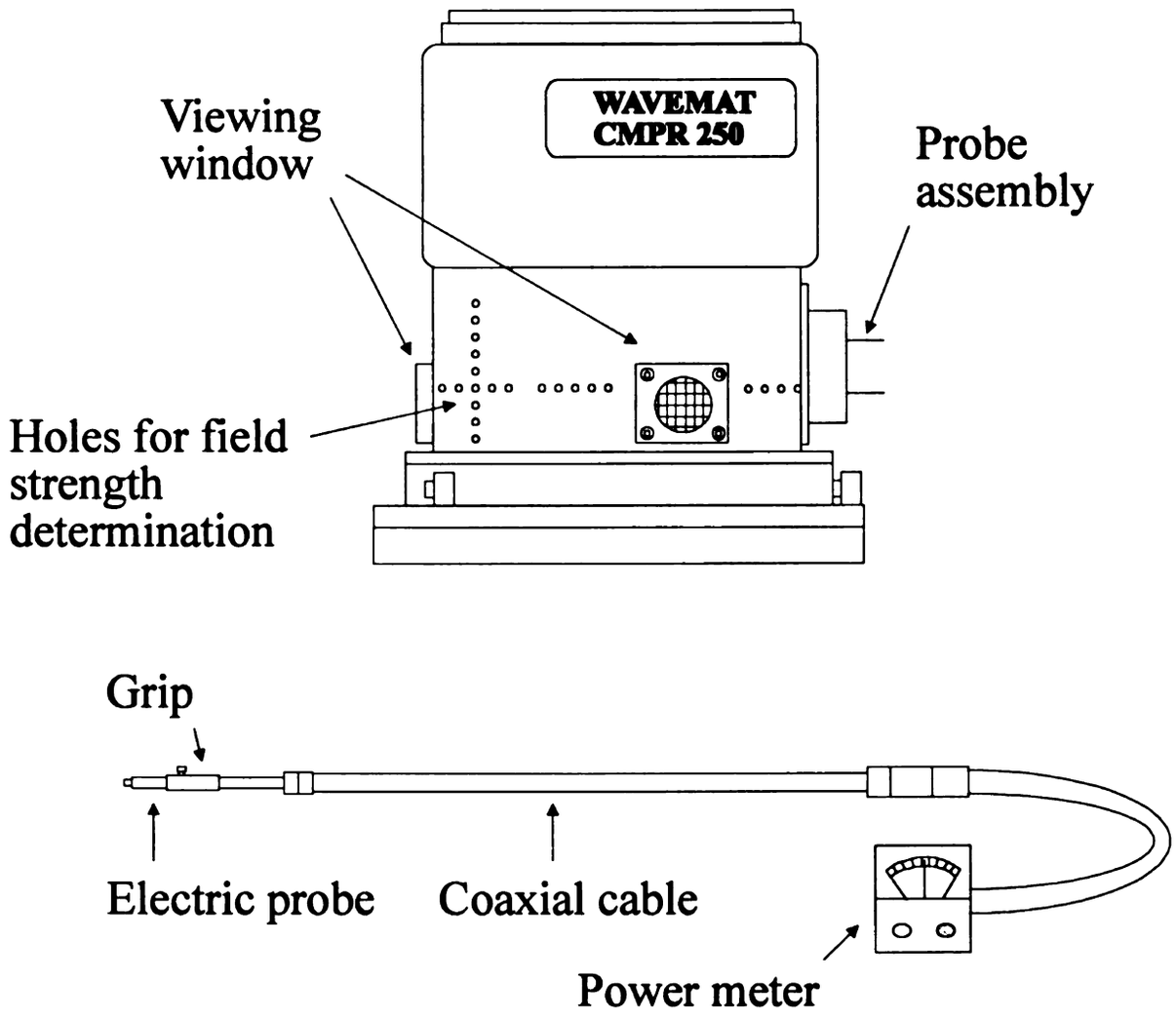

Figure V-2-3. Schematic of single-mode microwave cavity and schematic of electric probe for field strength determination.

radial component of relative electric field strength, E_r, around the cavity wall for various electromagnetic modes (Table V-2-2 and Figure V-2-3).

The empty microwave cavity or the cavity loaded with casket was tuned to a microwave resonant condition with an input power of 50 Watts. The microwave power then was measured using the electric probe as a function of azimuthial and axial positions along the cavity using holes (hole dimensions) in the cavity wall that were provided by the cavity vendor. During the measurements, the probe tip was positioned 1 mm inside from the inner wall of the cavity (Figure V-2-3)

3. HEATING OF MICROWAVE CASKETS

The heating experiments were done in two stages. First, the minimum coupling power was determined at various modes for each of the four caskets in Group 1 listed in Table V-2-1. In this study, the minimum coupling power is defined as a microwave input power required to heat the casket to 500°C within 30 minutes or less. A fixed microwave input power of 50 Watts was fed into the cavity loaded with caskets 1 - 4 (Table V-2-1) in the electromagnetic modes listed in Table V-2-2.

For the caskets in Group 1, the microwave cavity was initially tuned at a minimum coupling power until the caskets began to heat above 500°C. Based on the minimum coupling power determined for TM_{111} cavity mode for the four caskets in Group 1 (which varied from 100 Watts to 130 Watts), for each of the caskets in Group 2 and 3 the cavity was tuned to TM_{111} mode at 120 Watts for initial heating above 500°C (The input power of 120 Watts was sufficient to couple the microwaves to the caskets in Group 2 and 3). Then the microwave input power was increased by 30 Watts every three minutes up to a

maximum power of either 600 Watts or 1000 Watts. This rate of power increase resulted in a relatively slow heating rate ranging from 8°C/min. to 22°C/min. for the temperature range from 500°C to the maximum temperatures depending on casket and operating mode and helped to reduce the thermal gradients with the casket.

4. RESULTS AND DISCUSSION

4.1. Measurements of Reflected Power as a Function of Cavity Height, for Low and High Power Levels

During the low power measurements, for each cavity mode, the short position (i.e. cavity height) shifted as a function of the volume and the geometry of the refractory caskets (Figure V-2-4). The cavity height (short position) corresponding to the minimum reflected power for the apparent modes shifted by less than 1 cm from the theoretical cavity height for the various modes, except for the TM_{111} mode (see Table V-2-2). For the TM_{111} mode the cavity height shifted by up to about 2 cm.

For casket 1, the cavity height changed during microwave heating by up to about 3 cm (Figure V-2-5). The TE modes tend to transfer to TM modes during the tuning process performed during microwave heating. This shift or hybridization of the electromagnetic cavity modes resulted in similar maximum temperatures for adjacent TE and TM modes (Figure V-2-5).

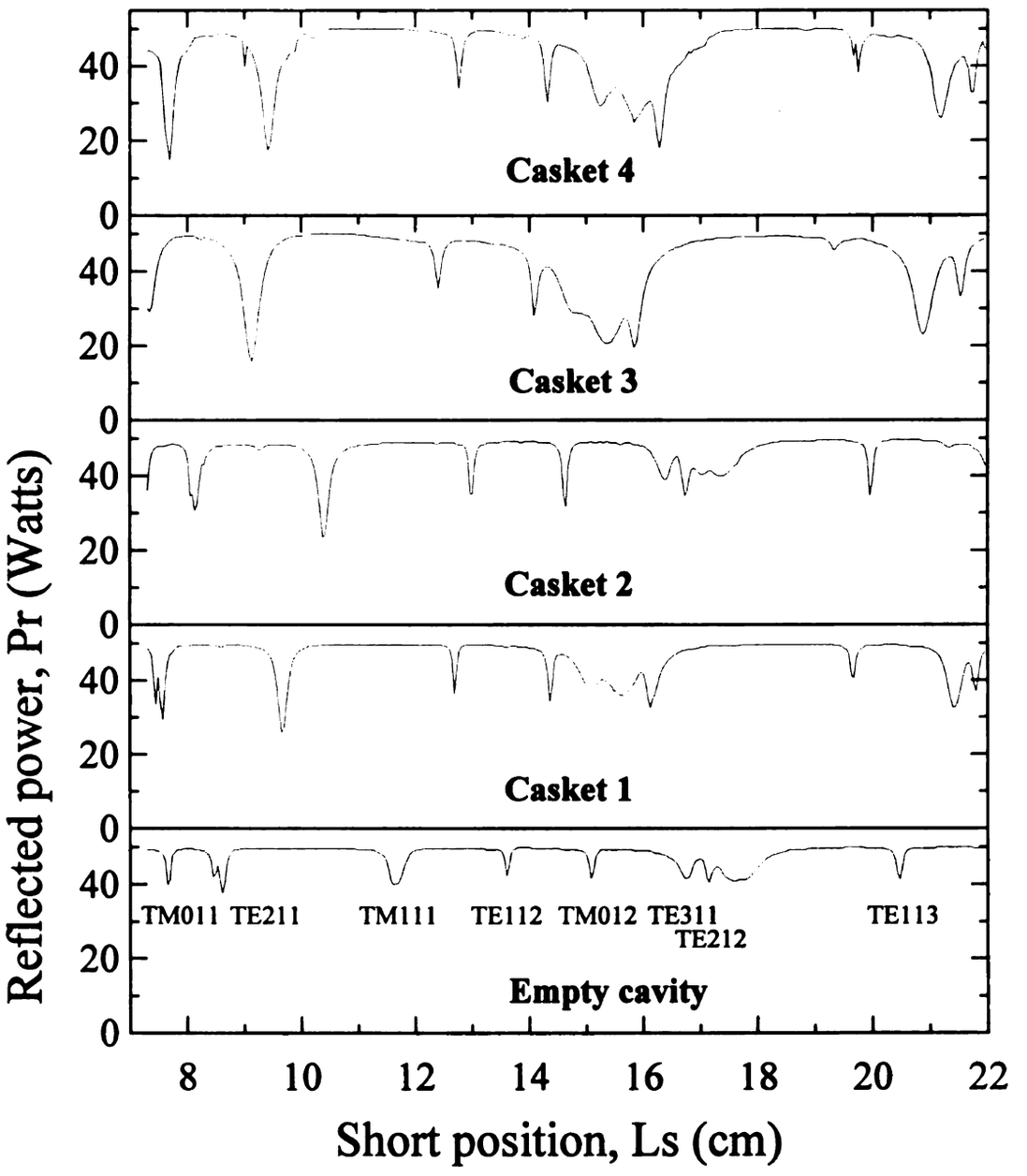

Figure V-2-4. Measurements of reflected power as a function of cavity height.

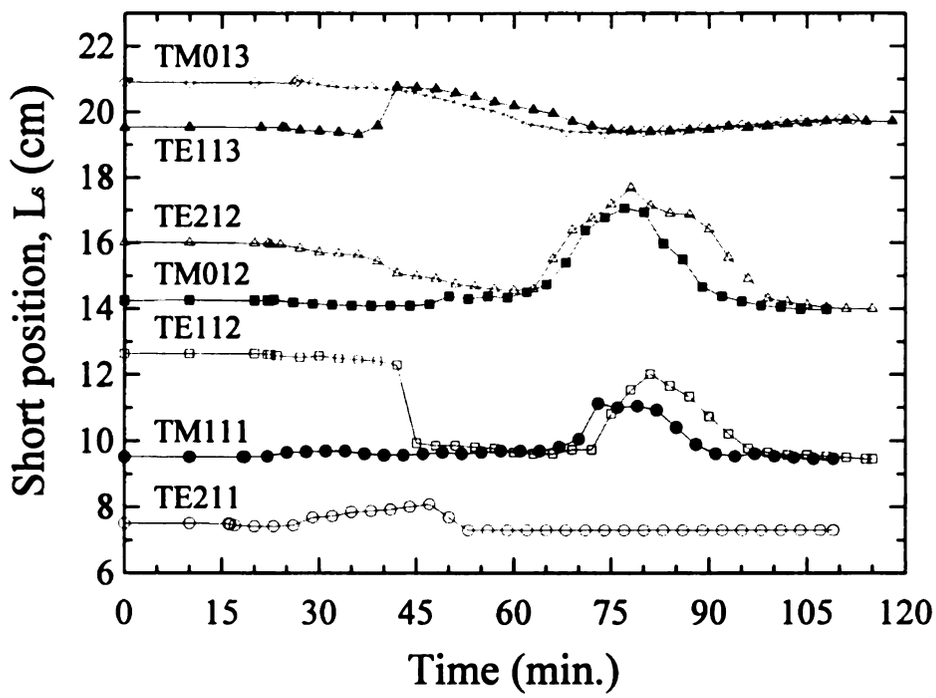

Figure V-2-5. Change of short position, L_s, (i.e. cavity height) as a function of time during microwave heating of Casket 1 at various modes.

4.2. Determination of relative radial component of electric field strength, E_r, around the cavity wall in various modes

The field patterns of relative radial component of electric field strength, E_r, was determined by measuring the power around the cavity wall using an electric probe as a function of positions in both circumferential direction and axial direction (Figure V-2-6). The field patterns of various cavity modes for the cavity loaded with different caskets were similar for the field patterns of the corresponding cavity modes determined for the empty cavity (Figure V-2-6). The determined field patterns allowed us to identify each cavity mode. In particular, the variations in the field pattern as a function of axial direction exactly matches the theoretically expected field patterns. For example, for

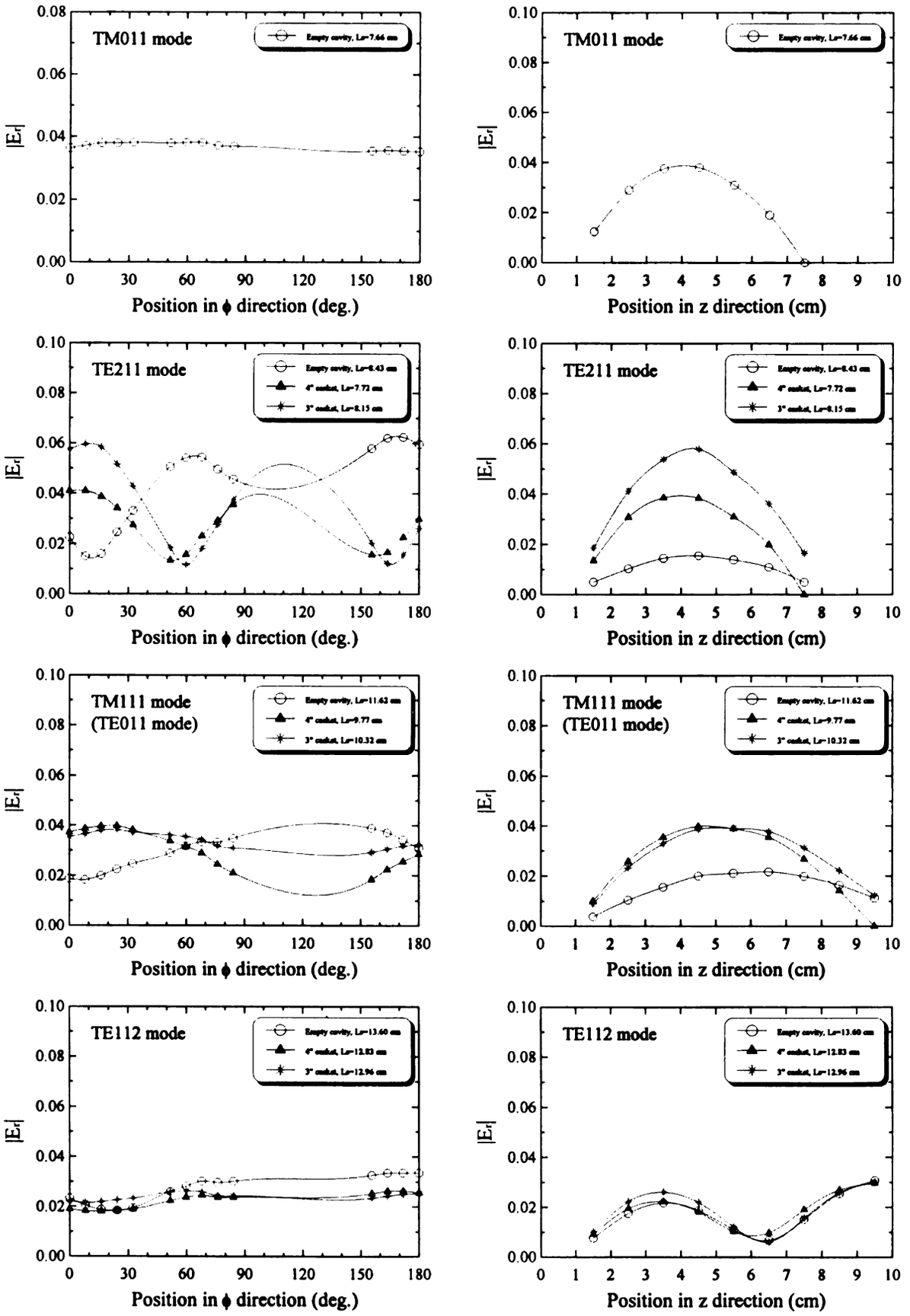

Figure V-2-6a. Relative radial component of electric field strength, E_r, around the cavity wall in various modes.

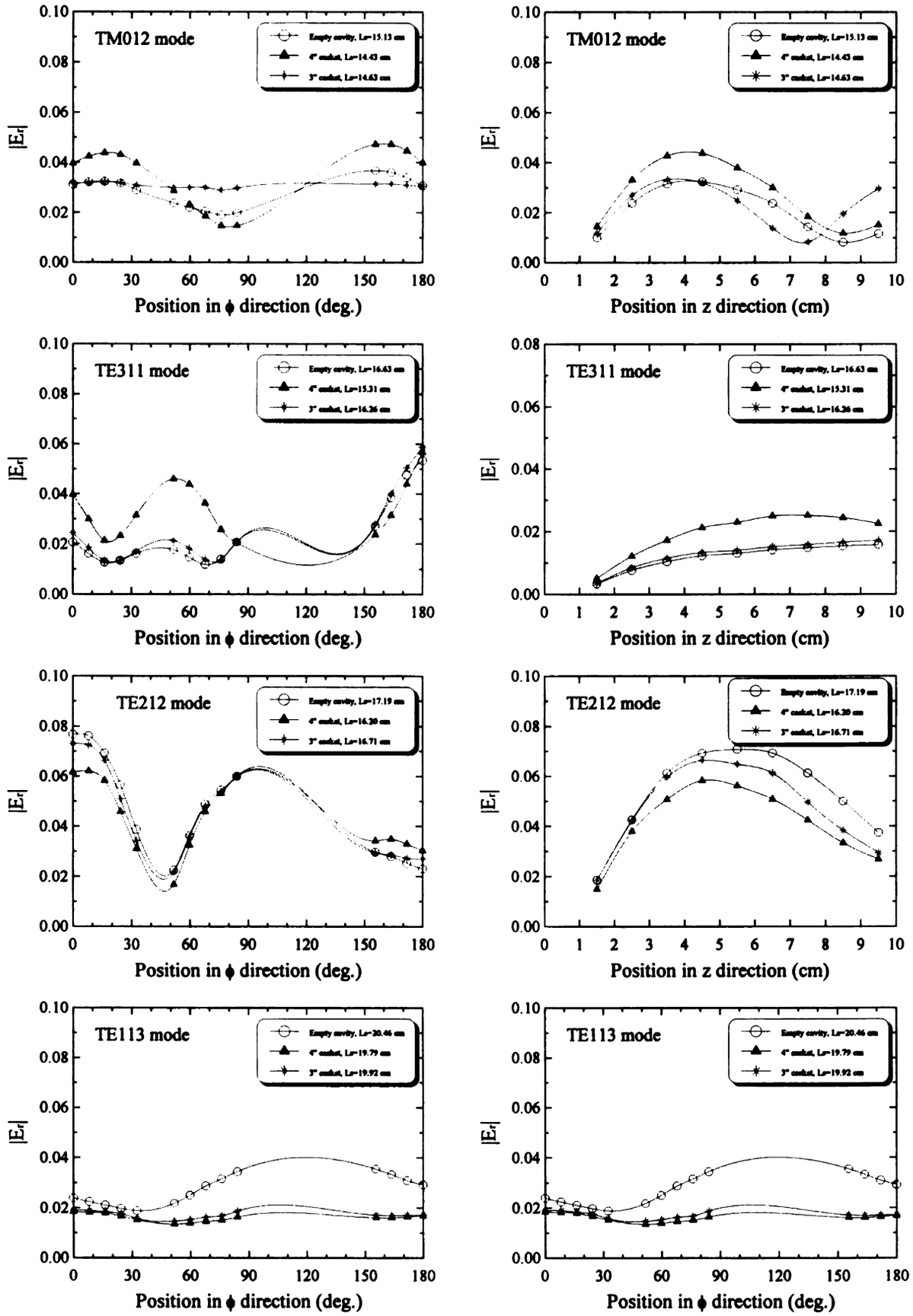

Figure V-2-6b. Relative radial component of electric field strength, E_r, around the cavity wall in various modes.

TE_{112} mode, the third subscript, 2, of the mode notation (which indicates there should exist two half cycles along the axial direction) can be determined for the cavity modes with resonant length of about 13 cm.

4.3. Dependence of heating characteristics on microwave cavity modes

In this study, the cylindrical single-mode microwave cavity was able to heat the caskets to relatively high temperatures in various cavity modes which were set up in the cavity at different cavity height (resonance length) (Tables V-2-3 to V-2-6). Depending on the cavity modes the temperature differed by up to about 230°C at 1000 Watts for Casket 1. The relative percent standard deviation of the temperature for a casket was less than 7% for Casket 3. The heating rate varied by up to about 6.6°C/min. from mode to mode for Casket 4. The highest relative percent standard deviation was about 18% for Casket 4.

5. CONCLUSIONS

For the caskets of various dimensions, the apparent TE modes showed lower minimum coupling power than apparent TM modes. For example, the minimum coupling power for TE modes ranged from 70 to 150 Watts, while for TM modes the minimum coupling power ranged from 100 to 300 Watts.

At high temperatures, the TE modes tend to hybridize into the TM modes as the cavity is tuned.

Table V-2-3. Summary of the heating behavior of Casket 1 (Table V-2-2) for various electromagnetic cavity modes.

Mode	Minimum input power for coupling within 30 min.	Temp. after coupling at minimum power	Temp. at 1000 Watts input power (at 600 Watts)	Average heating rate from 500°C to temp. at 1000 Watts (temp. at 600 Watts)
TE_{211}	80 Watts	658 °C	1248 °C (1055 °C)	8.0 °C/min. (10.7)
TM_{111}	130 Watts	764 °C	1392 °C (1133 °C)	9.8 °C/min. (12.2)
TE_{112}	90 Watts	704 °C	1396 °C (1134 °C)	9.6 °C/min. (12.0)
TM_{012}	150 Watts	814 °C	1454 °C (1186 °C)	11.1 °C/min. (14.9)
TE_{212}	90 Watts	762 °C	1455 °C (1172 °C)	10.3 °C/min. (12.7)
TE_{113}	90 Watts	852 °C	1431 °C (1100 °C)	9.9 °C/min. (11.2)
TM_{013}	170 Watts	870 °C	1478 °C (1134 °C)	11.4 °C/min. (14.2)

Table V-2-4. Summary of the heating behavior of Casket 2 (Table V-2-2) for various electromagnetic cavity modes.

Mode	Minimum input power for coupling within 30 minutes	Temperature after coupling at minimum power	Temperature at 600 Watts input power	Average heating rate from 500°C to temp. at 600 Watts
TE_{211}	80 Watts	685 °C	1520 °C	18.7 °C/min.
TM_{111}	100 Watts	798 °C	1519 °C	19.8 °C/min.
TE_{112}	70 Watts	774 °C	1519 °C	18.7 °C/min.
TM_{012}	220 Watts	1035 °C	1345 °C	21.4 °C/min.
TE_{212}	150 Watts	732 °C	1368 °C	20.0 °C/min.
TE_{113}	80 Watts	882 °C	1406 °C	16.9 °C/min.
TM_{013}	*	*	*	*

Table V-2-5. Summary of the heating behavior of Casket 3 (Table V-2-2) for various electromagnetic cavity modes.

Mode	Minimum input power for coupling within 30 min.	Temperature after coupling at minimum power	Temperature at 600 Watts input power	Average heating rate from 500°C to maximum temp.
TE_{211}	80 Watts	668 °C	1454 °C	17.5 °C/min.
TM_{111}	120 Watts	799 °C	1446 °C	18.9 °C/min.
TE_{112}	70 Watts	762 °C	1255 °C	13.9 °C/min.
TM_{012}	160 Watts	859 °C	1253 °C	16.4 °C/min.
TE_{212}	140 Watts	891 °C	1243 °C	15.5 °C/min.
TE_{113}	80 Watts	858 °C	1334 °C	15.4 °C/min.
TM_{013}	180 Watts	912 °C	1402 °C	20.5 °C/min.

Table V-2-6. Summary of the heating behavior of Casket 4 (Table V-2-2) for various electromagnetic cavity modes.

Mode	Minimum input power for coupling within 30 min.	Temp. after coupling at minimum power	Temperature at 1000 Watts input power (at 600 Watts)	Average heating rate from 500°C to temp. at 1000 Watts (temp. at 600 Watts)
TE_{211}	100 Watts	728 °C	1302 °C (1120 °C)	8.8 °C/min. (11.9)
TM_{111}	130 Watts	807 °C	1309 °C (1112 °C)	8.9 °C/min. (12.1)
TE_{112}	100 Watts	825 °C	1328 °C (1110 °C)	10.2 °C/min. (11.6)
TM_{012}	210 Watts	864 °C	1343 °C (1124 °C)	10.4 °C/min. (15.2)
TE_{212}	110 Watts	826 °C	1361 °C (1122 °C)	9.6 °C/min. (12.6)
TE_{113}	110 Watts	808 °C	1308 °C (1084 °C)	8.9 °C/min. (11.2)
TM_{013}	300 Watts	1020 °C	1303 °C (1062 °C)	11.2 °C/min. (17.8)

Table V-2-7. Temperatures and heating rates averaged for various cavity modes tuned to heat each type of casket.

Casket	Casket 1	Casket 2	Casket 3	Casket 4
Temp. at 600 Watts (°C)	1131	1446	1341	1105
Temp. at 1000 Watts (°C)	1408	*	*	1322
Heating rate from 500°C to max. temp. (°C/min.)	10.0	19.3	16.9	9.7

REFERENCES

1. Y. Liao, Microwave Devices and Circuits, 3rd ed., p. 16-21, p. 133-141, Prentice Hall, Englewood Cliffs, New Jersey (1990).

2. D.M. Pozar, Microwave Engineering, p. 34-38, p. 330-354, Addison-Wesley Publishing Company, Inc., Reading, Massachusetts (1990).

APPENDIX VI. THERMAL ETCHING

Figure VI-1. Surface profile for sintered AKP30 alumina, thermally etched via microwave heating for one hour at 1858K. (a) The surface profile data as displayed on the Digital Instruments AFM used in this study includes markers to analysis features such as the groove depth, as shown here (part a). (b) Line L is the path along which the surface profile data shown in (a) was collected. Triangular symbols in both (a) and (b) designate the same points.

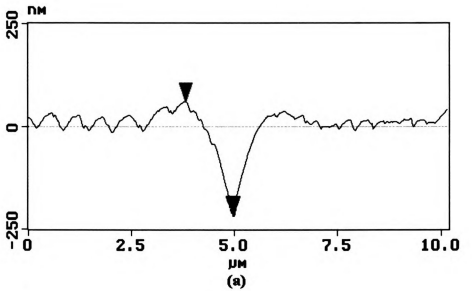

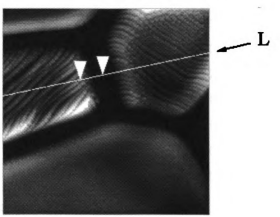

(b)

Figure VI-2. (a) AFM-measured groove width and (b) groove depth as a function of temperature for ADS-995.

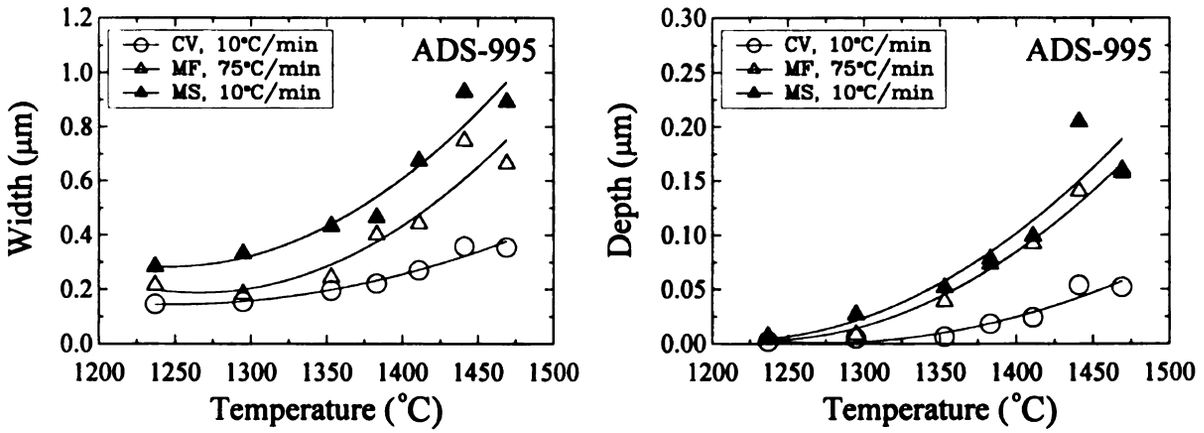

(a) (b)

Figure VI-3. (a) AFM-measured groove width and (b) groove depth as a function of temperature for AKP30.

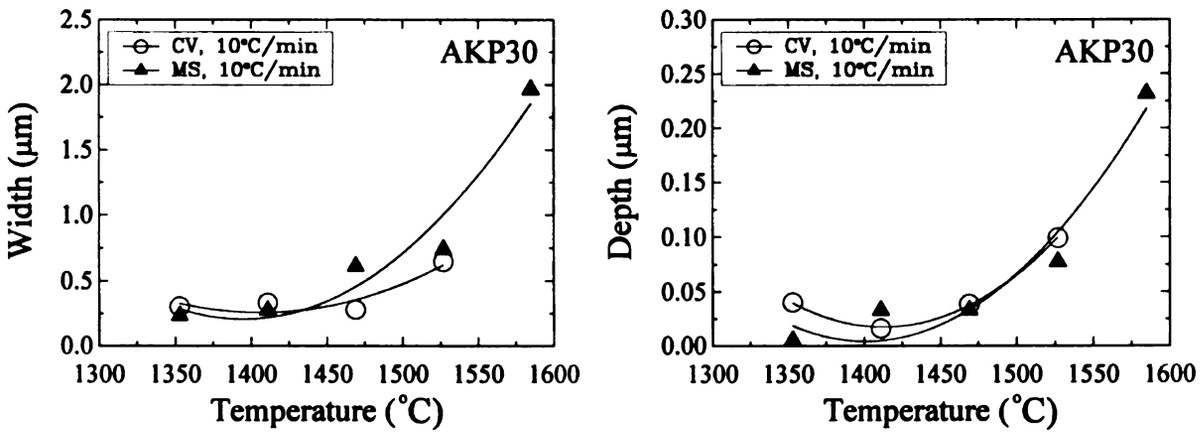

(a) (b)

Figure VI-4. (a) AFM-determined groove profiles of ADS-995 specimens heated in a microwave cavity and (b) - (e) the groove profiles determined by AFM and expected from least-squares fitting by equation 12 in Chapter 6, Part I, obtained from Mullins' theory.

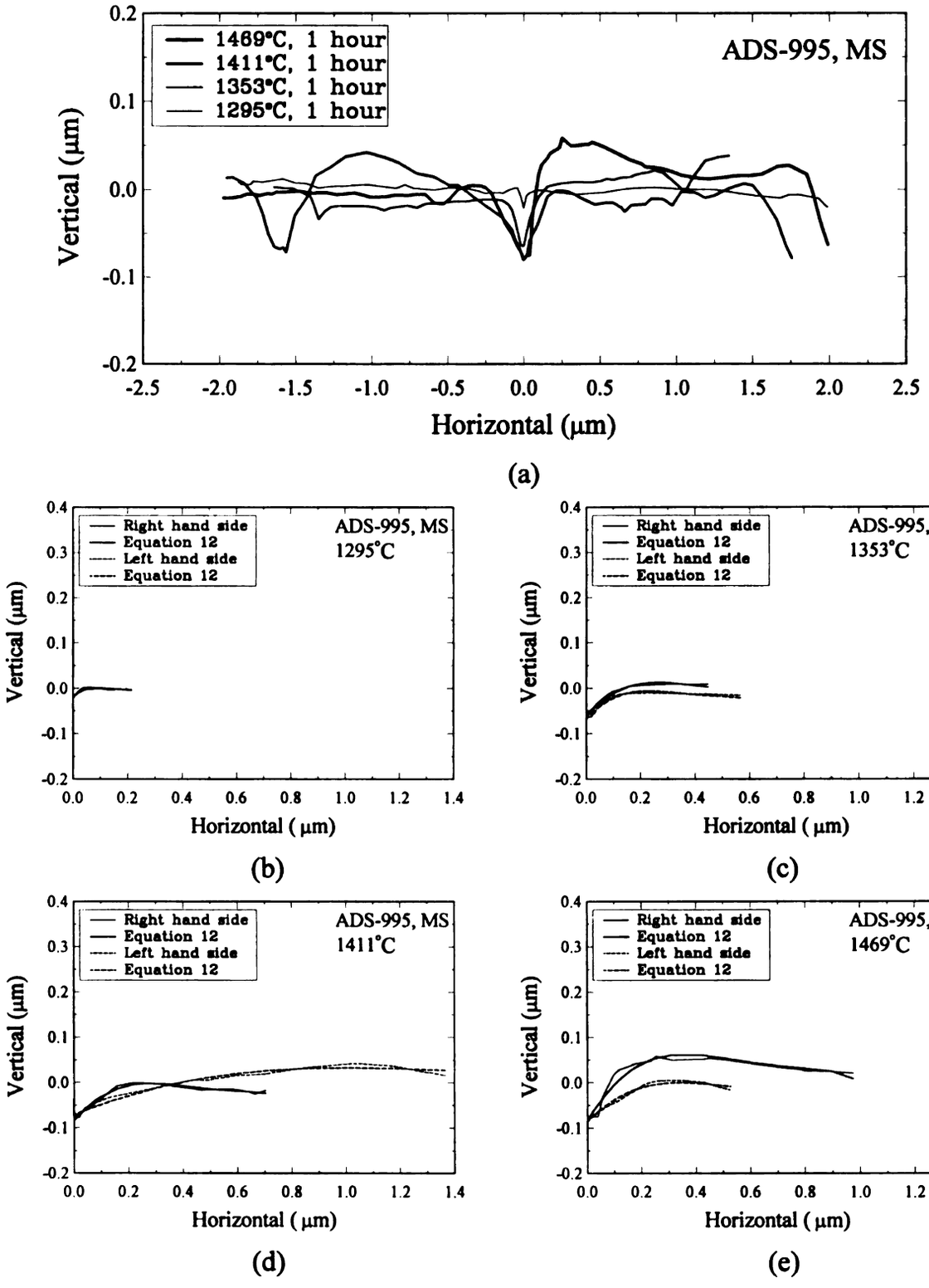

Figure VI-5. (a) AFM-determined groove profiles of AKP30 specimens heated in a conventional furnace and (b), (c) the groove profiles determined by AFM and expected from least-squares fitting by equation 12 in Chapter 6, Part I, obtained from Mullins' theory.

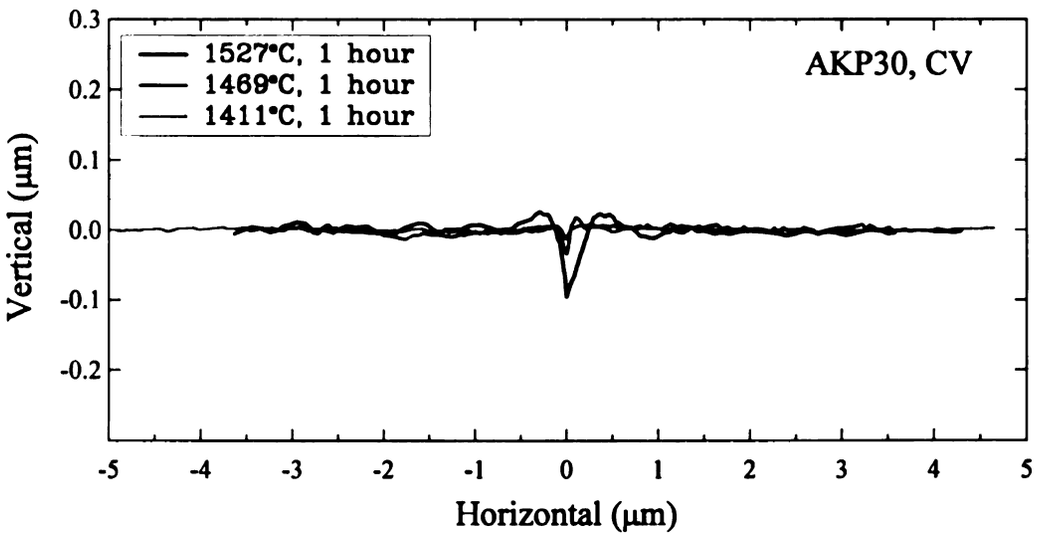

(a)

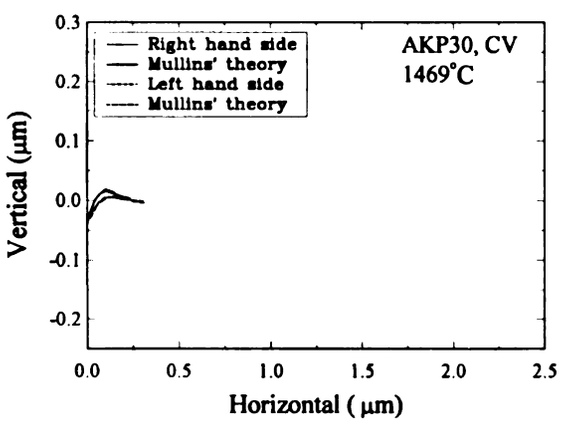

(b)

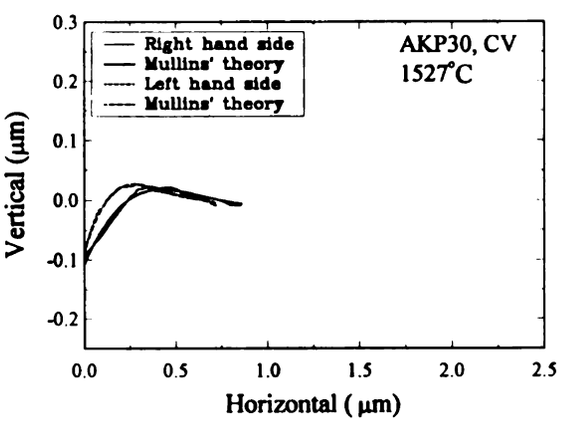

(c)

Figure VI-6. The ratio of AFM-measured groove depth to width, d/w as a function of reciprocal temperature. The curves represent a least-squares linear regression.

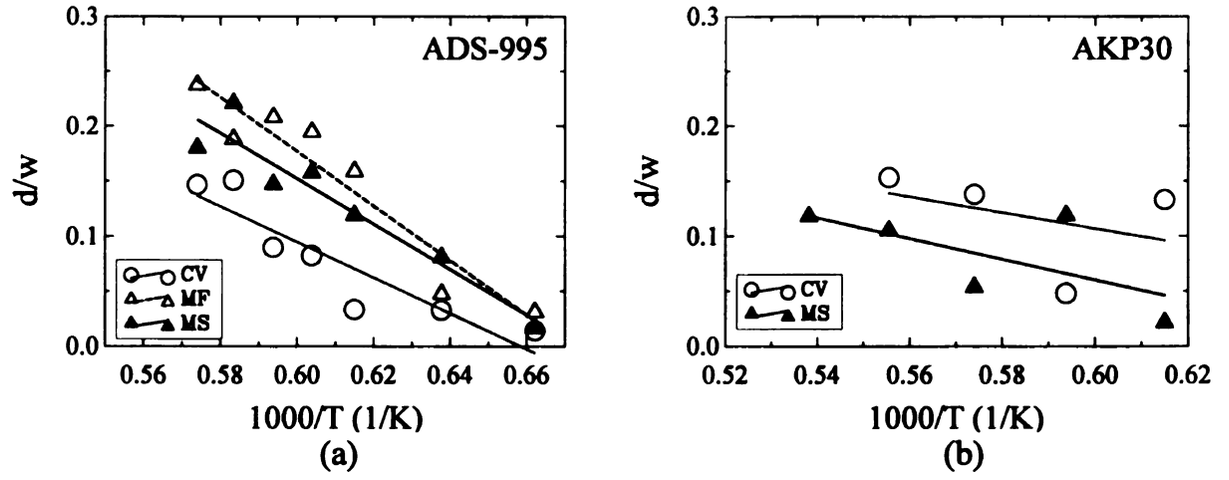

Figure VI-7. Linear thermal expansion coefficient as a function of temperature for polycrystalline α alumina [Wachtman]. The curve in (a) represents data fitting to a fourth order polynomial equation and the curve in (b) represents a linear fit of the data as a function of temperature, T.

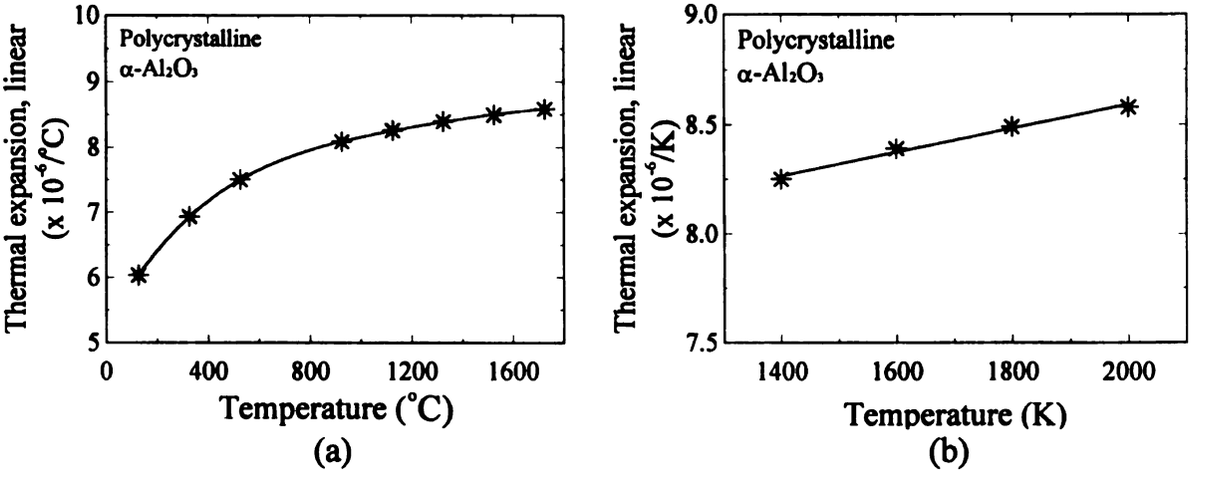

Table VI-1. Surface diffusion coefficients, D_S, calculated using equations 8 and 10 (Chapter 6, Part II) based on measurements of the groove depth & angle, the groove width, and the measured groove depth & angle, calculated by equation 7 (Chapter 6, Part II), respectively.

Material	Process	Temperature (K)	$D_S(d,\psi)$ (cm^2/sec)	$D_S(w)$ (cm^2/sec)	$D_S(d, cal.\psi)$ (cm^2/sec)
Coors ADS-995	CV 10 K/min.	1510	1.66×10^{-10}	7.34×10^{-12}	7.85×10^{-12}
		1568	6.64×10^{-11}	9.49×10^{-12}	1.21×10^{-11}
		1626	3.57×10^{-11}	2.71×10^{-11}	2.69×10^{-11}
		1656	1.65×10^{-10}	4.63×10^{-11}	3.99×10^{-11}
		1684	1.01×10^{-10}	1.06×10^{-10}	1.10×10^{-10}
		1714	8.91×10^{-10}	3.41×10^{-10}	4.05×10^{-10}
		1742	1.79×10^{-09}	3.40×10^{-10}	3.42×10^{-10}
	MF 75 K/min.	1510	9.07×10^{-10}	3.44×10^{-11}	3.13×10^{-11}
		1568	5.97×10^{-11}	1.92×10^{-11}	1.85×10^{-11}
		1626	1.50×10^{-10}	6.61×10^{-11}	5.78×10^{-11}
		1656	1.00×10^{-08}	4.96×10^{-10}	5.00×10^{-10}
		1684	2.97×10^{-09}	7.67×10^{-10}	6.91×10^{-10}
		1714	1.49×10^{-08}	6.50×10^{-09}	6.28×10^{-09}
		1742	1.43×10^{-08}	4.17×10^{-09}	4.16×10^{-09}
	MS 10 K/min.	1510	2.40×10^{-09}	1.04×10^{-10}	1.11×10^{-10}
		1568	6.00×10^{-09}	2.11×10^{-10}	1.90×10^{-10}
		1626	1.44×10^{-09}	6.53×10^{-10}	6.31×10^{-10}
		1656	1.79×10^{-08}	9.06×10^{-10}	8.81×10^{-10}
		1684	4.98×10^{-09}	4.12×10^{-09}	3.77×10^{-09}
		1714	4.13×10^{-08}	1.53×10^{-08}	1.71×10^{-08}
		1742	1.43×10^{-08}	1.36×10^{-08}	1.35×10^{-08}
Sumitomo AKP30	CV	1626	6.80×10^{-10}	1.56×10^{-10}	1.47×10^{-10}
		1684	4.89×10^{-10}	2.43×10^{-10}	2.02×10^{-10}
		1742	4.94×10^{-10}	1.32×10^{-10}	1.29×10^{-10}
		1800	3.68×10^{-08}	4.06×10^{-09}	3.74×10^{-09}
	MS	1626	1.80×10^{-09}	5.31×10^{-11}	4.48×10^{-11}
		1684	5.38×10^{-10}	1.12×10^{-10}	1.07×10^{-10}
		1742	4.44×10^{-09}	3.01×10^{-09}	2.84×10^{-09}
		1800	7.91×10^{-09}	6.87×10^{-09}	6.21×10^{-09}
		1858	1.29×10^{-06}	3.67×10^{-07}	3.39×10^{-07}